Modeling ocean transport and its biogeochemical impacts at global, regional, and sub-meso scales

by

Jing He

B.A., Middlebury College (2017)

Submitted to the Department of Earth, Atmospheric and Planetary Sciences
in partial fulfillment of the requirements for the degree of

Doctor of Philosophy

at the

MASSACHUSETTS INSTITUTE OF TECHNOLOGY

and the

WOODS HOLE OCEANOGRAPHIC INSTITUTION

June 2023

Author .....

Joint Program in Oceanography/Applied Ocean Science and Engineering
Massachusetts Institute of Technology
& Woods Hole Oceanographic Institution
March 17, 2023

Certified by .....

Dr. Amala Mahadevan
Thesis Supervisor
Woods Hole Oceanographic Institution

Accepted by .....

Dr. Amala Mahadevan
Chair, Joint Committee for Physical Oceanography
Massachusetts Institute of Technology
& Woods Hole Oceanographic Institution

Modeling ocean transport and its biogeochemical impacts at global, regional, and sub-meso scales

by

Jing He

Submitted to the Department of Earth, Atmospheric and Planetary Sciences
Massachusetts Institute of Technology & Woods Hole Oceanographic Institution
on March 17, 2023, in partial fulfillment of the
requirements for the degree of
Doctor of Philosophy

Abstract

Improving understanding of how carbon is cycled through the ocean is crucial for predicting, mitigating, and adapting to climate change. This thesis explores how horizontal and vertical currents at different scales impact biogeochemical cycling through the redistribution of tracers such as alkalinity, nutrients, and carbon. Starting at the large scale in Chapter 2, we use a mesoscale-permitting global ocean model to investigate ocean alkalinity enhancement as a negative emissions technology. We find that local ocean dynamics are crucial for determining optimal alkalinity addition locations that maximize carbon removal, while minimizing adverse ecological impacts. Among the best locations identified are coastal upwelling systems, which are also regions of high primary productivity due to the large influx of nutrients to the surface. We take a closer look at coastal upwelling systems in Chapter 3 to identify the dynamics that impact source waters of steady-state upwelling at a regional scale, and we propose a scaling relation in which wind stress and stratification sets the upwelling source depth. Looking more closely at an upwelling front in a high-resolution submesoscale-permitting model, we see enhanced vertical velocities that reach $\mathcal{O}(100$ m $\mathrm{d}^{-1})$. These submesoscale vertical velocities can enhance vertical transport, but they are very difficult to measure. In Chapter 4, we demonstrate the possibility of diagnosing the 3D submesoscale vertical velocity field from remotely-observable surface ocean observations with machine learning, which motivates future satellite missions for high-resolution remote-sensing of the surface ocean. Finally in Chapter 5, we evaluate the importance of resolving smaller scale submesoscale dynamics on the vertical transport of nutrient and phytoplankton carbon biomass in upwelling systems.

Thesis Supervisor: Dr. Amala Mahadevan
Title: Senior Scientist
Woods Hole Oceanographic Institution

Acknowledgments

This PhD would not have been possible without the help from many, many individuals who have impacted my academic journey and life. It is impossible to acknowledge and do justice to everyone, but if you are reading this right now, thank you.

First and foremost, I would like to thank my advisor, Amala Mahadevan, for supporting me over the course of this degree. Her enthusiasm and curiosity always inspires me as to what a scientist should be. Outside the pivotal role she played in guiding me through this thesis, Amala has always encouraged me to participate in extracurricular activities that are not necessarily directly related to this dissertation, but have greatly enriched my educational experience. I feel extremely lucky to learn from and work with such a brilliant, but more importantly, compassionate teacher, supervisor, and mentor.

A chapter of this thesis arose out of an internship project that was supervised by Michael Tyka, and I am very thankful for the opportunity to explore the emerging field of ocean carbon removal technologies with him. It was a pleasure learning and collaborating with him, and seeing a different view of research outside the traditional academia environment.

I am grateful to my committee–Stephanie Dutkiewicz, Eli Tziperman, and Eric D'Asaro–for sharing their valuable time, always being flexible with collaborating across time zones, and for all of their insightful feedback which greatly improved this thesis. Thank you to Glenn Flierl for chairing my defense, for all the work he has put into JCPO, and for generally being such a kind and thoughtful teacher.

The people in the Mahadevan Lab played a huge role in my decision to come to the Joint Program in the first place, and they are some of the reasons why I never regretted my choice. Thank you to all the past and present group members who have been part of my academic family: Mara Freilich, Sebastian Essink, Gualtiero Spiro Jaeger, Mathieu Dever, Kate Lowry, Cynthia Wu, Weiguang Wu, Katy Abbott, Helena Cheslack, Alex Kinsella, and Leo Middleton. I feel extremely privileged to be part of such a diverse research group where I learned so much from everyone, and I always enjoy any work and non-work activities with this group.

There are so many people who work hard behind the scenes to ensure that MIT, WHOI, and the Joint Program run smoothly. I would like to say a big thank you to everyone at Academic Programs Office, the PO front office at WHOI, and MIT EAPS headquarters. A special thank you goes to Kris Kipp, who has become a friend, and part of this work was completed one summer as her neighbor in Vermont.

Even though I had the unfortunate circumstance of being the only PhD PO student in my year, it is thanks to my peers at MIT and WHOI that my PhD experience rarely ever felt lonely. Their support and camaraderie made the past few years much more fun through providing company for lunches, Tosci runs, rock climbing, ski trips, potlucks, swimming at the beach, etc. I particularly would like to thank the Sunfish, the PO students, and my EAPs cohort, including but definitely not limited to: Fiona Clerc, Ellen Lalk, Kevin Doherty, Becca Chmiel, Riss Kellogg, Alia Hidayat, Adrian Garcia, Emmanuel Codillo, Lauren Dykman, Ben Granzow, Kalina Grabb,

Drew Hirzel, Nastasia Winey, Tyler Tamasi, Stephan Gallagher, Joleen Heiderich, Astrid Pacini, Suzi Clark, Sam Levang, Brian Kaiser, Glenn Liu, Michael Dotzel, Alan Gaul, Cora Hersch, Lukas Lobert, Kasturi Shah, Jonathan Lin, and Meghana Ranganathan. In addition, I have received mentoring from Effie Fine and Catherine Wilka, who have become friends and a wonderful long-distance support group over the years.

I am extremely grateful to friends from before and outside of grad school for their unwavering love and support, and for reminding me that there is much more to life outside of the PhD bubble. Some of my longest friendships from middle and high school include Katherine McNamara, Danielle Varnum, Dana Vandeburgh, Melanie Barber, and Tooba Gilani. Angela Wang in particular has been by my side for nearly 20 years, and I look forward to many more decades of friendship. I have been spoiled with always having the best friends as roommates: Emma Office, Brenda Li, Michelle Roman, and Hayle Wesolowski, who made 11 Cameron the most fun first apartment I could have ever asked for. Even though they live far away, I can always turn to Sylvia Al-Mateen, Kali McGown, and Jinseul Jun for anything. Emma Auden kept me company for numerous hours in coffee shops as I wrote this thesis, and I am not sure if I would have finished it otherwise. And to the Snacktasters and friends from college: Rene Gonzales, Christina Shen, Eduardo Alejandro, Francia Martinez, Kit Tse, Lisa Huo, Shannia Fu, Shuba Maniram, Sierra McKenzie, and SteVon Felton, thank you for always supporting from afar and for bringing light into my life during the darkest days of the Pandemic.

My partner, Ahmed Abdelqader, has been with me though all the highs and lows of my PhD, and his never-ending belief in me and my abilities helped carry me through the hardest times. I could not have asked for a better person to experience this and other adventures with. Thank you.

Last but certainly not least, thank you to my Mom and Dad for always giving me so much freedom and independence to explore my interests from a young age, and for always cheering me on no matter what I chose to pursue. Their love and home-cooked meals literally fueled this work, and I am so glad to have been able to live close to home and spend more time with them the past 5 plus years.

Funding for the work in this dissertation came from: NASA FINESST grant 80NSSC19K1350NASA, NASA 80NSSC19K1256, WHOI Academic Programs Office of Endowed Funds, Google, NSF OCE-I434788, ONR N000-14-15-1-2555, and ONR N00014-16-1-2470.

Contents

List of Figures

List of Tables

Chapter 1

Introduction

It can be difficult for many people (even oceanographers), as mostly land-dwellers, to fully appreciate the vastness of the ocean and the out-sized role it plays in our lives. Just looking at carbon storage capacity alone, the ocean contains ∼50 times more carbon than the atmosphere and over 10 times more carbon than in all the plants and soils on land (Friedlingstein et al. 2022). One of the many services we have to thank the ocean for is regulating atmospheric CO_2 concentrations, the leading cause of anthropogenic (human-caused) climate change. The ocean takes up about 30% of human-made CO_2 emissions through fossil fuel burning and land-use change (Fig. 1-1, Friedlingstein et al. (2022)), which is a tremendous help in slowing down global warming, but also comes at the cost of global ocean acidification (Sabine et al. 2004; Gruber et al. 2019). Unfortunately this help is not nearly enough, and we as a society need to rapidly decarbonize and achieve net negative emissions on the order of a few gigatonnes of carbon per year by 2050 to meet the Paris Agreement's ambitious goal of limiting warming to < 2 °C by 2100 (IPCC 2021). Given the ocean's impressive storage capacity and the urgency of our climate crisis, there are increasingly more proposed ocean-based negative emissions technologies (NETs) that aim to speed up and enhance oceanic uptake of CO_2 (National Academies of Sciences and Medicine 2021). However, with all NETs, we need to ensure that we are not doing more harm than good. This is a nontrivial task, as we are still trying to quantify and understand the natural ocean carbon cycle, a complex system in which physics, chemistry, and biology are intimately intertwined.

This dissertation primarily focuses on the physical transport of biogeochemical

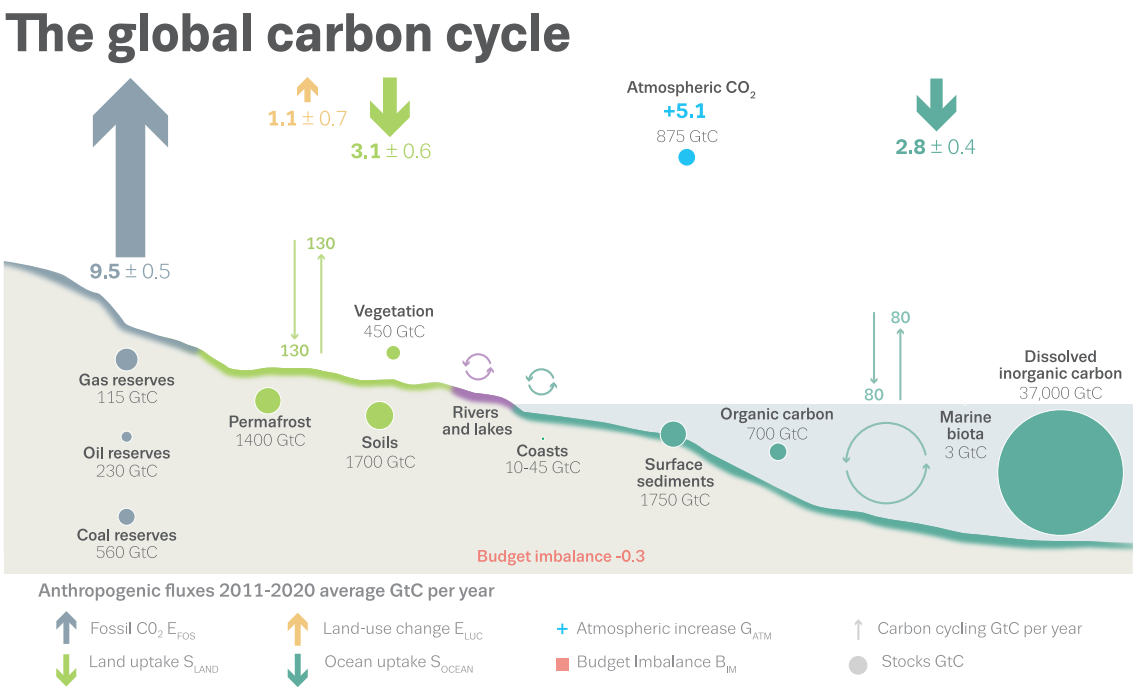

Figure 1-1: Schematic of the global carbon cycle. Bold arrows at the top indicate perturbations caused by anthropogenic activities globally averaged from 2011-2020, while thin arrows indicate fluxes and stocks of the natural carbon cycle. Numbers are all from Canadell et al. (2022), with the exception of carbon stocks in coasts which is from (Price and Warren, 2016). Figure is from Friedlingstein et al. (2022).

tracers that make up the carbon cycle, such as alkalinity, nutrients, dissolved inorganic carbon, and particulate and dissolved organic carbon. The remainder of this introductory chapter provides context for the rest of the thesis by providing an overview of the oceanic carbon cycle, ocean-based negative emissions technologies, and the role of vertical and horizontal transport at different scales.

1.1 The oceanic carbon cycle

The exchange of CO_2 across the air-sea interface depends on the difference in partial pressures of CO_2 (pCO_2) between the atmosphere and ocean. If the pCO_2 is higher in the atmosphere than in the ocean, then CO_2 will dissolve into the ocean. Dissolved $CO_{2(aq)}$ in seawater undergoes a series of chemical reactions that together make up

the carbonate system, described by the equation (Zeebe and Wolf-Gladrow 2001):

$$\begin{aligned} \mathrm{CO_{2(atm)}} &\rightleftharpoons \mathrm{CO_{2(aq)}} + \mathrm{H_2O} \rightleftharpoons \mathrm{H^+} + \mathrm{HCO_3}^- \\ &\rightleftharpoons 2\,\mathrm{H^+} + \mathrm{CO_3}^{2-}. \end{aligned} \tag{1.1}$$

Dissolved $CO_{2(aq)}$ reacts with water to form carbonic acid, which is a weak acid that quickly dissociates into a proton (H^+) and biocarbonate ion (HCO_3^-). Bicarbonate further dissociates into another proton and the carbonate ion (CO_3^{2-}). Carbon is stored in these different dissolved forms (dissolved CO_2, bicarbonate, and carbonate), which together is coined "DIC" for "dissolved inorganic carbon." DIC is the largest pool of oceanic carbon (Fig. 1-1), with higher concentrations at depth, and about 99% of DIC is in the form of bicarbonate and carbonate, due to the large amount of alkalinity in the ocean.

Only the surface ocean, defined as above the thermocline, is in contact with and can equilibrate with the atmosphere. A variety of processes transport carbon from the surface to the deep ocean below the mixed layer to maintain the vertical DIC gradient (low DIC at the surface, high DIC at depth). Depending on the depth of carbon sequestration, the deep ocean can be out of contact from the atmosphere for 100s to 1000s of years (Siegel et al. 2021), making it a potentially long term storage solution on human timescales. Broadly speaking, there are two ways carbon is transported from the surface to deep ocean: the solubility pump, and the biological carbon pump (BCP), which were first identified by Volk and Hoffert (1985). The solubility pump is based purely on chemistry and physics; its premise is that CO_2 is more soluble in cold water, and cold water is denser and tends to sink to the deep ocean. The Biological Carbon Pump, as the name implies, refers to the transport of organic carbon stemming from phytoplankton production (Fig. 1-2). Phytoplankton are microscopic photosynthesizing organisms that make up half of primary production on Earth and form the base of the marine food web. Using sunlight and nutrients, phytoplankton fix inorganic dissolved carbon into organic carbon stored in their cells. This organic carbon can then become part of other organisms that eat phytoplankton,

and the majority of this organic carbon stays in the upper ocean where it is recycled through the microbial loop. A small fraction of the organic carbon is transported to the deep ocean where it is remineralized back to DIC at depth. These various export pathways include (Boyd et al. 2019): gravitational sinking of organic particles such as dead phytoplankton and zooplankton fecal pellets (Sarmiento and Gruber 2006); vertical migration by zooplankton and fish that consume organic matter at the surface at night, and respire the carbon at depth during the day (Steinberg and Landry 2017; Archibald et al. 2019); and physical transport mechanisms including seasonal mixed layer shoaling (Dall'Olmo et al. 2016), large-scale (100-1000 km) physical circulation (Lévy et al. 2013), and subduction driven by mesoscale (10-100 km) and submesoscale (1-10 km) eddies (Lévy et al. 2013; Omand et al. 2015).

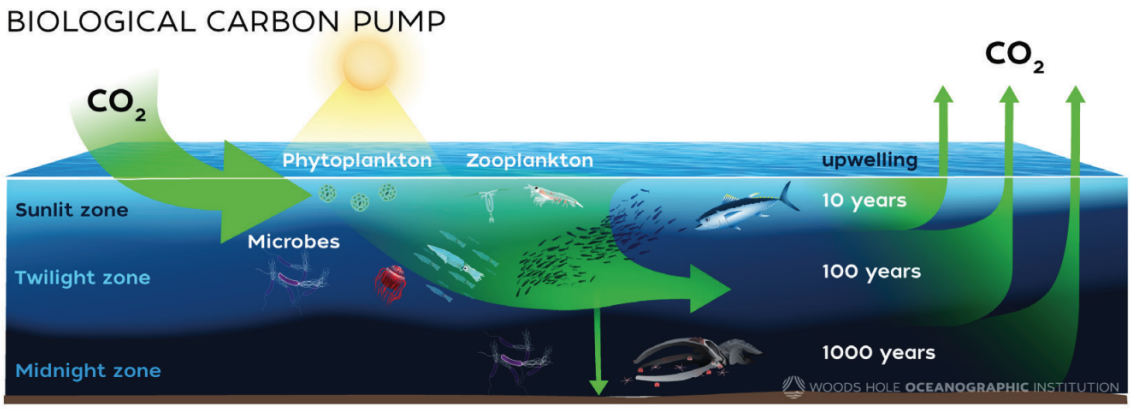

Figure 1-2: Simplified schematic of the biological carbon pump, showing ocean uptake of atmospheric CO_2, phytoplankton growth in the upper sunlit zone, and carbon export to depth. Ocean upwelling eventually brings sequestered carbon back to the surface at different timescales. Figure is from the NASEM Report (2021) and created by Natalie Renier, Woods Hole Oceanographic Institution.

The biological carbon pump is responsible for about 2/3 of the DIC gradient between the surface and deep ocean, while the solubility pump is responsible for the remaining 1/3 (Sarmiento and Gruber 2006). Due to difficulties in measuring carbon fluxes across the entire ocean, model uncertainty, and challenges in resolving all the different pathways from observations and models, there are large uncertainties in the total export rate of the BCP as well as the relative importance of different pathways

(Boyd et al. 2019; Nowicki et al. 2022). Improving our ability to quantify the BCP will be key for better understanding the natural ocean carbon cycle, and how it might change in a warming planet and under different potential NETs.

1.1.1 Ocean-based negative emission technologies

Marine NETs attempt to manipulate some part of the natural carbon cycle to enhance ocean uptake of atmospheric CO_2. The most well-studied NET is iron fertilization, which seeks to increases photosynthesis by phytoplankton, leading to more air-sea draw-down of CO_2, and ideally increased export of organic carbon to depth (National Academies of Sciences and Medicine 2021). The idea of artificial iron fertilization was spurred by Martin (1990)'s hypothesis that natural iron fertilization of the ocean from dust was responsible for the low atmospheric CO_2 levels of the Last Glacial Maximum about 20,000 years ago. This paper prompted a number of experiments, which demonstrated that iron fertilization does indeed lead to enhanced phytoplankton blooms and CO_2 uptake in high nutrient low chlorophyll (HNLC) waters where phytoplankton are limited by iron (De Baar et al. 2005; Boyd et al. 2007; Yoon et al. 2018). But, it is unclear how much increase in export is achieved, and how long the carbon is sequestered for. These questions relate back to the difficulty of measuring and quantifying the BCP, which is crucial for verifying carbon dioxide removal (CDR) projects. In addition, iron fertilization provides a cautionary tale of the need for regulation in the CDR space, as some private rogue actors sought to take advantage and profit off of a method that was not well proven yet (Fountain 2012), leading to potential unintended consequences and widespread public disapproval.

Another CDR method that was first proposed by Kheshgi (1995) and is gaining popularity in recent years is ocean alkalinity enhancement (OAE), which aims to manipulate the inorganic carbonate system in Eqn. 1.1. The idea is that by adding alkalinity—defined as a proton acceptor, such as OH^- (pure alkalinity) or a mineral like limestone ($CaCO_3$) that increases alkalinity when dissolved—to the surface ocean, we shift the equilibrium in Eqn. 1.1 to the right towards more bicarbonate and carbonate, and lowering the concentration of dissolved CO_2 in the ocean. This

increases ocean uptake of CO_2 from the atmosphere. The removed carbon is stored as DIC, which has a residence time of ∼100,000 years, making it an effectively permanent storage solution on human timescales (Renforth and Henderson 2017). Modeling studies have demonstrated that OAE has the potential to uptake and store nearly all anthropogenic emissions, but that leads to drastic increases in the ocean pH and calcite/aragonite saturation state Ω (where $\Omega < 1$ is corrosive to marine organisms with calcium carbonate shells) with unknown ecological consequences. Another major concern is that the increase in saturation state would lead to an increase in calcium carbonate precipitation (the formation of $CaCO_3$ particles) which would sink and remove alkalinity from the surface ocean, counteracting the effect of OAE (Bach et al. 2019). Early microcosm experiments in the North Atlantic surprisingly showed no significant increase in biologically produced $CaCO_3$ even at extreme amounts of added alkalinity addition of +2000 μmol/kg (about doubling the total alkalinity), but broader studies in different regions are still needed (Subhas et al. 2022). While OAE is attracting a lot of attention recently, there are still many big uncertainties and questions regarding its effectiveness, measurement and verification, fate of added alkalinity in the ocean, and unintended consequences, especially if it is to be deployed at scale.

1.2 Role of ocean dynamics

All of the processes mentioned above, including the natural carbon cycle and any human manipulations of it, occur in the context of a moving ocean. Ocean circulation consists of processes operating at a wide range of temporal and spatial scales, ranging from the global thermohaline circulation spanning tens of thousands of kilometers, to turbulence at the molecular scale, and myriad scales in between. Since biogeochemical tracers (e.g. phytoplankton, DIC, alkalinity, nutrients) are carried along with currents and can be transported significant distances, taking the background flow field into account is crucial for understanding biogeochemical cycling.

For instance, the strength of the biological carbon pump is dependent on the phy-

toplankton growth rate, which is controlled from the bottom-up by light and nutrient limitation. Light attenuates exponentially in the water column, and photosynthesis can only occur in the upper sunlit zone (Fig. 1-2) or "euphotic zone," defined as the depth where light is 1% of its surface value. Nutrients are typically depleted at the surface ocean due to photosynthesis and have higher concentrations at depth (Omand and Mahadevan 2015), where they are replenished through bacterial remineralization. Thus, physical processes that vertically transport nutrients from depth into the euphotic zone can lead to enhanced primary production. On the other hand, downwelling of phytoplankton out of the euphotic zone prevents further photosynthesis, but would enhance carbon export depending on how deep the phytoplankton are subducted. Vertical transport is also generally important because of the large vertical gradient in many other properties, such as DIC, alkalinity, and organic carbon, and vertical advection can help to subduct carbon or bring it in contact with the atmosphere.

Vertical transport also relates to the BCP through the concept of "new production," which was first defined by Dugdale and Goering (1967) as the primary production supported by inorganic "new" sources of nutrients, such as nitrate, into the euphotic zone. Nitrate is predominantly supplied to the euphotic zone through upwelling and diffusion, with secondary sources of nitrate stemming from river and sewage runoff, as well as from the atmosphere and through nitrogen fixation (Dugdale and Goering 1967). In contrast, primary production that uses "old" or recycled nutrients that were already in the euphotic zone, such as ammonium NH_4^+ from bacterial remineralization, is termed "regenerated production." In order for phytoplankton to maintain its population at steady state, globally new production must equal the carbon export due to the BCP (Dugdale and Goering 1967; Eppley and Peterson 1979). A simplified schematic of this nutrient cycling in the upper ocean is shown in Fig. 1-3. In sum, the vertical transport of nutrients promotes primary production and specifically new production, which can be an indicator of the strength of the biological carbon pump.

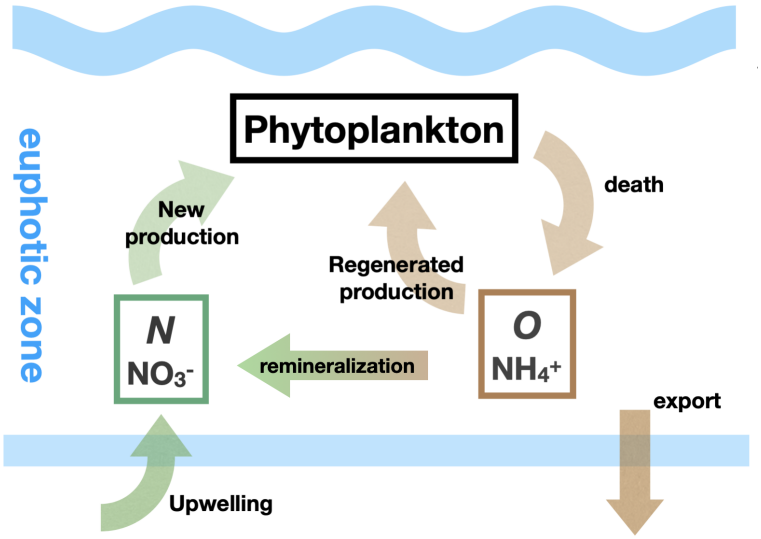

Figure 1-3: Simplified schematic of nutrient cycling in the upper ocean. Here, nitrate N is supplied to the euphotic zone through upwelling, and it supports new production. Phytoplankton die naturally or are consumed through predation and are then remineralized into ammonium or old nutrients O, which supports regenerated production. Ammonium is further remineralized into nitrate. In addition, there is an export of organic matter through the sinking of phytoplankton or zooplankton fecal pellets. In steady state, new production balances export production.

1.2.1 Coastal upwelling

Some of the most biologically productive parts of the ocean, resulting from intense vertical transport of nutrients to the surface, are coastal upwelling regions (Fig. 1-5). It is estimated that coastal upwelling regions make up less than 2% of the ocean's surface area, yet they account for about 11% of the world's oceanic primary production (Chavez and Toggweiler 1995), and the primary productivity in them supports about 20% of global fish catches (Pauly and Christensen 1995). Depending on the location, coastal upwelling regions may sequester copious amounts of CO_2 into the ocean via the BCP (Hales et al. 2005), or they could outgas CO_2 to the atmosphere through the upwelling high DIC waters (Friederich et al. 2008; Torres et al. 2002).

Coastal upwelling is driven by winds blowing parallel to a coast. At steady state, the dominant momentum balance in the surface frictional boundary layer is between rotation and friction. The resulting surface ocean velocity is not in the same direc-

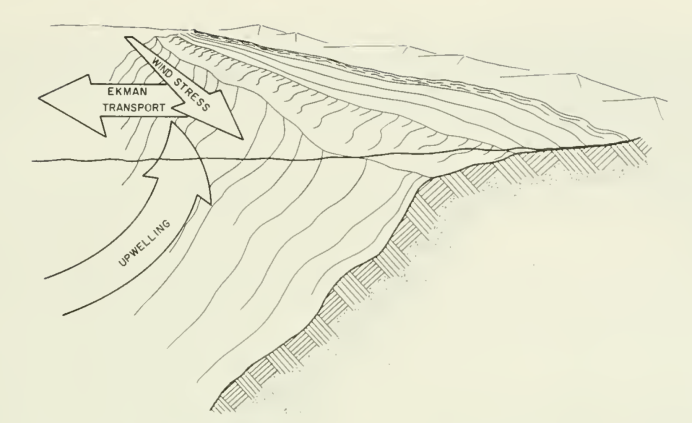

Figure 1-4: Coastal upwelling schematic, from Bakun (1973).

tion of the wind, but 45° to the right (left) of the wind in the Northern (Southern) Hemisphere, and the ocean velocity rotates with depth in the surface boundary layer (Ekman 1905). The depth integrated transport in the boundary layer (also known as the Ekman layer) is given by $\tau/\rho f$, where τ is the wind stress, ρ is the seawater density, and f is the Coriolis parameter. This depth-integrated transport is referred to as "Ekman transport." When this theory is applied to equatorward winds blowing parallel to eastern boundaries, also known as Eastern Boundary Upwelling Systems (EBUS) (Fig. 1-5a), the Ekman transport is directed offshore and is balanced by upwelling from depth (Fig. 1-4). The upwelling rate is equal to the offshore Ekman transport because of continuity, and this coastal upwelling occurs largely within a Rossby radius of the coast.

Ekman transport theory has been broadly applied to quantify upwelling strength based on the magnitude of the alongshore wind stress (e.g., Huyer 1983; Bakun 1990; Sydeman et al. 2014). Coastal upwelling is extensively well-studied in the literature, and there have been many expansions of Ekman theory to take into account the cross-shore structure of the wind and wind-stress curl driven upwelling, and the influence of onshore geostrophic currents (Estrade et al. 2008; Marchesiello and Estrade 2010; Rossi et al. 2013; Jacox et al. 2018). Ekman transport alone is not always a good indicator of nutrient upwelling and new production though, because that relies on not just the upwelling strength, but also the nitrate concentration of upwelled source

waters (Jacox et al. 2018). Furthermore, mixing of upwelled waters with surface waters is important for allowing phytoplankton growth, because if we adiabatically upwell water deplete of phytoplankton, then the surface phytoplankton is advected offshore and cannot access the nutrients. What sets the upwelling source depth, how might we expect it to change in a warming climate, and what impacts does that have on quantifying the upwelling nutrient flux and new production, are some of the motivating questions for Chapters 3 and 5.

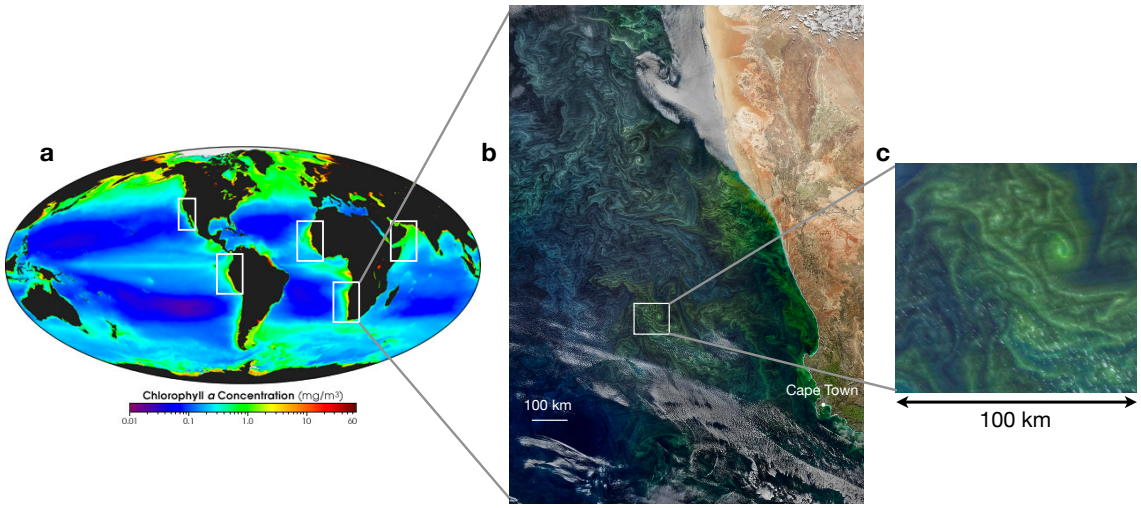

Figure 1-5: Example of chlorophyll variability across different spatial scales. a) On a global scale, climatological chlorophyll-a concentrations are low in oligotrophic subtropical gyres and enhanced in coastal upwelling regions (highlighted in boxes), as well as in the Southern Ocean and the North Atlantic. Chlorophyll data is from NASA SEAWIFS climatology. b) Zoom into the Benguela Upwelling System of the coast of Southwest Africa, ocean color image is from Aqua/MODIS on Sep. 2, 2017. c) Zooming in to a 100 km by 100 km patch in the Benguela Upwelling System reveals chlorophyll structures on the scale of 1-10 km.

1.2.2 Submesoscale vertical transport

If we look closely at an ocean color image from a coastal upwelling region, such as the Benguela Upwelling System in Fig. 1-5b, we clearly see the ubiquity of mesoscale eddies, which have spatial scales on the order of the Rossby deformation radius and nearly in geostrophic balance (the balance of the pressure gradient force and rota-

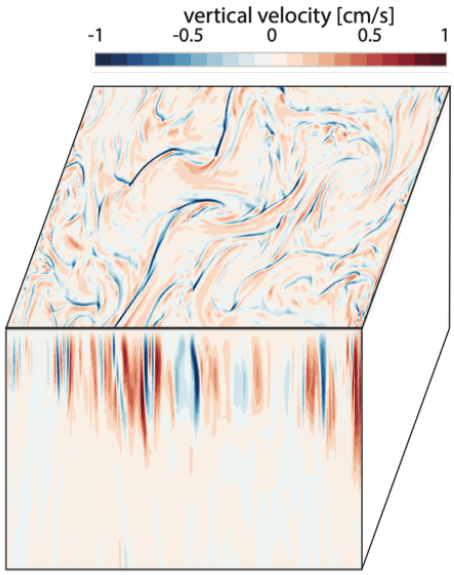

Figure 1-6: Example of a model submesoscale vertical velocity field. Figure from Mahadevan, 2019. Encyclopedia of Ocean Sciences.

tion). If we zoom in even further to a 100 km $\times$ 100 km patch of ocean in this upwelling system, we find even smaller eddies and filaments with scales of 1–10 km. This smaller scale is aptly named "submesoscale," which is dynamically defined as having $\mathcal{O}(1)$ Rossby and Richardson numbers. The Rossby number is a dimensionless number representing the ratio of advection to rotation, while the Richardson number represents the ratio of stratification to vertical shear. Thus, submesoscale phenomena are not as constrained by rotation as geostrophic currents, allowing for enhanced vertical velocities w of up to $\sim$100 m d^{-1}, an order of magnitude larger than mesoscale w (Thomas et al. 2008). Another characteristic of submesoscale vertical velocities is that they are skewed to have more intense downwelling velocities concentrated in thin filaments, with weaker upwelling velocities spread over a larger area (Shcherbina et al. 2013), as can be seen in Figure 1-6.

An open question is to what extent do submesoscale dynamics affect the larger scale ocean state. Submesoscale dynamics may be particularly important for primary production because biological timescales align with submesoscale time scales (Freilich et al. 2022; Mahadevan 2016). Recent studies also indicate that resolving the submesoscales is important for the vertical transport of heat, carbon, and nutrients between

the surface and deep ocean (e.g. Omand et al. 2015; Su et al. 2018; Ruiz et al. 2019; Uchida et al. 2019), as their effects are not fully parameterized in coarser resolution global ocean or climate models. On the other hand, Resplandy et al. (2019) finds that while submesoscale eddies lead to local hotspots of intense carbon subduction, they contribute very little to the annual carbon flux on a regional scale due to compensation between upward and downward fluxes. A challenge to studying the effects of submesoscale dynamics on vertical transport is the difficulty in measuring the very small and noisy vertical velocity over a large region. Chapters 4 and 5 aim to make progress on this front.

1.2.3 Horizontal transport

In addition to vertical transport, we would be remiss to not also mention the important role lateral advection and diffusion plays in transporting and dispersing biogeochemical tracers large distances in the ocean. The ocean has a very small aspect ratio given by D/L, where D is the depth and L is the horizontal scale. Consequently, horizontal motions are often orders of magnitude larger than vertical motions, which are also constrained by the ocean's stratification. The ability of ocean currents to rapidly transport and disperse material has been topic of interest that has been studied for decades (Richardson and Stommel 1948; Ebbesmeyer and Ingraham Jr 1994), with many applications ranging from nuclear waste discharge (Rypina et al. 2013) to larval dispersal (Pineda et al. 2007). It is no surprise that lateral transport is also important to consider in the context of NETs that involve adding material into the ocean that will carried far distances by currents, such as alkalinity. Moreover, ocean currents are extremely diverse across the globe, ranging from persistently strong strong western boundary currents, to currents that reverse seasonally with the Monsoon in the Arabian Sea and Bay of Bengal, and all the eddies in between (Fig. 1-7). In Chapter 2, we investigate what this variability in ocean dynamics at a global level means for coastal ocean alkalinity enhancement.

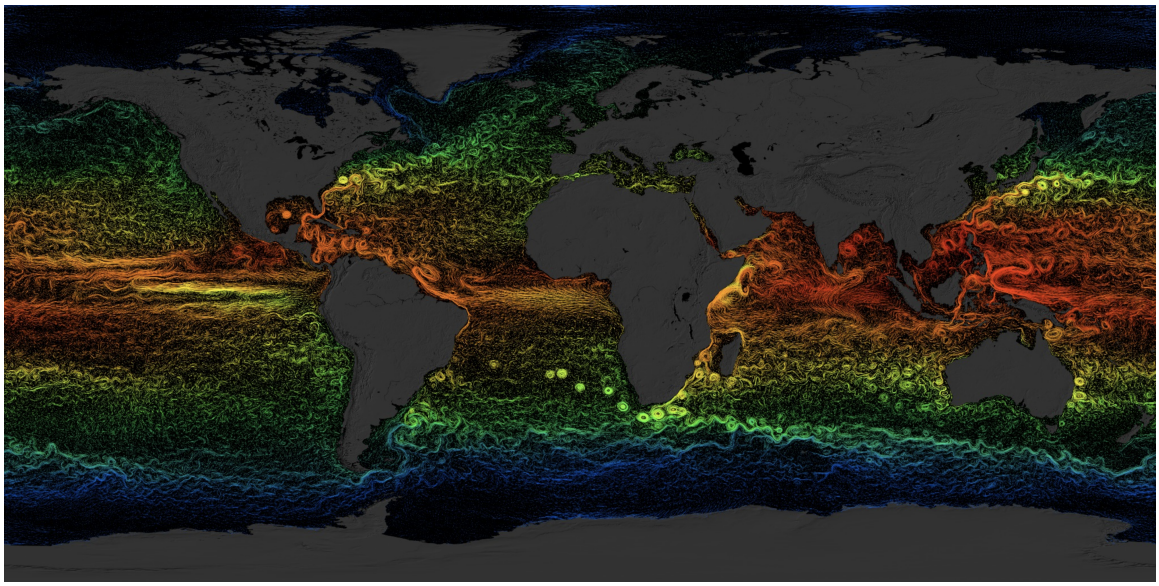

Figure 1-7: Global ocean sea surface temperature and currents from Estimating the Ocean Circulation and Climate, Phase II (ECCO2). Lines indicate sea surface currents, and they are colored by sea surface temperature, with reds indicating warmer temperature and blues representing colder temperatures. The horizontal resolution is 0.25°. Image is from NASA Scientific Visualization Studio.

1.3 Overview of thesis

This thesis contains four chapters that altogether contribute to improving our understanding of the role of physical transport in the ocean carbon cycle. More basic science understanding of the ocean carbon cycle is needed, and this work contributes to improving fundamental estimates of vertical nutrient transport and carbon export in highly productive coastal upwelling systems, which are of relevance to the ocean's natural biological carbon pump. At the same time, we cannot wait to act on climate change, so in parallel with basic science research, studies of negative emissions technologies are also needed. This work contributes to the latter by exploring the feasibility and practical constraints of coastal ocean alkalinity enhancement.

Starting at the global scale, in Chapter 2 we use a mesoscale-permitting global ocean model to investigate ocean alkalinity enhancement as a negative emission technology, and we find that local ocean dynamics are crucial for determining optimal alkalinity addition locations that maximize carbon removal while minimizing adverse

impacts on the local ecology. Among the best locations identified are coastal upwelling regions, which are also regions of high primary productivity due to large vertical transport of nutrients. We take a closer look at coastal upwelling systems in Chapter 3 to identify the dynamics that impact source waters of steady-state upwelling at a regional scale, and we find that wind stress and stratification sets the depth of upwelling. Zooming in even further on the coastal upwelling front, in a submesoscale-permitting model, enhanced vertical velocities at fine-scale fronts, eddies, and filaments have the potential for enhanced vertical transport, but are difficult to observe. In Chapter 4, we demonstrate that it is possible to diagnose the 3D submesoscale vertical velocity from remotely-observable surface ocean data using machine learning, which movtivates existing and future satellite missions for high-resolution remote-sensing of surface ocean. Finally in Chapter 5, we evaluate the impacts of the source depth theory and predicted 3D w field on nutrient upwelling and carbon export. We summarize the thesis and provide an outlook for future directions of research in Chapter 6.

Chapter 2

Limits and CO_2 equilibration of near-coast alkalinity enhancement

Abstract

Ocean alkalinity enhancement (OAE) has recently gained attention as a potential method for carbon dioxide removal (CDR) at gigatonne (Gt) scale, with near-coast OAE operations being economically favorable due to proximity to mineral and energy sources. In this paper we study critical questions which determine the scale and viability of OAE. Which coastal locations are able to sustain a large flux of alkalinity at minimal pH and Ω_{Arag} (aragonite saturation) changes? What is the interference distance between adjacent OAE projects? How much CO_2 is absorbed per unit of alkalinity added? How quickly does the induced CO_2 deficiency equilibrate with the atmosphere? Choosing relatively conservative constraints on ΔpH or $\Delta\Omega_{\mathrm{Arag}}$, we examine the limits of OAE using the ECCO LLC270 (0.3°) global circulation model. We find that the sustainable OAE rate varies over 1–2 orders of magnitude between different coasts and exhibits complex patterns and non-local dependencies which vary from region to region. In general, OAE in areas of strong coastal currents enables the largest fluxes and depending on the direction of these currents, neighboring OAE sites can exhibit dependencies as far as 400 km or more. At these steady state fluxes most regional stretches of coastline are able to accommodate on the order of 10s to 100s of megatonnes of negative emissions within 300 km of the coast. We conclude that near-coastal OAE has the potential to scale globally to several Gt CO_2 yr^{-1} of drawdown with conservative pH constraints, if the effort is spread over the majority of available coastlines. Depending on the location, we find a diverse set of equilibration kinetics, determined by the interplay of gas exchange and surface residence time. Most locations reach an uptake efficiency plateau of 0.6–0.8 mol CO_2 per mol of alkalinity after 3–4 years, after which there is only slow additional CO_2 uptake. Regions of

This chapter was originally published as He, J., and M. D. Tyka, 2023a: Limits and CO_2 equilibration of near-coast alkalinity enhancement. *Biogeosciences*, **20**, 27–43, doi: 10.5194/bg-20-27-2023

significant downwelling (e.g., around Iceland) should be avoided by OAE deployments, as in such locations up to half of the CDR potential of OAE can be lost to bottom waters. The most ideal locations, reaching a molar uptake ratio of around 0.8, include North Madagascar, California, Brazil, Peru and locations close to the Southern Ocean such as Tasmania, Kerguelen and Patagonia, where the gas exchange appears to occur faster than the surface residence time. However, some locations (e.g., Hawaii) take significantly longer to equilibrate (up to 8–10 years) but can still eventually achieve high uptake ratios.

2.1 Introduction

To mitigate the worst effects of climate change, the Paris Agreement aims to limit global temperature warming to below 2 °C. This requires not only rapid decarbonization, but also negative CO_2 emission technologies (NET) (Rogelj et al. 2018). About 150–800 $GtCO_2$ of net negative emissions are needed in the IPCC SSP1-1.9–SSP1-2.6 scenarios (in addition to decarbonization) to limit global warming to 2 °C by 2100, and this scenario further assumes net negative annual emissions towards the end of the century (Rogelj et al. 2018; Metz et al. 2005; IPCC 2021).

On geological time scales the Earth regulates atmospheric CO_2 concentrations by the combined action of surface rock weathering and ocean CO_2 uptake (Penman et al. 2020). High CO_2 conditions lead to elevated temperatures and an intensified hydrological cycle, which increases silicate rock weathering (Archer et al. 2009). The subsequently dissolved alkalinity increases the ocean's capacity for CO_2 and the excess atmospheric CO_2 dissolves into the ocean, largely reacting to form (bi)carbonate ions (Zeebe and Wolf-Gladrow 2001). Indeed the ocean's total dissolved inorganic carbon (DIC) exceeds that of the current atmosphere by 50-fold (Sarmiento and Gruber 2006).

This mechanism operates on a 10–100 ka time scale (Archer et al. 2009), limited by the slow intrinsic kinetics of silicate rock dissolution and the slow introduction of unweathered rock. Exposure of fresh igneous rocks has been linked to rapid cooling of the Earth's past climate (Gernon et al. 2021). Unfortunately, this natural homeostat operates too slowly to mitigate anthropogenic climate change this century. Ocean alkalinity enhancement (OAE) (Renforth and Henderson 2017) is a proposed approach to accelerate this process in order to increase the ocean's capacity for CO_2 and draw down some of the anthropogenic atmospheric CO_2.

The kinetics of rock dissolution can be accelerated in a number of ways. The simplest approach is to increase the rock's surface area through grinding. Powdered rocks such as olivine can then be added to the ocean and will dissolve over the course of years to decades, adding alkalinity (Hangx and Spiers 2009; Schuiling and De Boer

2011; Renforth 2012; Montserrat et al. 2017; Rigopoulos et al. 2018; Meysman and Montserrat 2017). Alternatively, some rocks (e.g., $CaCO_3$) may be preprocessed by calcining, transforming them into more rapidly dissolving substances, such as CaO (Kheshgi 1995). Major concerns with these approaches are the risk of $CaCO_3$ precipitation (Moras et al. 2022; Hartmann et al. 2022), which would remove alkalinity from the ocean, and the introduction of co-contaminants into the ocean. Iron, abundant in most olivine minerals, could inadvertently fertilize the ocean and cause significant ecological effects (Bach et al. 2019). Silicates would likely shift the phytoplankton species composition towards diatoms (Bach et al. 2019). The impact of heavy metals, such as nickel (Guo et al. 2022) is likely complex (Ferderer et al. 2022) and species-specific. Finally, changes in turbidity and large energy costs of grinding (Li and Hitch 2015) make deployment of particles <10 μm impractical, while deployment of coarser particles is limited to shallow waters, as the dissolution is much slower (Montserrat et al. 2017). The long dissolution times also delay the beneficial effects on atmospheric CO_2 concentrations, likely by decades.

An alternative to direct addition of rock mass to the ocean are electrochemical methods which effectively remove acidity from seawater and neutralize it using rocks on land. Acid could be neutralized by using mine tailings and other industrial wastes or by pumping it into underground basalt formations (Matter et al. 2009; McGrail et al. 2006; Goldberg et al. 2008). Several variants has been proposed based on electrolysis (House et al. 2007; Rau 2009; Davies et al. 2018) or bipolar electrodialysis (Eisaman et al. 2018; de Lannoy et al. 2018; Digdaya et al. 2020), all essentially producing either pure NaOH or a basified seawater stream, which would be returned to the ocean to increase the pH and elicit CO_2 drawdown. The disadvantage is the significant electrical energy requirement and the fact that the produced alkalinity is relatively dilute ($\sim$1 mol kg^{-1}; de Lannoy et al., 2018), exacerbating transport costs out to sea compared to shipping powdered rock. Prior assessments of shipping costs (Renforth 2012) when using dedicated fleets have focused on transport of rock-based solid alkalinity (notably olivine), which has a high molality of alkalinity ($\sim$25 mol kg^{-1}).

Regardless of the alkalinity source, OAE methods leverage the marine carbonate system (Renforth and Henderson 2017), a multiple equilibrium state (Zeebe and Wolf-Gladrow 2001) described by the reaction

$$\begin{aligned} \mathrm{CO_{2(atm)}} &\rightleftharpoons \mathrm{CO_{2(aq)}} + \mathrm{H_2O} \rightleftharpoons \mathrm{H^+} + \mathrm{HCO_3^-} \\ &\rightleftharpoons 2\,\mathrm{H^+} + \mathrm{CO_3^{2-}}. \end{aligned} \tag{2.1}$$

Dissolved inorganic carbon (DIC) is the combined concentration of all carbonate species. Addition of alkalinity (e.g., $\mathrm{OH^-}$) shifts the above equilibrium to the right by consuming H+ ions, thus lowering the partial pressure of $\mathrm{CO_2}$ in the ocean and driving further ocean $\mathrm{CO_2}$ uptake (Middelburg et al. 2020; Zeebe and Wolf-Gladrow 2001). As the sea-surface $\mathrm{CO_2}$ exchange is rate limiting (surface water experiences an equilibration time scale on the order of weeks to years; Jones et al. (2014)), the addition of alkalinity causes a local increase in pH and aragonite saturation (Ω_{Arag}) and a decrease in $p\mathrm{CO_2}$, all of which could potentially affect the local ecology (Subhas et al. 2022; Ferderer et al. 2022; Bach et al. 2019). Furthermore, increases in aragonite saturation could lead to precipitation of calcium carbonate, which removes alkalinity from the surface water and is counterproductive with respect to $\mathrm{CO_2}$ uptake (Moras et al. 2022; Hartmann et al. 2022). A number of previous studies have used ocean circulation models combined with a carbon cycle model to estimate the carbon uptake potential of various hypothetical OAE scenarios (Köhler et al. 2013; González and Ilyina 2016; Feng et al. 2017; Ilyina et al. 2013; Keller et al. 2014; Burt et al. 2021; Tyka et al. 2022). Some of these studies investigated very high rates of alkalinity injection to test the limits of OAE. Ilyina et al. (2013) simulated alkalinity addition on the order of 2.8 P mol $\mathrm{yr^{-1}}$ (for an approximate uptake of 50 Gt $\mathrm{CO_2}$ $\mathrm{yr^{-1}}$). González and Ilyina (2016) added enough alkalinity to remove around 44 Gt $\mathrm{CO_2}$ $\mathrm{yr^{-1}}$. Both these studies found drastic changes in pH and the carbonate saturation state.

Most of these simulations consider globally uniform alkalinity injection patterns, which is unrealistic for practical deployment and provides little insight into which geographical locations are ideal for conducting OAE. An ideal region (for purposes

of negative emissions) minimizes the effect of added alkalinity on the local carbonate system and ecology, while maximizing the CO_2 uptake per unit alkalinity added.

Several authors have conducted scenario-driven and locally resolved simulations. Köhler et al. (2013) investigated finely ground olivine addition from ship tracks for a total uptake of 3.2 Gt CO_2 yr^{-1}, simulating the distribution of alkalinity via ballast water of commercial ships. These ship tracks span the full ocean extent from 40° S to 60° N, although heavily weighted to the area between 20° and 50° N.

Feng et al. (2017) simulated adding olivine along global coastlines where continental shelves are shallower than 200 m. They found that to stay below aragonite saturation levels of Ω_{Arag}=3.4 and Ω_{Arag}=9, coastal olivine addition can remove around 12 and 36 Gt CO_2 yr^{-1} respectively. Some more spatially resolved studies have been undertaken. Burt et al. (2021) tested regional alkalinity addition based on eight hydrodynamic regimes in a 1.5° model, and Tyka et al. (2022) simulated alkalinity addition at individual points in a 6° lat-long grid. Both studies revealed that the pH sensitivity and the efficiency of CO_2 uptake vary geographically and temporally.

Here, we also study alkalinity addition through a practical and economic lens, focusing on electrochemical methods, which produce NaOH or other rapidly dissolving forms of alkalinity. We begin with the assumption that the optimal places for electrochemical alkalinity production would be on the coast, with access both to seawater and low-cost renewable electricity. To minimize risks to coastal ecosystems and ensure adequate spreading and quick dilution, the alkalinity would be transported some distance offshore. This is increasingly critical for larger scale deployments to avoid high concentrations of alkalinity. We wish to determine how far offshore and over what area alkalinity can be added to the surface ocean while staying within conservative biological and geochemical limits. While these issues are less relevant to initial small-scale OAE, our goal is to examine the limits of the technology's potential scale. A judicious amount of OAE may also be beneficial by stabilizing or reversing the anthropogenic acidification of the surface ocean (Albright et al. 2016; Feng et al. 2016). Specific implementations of OAE may also be subject to additional limitations such as trace metal contamination (Guo et al. 2022; Bach et al. 2019), which we do

not address here.

Increases in alkalinity change the activities of all forms of CO_2 in the carbonate system (Middelburg et al. 2020; Zeebe and Wolf-Gladrow 2001), many of which are relevant to marine organisms (Riebesell and Tortell 2011). Both the direct impact on marine species and the risk of triggering calcium carbonate precipitation must be considered (Bach et al. 2019; Hartmann et al. 2022). Given the complexity of the carbonate system and the variety of responses to each parameter there is no single "correct" choice of proxy (Fassbender et al. 2021) by which to quantify the shift in carbonate state, although the parameters are strongly correlated with each other. Furthermore, what constitutes a safe limit for any given ocean parameter is under debate and likely varies significantly between regions; thus, a blanket hard limit is difficult to establish. Here we use two proxies to quantify changes in the carbonate system: ΔpH and Ω_{Arag}.

Prior studies simulated the addition of uniform amounts of alkalinity over some defined area and measured the varying response of ocean parameters. However, because the sensitivity of these parameters varies over more than one order of magnitude, we designed our experiment in reverse, i.e., we adjust the alkalinity addition rate in each grid cell to result in a uniform and relatively small change of a given parameter. We can then examine how the injection rate varies and construct maps that indicate regions of high suitability for OAE.

Finally, to assess the effectiveness and time scale of CO_2 uptake due to an OAE deployment in a given region of interest, we can define the uptake efficiency as

$$\eta_{CO_2}(t) = \frac{\Delta\text{DIC}(t)}{\Delta\text{Alk}}, \tag{2.2}$$

where t denotes the time since alkalinity was added and η_{CO_2} is a unitless molar ratio. Following the addition of some quantity ΔAlk to seawater, the ocean will begin taking up CO_2, eventually reaching a maximum (Renforth and Henderson 2017; Tyka et al. 2022). The exact value depends on the parameters of the carbonate system, i.e., Alk, DIC, temperature etc., with a typical range of 0.75–0.85 (Tyka et al.

2022). However, the kinetics of this equilibration are known to vary spatially due to differences in the gas exchange time scales and the surface residence time of CO_2-deficient water (Jones et al. 2014; Burt et al. 2021). We thus conducted simulated experiments with short localized pulse injections, followed by tracking of the total excess alkalinity and DIC relative to a reference simulation as done previously with a much coarser model (Tyka et al. 2022). This gives an accurate picture of where alkalinity from a particular injection point is advected to, how much alkalinity is lost to the deep ocean, and how much and when CO_2 uptake can be expected.

2.2 Methods

2.2.1 The model

We use the ECCO LLC270 physical fields (Zhang et al. 2018) to simulate the transport of alkalinity by currents and model alkalinity addition in near-coast areas globally. We inject alkalinity to the simulation in strips along all global coastlines, 37 km wide and larger. The ECCO fields is an ocean state estimate based on the MIT General Circulation Model (MITgcm) (Marshall et al. 1997) that also integrates all available ocean data since the onset of satellite altimetry in 1992. ECCO uses the adjoint method to iteratively adjust the initial conditions, boundary conditions, forcing fields, and mixing parameters to minimize the model-data errors (Wunsch et al. 2009; Wunsch and Heimbach 2013). This produces a three-dimensional continuous ocean state estimate that agrees well with observational data. We use the LLC270 configuration with a $1/3^\circ$ horizontal resolution (Zhang et al. 2018). All input and forcing files needed to reproduce the ECCO state estimates and the source code are freely available online, and we use them to reproduce the LLC270 flow fields. The LLC270 configuration uses a lat-long-cap (LLC) horizontal grid, which uses five faces to cover the globe. The horizontal resolution ranges from 7.3 km at high latitudes to 36.6 km at low latitudes, and has 50 vertical layers with the grid thickness ranging from 10 m near the ocean surface to 458 m at the bottom (Zhang et al. 2018). We use the iteration-42 state

estimate described in Carroll et al. (2020), which spans the years 1992–2017.

To represent the ocean carbonate system we used the gchem and DIC packages within MITgcm. The ocean carbon model was based on Dutkiewicz et al. (2005) and uses four biogeochemical tracers (DIC, alkalinity, phosphate, and dissolved organic phosphorus) to simulate the carbonate system. In this model, DIC is advected and mixed by the physical flow fields from the MITgcm, and the sources and sinks of DIC are: CO_2 flux between the ocean and atmosphere, freshwater flux, biological production, and the formation of calcium carbonate shells. The biogeochemical tracers were initialized with contemporary data from GLODAPv2 mapped climatologies (Lauvset et al. 2016; Olsen et al. 2017) where possible, or using data from Dutkiewicz et al. (2005) and were allowed to relax locally by running 100 years of forward simulation (looping the ECCO forcing fields). Atmospheric CO_2 concentrations were held constant at 415 μatm, rather than trying to anticipate future emission scenarios. The surface carbonate tracers were found to stabilize during this time.

As we are not simulating a full Earth system, our model does not account for feedbacks of other carbon sinks which reduce the impact of moving CO_2 from the atmosphere to the ocean (Keller et al. 2018a). Wind speeds, used to calculate the gas exchange, are imported from the LLC270 forcing data and the air-sea exchange of CO_2 is parameterized with a uniform gas transfer coefficient (Wanninkhof 1992). To simulate ocean OAE, we forced the simulation by adding pure alkalinity to the surface ocean in specified locations to the top grid cell (10 m depth) and at a parameterized rate; this assumes that alkalinity is of an effectively instantly dissolving nature, such as an NaOH solution. This avoids complicating factors arising from slower dissolving materials such as fine olivine powder, for which dissolution rates vary with ocean conditions and may sink out of the surface layers before complete dissolution (Fakhraee et al. 2022). We focused on alkalinity addition in coastal bands following shorelines because that is economically most viable and accessible for shipping or pipelines. Feedbacks of elevated alkalinity on the rate of surface calcification are also not explicitly modeled.

Six coastal strips are examined with widths of approximately 37, 74, 111, 185,

296 and 592 km, although they vary slightly due to the varying grid cell sizes in the LLC270 grid. Feng et al. (2017) used a coarser 3.6° longitude by 1.8° latitude model, and their injection pattern roughly corresponds to our 296 km coastal strip. The much finer LLC model allows us to resolve coastal features in greater detail and to test thinner injection strips. We also examined injection in discrete locations spaced 200 or 400 km apart along the coastline, in circular patches ∼120 km wide.

All runs presented in this paper use the same approach: First a reference simulation is run (spanning 20 ECCO years 1994–2014). Then a second run is conducted with the same starting conditions, with an alkalinity forcing added, which perturbs the system in some way. We then analyze the difference in the carbonate systems (ΔpH, $\Delta\Omega$, ΔDIC, etc.) between these two runs. As the carbonate model does not influence the flow field, there is no divergence in the flow fields over the 20 simulation years and the 2 trajectories are directly comparable. These simulations are run on a small MPI cluster (13 machines, 59 processes each) on Google Cloud Engine, and take about 6 h of wall time per simulation year.

2.2.2 pH and Omega limits

The carbonate chemistry in different regions varies in its sensitivity to alkalinity injection, owing to local differences in ocean circulation, gas exchange and carbonate chemistry. The goal of our experiments is to determine the maximal alkalinity addition rate which can be sustained at any given grid point and limits the change in one of two surface parameters, pH and the aragonite saturation Ω_{Arag} to some chosen value.

Here we chose target constraints $\Delta\mathrm{pH}_{\mathrm{tgt}}$=0.1 or $\Delta\Omega_{\mathrm{tgt}}$=0.5. These values are somewhat arbitrary and serve simply to calculate the relative sensitivity of different regions. However, as an intuitive point of reference, the already incurred anthropogenic surface acidification since preindustrial times (Doney et al. 2009) is $\Delta\mathrm{pH}\approx -0.1$. Likewise a change of $\Delta\Omega_{\mathrm{Arag}}$=+0.5 is unlikely to trigger carbonate precipitation according to Moras et al. (2022) who established an Ω_{Arag} threshold of 5.

An alternative approach would have been to set absolute thresholds for pH and/or Omega; however, we did not pursue this for the following reasons. For the estimation of biological impact a relative change to current conditions seems most appropriate as the local ecosystem is adapted to the local conditions and many biologically relevant stressors change proportionally to the relative concentration change. For example, the energy expenditure of an organism to maintain its intracellular pH is approximately proportional to the logarithm of the proton concentration difference. For purposes of estimating the precipitation limit an absolute threshold would indeed be more appropriate. However, in polar latitudes where Ω_{Arag} is currently low, the change in alkalinity required to reach the limit (e.g., $\Omega_{\mathrm{Arag}}>5$, Moras et al. (2022)) would be so large that it would no longer represent a realistic scenario, easily exceed the above relative pH limits and likely exceed the bounds of the simulation's predictive domain. We note that our choice of a relative Omega constraint means that we obtain a lower bound on the true OAE limit, with respect to Omega.

In practice, which limits are acceptable is subject to debate and likely different in different locations. We do not attempt to anticipate the acceptable limits here, focusing merely on the relative capacity of different ocean regions with respect to these ocean parameters. Our approach is as follows: each surface grid point that is part of the coastal injection strip is given a particular baseline injection rate r (in mol m^{-2} s^{-1}). At every time step and for every grid point, the local (in time and space) ΔpH is calculated using the carbonate model and a reference value obtained from an unperturbed reference simulation ($\Delta\mathrm{pH}$ = pH - $\mathrm{pH}_{\mathrm{ref}}$). If this value is lower than $\Delta\mathrm{pH}_{\mathrm{tgt}}$, then alkalinity is added according to the baseline rate. If not, then addition is skipped for this time step.

This mechanism is insufficient to ensure the pH does not exceed the maximal value, as the change in pH is determined not only by the local alkalinity addition, but also by advection of alkalinity from neighboring cells and seasonally varying biological activity. We thus iteratively adjusted the baseline rate for each grid cell to empirically determine a rate which gives rise to approximately the desired ΔpH in the following way.

First a pilot simulation was run where the baseline rate was set uniformly to an extreme value of r=400 mol m^{-2} s^{-1}, (higher than any region can accommodate). We ran this simulation for 3 years and recorded the observed amount of addition at each grid cell (generally much lower than the baseline as the above algorithm prevents excessive addition). Second, we reran the simulation using a new, position-dependent baseline rate calculated from the amounts actually added from the pilot simulation using a linear extrapolation to our desired pH maximum. We ran this second simulation for 8 years. We found that the observed ΔpH was now generally very close to the desired ΔpH_{tgt}. However, some regions still exceeded the target value while others undershot. We thus performed a third simulation where we adjusted the addition rate at any grid point inversely proportional to the observed pH deviation, yielding a final third simulation which was allowed to run for 20 years using the ECCO forcing fields from 1995 to 2014. We found that this procedure yielded a relatively narrow distribution of ΔpH or $\Delta\Omega_{Arag}$ for all grid points in the injection strip, although some variability remained (Fig. 2-9 in the Supplement). A separate iterative optimization was performed for every injection pattern. Grid points outside of the injection strip showed much smaller changes in pH and never exceeded the target ΔpH. The same procedure was used in a separate set of experiments for $\Delta\Omega_{Arag}$.

Once the rate of OAE is stable and acceptable, we can measure how much alkalinity is being added at each grid point. Note that because of the considerable interdependence between nearby grid points there is no one unique injection pattern that satisfies the ΔpH or $\Delta\Omega_{Arag}$ condition; however, multiple independent optimization runs started at different ECCO years yield injection patterns that match very closely.

2.2.3 Pulse additions

When alkalinity is added to the surface ocean it lowers the partial pressure of CO_2 (pCO_2) and thus increases the rate at which CO_2 dissolves in the ocean surface. The effectiveness η_{CO_2} of this uptake is determined by a number of factors which vary significantly by location. The time scale of gas exchange τ_{CO_2} is approximately 3–9

months and varies by location (Jones et al. 2014), while the residence time τ_{res} of water parcels in the mixed layer varies over shorter times between 2 and 20 weeks.

Thus the resultant equilibration efficiency ratio $\tau_{\text{res}}/\tau_{CO_2}$ was found to be significantly below 1.0 in 95 % of ocean locations (Jones et al. 2014). However, CO_2-deficient water parcels initially lost from the mixed layer can remix into the mixed layer at some later time and thus drive further equilibration elsewhere and over longer time scales. This longer term effect was not explicitly modeled in previous work (Jones et al. 2014) and results in a complex equilibration curve which is not well captured by a single exponential function. As the kinetics of this longer term equilibration depend on the deep transport and mixing of the lost alkalinity, it has to be simulated explicitly.

We extend the work of Jones et al. (2014) by simulating pulse injections of alkalinity in a variety of locations using the ECCO flow fields. These simulations explicitly include all the relevant aspects together (gas exchange, Revelle factor, surface transport, mixed layer-depth, residence time and remixing), by measuring the actual excess CO_2 uptake of the ocean relative to the unperturbed reference simulation. However, because the alkalinity is also distributed horizontally over great distances and mixes from different origins, it is impossible to disambiguate the CO_2 uptake time scale of different injection points from a single simulation. One solution to this problem is to use a Lagrangian approach (van Sebille et al. 2018) which allows the tracking of stochastic particles. Here we chose a simpler approach. For a select number of coastal locations we run a separate simulation and inject a 1-month pulse of alkalinity. Following the pulse we monitor the total excess DIC in the ocean relative to a reference simulation, the distribution of alkalinity across the depth layers, and the pCO_2 deficit at the surface over time. Ideally the length of the pulse would be a single time step; however, this would either necessitate an extreme addition rate or a tiny total quantity of added alkalinity, which would lead to a poor signal to noise ratio during analysis. The choice of pulse length thus represents a compromise, as this length is still much shorter than the overall relaxation time. Ideally such a pulse injection experiment could be conducted for every grid point (as was done with a coarse model

in Tyka et al., 2022) and at different times of the year. However, because each pulse requires a whole separate simulation, this exceeded our computation capacity with the high-resolution ECCO model. Thus we chose 17 individual locations of interest along most major coastlines with pulses occurring in January.

2.2.4 Alkalinity injection from ships

In addition to the steady-state perturbation of ocean parameters over large areas of OAE deployment, it is critical to examine the short-term impacts that arise right at the injection site, which will temporarily take the local carbonate system into an extremely alkaline regime. This is unlikely to be a concern for gradually dissolving alkalinity such as ground olivine (Hangx and Spiers 2009; Schuiling and De Boer 2011), but highly relevant for rapidly dissolving alkalinity such as NaOH solution or other solubilized alkaline media.

Of interest is the dilution speed of the added alkalinity (we assume here a solution of 1 M NaOH) against the time scale at which homogeneous nucleation of aragonite is triggered and needs to be avoided. The most natural approach, used also in waste disposal, would be to inject directly into the turbulent wake of the ship to mix the discharge with seawater as rapidly as possible (Renforth and Henderson 2017). The dilution kinetics have been studied and modeled in previous work (Chou 1996; IMCO 1975) and large discrepancies exist between the published models. The IMCO model uses the following empirical form for the unitless dilution factor as function of time t:

$$D(t) = \frac{c}{Q} U^{1.4} L^{1.6} t^{0.4}, \tag{2.3}$$

where t is time (seconds), Q is the release rate ($m^3\ s^{-1}$), U is the speed of the ship ($m\ s^{-1}$), and L is the waterline length (m). C is an empirical constant, set to 0.003 for release from a single orifice and 0.0045 for release from multiple ones. Intuitively, larger speeds and longer ships have more turbulent wakes, producing faster dilution. Chou (1996) used the following similar model which instead of waterline length uses the width of the ship, B, in units of meters, to account for the ship size.

$$D(t) = \frac{0.2108}{Q} U^{1.552} B^{1.448} t^{0.552}. \tag{2.4}$$

Chou's formula gives much faster dilution rates and was verified against field testing data. Other work (Lewis 1985; Byrne et al. 1988; Lewis and Riddle 1989) used even higher exponents on the time t so we take the IMCO formula to be an upper limit although in general no universally applicable law can be expected as the dispersion time scale will inevitably depend on local conditions. For a given starting concentration C_0 of the alkaline effluent (e.g., 1 mol L^{-1} NaOH) we can calculate the resultant alkalinity by considering the dilution with seawater with alkalinity Alk_0

$$\mathrm{Alk}(t) = \frac{1}{D(t)} C_0 + \left(1 - \frac{1}{D(t)}\right) \mathrm{Alk}_0. \tag{2.5}$$

We can then determine the pH(t) and the carbonate saturation state Ω(t) by solving the carbonate system at any given Alk(t). We used PyCO2SYS (Humphreys et al. 2020) to solve the carbonate system numerically, assuming PyCO2SYS default values and Alk_0 = 2300 μmol kg^{-1} and DIC = 2050 μmol kg^{-1}. These analytical models are valid only on time scales smaller than 1 h, after which dilution kinetics are driven by the local background turbulence rather than the immediate influence of the wake turbulence. Thus longer scale dilution effects will vary substantially from location to location. As the time scale considered here is much shorter than the typical CO_2 gas exchange time scale, we do not explicitly model CO_2 uptake during this initial dilution.

2.2.5 Estimation of transport costs

Alkalinity prepared on land must be transported out to sea, which adds to the total cost of the achieved negative emissions (in USD per tonne CO_2). While at very small scale it could be released right at the coast, for larger overall OAE deployment the alkalinity will need to be spread over greater areas (to avoid excessive local pH or Omega changes) which increases the cost for every additional unit of alkalinity added.

Having obtained maps of the allowable rate of OAE in any given area, we can estimate the transport costs for each of our simulated scenarios. Large-scale maritime shipping costs are currently around USD 0.0016–0.004 per tonne per kilometer (Renforth 2012). For each grid point where alkalinity is injected, we calculate the distance D to the nearest coast, and take double that to be the minimum round trip distance for a ship to travel. Realistically, a ship will have to travel farther than D since it needs to go to the nearest port or NaOH factory, so this is the lower bound on the transport distance. This allows us to calculate the lower bound of the shipping cost per tCO_2 for each grid point. The scenario model provides the alkalinity injection rate for each grid point, and assuming an eventual uptake efficiency $\eta_{CO_2} = 0.8$ we can obtain the total shipping cost for every grid point. Summing the total cost over all grid points in which injection occurs and dividing by the total expected global CO_2 uptake yields a lower bound of the average effective global transport cost per tonne CO_2.

2.3 Results and discussion

2.3.1 Injection capacity

In all our simulations the alkalinity flux in the injection grid cells was iteratively adjusted to elicit a change in pH or the change in Omega (although not simultaneously) to a value of either ΔpH = +0.1 or $\Delta\Omega_{\text{Arag}}$= +0.5, respectively. Due to the correlation between neighboring grid cells, seasonal and year-to-year changes in currents and biotic activity, these constraints are not perfectly satisfied but we were able to confine them to a narrow range around the desired value (Fig. 2-9). The injection rate as well as ΔpH and $\Delta\Omega_{\text{Arag}}$, stabilize within the first 5–6 years of the simulation and remain stable for the remainder of the simulation (Fig. 2-9), indicating that a steady state is reached where the alkalinity addition rate is matched by outflowing alkalinity into open ocean areas and by neutralization by atmospheric CO_2. Note that while the time-averaged ΔpH is close to 0.1, there is significant temporal variability that leads to ΔpH slightly exceeding 0.1 at some parts of the year (Fig. 2-9).

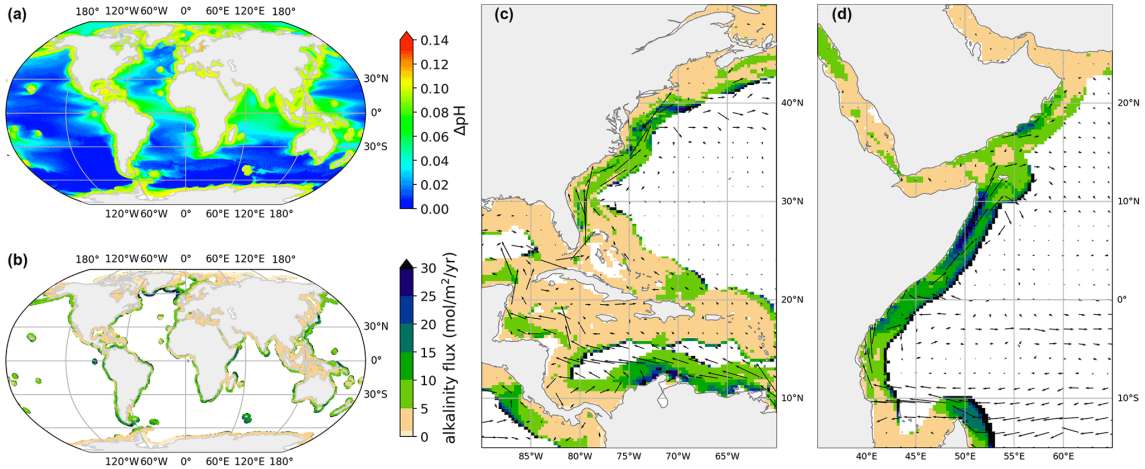

Figure 2-1: Shown is a coastal injection in a strip 296 km wide, subject to ΔpH_{tgt}=0.1. All time-averages ran over 5–20 years. (a) Averaged pH change compared to a reference simulation with no added alkalinity. (b) Average alkalinity flux at each grid point from the coast. (c, d) Injection flux for two example regions. Annually averaged surface currents are overlaid as a vector field.

As expected, ΔpH or $\Delta\Omega_{Arag}$ outside the injection grid cells is much lower and never exceeds the target value. However, the effect on adjacent areas outside of the injection grid points is variable and depends on the pattern of ocean currents that sweep alkalinity away from injection areas. For instance, western boundary currents carry the coastal excess alkalinity far out into the open ocean, so we see elevated changes in the North Atlantic and Indian oceans, even outside the injection areas.

For each injection pattern and chosen limit we can now obtain a global map of steady-state alkalinity flux (mol m^{-2} yr^{-1}), which shows the variability of capacity for OAE (Fig. 2-1b, c and d). We note substantial variability on multiple scales. Firstly on a large scale, some coastal areas have a fundamentally greater capacity for distributing and neutralizing alkalinity flux than others (see also Fig. 2-2b). Large capacities are found around islands which sit in or near ocean currents, as those rapidly sweep the alkalinity away from near-coast areas. Examples include Kerguelen, Easter Island and Hawaii. Continental coasts which exhibit large capacities are found around South and East Africa, off the coast of Peru and Brazil, Southeast Australia and the west coast of Japan. Finally, an area of very large tolerance for alkalinity addition is found in the northern Atlantic. However, as will be shown later, this is

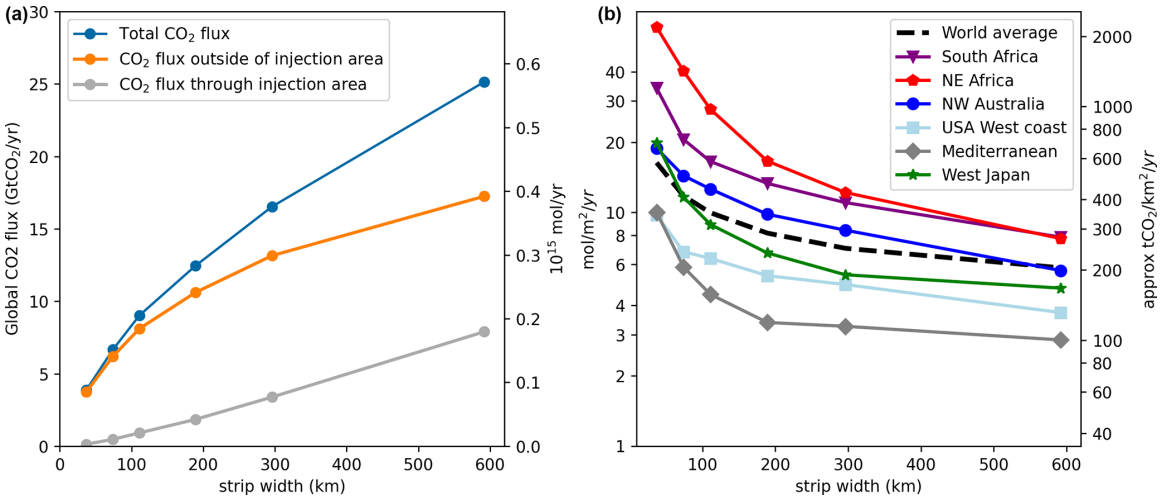

Figure 2-2: (a) Total CO_2 flux (Gt CO_2 yr^{-1}), subject to ΔpH_{tgt}=0.1, broken down into flux through the injection area and outside of the injection area. (b) Dependence of the averaged injection flux (mol m^{-2} yr^{-1}) on the width of the coastal injection strip for different coastal regions and strip widths. The black dashed line averages all coastal regions.

due to downwelling and deep water formation, which is highly undesirable for OAE as the alkalinity cannot efficiently equilibrate with the atmosphere before being lost. Conversely inland seas and partially enclosed seas exhibit the smallest capacity for OAE, notably the Red Sea, the Mediterranean and the Baltic Sea. An interesting counterexample is the Gulf of Mexico and the Caribbean Sea which, owing to the traversing Gulf Stream, have significant capacity for OAE. We found no correlation between background pH and OAE rate, as the influence of local ventilation due to currents dominates the capacity for alkalinity addition.

As expected, the large scale patterns obtained by limiting $\Delta pH = 0.1$ or $\Delta\Omega_{Arag}$=0.5 are very similar (Fig. 2-10) up to a linear factor and highly correlated on a per grid cell basis. This is consistent with the observation that OAE capacity is primarily influenced by local currents. However, we note that the fundamental sensitivities of pH and Ω_{Arag} with respect to Alk change quite differently from the poles to the equator. In particular, $\partial pH/\partial Alk$ decreases from $\sim 2.6 \times 10^3$ L mol^{-1} at the poles to $\sim 1.0 \times 10^3$ L mol^{-1} at the equator, while $\partial\Omega/\partial Alk$ increases from $\sim 7.6 \times 10^3$ L mol^{-1} at the poles to $\sim 11 \times 10^3$ L mol^{-1} at the equator (computed from GLODAPv2, Lauvset et al., 2016; Olsen et al., 2017 data and PyCO2SYS; Humphreys et al., 2020;

Lewis and Wallace, 1998). Furthermore, from the perspective of preventing precipitation due to excessive Ω_{Arag}, the available headroom is much smaller at tropical latitudes, where Ω_{Arag} is already close to 4, than near the poles where Ω_{Arag} is as low as 1–2 (Lauvset et al. 2016; Olsen et al. 2017). Thus, as our relative $\Delta\Omega_{\mathrm{Arag}}$ limit was set to 0.5, the OAE limits obtained here should be considered a lower bound with respect to calcite precipitation, i.e., polar regions could tolerate a much larger addition rate. For pH the actual ecologically tolerable limits will vary from coast to coast, and we do not attempt to anticipate them here. We note, however, that for our examined constraints (both of which are very conservative) a significant amount of negative emissions can be obtained even in very narrow coastal strips as the transport out to open sea is very efficient. This observation is consistent with prior work by Feng et al. (2017).

On a fine scale we find that the sustainable injection flux varies over 2–3 orders of magnitude between nearby grid points (Fig. 2-9) with a distribution that is approximately log-normal. The variance is even larger for thin injection strips (Fig. 2-9) and very large fluxes can be sustained in some locations if the net transport of alkalinity out of the strip is high enough. Depending on the prevailing currents, the highest injection rate can be found both on the outside and inside of the injection strip.

For all regions we observed that while widening the injection strip increases the total allowable rate of alkalinity injection, the increase is sublinear (Fig. 2-2a). Every additional unit of alkalinity added needs to be transported further offshore and the average injection rate decreases per unit area. This is consistent with the view that the majority of the neutralization of the added alkalinity by invading CO_2 occurs outside the injection strip and the local pH is primarily determined by the rate of transport of alkalinity into other areas (Burt et al. 2021). This is confirmed by integrating the total CO_2 flux over the injection strip and over the rest of the ocean surface, relative to the reference simulation. Figure 2-2a shows that especially for thin coastal injection strips, direct gas exchange through the strip surface accounts for only a minor component of the induced CO_2 uptake and the majority occurs outside of the injection areas. As the strip widens, however, this fraction significantly

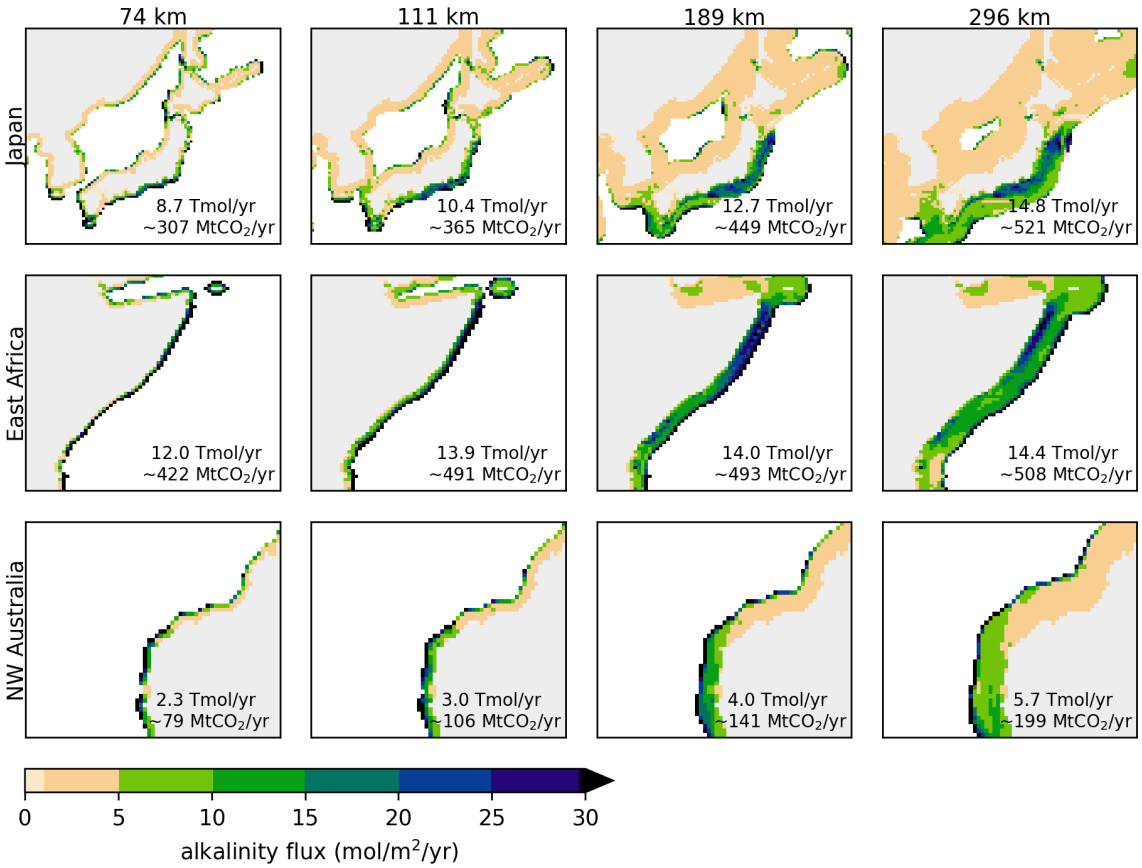

Figure 2-3: Injection flux (mol m^{-2} yr^{-1}) shown for different strip widths in 3 different regions (from top to bottom: Japan, East Africa and Northwest Australia). The inset text indicates the total alkalinity added per year in the shown area.

increases. Especially in regions with weak transport we observe that often a larger quantity of alkalinity can be added right at the border of the strip than in the middle, as alkalinity can dilute to bordering areas that are not directly receiving alkalinity (Fig. 2-3). Indeed, the largest alkalinity fluxes observed occur when the strip widths are very thin (Fig. 2-9). The consequence is that any particular coastal region can increase its capacity for injection by going further out to sea, but that there are diminishing returns of doing so, i.e., the increase in capacity is sublinear with width.

The influence of widening the injection area is also shown in detail for three regions in Fig. 2-3 and a larger number of regional details are included in the Supplement in Fig. 2-12. Widening strips allows more alkalinity to be added overall. However, saturation of near-coast areas occurs in most regions (especially evident in Northwest

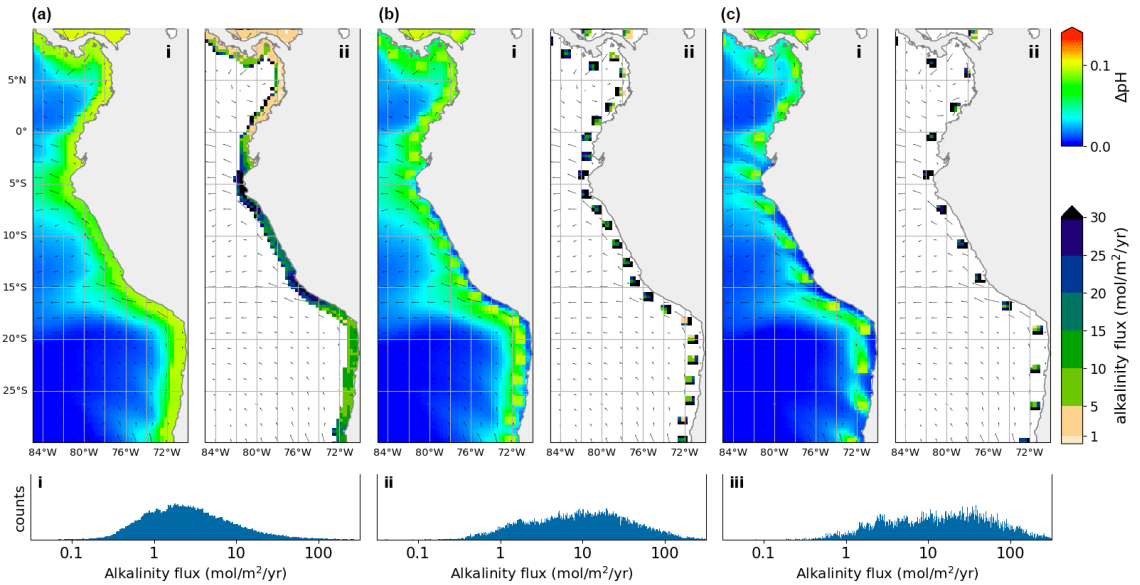

Figure 2-4: Alkalinity enhancement in three different patterns, exemplified at the west coast of South America: (a) Injection in a contiguous strip. (b) Injection in 200 km separated patches. (c) Injection in 400 km separated patches. The total globally area-integrated OAE rate for the three injection patterns was (a) 336 Tmol yr^{-1}, (b) 312 Tmol yr^{-1} and (c) 233 Tmol yr^{-1}, respectively. The sub panels show (i) time averaged pH change, (ii) alkalinity flux, (iii) distribution of alkalinity flux (globally).

Australia). The largest injection flux is often found directly at the strip boundary, owing to easy diffusion out to open sea. However, it is not always the case that the highest injection flux occurs at the strip edge, as seen in the Japan and East Africa examples. These findings illustrate the highly non-local nature of the injection capacity.

In general we find that the sensitivity of pH and Ω_{Arag} at any given grid point is highly dependent on the surrounding pattern of injection. We conducted two additional experiments in which rather than a contiguous strip, injection occurred at discrete points placed either 200 or 400 km apart. At 200 km apart we observed much higher injection fluxes in each injection patch, but the total global injection flux barely changed (Fig. 2-4). Placing injection patches 400 km apart instead of 200 km apart did not further increase the sustainable flux in each injection patch, and reduced the overall injection capacity by 25%. This suggests that at 200 km there is still significant cross-correlation between neighboring patches, which is apparent when looking at the

pH changes observed: the pH impact bleeds into neighboring patches (Fig. 2-4b). At 400 km apart, however, there is much less interference between adjacent patches and the injection limits are simply dominated by local current patterns (Fig. 2-4c). These observations are consistent with prior work (Jones et al. 2012) which found a global median pCO_2 autocorrelation length of about 400 km. Thus in order to maximize any particular coastline's injection potential, injection areas should be placed at most 200–400 km apart; however, the exact optima will depend on the local current patterns. The location of ports, infrastructure, access to electricity and/or alkaline minerals will dictate the choice of locations. The correlation between neighboring injection locations has ramifications for the planning, monitoring and governance of different OAE projects, as they will affect each other in downstream coastal areas. For monitoring and verification purposes it will be impossible to disambiguate CO_2 drawdown caused by different OAE projects by measurement alone. Any plans to add alkalinity to the ocean will need to be simulated specifically, ideally with regionally optimized models, and take into account already occurring OAE projects nearby.

2.3.2 CO_2 uptake time scales

To measure localized CO_2 uptake time scales, we conducted a total of 17 pulse injections (as described in the methods section), placed near all major coastlines. We generally chose locations previously determined as areas of high alkalinity tolerance. Firstly, we observed a very large variety of CO_2 uptake time scales (Fig. 2-5) both in the short term (after 1 year) and in the medium term (after 10 years). After 1 year the molar uptake fraction $\eta_{CO_2} = \Delta DIC/\Delta Alk$ varied between 0.2 and 0.85 and after 10 years most locations resulted in an uptake fraction of 0.65–0.80 consistent with previous work (Tyka et al. 2022; Burt et al. 2021).

A typical behavior is observed, for example, when releasing alkalinity at the northern coast of Brazil (Fig. 2-6a). Here the alkalinity remains long enough at the surface to realize its full CO_2 uptake potential within 2—3 years. A number of other tested locations follow this general pattern and are efficient for OAE deployment (Fig. 2-5a). Here the equilibration follows roughly a single exponential relaxation.

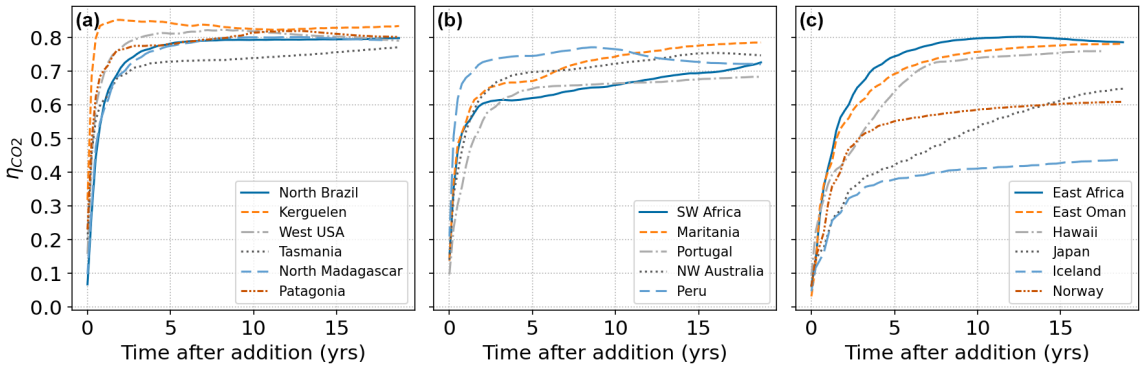

Figure 2-5: CO_2 uptake relative to alkalinity addition (molar ratio η_{CO_2}=ΔDIC/ΔAlk) following pulse additions at 17 different locations. (a) Locations which equilibrate fast and reach close to the theoretical maximum of CO_2 uptake ($\sim$0.8). (b) Locations which equilibrate fast but reach a lower plateau of relative CO_2 absorption (0.6–0.8) with slow further progression. (c) Locations with slow equilibration or significant loss of alkalinity to the deep. Note that in some cases despite the slower initial equilibration high uptake ratios can be eventually achieved.

Another set of locations appear to lose a significant amount of alkalinity to deeper layers before atmospheric equilibration is achieved (Fig. 2-5b, c). For example, injection off the coast of Japan resulted in slow initial uptake as a portion of the alkalinity is quickly subducted (Fig. 2-6b). However, in the following decade remixing with surface waters gradually returns this alkalinity back towards the surface resulting in slow but steady CO_2 uptake (Fig. 2-6b). Other examples of this delayed CO_2 equilibration are shown in Fig. 2-5b. These locations exhibit a short mixed layer residence time and have a poor equilibration efficiency (Jones et al. 2014), but equilibration is eventually achieved in the following decades. Changes in surface pCO_2 and alkalinity will also potentially affect biological CO_2 uptake and calcification rates; however, these dependencies are not captured by the carbonate model used here (Dutkiewicz et al. 2005) and will need to be examined by future studies.

Finally, some extreme examples of poor long-term equilibration efficiency are found in areas of deep water formation, such as the North Atlantic. Here a CO_2 uptake ratio of just over 0.4 is achieved and even after 20 years very little further progress is made (Fig. 2-6c). Around half of the added alkalinity is subducted very deep and will likely remain out of contact with the atmosphere until the global over-

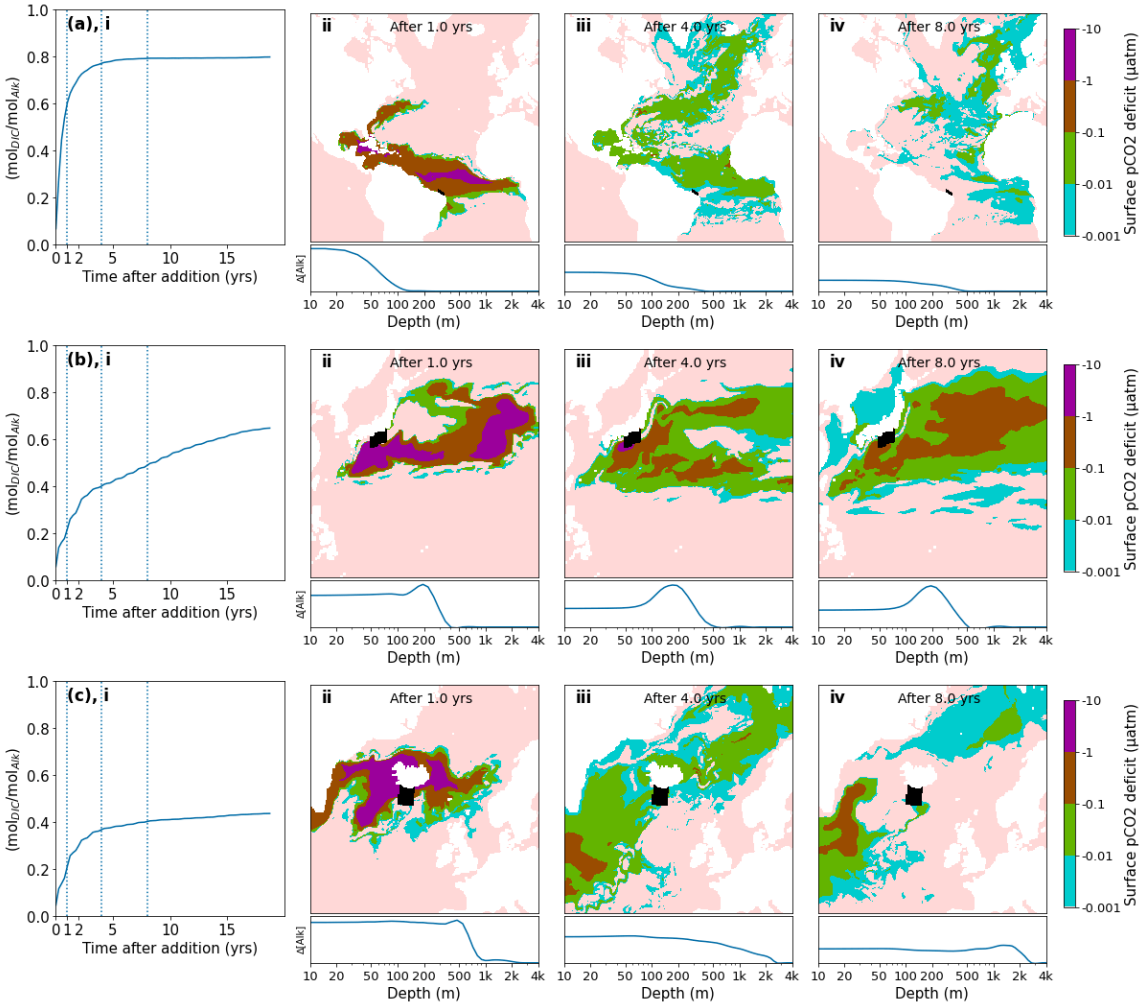

Figure 2-6: Pulse additions of alkalinity in 3 representative locations: (a) Brazil, (b) Japan, (c) Iceland. (i) Excess quantity of CO_2 absorbed (relative to the reference simulation) over time following a 1 month pulse injection at various near coast locations, expressed as a molar fraction of the amount of alkalinity added (η_{CO_2}). A significant variation of uptake time scales is observed, depending on the speed at which excess alkalinity is removed from surface layers, both in the short term and in the long term. (ii–iv) Spatial detail of surface pCO_2 deficit and depth residence of excess alkalinity for the same 3 locations shown in (i). The initial injection location is indicated by a black area. The surface pCO_2 deficit is plotted over time (note the log scale of the color map), indicating areas which are absorbing extra CO_2 (or emitting less CO_2) compared to the reference simulation. Below, the relative excess alkalinity is plotted against the depth of the water column (averaged over all lat/long grid points for each depth). Further locations are shown in detail in Fig. S5.

turning circulation returns these waters to the surface, on the time scale of many hundreds of years. We did not examine the dependence of the time of year (all of our pulses occurred in January) nor were we able to conduct an exhaustive set of locations as was done previously with a coarser global circulation model (Tyka et al. 2022). We note that for all cases the alkalinity-induced CO_2 deficit spreads over a very large area within 1 year and a significant fraction of the CO_2 uptake occurs after the deficits have diluted to the sub-μatm range. This makes direct monitoring and verification of OAE extremely challenging and will likely need to rely on modeling and indirect experimental verification.

2.3.3 Alkalinity injection from ships

Other than potential ecological impacts on marine life intersecting the caustic release wake of an OAE ship, one concern is that a short Ω_{Arag} spike could induce precipitation of $CaCO_3$ (Renforth 2012). Once nucleated, the $CaCO_3$ particles could continue to grow, even when the pH has returned to normal ocean levels ($\approx$8.1) because the ocean is supersaturated with respect to calcite ($\Omega_{\text{Calc}}\approx$2.5–6) and aragonite ($\Omega_{\text{Arag}}\approx$1.5–4) (Lauvset et al. 2016; Olsen et al. 2017). While the nucleation of $CaCO_3$ is strongly inhibited by the presence of magnesium in seawater (Sun et al. 2015; Pan et al. 2021), the growth of existing crystals may not be (Moras et al. 2022; Hartmann et al. 2022). Only once the $CaCO_3$ particle has reached a size and density that causes it to sink would it stop removing alkalinity from the surface ocean. Thus, depending on the number of particles nucleated, the alkalinity removed from the surface ocean can be larger than the alkalinity added (Moras et al. 2022; Hartmann et al. 2022; Fuhr et al. 2022).

As the immediate dilution dynamics of alkalinity injected into the wake of a ship are far below the resolution of the ECCO LLC270 global circulation model, we examine this process analytically, as described in the methods section. The relevant time scales are compared in Fig. 2-7. The predicted pH and Ω_{Arag} as a function of time are shown in blue, based on the dilution formulas given by IMCO (1975) and Chou (1996).

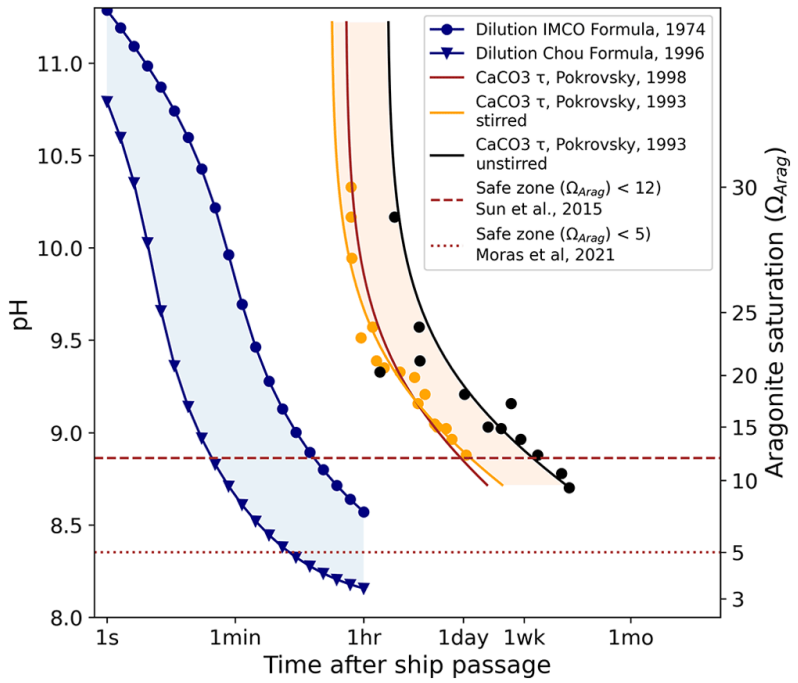

Figure 2-7: The expected time evolution of pH (left scale) and Ω_{Arag} (right scale) due to dilution for alkalinity injection into a ship wake. Here we assume a large tanker (275 m long, 50 m wide, traveling at 6 m s^{-1}) releasing 1.0 M NaOH at a rate of 5 m^3 s^{-1}. Ships of this size have a capacity of 100–200 kt of cargo which would take 6–12 h to discharge. Two previously published dilution models are shown in blue with a large variance apparent. For comparison, the time scales of homogeneous nucleation are also shown (yellow, brown and black). The dashed and dotted lines indicate the estimated Ω limits for precipitation. Despite the substantial uncertainty in the existing models, dilution can proceed at least 1–2 orders of magnitude faster than precipitation is expected to occur.

Also shown are the homogeneous nucleation times of $CaCO_3$ for comparison. Several studies (Pokrovsky 1994, 1998) have measured the homogeneous nucleation of $CaCO_3$ in seawater at different saturation states down to Ω_{Arag}=9. Three of these models are plotted in shades of orange and black in Fig. 2-7. Theoretical studies (Sun et al., 2015) suggest that for Mg : Ca ratios of 5.2, as found in seawater, no nucleation of aragonite occurs at all below Ω_{Calc}=18 (equivalent to $\Omega_{Arag}\approx$12), due to inhibition by magnesium. This is consistent with Morse and He (1993); however, time scales only up to a few hours were examined. Moras et al. (2022) suggested a safe limit of Ω_{Arag}=5 based on alkalinity addition using CaO. Figure 7 shows that ship-wake dilution proceeds at least one order of magnitude faster than the homogeneous nucleation time; thus, we can expect that $CaCO_3$ particles will not be induced to nucleate.

At the immediate injection site where the pH exceeds $\sim$ 9.5–10.0, the temporary precipitation of $Mg(OH)_2$ is expected, which redissolves readily upon dilution (Pokrovsky and Savenko 1995) and buffers the pH against further increase (not accounted for in Fig. 2-7). The temporary reduction in the Mg : Ca ratio could make $CaCO_3$ nucleation more favorable, but the time spent in this state (<1 min) is likely still well below the required nucleation time.

2.3.4 Transport costs

Alkalinity prepared on land must be transported out to sea, which incurs costs. Having obtained maps of the sustainable rate of OAE in any given area, we can estimate the transport costs for each of our simulated scenarios as described in the methods section. Furthermore, the quantity of alkalinity per tonne depends on the molality of the material moved. For rock-based methods (Hangx and Spiers 2009; Schuiling and De Boer 2011; Renforth 2012; Montserrat et al. 2017; Rigopoulos et al. 2018; Meysman and Montserrat 2017), the molality of solid alkaline materials such as olivine is $\sim$ 25 mol kg^{-1}. For electrochemical alkalinity methods (House et al. 2007; Rau 2009; Davies et al. 2018; Eisaman et al. 2018; de Lannoy et al. 2018; Digdaya et al. 2020) that produce alkaline liquids, it will be closer to 1 mol kg^{-1}, depending on the industrial processes used and effort spent concentrating the alkaline solution. Figure 2-8

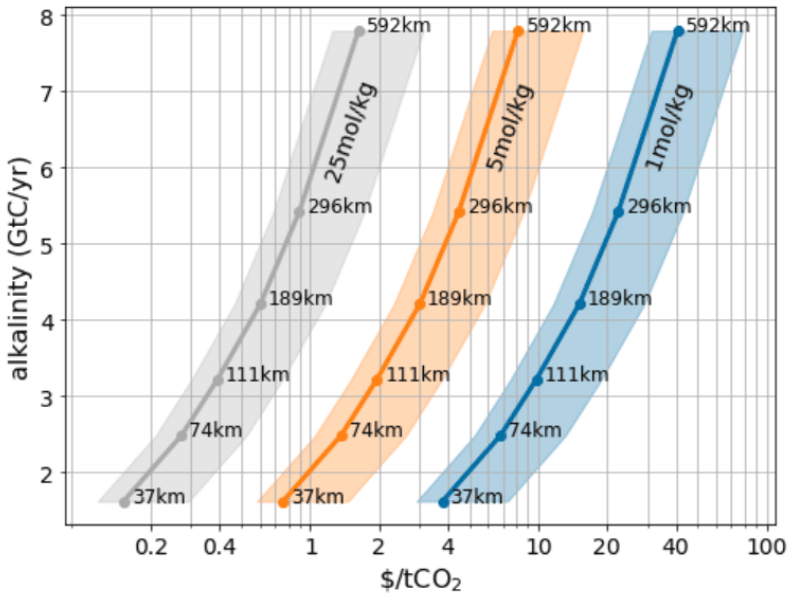

Figure 2-8: Total carbon uptake potential for a variable alkalinity addition strategy that results in a maximal pH change of 0.1 (see Fig. 1 for an example). Carbon uptake is estimated at η_{CO_2}=0.8. The strip widths necessary are indicated for each point. Shading denotes the shipping cost uncertainty, which ranges from USD 0.0016 to 0.004 per tonne per kilometer (Renforth 2012).

shows how the transportation costs are influenced by the total desired negative emissions (larger scale requires transport further offshore). For concentrated alkalinity (such as ground rocks) transport costs are not a major contributor to cost, consistent with prior work (Renforth 2012). However, for dilute alkalinity, such as that obtained from electrochemical processes, transportation could become a significant contributor to the overall cost. A potential low-cost solution could be, for example, the near-coast precipitation (Thorsen et al. 2000; Davies et al. 2018; Sano et al. 2018) of $Mg(OH)_2$ with subsequent redissolution of the solid $Mg(OH)_2$ after transport out to sea. However, economic tradeoffs between the cost of concentrating the alkalinity and the cost of transportation will need to be made.

2.4 Conclusions

In this paper we examined the suitability and effectiveness of near-coast regions of the ocean for alkalinity enhancement (OAE). We conducted a series of high resolution

(0.3°) global circulation simulations in which alkalinity was added to coastal strips of varying width under the constraint of limited ΔpH or $\Delta\Omega_{\mathrm{Arag}}$. We found that the resultant steady-state rate at which alkalinity can be added at any given location exhibits complex patterns and non-local dependencies which vary from region to region. The allowable injection rate is highly dependent on the surrounding injection pattern and varies over time, responding to external seasonal factors which are not always predictable. This makes it difficult to prevent occasional short spiking beyond the specified limit, thus potentially requiring that the limit is set conservatively in practice. These difficulties are also expected to arise in practice and have repercussions on how such OAE would be performed in reality and how it would be monitored, reported and verified (MRV). The non-local nature of the pH effect also likely requires different adjacent countries to coordinate their OAE efforts.

We found that even within the relatively conservative constraints set, most regional stretches of coastline are able to accommodate on the order of 10s to 100s of megatonnes of negative emissions, with areas with access to fast currents being able to accommodate more, such as East Africa or the coast of Peru. Globally we conclude that near-coastal OAE has the potential to scale to a few gigatonnes of CO_2 drawdown, if the effort is spread over the majority of available coastlines. However, given that many other factors will determine suitable locations (such as availability of appropriate alkaline minerals, low-cost energy and geopolitical suitability) the global potential may be lower in practice. We also examined the cost of transport of alkalinity, which increases with global deployment size as the alkaline material needs to be spread over greater distances from the shore. For alkalinity schemes based on dry minerals the transport costs remain minor, but for electrochemical methods, which produce more dilute alkalinity, this may present limits to scaling.

We also examined the effectiveness and time scale of alkalinity enhancement on uptake of CO_2, through pulsed injections and subsequent tracking of surface water equilibration. Depending on the location, we find a complex set of equilibration kinetics. Most locations reach a plateau of 0.6–0.8 mol CO_2 per mol of alkalinity after 3–4 years, after which there is little further CO_2 uptake. The plateau efficiency

depends on the amount of alkalinity lost to the deep ocean which will not equilibrate with the atmosphere until it returns to the surface, on the time scale of 100–500 years or more. The most ideal locations, reaching close to the theoretical maximum of ≈0.8, include north Madagascar, Brazil, Peru, and locations close to the Southern Ocean, such as Tasmania, Kerguelen and Patagonia, where the gas exchange appears to occur faster than the surface residence time. The variation of the achievable CO_2 drawdown per unit alkalinity on time scales relevant to the climate change crisis and the speed at which equilibration is reached poses further difficulty for verification of CDR credits.

Further study to determine these uptake efficiencies, at a finer location sample resolution and ideally with model ensembles, are needed for optimal placement of OAE deployments. While our results give an overall picture and are indicative of the complexity, more sophisticated biogeochemistry models (Carroll et al. 2022) and higher resolution regionally coupled biogeophysical models (e.g. Sein et al. 2015; Wang et al. 2023) will be essential for simulation and deployment of real-world OAE projects. It would also be interesting to examine how the CDR efficiency and OAE limits change in different future emission scenarios. At higher pCO_2 the ocean surface would be more acidic, and thus a larger OAE rate could be sustained without exceeding preindustrial surface pH. Increased stratification may increase surface residence times, thus decreasing the equilibration time. Furthermore, changes in biological activity, general circulation patterns and atmospheric dynamics further complicate the picture. Such effects and their interplay could potentially be studied in a full Earth system model under different emission scenarios.

Code and data availability Code and data are available at Zenodo https://doi.org/10.5281/zenodo.7460358 (He and Tyka 2023b).

Acknowledgements We would like to thank Chris Van Arsdale, Lennart Bach, Brendan Carter, Matt Eisaman and Matthew Long for many helpful comments on the manuscript.

2.A Appendix

Supporting Information for "Limits and CO_2 equilibration of near-coast alkalinity enhancement"

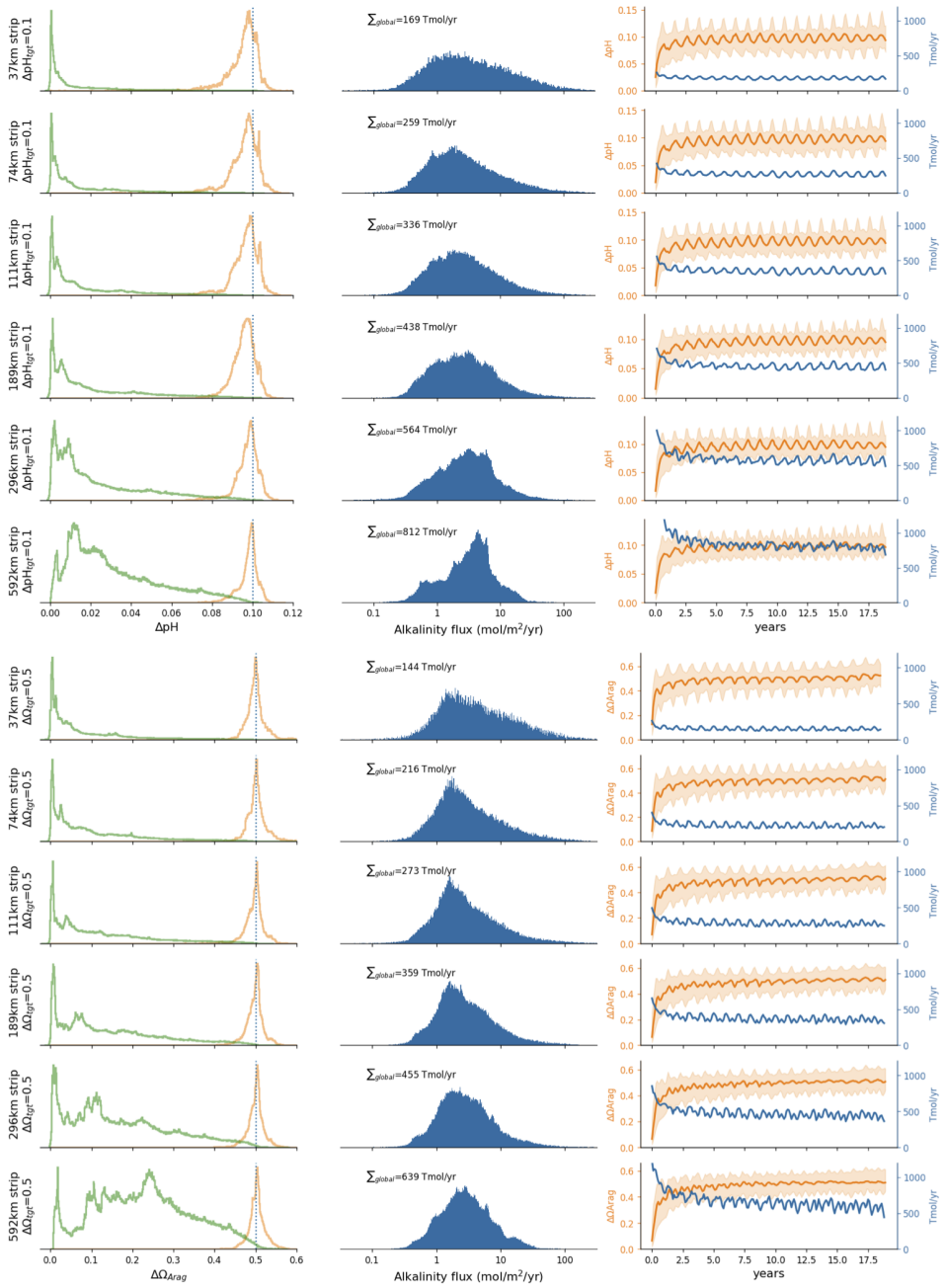

Figure 2-9: The left column shows normalized histograms of the annually averaged ΔpH or $\Delta\Omega_{\text{Arag}}$ over all grid points in the injection strip (orange) or outside the strip (green). The dotted vertical line indicates the respective target constraint. The middle column shows the distribution of the sustained alkalinity flux in the injection grid points. Note the x-axis is log-scaled, showing that injection flux spans >2 orders of magnitude. The total global injection rate is shown above the histogram. The right column shows the total global alkalinity addition rate (summed over all grid points in the coastal strip) in blue and median pH change from the reference simulation (exclusively over grid points in the strip) in orange. The shading shows the 10th and 90th percentile range. The addition rate and pH change stabilize after 5 years.

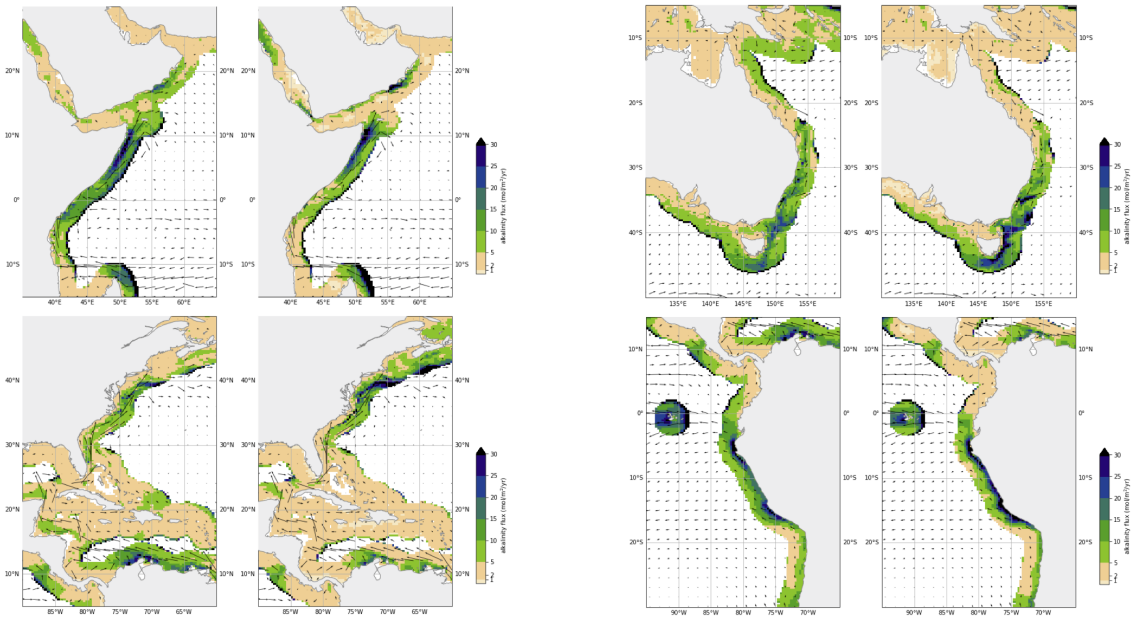

Figure 2-10: Comparison of injection patterns using a pH constraint ΔpH_{tgt}=0.1 (left) or a carbonate saturation constraint $\Delta\Omega_{tgt}$=0.5 (right) for four different regions.

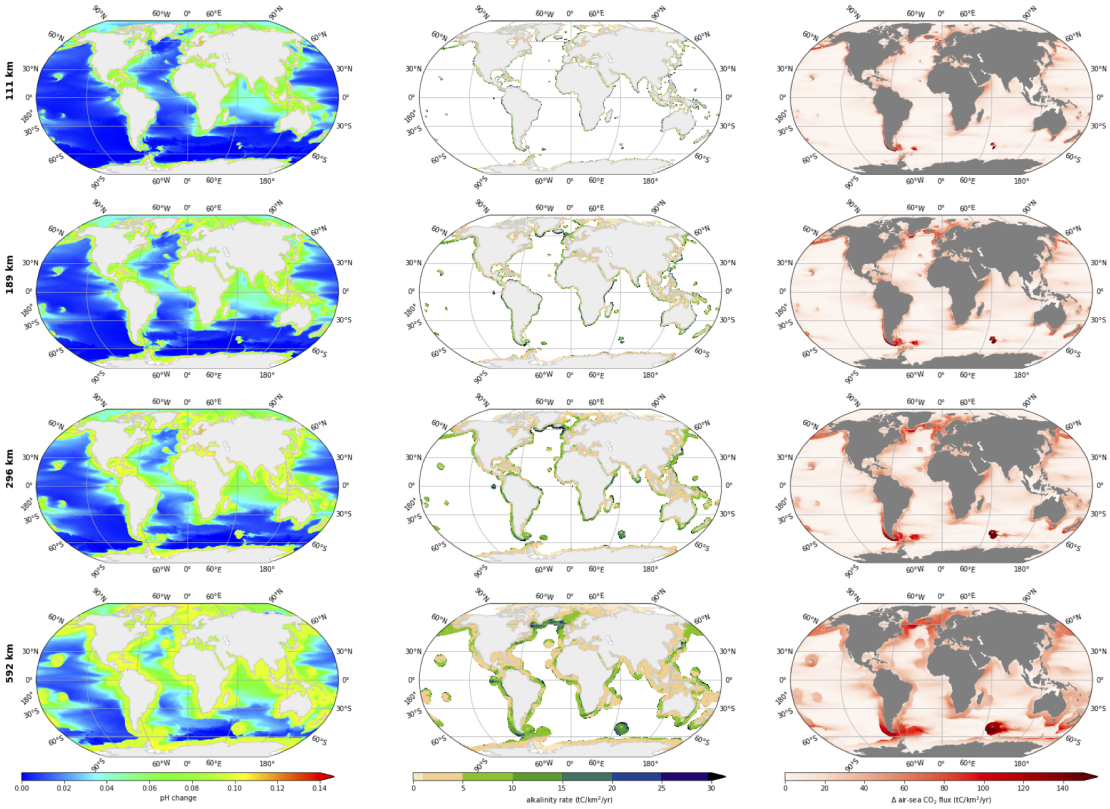

Figure 2-11: Mean pH change (left column) and alkalinity addition rate (middle column) for different strip widths. The pH change and alkalinity addition rate is averaged from years 5-20 in the simulation. Strip widths of 37 km and 74 km are not shown since they are too thin to see clearly in the global figures. Right column shows change in mean CO_2 flux relative to the reference simulation.

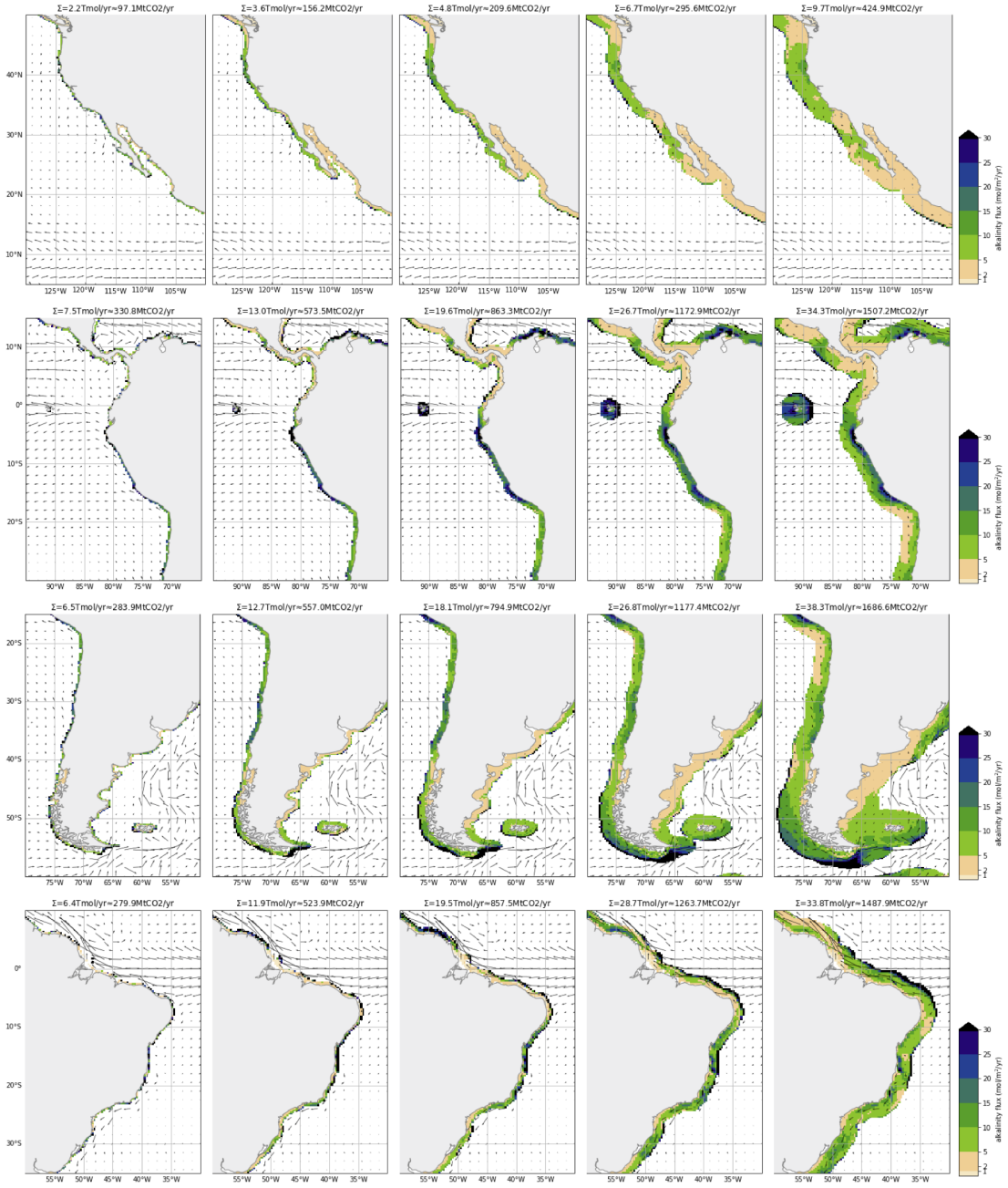
Σ=2.2Tmol/yr≈97.1MtCO2/yr
Σ=3.6Tmol/yr≈156.2MtCO2/yr
Σ=4.8Tmol/yr≈209.6MtCO2/yr
Σ=6.7Tmol/yr≈295.6MtCO2/yr
Σ=9.7Tmol/yr≈424.9MtCO2/yr
Σ=7.5Tmol/yr≈330.8MtCO2/yr
Σ=13.0Tmol/yr≈573.5MtCO2/yr
Σ=19.6Tmol/yr≈863.3MtCO2/yr
Σ=26.7Tmol/yr≈1172.9MtCO2/yr
Σ=34.3Tmol/yr≈1507.2MtCO2/yr
Σ=6.5Tmol/yr≈283.9MtCO2/yr
Σ=12.7Tmol/yr≈557.0MtCO2/yr
Σ=18.1Tmol/yr≈794.9MtCO2/yr
Σ=26.8Tmol/yr≈1177.4MtCO2/yr
Σ=38.3Tmol/yr≈1686.6MtCO2/yr
Σ=6.4Tmol/yr≈279.9MtCO2/yr
Σ=11.9Tmol/yr≈523.9MtCO2/yr
Σ=19.5Tmol/yr≈857.5MtCO2/yr
Σ=28.7Tmol/yr≈1263.7MtCO2/yr
Σ=33.8Tmol/yr≈1487.9MtCO2/yr
alkalinity flux (mol/m²/yr)

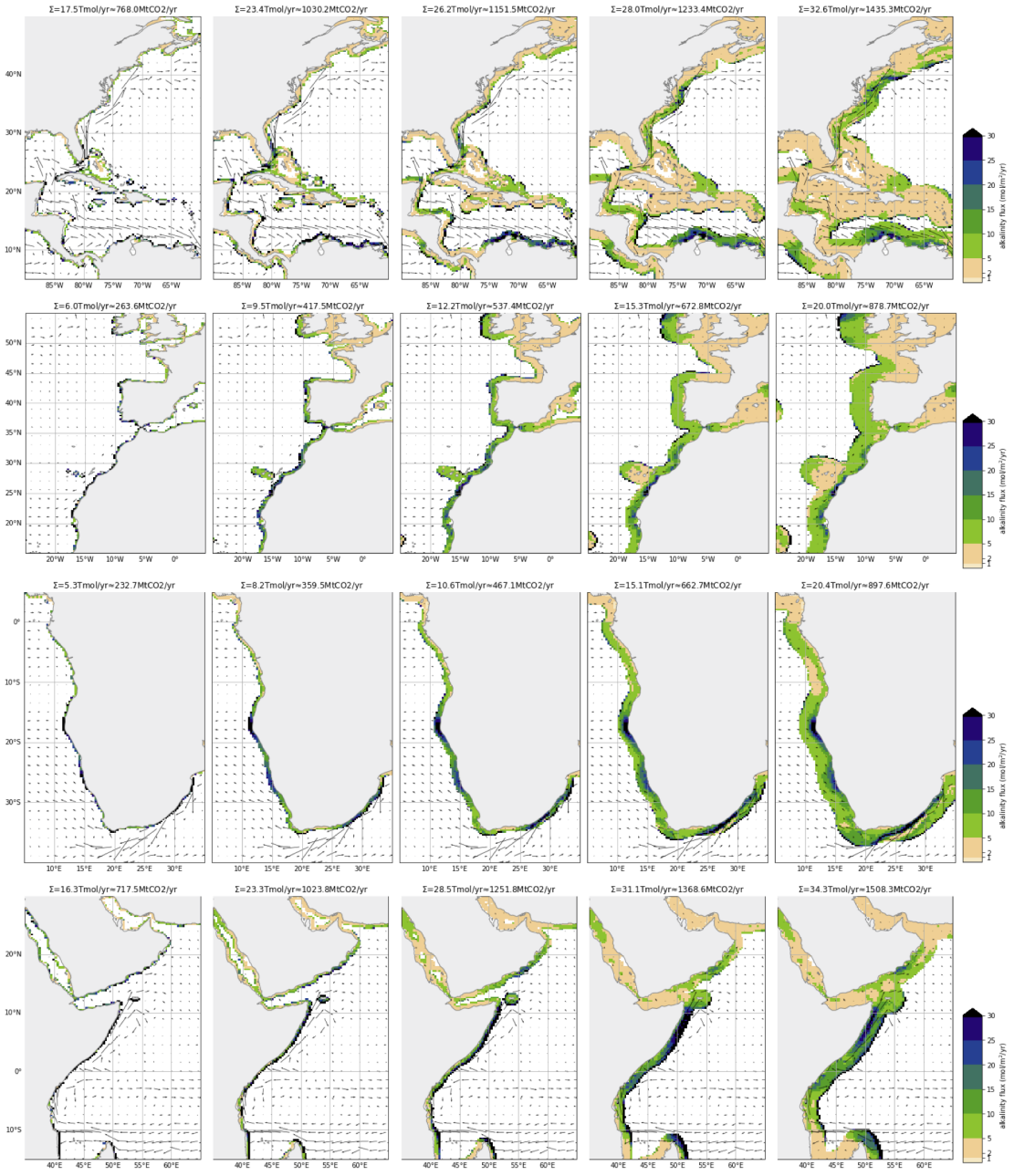
Σ=17.5Tmol/yr≈768.0MtCO2/yr
Σ=23.4Tmol/yr≈1030.2MtCO2/yr
Σ=26.2Tmol/yr≈1151.5MtCO2/yr
Σ=28.0Tmol/yr≈1233.4MtCO2/yr
Σ=32.6Tmol/yr≈1435.3MtCO2/yr
Σ=6.0Tmol/yr≈263.6MtCO2/yr
Σ=9.5Tmol/yr≈417.5MtCO2/yr
Σ=12.2Tmol/yr≈537.4MtCO2/yr
Σ=15.3Tmol/yr≈672.8MtCO2/yr
Σ=20.0Tmol/yr≈878.7MtCO2/yr
Σ=5.3Tmol/yr≈232.7MtCO2/yr
Σ=8.2Tmol/yr≈359.5MtCO2/yr
Σ=10.6Tmol/yr≈467.1MtCO2/yr
Σ=15.1Tmol/yr≈662.7MtCO2/yr
Σ=20.4Tmol/yr≈897.6MtCO2/yr
Σ=16.3Tmol/yr≈717.5MtCO2/yr
Σ=23.3Tmol/yr≈1023.8MtCO2/yr
Σ=28.5Tmol/yr≈1251.8MtCO2/yr
Σ=31.1Tmol/yr≈1368.6MtCO2/yr
Σ=34.3Tmol/yr≈1508.3MtCO2/yr
alkalinity flux (mol/m²/yr)

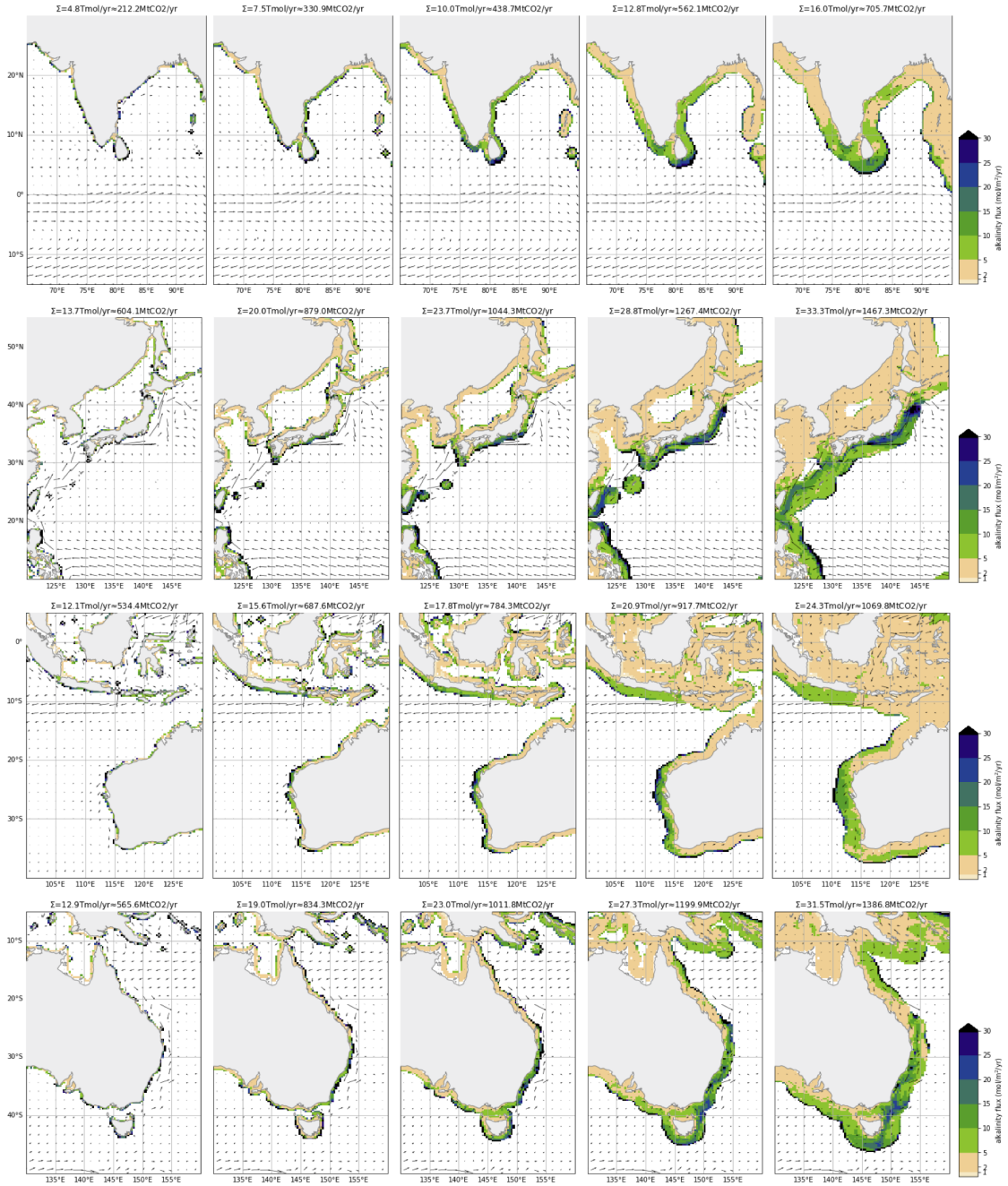

Figure 2-12: Detailed regional plots showing alkalinity fluxes, spanning the majority of coastlines. The total injection rate (in Tmol/yr) is indicated above each panel. The conversion into approximate negative emissions (in MtCO2/yr) assumes an uptake efficiency of 0.8. The panels cover most major coastlines running top to bottom from the Pacific Northwest down the west coast of the Americas, up the east coast of the Americas, Europe, west coast of Africa, east coast of Africa, India, and finally Japan and Australia.

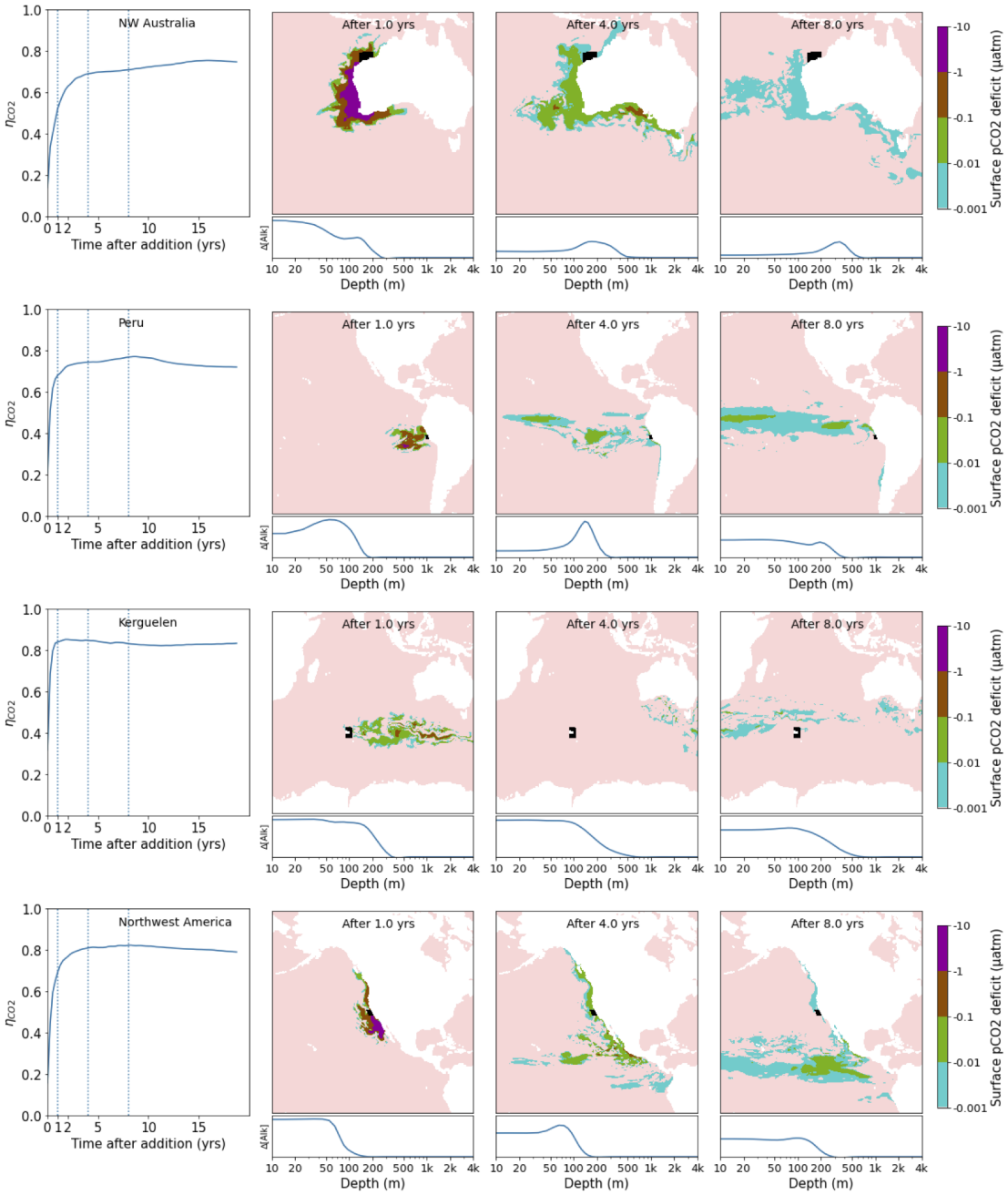
NW Australia
Peru
Kerguelen
Northwest America
After 1.0 yrs
After 4.0 yrs
After 8.0 yrs
η_{CO2}
Time after addition (yrs)
Δ[Alk]
Depth (m)
Surface pCO2 deficit (µatm)

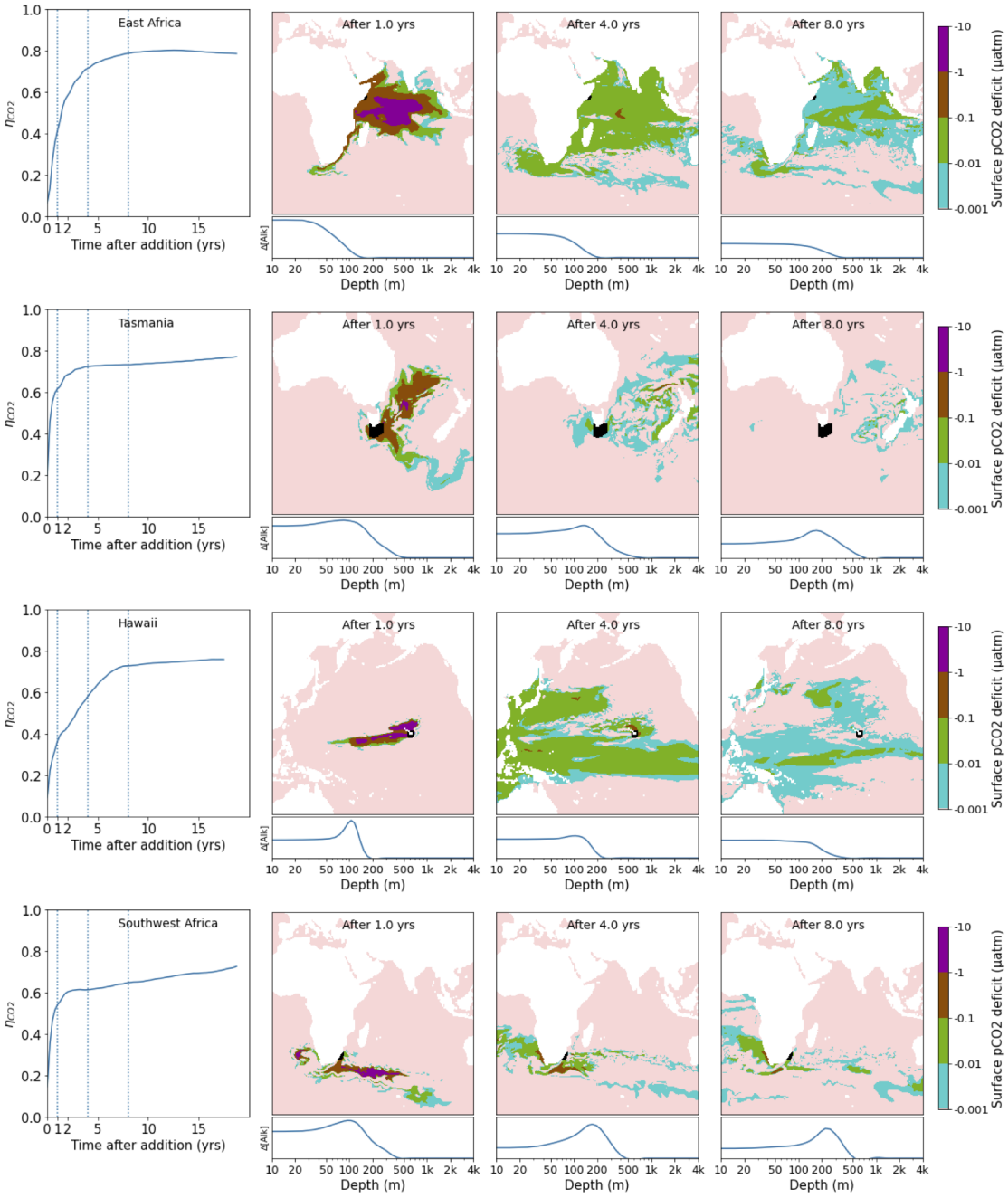
East Africa
Tasmania
Hawaii
Southwest Africa
η_{CO2}
Time after addition (yrs)
After 1.0 yrs
After 4.0 yrs
After 8.0 yrs
Δ[Alk]
Depth (m)
Surface pCO2 deficit (µatm)

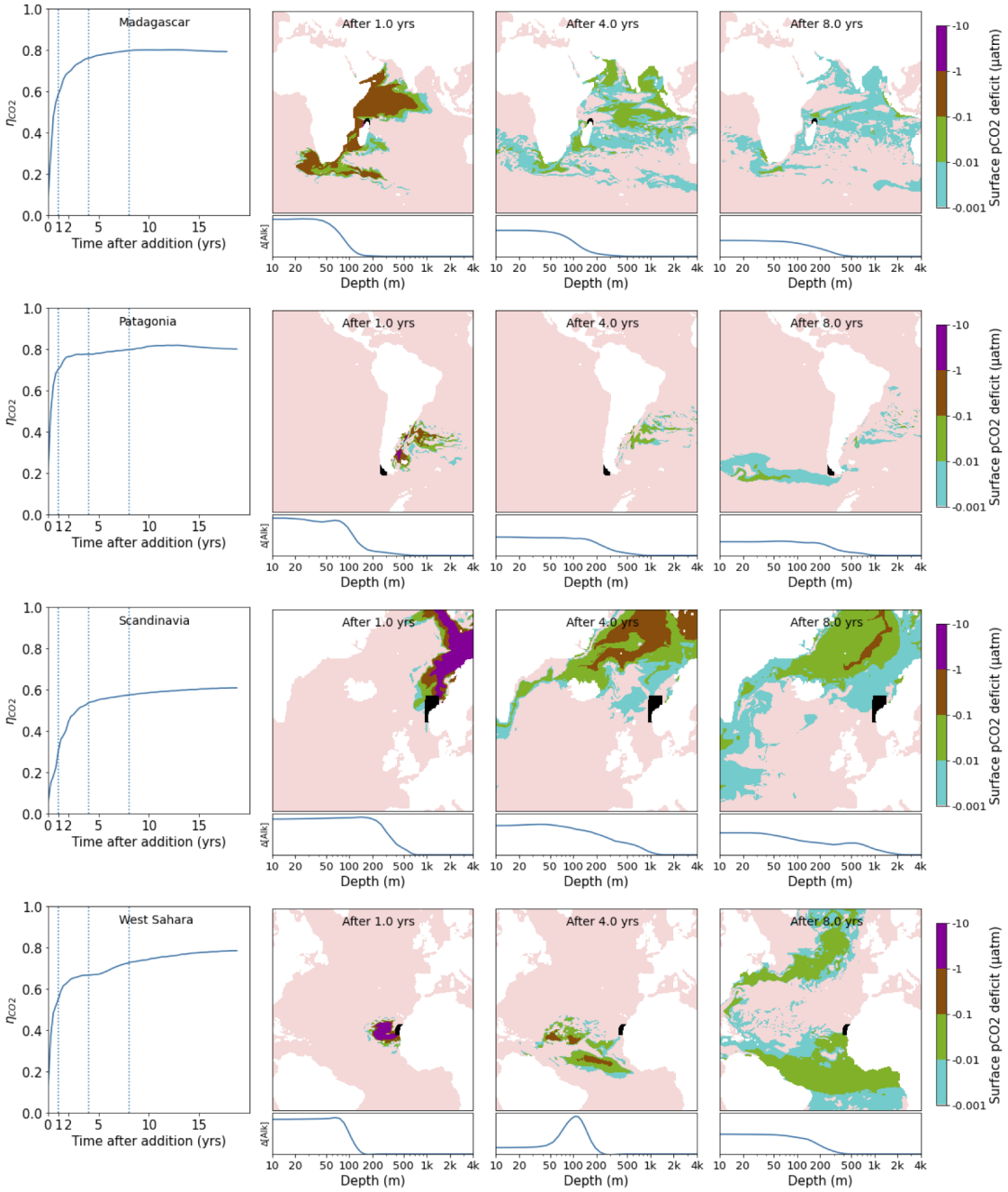
Madagascar
Patagonia
Scandinavia
West Sahara
After 1.0 yrs
After 4.0 yrs
After 8.0 yrs
η_{CO2}
Time after addition (yrs)
Δ[Alk]
Depth (m)
Surface pCO2 deficit (µatm)

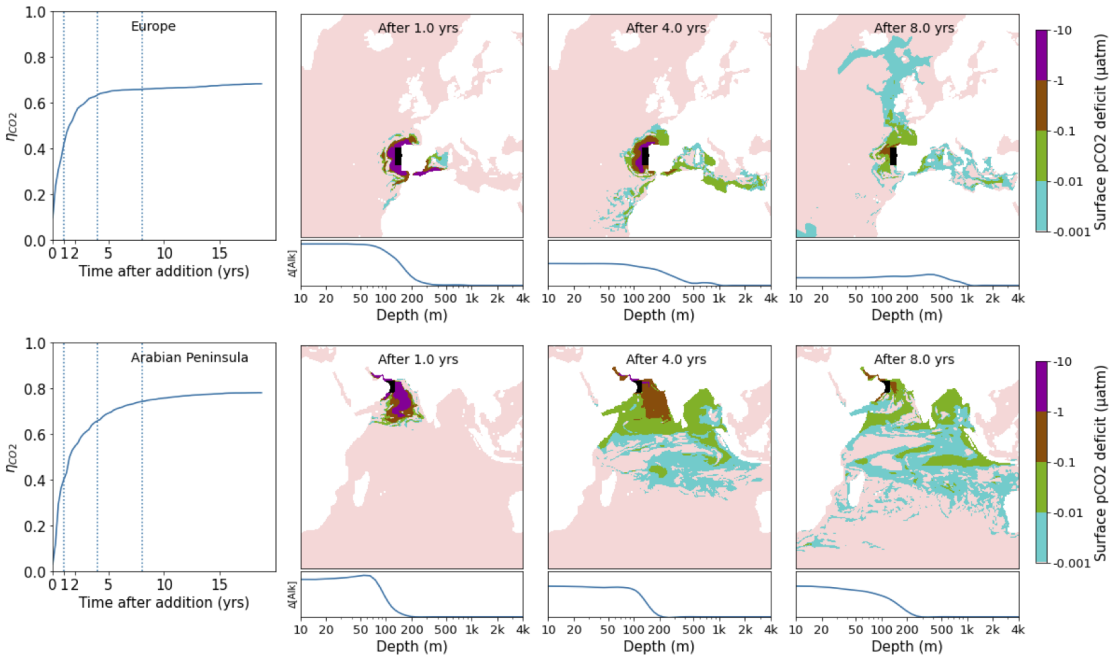

Figure 2-13: Pulse additions of alkalinity in additional locations. Due to computational constraints only a small number of pulse locations could be explored. The locations were chosen as examples, coarsely distributed along all major coastlines, in order to find and demonstrate the breadth of possible CO_2 uptake kinetics.

Chapter 3

How the source depth of coastal upwelling relates to stratification and wind

Abstract

Wind-driven coastal upwelling is an important process that transports nutrients from the deep ocean to the surface, fueling biological productivity. To better understand what affects the upward transport of nutrients (and many other properties such as temperature, salinity, oxygen, and carbon), it is necessary to know the depth of source waters (i.e. "source depth") or the density of source waters ("source density"). Here, we focus on the upwelling driven by offshore Ekman transport and present a scaling relation for the source depth and density by considering a balance between the wind-driven upwelling and eddy-driven restratification processes. The scaling suggests that the source depth varies as $(\tau/N)^{1/2}$, while the source density goes as $(\tau^{1/2}N^{3/2})$. We test these relations using numerical simulations of an idealized coastal upwelling front with varying constant wind forcing and initial stratification, and we find good agreement between the theory and numerical experiments. This highlights the importance of considering stratification in wind-driven upwelling dynamics, especially when thinking about how nutrient transport and primary production of coastal upwelling regions might change with increased ocean warming and stratification.

This chapter was originally published as He, J., and A. Mahadevan, 2021: How the source depth of coastal upwelling relates to stratification and wind. *Journal of Geophysical Research: Oceans*, **126 (12)**, e2021JC017 621, doi: 10.1029/2021JC017621.

3.1 Introduction

Coastal upwelling driven by alongshore winds is an important physical process that brings water from the deep ocean up to the surface. This upwelling results in the vertical transport and redistribution of oceanic properties and has many consequences. For instance, the upwelling of colder waters from depth can influence regional weather and climate by lowering the sea surface temperature (Izumo et al. 2008). Moreover, the vertical transport of nutrients in coastal upwelling regions fuels high primary production (Chavez and Messié 2009; Carr 2001; Messié et al. 2009), and upwelling of dissolved inorganic carbon affects the air-sea exchange of carbon dioxide (Hales et al. 2005; Friederich et al. 2008; Torres et al. 2002).

Coastal upwelling is typically driven by an alongshore wind stress that results in offshore Ekman transport given by $V_E = \tau/\rho f$, where τ is the alongshore wind stress, ρ is the seawater density, and f is the Coriolis parameter. From continuity, the offshore Ekman transport is balanced by upwelling, so V_E is also the volumetric upwelling rate of water per unit length of coastline. Coastal upwelling occurs largely within a Rossby radius of the coast, but farther offshore, Ekman pumping or suction driven by the wind stress curl may also contribute to downwelling or upwelling (Pickett and Paduan 2003; Koračin et al. 2004). The vertical velocities arising from the wind stress curl are typically weaker than those associated with offshore Ekman transport, but act over a larger area offshore, and so it may be important to consider both Ekman transport and Ekman pumping/suction depending on the region of interest (Enriquez and Friehe 1995; Pickett and Paduan 2003; Koračin et al. 2004).

Ekman transport theory has been applied extensively to quantify upwelling strength – such as through an upwelling index – based on the magnitude of the alongshore wind stress (e.g., Huyer 1983; Bakun 1990; Sydeman et al. 2014). There have been further expansions of Ekman theory to create new indices for upwelling intensity that account for wind-stress curl driven upwelling and the influence of onshore geostrophic flow (Estrade et al. 2008; Marchesiello and Estrade 2010; Rossi et al. 2013; Jacox et al. 2018). However, the upwelling intensity, which describes the volumetric rate

of upwelled water, is just a piece of the puzzle. Because the ocean is stratified with lighter layers of water above denser layers, many properties (e.g. temperature, salinity, nutrients, dissolved inorganic carbon, and oxygen) also exhibit strong vertical gradients in the water column. In a coastal upwelling region, isopycnals tilt up and outcrop near the coast, so the vertical gradients give rise to horizontal surface gradients, which we are then able to observe from satellite imagery. In order to quantify what properties are brought to the surface, it is important to consider the depth from which water originates, i.e. its source depth D_s. For instance, consider a typical temperature distribution that decreases monotonically with depth; upwelling water from 50 m will result in a different SST than if the water upwelled from 150 m. Similarly, instead of depth, we can also think about the density of water that is upwelled, which is useful for properties such as nitrate that correlate strongly with density (Omand and Mahadevan 2013). An example of accounting for upwelling source waters is the "Biologically Effective Upwelling Transport Index," which estimates the upward nitrate flux by multiplying the vertical transport by the nitrate concentration at the base of the mixed layer, where the mixed layer depth is taken to be the source depth (Jacox et al. 2018).

The effect of different upwelling source depths on the SST and phytoplankton productivity are clearly observable in the Arabian Sea (AS) and Bay of Bengal (BoB). Southwesterly winds blow over both basins during the summer monsoon, which causes upwelling along the western coasts of the AS and BoB. Interestingly though, observations show dramatically stronger effects in the AS compared to the BoB. For instance, climatological SST in the western AS cools by 4.4 °C from May to August, while SST in the western BoB only cools by 1.3 °C during this same time frame (Fig. 3-1). It is easy to point to the stronger southwesterly wind stress in the AS (0.19 Nm^{-2} in the western AS compared to 0.06 Nm^{-2} in the western BoB) as being chiefly responsible for the different upwelling responses (Fig. 3-1b). In addition to the large difference in winds, the BoB is also strikingly more stratified than the AS year round. The density stratification, characterized by the square of the buoyancy frequency $N^2 = -\frac{g}{\rho}\frac{\partial \rho}{\partial z}$, when depth-averaged over the upper 250 m in the BoB is about double that in the

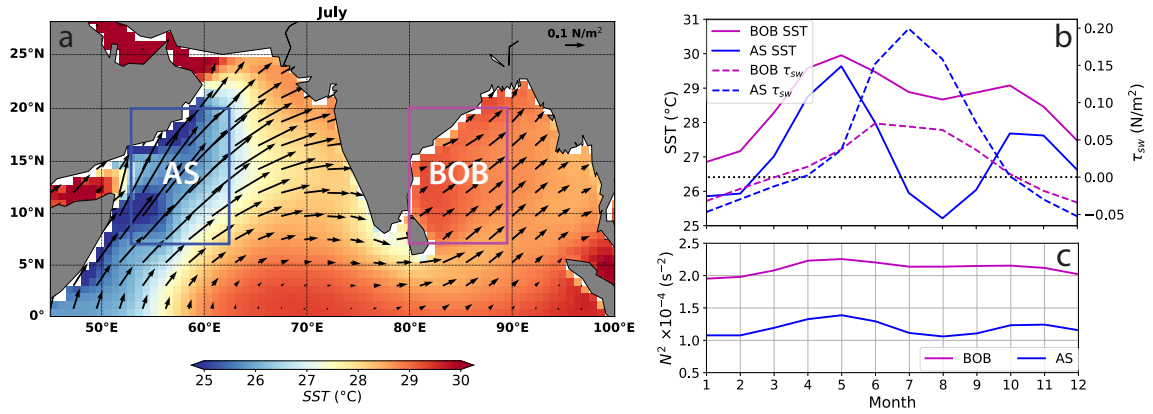

Figure 3-1: Monthly climatology for the Arabian Sea (AS) and Bay of Bengal (BoB) calculated for the period 1989-2017. **a.** Sea surface temperature (SST, color) and wind stress (arrows) in the Arabian Sea (AS) and Bay of Bengal (BoB) for July. **b.** Seasonal cycle of SST and southwesterly wind stress averaged in the regions denoted by boxes in panel a. **c.** Seasonal cycle of depth-averaged N^2 in the upper 250 m of the ocean in the AS and BoB boxes. SST and wind data are from monthly ERA-Interim Reanalysis (Dee et al. 2011), wind stress is calculated with the Large and Pond (1981) formula, and N^2 is calculated from the MIMOC climatology (Schmidtko et al. 2013) using the Gibbs Seawater Toolbox (McDougall and Barker 2011).

AS (Fig. 3-1c). Prasanna Kumar et al. (2002) concluded that the weaker wind-driven mixing in the BoB is unable to break through the strong surface stratification and entrain cold nutrient-rich water from below, which explains the higher SST and lower productivity in the BoB compared to the AS. Similarly, stratification would also counter the effect of wind-driven coastal upwelling and contribute to a shallower upwelling source depth near the western margin of the BoB compared to the AS. The contrasting response to coastal upwelling in the AS and BoB motivates the question as to what sets the source depth and source density of upwelling and how these differ between the two basins.

Previous methods for estimating source depth include using an offshore profile and identifying the depth where the density is the same as the onshore surface density (Carr and Kearns 2003), identifying the intersection of offshore and onshore temperature-salinity diagrams (Carmack and Aagaard 1977; Messié et al. 2009) or similarly using salinity and silicate as depth tracers (van Geen et al. 2000), and tracking virtual particles in a numerical ocean model (Chhak and Lorenzo 2007). More

recently, Jacox and Edwards (2011, 2012), following the theory of Lentz and Chapman (2004), investigated how the shelf slope and stratification affect the cross-shelf circulation and source depth in a two-dimensional model. They found that the source depth varies with the topographic Burger number, which is dependent on stratification, bottom slope, and f (cf. Fig. 3 Jacox and Edwards 2012). Furthermore they fit empirical models for the temporal evolution of source depth and upwelled nitrate (cf. Eq. (9), Table 2 Jacox and Edwards 2011) to model how the source depth grows over the course of an individual upwelling event lasting a few days.

In this study, we move beyond one- and two-dimensional models and empirical studies to consider how wind and stratification affect the source depth. Without considering the spatio-temporal variability in the winds or sloping topography that includes a continental shelf and slope, we argue that the source depth in an upwelling region results from a balance between the wind-driven overturning and eddy-driven restratification. It is shown that alongshore winds give rise to an upwelling front that exhibits baroclinic instability (Brink 2016; Brink and Seo 2016; Thomsen et al. 2021). These eddies are ubiquitous in upwelling fronts and tend to flatten isopycnals, thereby countering the steepening of isopycnals due to Ekman transport (Durski and Allen 2005; Capet et al. 2008), and preventing (or slowing) an indefinite increase in the source depth. This countering effect of eddies has been related to reduced nutrient concentrations and primary production in nearshore coastal upwelling regions (e.g., Gruber et al. 2011; Hernández-Carrasco et al. 2014), but to our knowledge, it has not yet been applied to estimating the source depth. We use a three-dimensional numerical model of an upwelling system to experiment with a range of parameters and test the theory. Our theory is applicable in the mean (seasonal or longer-term average) sense to any coastal upwelling region, such as the Eastern Boundary Upwelling Systems (EBUS), and for assessing how such regions may differ from each other or be affected by climate change.

In what follows, we begin, in Sec. 3.2, by developing a theoretical scaling relation for source depth, D_s as a function of windstress, τ, and stratification, N^2, in a dynamically equilibrated upwelling front. We then extend this to estimate the source

density, or the density difference of the source waters from the undisturbed (offshore) surface density. In Sec. 3.3, we describe the idealized numerical model, experiments, and methods for testing the scaling relation. The results of the numerical experiments and comparison to the scaling relation are presented in Sec. 3.4. In Sec. 3.5, we discuss potential implications of the source depth scaling on upwelling regions undergoing climate change before summarizing and concluding in Sec. 3.6.

3.2 Theoretical estimate of source depth

To develop a scaling for the quasi-balanced source depth, we begin by considering an idealized ocean initially at rest with horizontal isopycnals and a constant stratification. When a steady upwelling-favorable wind is imposed, an offshore Ekman transport is developed at the surface with a return flow in the interior, which results in an wind-driven overturning circulation denoted by the stream function ψ_w (Fig. 3-2). As dense water upwells near the coast, isopycnals steepen and outcrop at the surface, creating an upwelling front with a cross-shore buoyancy gradient as described by Allen et al. (1995). If the wind persists in maintaining the upwelling front, the front eventually becomes baroclinically unstable (Durski and Allen 2005; Brink 2016) and generates eddies. We assume the diapycnal mixing is small and that most transport occurs along isopycnals, so the effect of the eddies is to adiabatically flatten isopycnals in the along-front mean sense (Lee et al. 1997; Marshall and Radko 2003). This slumping of isopycnals and re-stratifying of the upper ocean by eddies is described by the eddy stream function ψ_e, which acts in the opposite direction to ψ_w (Fig. 3-2). A dynamical equilibrium is achieved when the mean along-front wind-driven steepening of isopycnals is countered by the eddy-driven slumping (Fig. 3-2). This is the same idea as the eddy equilibration mechanism of Marshall and Radko (2003) for the Southern Ocean, except that a coastal upwelling front is on a much smaller scale than the Southern Ocean front (100 km as opposed to 2000 km). Recently, Thomsen et al. (2021) applied this Southern Ocean analogy to upwelling systems and found that in the absence of heat flux, baroclinic instabilities do indeed

lead to a near complete cancellation of Ekman upwelling. Furthermore, Mahadevan et al. (2010) showed that the residual mean framework is also applicable to an open ocean non-quasigeostrophic mixed layer front, and here we follow their approach in balancing ψ_w with ψ_e to solve for the equilibrated source depth.

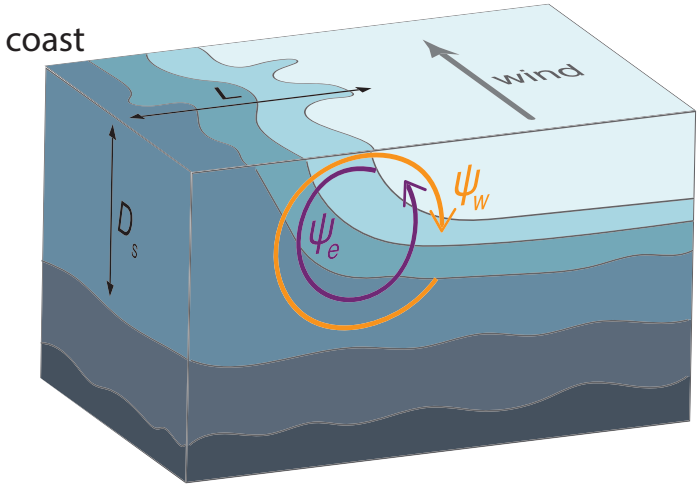

Figure 3-2: Schematic of a steady state upwelling front in the northern hemisphere. The shading denotes layers of different potential density with isopycnals denoted by the interfacial surfaces. The coast is on the left, and an alongshore wind blowing into the page causes an offshore Ekman transport that results in a wind driven overturning circulation, ψ_w. Baroclinic instabilities produce an opposing eddy-driven circulation (in the along-shore mean) given by the streamfunction ψ_e. The width of the front is L, and the source depth is D_s.

3.2.1 Source depth scaling

The wind-driven overturning circulation ψ_w is simply given by the Ekman transport

$$\psi_w = \frac{-\tau}{\rho_0 f}, \tag{3.1}$$

but we need choose a form for the eddy-driven stream function ψ_e. We use the mixed-layer instability parameterization for ψ_e (Fox-Kemper et al. 2008; Fox-Kemper and Ferrari 2008), given by

$$\psi_e = C_e \frac{D_s^2 b_y}{f}, \tag{3.2}$$

where b_y (s^{-2}) is the surface lateral buoyancy gradient, and buoyancy is defined as $b \equiv -g\frac{\rho}{\rho_0}$ (ms^{-2}). The coefficient is $C_e = 0.06$. In the Fox-Kemper et al. (2008) formulation, the strength of ψ_e depends on the mixed layer depth, but here we use the source depth, D_s, as the vertical scale, since this is the unstratified depth in the upwelling region shoreward of the upwelling front. With this choice for ψ_e, we assume that baroclinic instability is dominant in the upper ocean region of interest, and we later show in Sec. 3.4 that this choice adequately captures the eddy dynamics in our numerical model. One thing to note is that the baroclinic instabilities represented by ψ_e act in the upper ocean, while the wind-driven overturning circulation acts throughout the water column, so a balance can only be achieved in the upper ocean. However, we are primarily concerned with water entering the mixed layer and reaching the surface, so we focus on the balance of stream functions above the source depth and assume the wind-driven circulation is closed in the interior.

The lateral buoyancy gradient b_y scales as

$$b_y \sim \frac{\Delta b}{L}, \tag{3.3}$$

where Δb is the surface buoyancy difference across the upwelling front and L is the width of the front (Fig. 3-2). Typically if a pycnocline is present in the initial conditions, then the upwelled pycnocline is called the upwelling front since it has the greatest density gradient. In the case of 2D upwelling, this upwelling front will move offshore with time due to Ekman transport, so the front width will be narrower and quite different from the distance between the coast and the front (Szoeke and Richman 1984). However, in our idealized setup with uniform vertical stratification, L extends all the way to the coast and it is proportional to the cross-shore distance over which the isopycnals are sloping, which is the Rossby deformation radius. Though the eddy field will have some affect the surface front width, we take L to be the proportional to the Rossby radius of deformation. Lentz and Chapman (2004) found $L = 4ND_s/f$ from simulations of multiple coastal upwelling regions, and we also find that taking $L = 4ND_s/f$ generally agrees with the surface expression of the front across our

simulations (see Fig. 3-14; Supplementary materials).

Next, the stratification N^2 is defined as the vertical buoyancy gradient b_z, which is approximately

$$N^2 = b_z \sim \frac{\Delta b}{D_s}, \tag{3.4}$$

where Δb is now the buoyancy difference between the surface and at a depth D_s. If we assume that coastal upwelling simply tilts isopycnals so that vertical buoyancy gradients become lateral surface buoyancy gradients, then Δb in Eqs. (3.3) and (3.4) are the same. This allows us to substitute $\Delta b = N^2 D_s$ from Eq. (3.4) into Eq. (3.3), and we can now relate the lateral buoyancy gradient to stratification and the source depth. Further, substituting $L = 4ND_s/f$ into Eq. (3.4) yields $b_y = Nf/4$.

Lastly, balancing ψ_w with ψ_e from Eqs. (3.1) and (3.2) and making the substitution $b_y = Nf/4$ yields the following scaling estimate for the source depth

$$D_s = C_s \left(\frac{\tau}{\rho_0 N f} \right)^{1/2}, \tag{3.5}$$

where $C_s = (4/C_e)^{1/2} = 8.16$ for $C_e = 0.06$. Equation (3.5) tells us that $D_s \sim \tau^{1/2}$, as stronger winds drive greater offshore Ekman transport, resulting in the upwelling of deeper water. Conversely, $D_s \sim N^{-1/2}$, since increased stratification creates a larger lateral density gradient, which strengthens the eddy overturning circulation (Eq. 3.10) to reduce upwelling depth. Lastly, the 1/2 power-law in Eq. (3.5) implies that source depth is most sensitive to changes when τ/N is small, i.e. in strongly stratified regions with weak wind.

Interestingly Eq. (3.5) gives the same scaling as the Pollard-Rhines-Thompson (PRT) wind-driven mixed layer depth as both are dependent on $(\tau/\rho_0 f N)^{1/2}$. However, Eq. (3.5) arises from a different process (balancing eddy restratification with upwelling) than the Richardson-number criteria that is used for the PRT depth (Pollard et al. 1973). One difference is that the coefficient for the PRT depth is around 0.57-1.29 (Lentz 1992), while the coefficient in Eq. (3.5) is about 8 times larger. It makes sense that the source depth varies in a way similar to the mixed layer depth

since the source depth has to be at least as deep as the mixed layer depth. Moreover, it is reassuring that the PRT depth has been shown to match well with observed mixed layer depths in upwelling regions around the world (Lentz 1992; Dever et al. 2006), and the onshore velocities are found to peak below the PRT depth (Dever et al. 2006). So it seems reasonable that the source depth would correlate with the PRT depth, but be deeper overall.

3.2.2 Density of upwelled water

While it is intuitive to think of a source depth, many variables of interest in the ocean–such as temperature and nitrate–have a stronger correlation with density than depth (Omand and Mahadevan 2013). Thus, depending on the application, it may be useful to think in terms of the density of upwelled water instead of its source depth. We denote the upwelling density as a density offset $\Delta\rho$ from offshore surface waters ρ_{offshore}, so the true density of water upwelled near the coast is equal to $\Delta\rho + \rho_{\text{offshore}}$.

To obtain a scaling relation for $\Delta\rho$, we use Eq. (3.4) to make the substitution $D_s = -\frac{g}{\rho_0}\frac{\Delta\rho}{N^2}$ in Eq. (3.5). Equation (3.5) can then be recast as a scaling relationship for $\Delta\rho$ as a function of the wind stress and stratification:

$$\Delta\rho = \frac{C_s}{g}\left(\frac{\rho_0\tau}{f}\right)^{1/2} N^{3/2}. \tag{3.6}$$

In contrast to the source depth in Eq. (3.5), the density offset scales with $N^{3/2}$ since larger vertical density gradients (N^2) result in a greater surface lateral density difference ($\Delta\rho$) and equivalently, a larger density offset from the source of upwelling. $\Delta\rho$ scales as $N^{3/2}$ instead of N^2, because stronger stratification also strengthens the eddy overturning circulation and weakens upwelling. Thus, eddies reduce the extent to which stratification influences the density offset, but $\Delta\rho$ still has a stronger dependence on stratification than wind. Any combination of wind stress and stratification yields a unique source depth and density offset, which means we can use D_s and $\Delta\rho$ interchangeably and easily convert between the two.

3.3 Methods

To evaluate Eqs. (3.5) and (3.6), we use a three-dimensionsal (3D) numerical ocean model configured in a periodic channel with stratification and wind stress that represent the range observed in the Arabian Sea and Bay of Bengal. We run simulations with different values of wind stress and initial stratification to test how the source depth and density offset respond. In these simulations, we use a constant value of wind stress and uniform N^2 for the majority of cases, although we also test the scaling with more realistic profiles of $N^2(z)$. From the model outputs, we calculate the source depth D_s and density offset $\Delta\rho$ based on the upwelling in the 3D numerical model and compare those to theoretical estimates of D_s and $\Delta\rho$ from Eqs. (3.5) and (3.6).

3.3.1 Numerical model

We use the Process Study Ocean Model, which numerically solves the nonhydrostatic Bousinesq equations (Mahadevan et al. 1996a,b). The model domain is a flat-bottomed re-entrant channel on an f-plane centered at a latitude of 15°N, approximately the mid-latitude of the AS and BoB. The channel extends 96 km in the alongshore (x) direction, 384 km in the cross-shore (y) direction, and has a total depth of 500 m (in the z direction). The horizontal grid resolution is 1 km, and there are 32 stretched vertical levels ranging in thickness from 1 m at the surface to 36 m at the bottom. A horizontal resolution of 2 km is also tested and it did not significantly alter the source depth, but we use 1 km which is consistent with Durski and Allen (2005). The boundary conditions are periodic in the alongshore direction, and no-flow boundary conditions are enforced at the walls in the cross-shore direction. The cross-shore width is chosen to be large enough so that the offshore boundary does not influence the upwelling dynamics at the coast located at $y = 0$ km. Deepening the domain to 1000 m and doubling the width of the channel in the y direction has no significant effect on the source depth. The model is initialized with the same vertical density profile throughout the domain and is started from a state of rest with no

initial horizontal gradients.

A wind stress $\tau = (\tau^x, 0)$ is applied in the negative x direction, which drives upwelling at the coast located at $y = 0$ (Fig. 3-3). The alongshore wind stress is $\tau^x = -\tau_{max}$ everywhere except near the offshore wall, where τ^x decays linearly to 0 from $y = 234$ km to $y = 385$ km to spread the downwelling over a large area far offshore. At the start of the model run τ is increased linearly from 0 to τ^x over the first 10 days to gradually spin up the model and avoid generating strong internal waves. After day 10, the wind stress is held constant.

To test the validity of explaining source depth with the dynamical equilibrium proposed, we need to be careful with the model mixing scheme. Here, we aim to characterize the source depth that results from the balance between coastal upwelling and eddy-restratification, which are both largely adiabatic processes. But, the source depth could also deepen due to vertical mixing, a diapycnal process. In order to focus on the adiabatic processes, we use a simple mixing scheme that results in a predictable mixed layer depth, which is less than the source depth. This ensures that the source depth is not influenced by diabatic mixing. In the horizontal, we use a constant eddy diffusivity and viscosity of $K_h = 1$ m^{2}s^{-1} in all the simulations. The vertical eddy diffusivity and viscosity K_z is dependent on the wind stress and is parameterized following Mahadevan et al. (2010) as

$$K_z = \max\left\{\frac{1}{2}K_{max}\left[1 + \tanh\left(\frac{z+\delta_E}{\Delta}\pi\right)\right], K_{min}\right\}, \tag{3.7}$$

where $\delta_E = \frac{0.4}{f}\left(\frac{\tau}{\rho}\right)^{1/2}$ is the depth of the surface Ekman layer and Δ (m) is the transition height (see Fig. 3-3). All of the numerical experiments used $K_{max} = 10^{-2}$ m^{2}s^{-1}, $K_{min} = 10^{-5}$ m^{2}s^{-1}, and $\Delta = 0.5\delta_E$, based on Mahadevan et al. (2010).

Equation (3.7) creates a surface mixed layer whose thickness depends on the wind stress while neglecting the effect of air-sea buoyancy fluxes (e.g. heating or cooling), which are not included in the model. A constraint is that the source depth D_s cannot be shallower than the mixed layer depth MLD, and is in fact much deeper in the simulations. By purposefully making the model mixing independent of N^2, we are able

to evaluate the effect of N^2 on the eddy restratification process without concern that lowered stratification might increase mixing, and thereby enhance the source depth. If we were to use a more sophisticated, but less interpretable, turbulence closure scheme –such as Mellor-Yamada , k-ϵ, or K-Profile Parameterization (Wijesekera et al. 2003; Mukherjee et al. 2016)– as is commonly used in coastal settings, then it would less clear how much vertical mixing affects the source depth. This would make it more difficult to isolate the dependence of source depth on the balance between ψ_w and ψ_e.

We run nine experiments varying the initial N^2 between 10^{-5} and 10^{-4} s^{-2} and varying τ_{max} between 10^{-2} and 10^{-1} Nm^{-2}. The stratification values were chosen to approximately span the range of observed N^2 (averaged over the top 500 m) in the Arabian Sea and Bay of Bengal. While the southwesterly wind stress reaches 0.2 Nm^{-2} in the Arabian Sea, this high a value was difficult to implement since the wind in the model blows constantly for months and it would necessitate a very small time step. So we cap the highest constant wind stress in our model simulations at 0.1 Nm^{-2}. Three additional experiments are run with the initial $N^2(z)$ varying with depth to test the effects of using more realistic density stratification profiles. For these three experiments, we vary the thickness of the initial mixed layer (ML) and the peak stratification in the initial profile N^2_{peak}, but maintain the same depth-averaged stratification in the upper 250 m. These additional three experiments are further explained in Sec. 3.4.3. Table 3.1 summarizes the parameters used in each experiment. Each simulation is integrated forward in time with a time step of 108 s (for $\tau_{max} = 0.1$ Nm^{-2}) or 216 s (all other experiments) for at least 30 days after the upwelling front becomes unstable. The total time period of the simulations ranged from 60 days to 180 days, depending on how long it takes for the front to become unstable. Outputs are saved at 1-day intervals.

Our simulations are designed to be as simple as possible while still capturing the dynamics of interest - i.e., the competition between the wind-driven upwelling and eddies. As a result, several other factors that affect upwelling are neglected. To start, we ignore bottom topography, which impacts the source depth through altering the cross-shore velocity and its depth structure (Lentz and Chapman 2004; Choboter

et al. 2011; Jacox and Edwards 2011, 2012). Here we focus on upwelling just from the interior and not coming up slope through the bottom boundary layer. Moreover, Brink (2016) found that the available potential energy for baroclinic instability, as well as the eddy kinetic energy and eddy length scale, all depend on the bottom slope. In addition, there is no bottom friction in the experiments shown here; we find that the inclusion of bottom friction does not significantly alter the source depth, so it is omitted to exclude having another parameter to tune. Because a constant wind stress is applied for months in the model, we see unrealistically large horizontal velocities of up to 2 ms^{-1} in some simulations. For simplicity though, we keep the wind stress constant in time, without any cross-shore component or wind stress curl. To keep the wind-driven upwelling circulation ψ_w simple, we omit other processes that affect the cross-shore circulation such as an alongshore pressure gradient, which would drive onshore geostrophic transport and decrease the upwelling velocities (Marchesiello and Estrade 2010). Lastly, a consequence of the minimal mixing is that surface Ekman transport sometimes results in unstable density profiles near the surface. This could be remedied by adding a convective mixing scheme, but is avoided because we find it results in unrealistic horizontal grid-scale gradients (Cessi 1996). We think that these unrealistic artifacts of the model do not affect the overall results of this study.

3.3.2 Source depth calculation

We determine the "true" source depth in the model by using passive tracers to track the initial depth of water parcels. The model is initialized with 32 separate passive tracers, one at each vertical level. Each tracer is initialized to have a concentration of 1 in its starting grid cell and 0 everywhere else. As water advects in the model, each grid cell will have a combination of tracers from various starting depths. We obtain a single source depth for each grid cell by taking a weighted average of all the initial depths of the tracers present, weighted by the tracer concentrations. Mathematically, this is defined as

Table 3.1: Alongshore wind stress τ_{max}, depth-averaged initial stratification (N^2_{avg}) in upper 250 m, and details about the shape of the initial N^2 profile for the various simulations in this paper. The first nine experiments are initialized with an uniform N^2 profile. The experiments "small peak," "large peak," and "deep ML" are initialized with non-constant N^2 profiles with varying mixed layer thickness (ML) and peak N^2 values (N^2_{peak}) (Fig. 3-9).

Experiment	τ_{max} ($\mathrm{Nm^{-2}}$)	N^2_{avg} ($\mathrm{s^{-2}}$)	N^2 shape	
lowW_lowN	10^{-2}	10^{-5}	constant	
lowW_medN	10^{-2}	5.5×10^{-5}	constant	
lowW_highN	10^{-2}	10^{-4}	constant	
medW_lowN	$5.5\times\ 10^{-2}$	10^{-5}	constant	
medW_medN	$5.5\times\ 10^{-2}$	5.5×10^{-5}	constant	
medW_highN	$5.5\times\ 10^{-2}$	10^{-4}	constant	
highW_lowN	10^{-1}	10^{-5}	constant	
highW_medN	10^{-1}	5.5×10^{-5}	constant	
highW_highN	10^{-1}	10^{-4}	constant	
			ML (m)	N^2_{peak} ($\mathrm{s^{-2}}$)
small peak*	10^{-1}	10^{-4}	25	10^{-3}
large peak*	10^{-1}	10^{-4}	25	2×10^{-3}
deep ML*	10^{-1}	10^{-4}	75	10^{-3}

*See Sec. 3.4.3 for more details.

$$D_s = \frac{\sum_{i=1}^{M} c_i d_i}{\sum_{i=1}^{M} c_i}, \tag{3.8}$$

where M is the number of tracers (32 in this case), d_i is the initial depth of tracer i, and c_i is the concentration of tracer i. The density offset $\Delta\rho$ is calculated the same way using Eq. (3.8) by replacing d_i with $\Delta\rho_i$, where $\Delta\rho_i$ is the initial density offset of tracer i from the surface density. For the case of initial constant stratification, $\Delta\rho_i = -\frac{\rho_0}{g} N^2 d_i$. This allows us to easily convert between D_s and $\Delta\rho$ calculated in the model to $\Delta\rho$ using $\Delta\rho = -\frac{\rho_0}{g} N^2 D_s$.

We calculate the source depth over a time period when the model has achieved a dynamic equilibrium. This is identified as a 20 day period of the model run with the minimal change in eddy kinetic energy (EKE) (Supporting Information, Figs. 3-12, 3-13). The EKE is calculated as $EKE = \frac{1}{2}(u'^2 + v'^2 + w'^2)$, where u', v', w' are respectively the alongshore, cross-shore, and vertical velocity anomalies from the alongshore mean. For each simulation, we identify the period of dynamic equilibrium

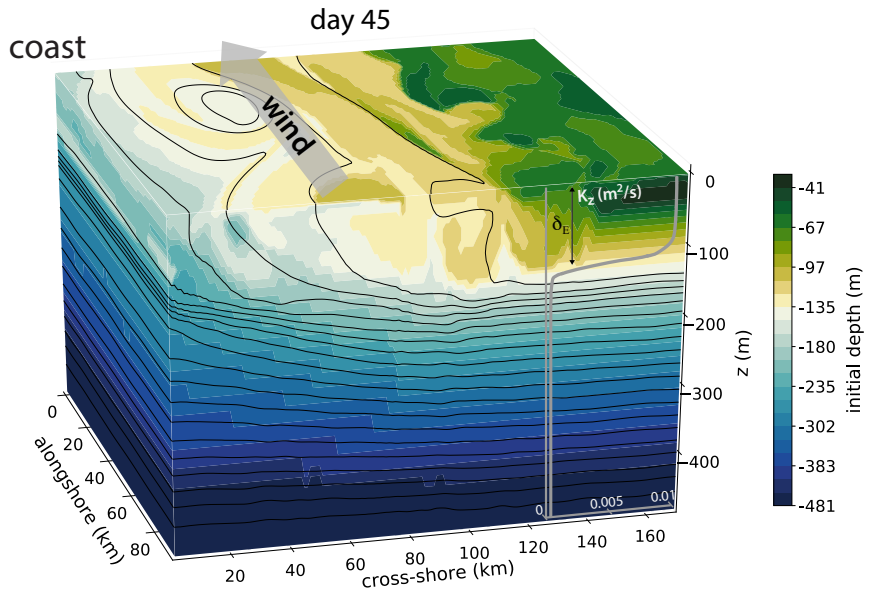

Figure 3-3: Model setup and snapshot of isopycnals (black contours, interval of 0.15 kg/m^3) and depth tracers at day 45 for experiment highW_highN (Table 3.1). A steady alongshore wind blows into the page, driving coastal upwelling at the western coast of the domain. The initial depth of the dominant tracer in each grid cell is shown in colors, and the shape of the vertical diffusivity (and viscosity) K_z profile is also indicated.

as the 20-day period where the linear regression of the depth-averaged EKE in a nearshore 150 km band has the smallest slope, so the change in EKE with time is minimized during this period. We also find that our main results are robust to different choices of the 20-day time windows.

Then for each day, we determine the source depth for a particular simulation by averaging over the upwelling area, defined by a distance r from the coast and a depth δ from the surface. We take r to be 30 km to represent a narrow coastal band where the deepest isopycnals are outcropping right at the coast. As for δ, since we are considering water parcels that reach the surface, we choose δ to include just the top 3 layers of grid cells representing the upper 11.7 m. We find that varying δ between the top 2 to 4 grid cells (which changes δ between 6.1 and 17.6 m) and varying r between 10 and 40 km alters the source depth by about 10 m. Averaging over the area given by r and δ gives a single source depth for each cross-shore transect in the model. The source depth is then calculated according to Eq. (3.8) for each day of the 20-day

period and for each cross-sectional slice in the alongshore direction (we average 96 cross-shore slices of the model over 20 snapshots, i.e., over $n = 1920$ realizations). We report the median D_s during this period, as well as the 10th and 90th percentile values.

3.4 Results

3.4.1 Evolution of model eddy field

We now have everything we need to estimate D_s and $\Delta\rho$ from the scaling relations developed in Sec. 3.2 (Eqs. 3.5 and 3.6) and compare those to the actual source depths and density offsets calculated from tracers. But before doing that, we first show that the model produces reasonable upwelling dynamics and check that our assumption of a dynamic equilibrium is valid. Prior the onset of instabilities, the model produces the expected two-dimensional Ekman response (Fig. 3-4a). There is an offshore Ekman transport in the surface boundary layer with a weak return flow distributed throughout the interior, which is consistent with previous descriptions of coastal upwelling (e.g. Allen et al. 1995; Brink 1983; Huyer 1983; Lentz and Chapman 2004). Isopycnals steepen and outcrop near the coast, and we see the formation of a lateral density front and an alongshore surface-intensified jet in the same direction as the wind (Fig. 3-4a). Note that the jet velocities are larger than what is observed in the ocean because the wind is blowing nonstop in our model over many days, and the example shown is a strong wind case. Moreover, the upwelling transport in the model, calculated from integrating vertical velocities within a Rossby radius of the coast at the Ekman depth, is consistent with the theoretical value given by $\tau/\rho f$.

Far offshore, beyond the region of interest, isopycnals are flat and the flow is barotropic, so the onshore return flow is uniformly distributed with depth below the mixed layer. One concern, with two-dimensional models or channel models such as ours, is that if the model is run for long enough, the deep offshore waters will reach the coast and the model will no longer be realistic. However, our simulations

are not run long enough that this is an issue. For example, on day 20 in experiment highW_highN shown in Fig. 3-4a, the onshore return flow is approximately barotropic around 275 km offshore with a velocity < 0.01 ms^{-1}. It would take over 300 days for water from $y = 275$ km to reach the coast, which is far longer than the length of any of our simulations (which extend up to 180 days at most). Furthermore, 300 days is a lower-bound estimate and this timescale will be much larger for simulations with a weaker wind and weaker cross-shore velocities.

As the wind forcing persists, the front continues to intensify until it becomes baroclinically unstable (Fig. 3-4b). The emergence of eddies can be seen in the surface fields as well as in the EKE (Fig. 3-12), which is initially zero during the spin-up of the simulations and then sharply increases when instabilities emerge. The onset of instabilities takes anywhere from 30 days for the high wind stress simulations, to over 100 days for the lower wind stress simulations. As expected, the EKE increases with stratification (due to an increased source of available potential energy) and wind stress.

The EKE is typically much larger than the mean kinetic energy (Fig. 3-12). This behavior is consistent with the findings of Brink (2016). Lastly, there is a range of front widths L across the various simulations, which can be seen qualitatively in Fig. 3-6. Overall the front widths are consistent with the Rossby deformation radius. For a given stratification, medium and high winds result in a wider front since D_s is greater. And for a fixed wind stress, medium and high stratification gives rise to larger L than weak stratification.

Next, we check the plausibility of assuming a balance between ψ_w (Eq. 3.1) and ψ_e (Eq. 3.2). Qualitatively, we see from Fig. 3-4 that eddies re-stratify the surface; the isopycnals are less vertical on day 45, a few days after the onset of baroclinic instabilities, as compared to day 20. We also directly calculate and compare ψ_w (Eq. 3.1) and ψ_e (Eq. 3.2) from the model fields (Fig. 3-5) to evaluate the balance between the wind-driven steepening and eddy-driven slumping of isopycnals. Similar to Mahadevan et al. (2010), we calculate ψ_w from the model velocity fields as

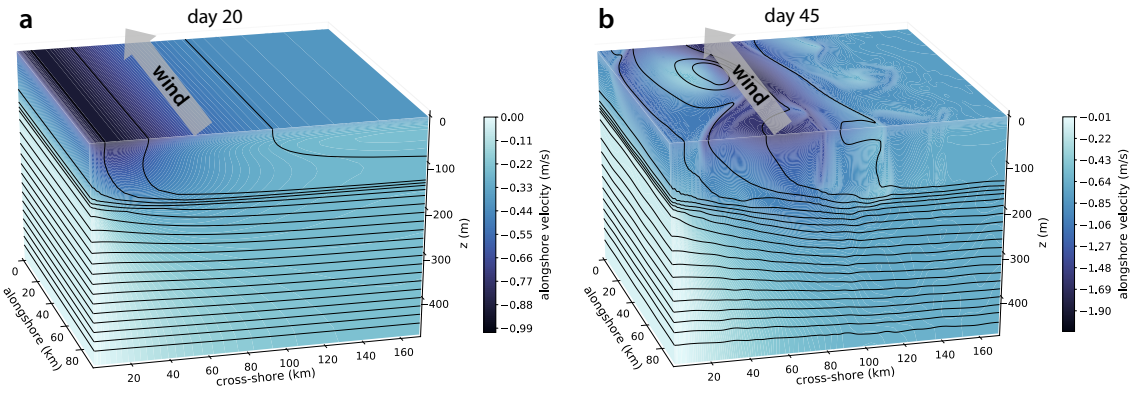

Figure 3-4: Alongshore velocity u (colors) and density (black contours) at days 20 and 45 of experiment highW_highN (Table 3.1). **a.** Initially, after the alongshore wind is turned on, there is a 2D response that produces an upwelling front and an alongshore geostrophic jet. Deeper isopycnals outcrop near the coast and are nearly vertical in the upwelling region. **b.** At a later time, the front then becomes baroclinically unstable and the resulting eddies slump the isopycnals. The density contour interval is 0.15 kg/m^3. This is an idealized model setup with a constant wind blowing continuously, so the lateral velocities are larger than what would be observed in the real ocean.

$$\psi_w = -\int_0^z \bar{v}\ dz = \int_0^y \bar{w}\ dy, \tag{3.9}$$

where the overbar denotes an alongshore average. The eddy stream function ψ_e is typically defined as $\psi_e = \overline{v'b'}/\bar{b}_z$ in the interior (Andrews and McIntyre 1976) and $\psi_e = \overline{-w'b'}/\bar{b}_y$ for the boundary layer (Held and Schneider 1999). These two forms were combined into a more general definition in Cerovečki et al. (2009), in which a coordinate stretching factor ϵ is added to correct for the small aspect ratio seen in the ocean and in our model. Here, we use the Cerovecki formulation of ψ_e that is also used in Mahadevan et al. (2010):

$$\psi_e = \epsilon \left(\frac{\epsilon \overline{v'b'}\bar{b}_z - \frac{1}{\epsilon}\overline{w'b'}\bar{b}_y}{\bar{b}_y^{\,2} + \epsilon^2 \bar{b}_z^{\,2}} \right), \tag{3.10}$$

where the primes denote deviations from the alongshore mean ($v' = v - \bar{v}$, $w' = w - \bar{w}$), and $\epsilon = 10^{-3}$ is a dimensionless vertical stretching factor. Mahadevan et al. (2010) found that the results are not sensitive to varying ϵ between 10^{-2} and 10^{-4}.

A cross-sectional slice of ψ_w and ψ_e calculated using Eqs. 3.9 and 3.10 on day

45 for experiment highW_high_N (Table 3.1) is shown in Fig. 3-5. The colorbars are scaled so that positive values are orange and negative values are purple, with white being zero. As expected, ψ_w is predominantly positive, indicating a clockwise circulation that upwells dense water near the coast at $y = 0$ (Fig. 3-5a). On the other hand, ψ_e is mostly negative, so it drives a counter-clockwise circulation that opposes ψ_w (Fig. 3-5b). Averaged over the region of sloping isopycnals (130 km from the coast), ψ_e and ψ_w are similar in magnitude and approximately balance each other above the source depth (Fig. 3-5c). The Fox-Kemper et al. (2008) parameterization for mixed-layer instabilities ψ_{MLI}–from Eq. (3.2), where we replaced b_y with $Nf/4$–is shown in the gray-dashed line in Fig. 3-5c, and it seems to be an appropriate choice since it adequately captures the eddy activity in the simulations. We also experiment with using the parameterization of Marshall and Radko (2003) for mesoscale eddies, but it does a much poorer job of capturing the vertical structure and magnitude of ψ_e in our model. The other experiments with different parameter choices look qualitatively similar to Fig. 3-5 in that ψ_e and ψ_w are of opposite signs and similar order of magnitude, and that ψ_{MLI} adequately captures the magnitude and structure of ψ_e. Thus, we feel confident in our choice of eddy parameterization and assumption of a quasi-balanced state in the overturning.

3.4.2 Evaluation of scaling relations

Finally, we can use our model experiments to assess the scaling relations for source depth (Eq. (3.5)) and density offset (Eq. (3.6)). Figure 3-6 shows a snapshot of the source depth calculated from tracers across the nine main simulations (Tab. 3.1). In general, for a given stratification, the source depth increases as expected with stronger winds. For a fixed wind stress, we see the source depth decreasing with higher stratification as predicted by Eq. (3.5). In addition, the density contours in Fig. 3-6 are all at the same 0.05 kgm^{-3} intervals, which allows us to compare the density offset ($\Delta\rho$, i.e. the difference in density across the front) between simulations. It is clear that $\Delta\rho$ is directly related to stratification, as evidenced by the increasing number of contours as stratification increases, which is consistent with Eq. (3.6).

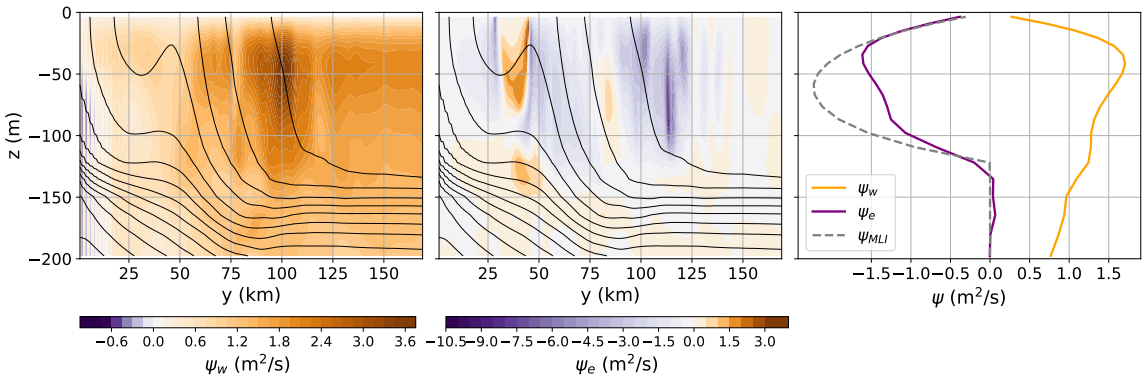

Figure 3-5: **a.** Wind-driven overturning stream function ψ_w and **b.** eddy-induced overturning stream function ψ_e for experiment highW_highN (Table 3.1). The along-shore averaged isopycnals are shown in black contours, and the cross section is from day 45. The colorbars are scaled so that zero is white, positive values are orange, and negative values are purple. **c.** Stream functions averaged over the region of sloping isopycnals (from the coast to y=130 km) in the cross-shore direction. The Fox-Kemper et al. (2008) parameterization for mixed-layer instabilities ψ_{MLI} (using Eq. (3.2), where $b_y = Nf/4$) is also shown in the dashed gray line.

One point to highlight is that a deeper source depth does not necessarily imply a larger density offset, which is what we might intuitively expect. This is because the conversion from D_s to $\Delta\rho$ depends on N^2, so the stratification plays an important role in determining $\Delta\rho$. An example of this can be seen in Figs. 3-6c and 3-6i. The former simulation has a much deeper D_s of over 250 m and a $\Delta\rho$ of about 0.15 kgm^{-3} (Fig. 3-6c), while the latter case has a shallower D_s of about 140 m and a much larger $\Delta\rho$ of approximately 0.8 kgm^{-3} (Fig. 3-6i).

To more quantitatively assess the agreement between the "true" tracer-estimated source depth and Eq. (3.5), we compare the range of D_s calculated from the model against the theoretical predictions. Figure 3-7 is a scatter plot showing the median source depth from tracers with error bars denoting the 10th and 90th percentiles. The 1:1 linear regression line representing perfect agreement between Eq. (3.5) and the tracer-calculated D_s is shown and it has a correlation coefficient of $r^2 = 0.93$. The r^2 value is calculated for the nine experiments that are initialized with a constant N^2 (Table 3.1), which are the black points in Fig. 3-7. Not only is there good correlation between the modeled and predicted D_s–which gives us confidence in the 1/2 power

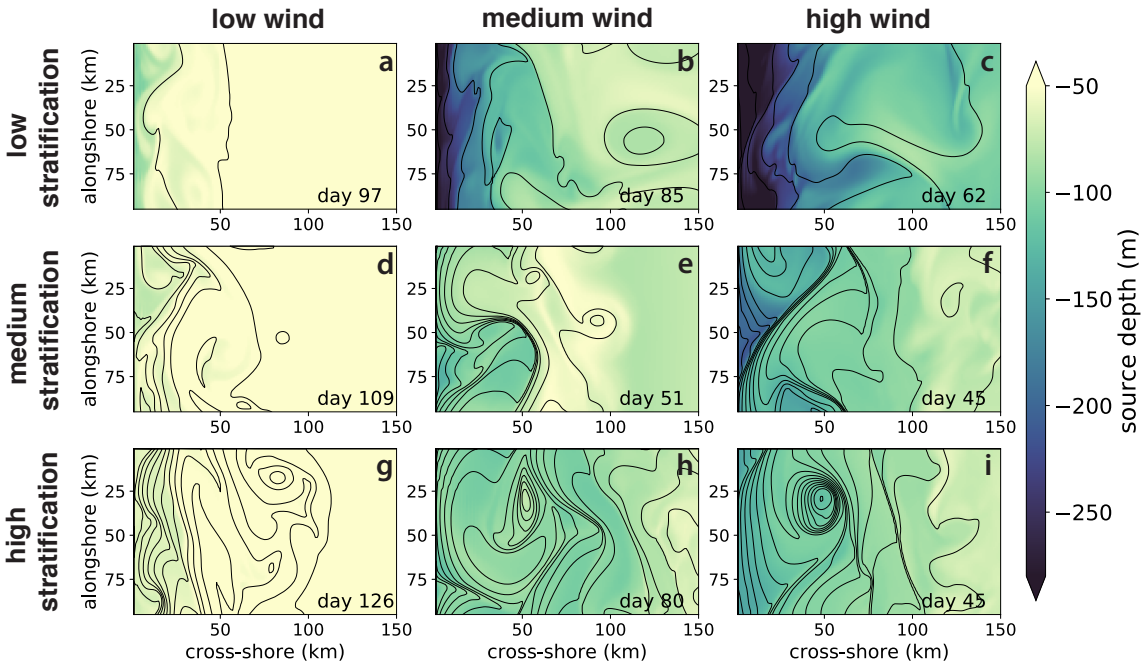

Figure 3-6: Surface isopycnals (black contours) and source depth (color) in each grid point for a snapshot in time in each of the nine main simulations with constant stratification (Tab. 3.1). The source depth is calculated from tracers and averaged in the top 3 grid cells representing the upper 11.7 m of the ocean, and the day from which the snapshot is taken is midpoint of the 20-day analysis period for each simulation. The isopycnal interval is 0.05 kgm^{-3}.

law relation–but Eq. (3.5) also captures the right magnitude of the source depth. The mean and standard deviation of the absolute error is 11.88 ± 8.84 m. The source depth in our simulations range from 50–280 m, so an average error of about ten meters makes Eq. (3.5) sufficient for order-of-magnitude estimates.

There are two outliers on the lower left of Fig. 3-7 with $D_s \sim 60$ m that are higher than predicted and do not fall on the 1:1 line very well. These points correspond to the lowW_medN and lowW_highN simulations (Table 3.1), which have predicted source depths of 48 m and 42 m, respectively, according to Eq. (3.5). The predicted source depths for these two experiments turn out to be very close to the Ekman depth δ_E from Eq. (3.7), whose value is $\delta_E = 33$ m with a transition depth of $\Delta = 16.5$ m. Thus, these two experiments may be examples in which the turbulent surface mixed layer given by Eq. 3.7 is actually too deep, and as a result, the source depth in the model is deepened due to mixing.

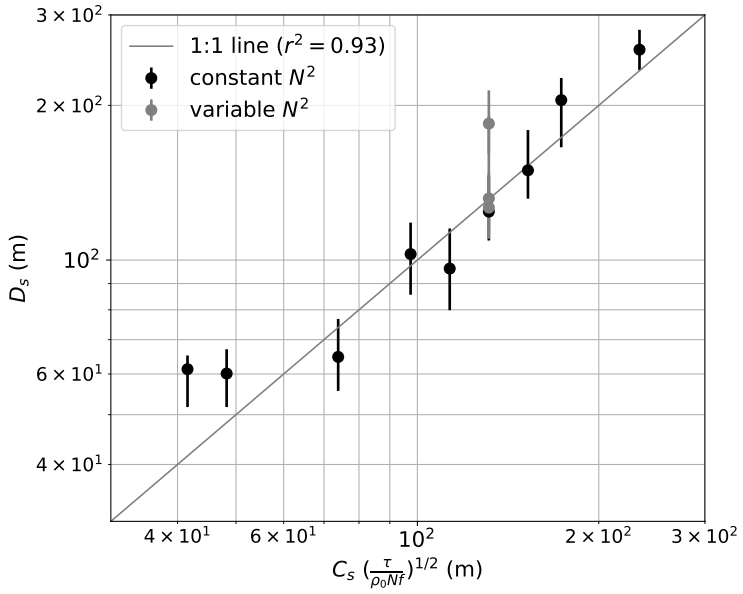

Figure 3-7: "True" source depth calculated from tracers in the numerical model (D_s) compared to the scaling relation in Eq. (3.5) $C_s(\frac{\tau}{\rho_0 Nf})^{1/2}$. The median value is shown with error bars denoting the 10th and 90th percentiles, and the gray line shows the 1:1 line. ρ_0 is taken to be constant reference density of 1027 kg/m^3.

For completeness we can conduct the same comparisons between the true density offset in the model and predictions of Eq. (3.6), which is shown in Fig. 3-8. Similar to Fig. 3-7, the points closely follow the 1:1 line and the correlation coefficient is very high with $r^2 = 0.95$. Again, the r^2 value is calculated only for the black points which are the experiments with a constant initial N^2. We should not expect r^2 to be the same for source depth and density offset because these two quantities are not simply related by a scalar; instead, we scale D_s by a variable N^2 to obtain $\Delta\rho$ (because $\Delta\rho = -\frac{\rho_0}{g} N^2 D_s$). The higher r^2 is an artifact of this transformation, and should not be interpreted as the density offset scaling relation being superior to the source depth scaling. The mean average error and standard deviation for $\Delta\rho$ is 0.055 ± 0.057 kgm^{-3}, while $\Delta\rho$ ranges from 0.07 to 2 kgm^{-3}. So again, Eq. (3.6) seems appropriate for order-of-magnitude scaling purposes.

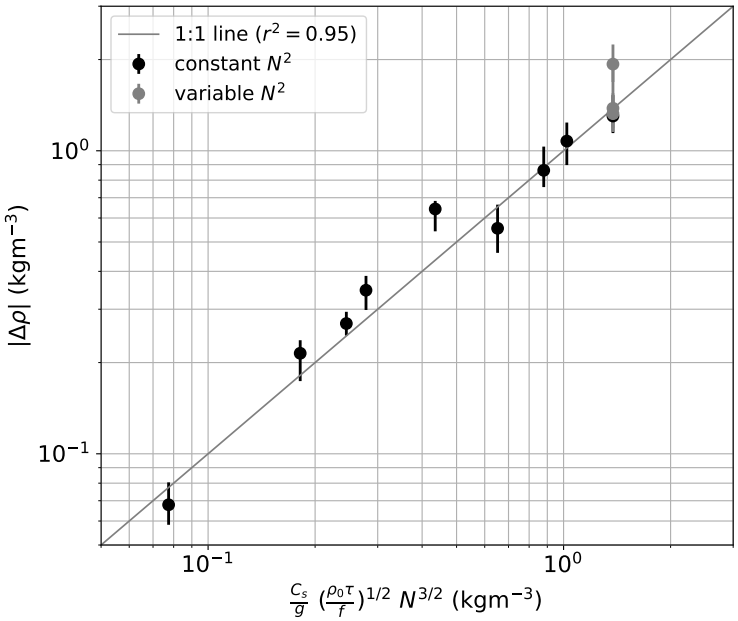

Figure 3-8: Density offset expressed as the difference in density between the surface and the upwelled water $\Delta\rho$ calculated from the numerical model compared to the scaling relation in Eq. (3.6) $\frac{C_s}{g}(\frac{\rho_0\tau}{f})^{1/2}\ N^{3/2}$. The median value is shown with error bars denoting the 10th and 90th percentiles, and the gray line shows the 1:1 line. ρ_0 is taken to be constant reference density of 1027 kg/m^3.

3.4.3 More realistic N^2 profiles

So far, we have presented results from simulations initialized with a uniform vertical density gradient. Typically in the ocean, N^2 is small and uniform in the surface mixed layer, reaches a peak at the base of the mixed layer, and then decays below that to become small in the interior. This raises the question of whether the scaling relations hold for more realistic N^2 profile shapes. How much does the shape of the initial N^2 profile matter? In the case of non-uniform stratification, what value of N^2 should one use in Eq. (3.5)? To investigate this, we run three additional simulations whose initial N^2 profiles are more realistic (Fig. 3-9). We experiment with varying the peak N^2 value and the mixed layer depth, but we maintain the same the average stratification in the upper 250 m at 10^{-4} s^{-2} (Fig. 3-9). This way, the depth-integrated N^2 in the upper 250 m–which is just the density difference between the surface and 250 m–is the same. This allows us to compare the effects of only varying the shape of the density profiles, while holding the total stratification constant. In addition,

the depth-averaged stratification over the full 500 m depth is about 5.5×10^{-5} s^{-2} for the three simulations, which is the same as the medium stratification experiments (Table 3.1). A constant wind forcing of $\tau = 0.1$ Nm^{-2} is used for all three simulations, so these results are meant to be compared to the highW_highN and highW_medN experiments (Table 3.1).

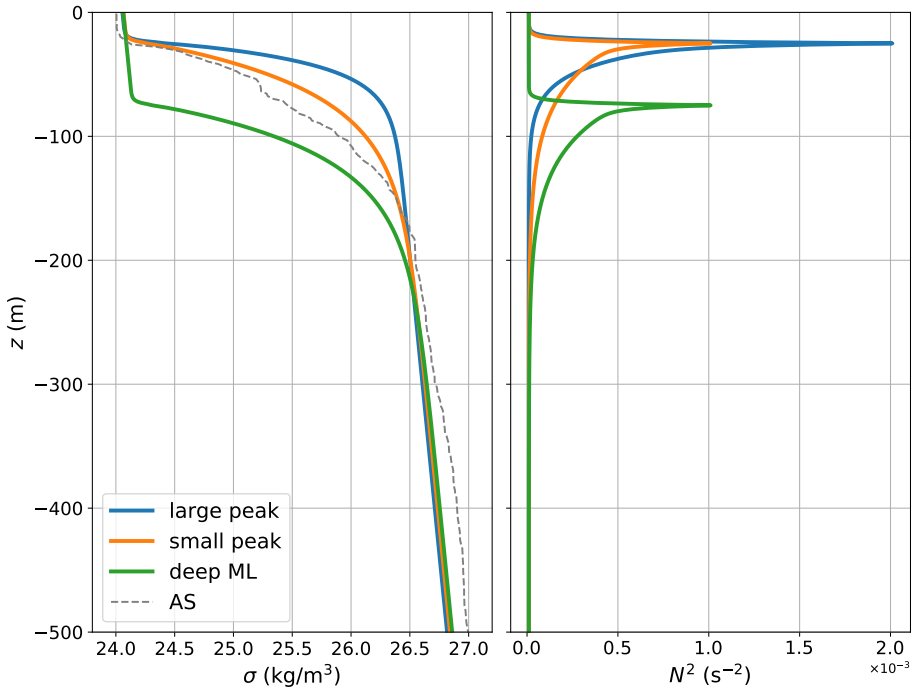

Figure 3-9: Initial potential density profiles minus 1000 kgm^{-3} (σ, left) and corresponding N^2 profiles (right) for the three experiments that have a non-constant initial stratification (see Table 3.1). An Argo density profile from the Arabian Sea in July 2017 is also plotted in the gray dashed line to serve as an example of a realistic density profile.

The source depth and density contours for a snapshot in each of the three simulations are shown in Fig. 3-10. There is not a drastic difference in source depth between the small peak and deep ML experiments in Fig. 3-10 and Fig. 3-6f and i, which has the same wind stress and average stratification. However, the large peak simulation has a noticeably deeper source depth. Testing the tracer-calculated source depths against Eq. (3.5) with $N^2 = 10^{-4}$ s^{-2} and $N^2 = 5.5 \times 10^{-5}$ s^{-2} shows that a better agreement is achieved for the small peak and deep ML experiments when the higher stratification value is used. This hints that it is the total stratification in the

upper ocean above the source depth that should be used in the scaling relation, and not the full water-column integrated stratification. After all, it is the upper ocean stratification that is relevant for the generation of available potential energy through upwelling and subsequent baroclinic instabilities.

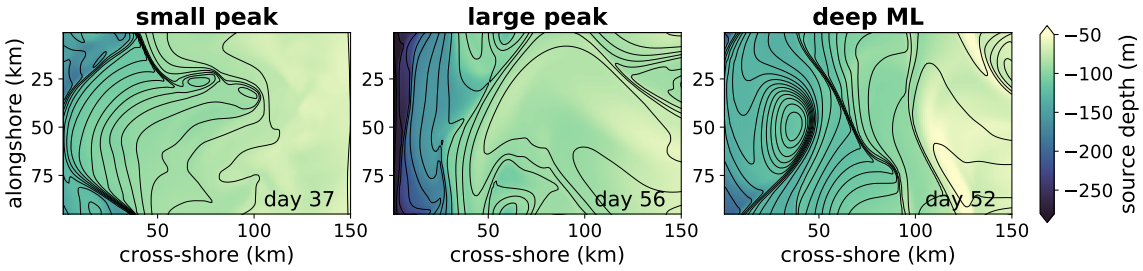

Figure 3-10: Same as Fig. 3-6 except the three simulations shown have non-uniform initial stratification profiles and the same wind stress of 0.1 Nm^{-2} (see Tab. 3.1).

The gray dots in Fig. 3-7 show the range of source depths from these three experiments and the scaling-predicted value using the average initial stratification in the upper 250 m. The small peak and deep ML source depths are clustered very closely around the point corresponding to the highW_highN experiment. The median source depths of the small peak, deep ML, and highW_highN simulations are 126.51 m, 131.82 m, and 124.25 m respectively, which are all within the range of the error bars. The large peak simulation has a deeper D_s of 184.36 m, although its error bars slightly overlaps with the other simulations (Fig. 3-7). Similarly, the density offsets of the small peak and deep ML experiments are close to that of the highW_highN simulation (Fig. 3-8 gray dots), while the large peak experiment has a higher density offset value.

To understand why the large peak experiment has a deeper source depth, we can look at the nearshore density structure of these three simulations during the analysis period (Fig. 3-11). Despite being initialized with the same depth-integrated stratification, the nearshore stratification after the spin-up phase is actually weakest in the large peak experiment. This is because the strong initial stratification in the large peak experiment is quickly erased by the wind-driven mixing in the model, and the large peak case has the weakest initial stratification below the mixed layer (Fig. 3-

9). Thus, the stratification that was actually present to energize the baroclinic eddies is weaker than in simulations with higher stratification below the wind-driven mixed layer. In this contrived experiment where depth-integrated N^2 was held constant, altering the mixed layer depth did not affect the source depth, but changing the N^2 peak did significantly affect D_s. The effects of the initial vertical density structure is an interesting question to investigate further in future studies.

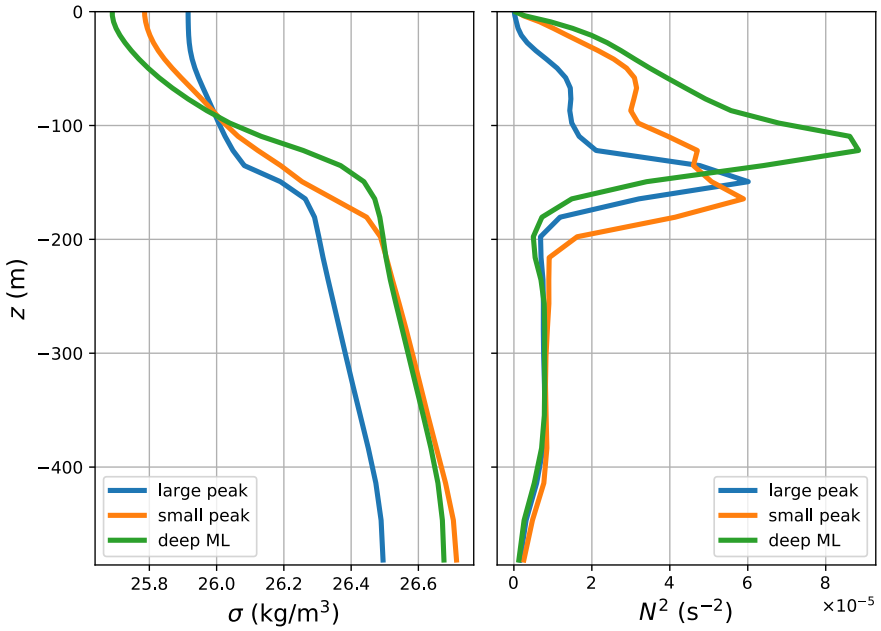

Figure 3-11: Nearshore density profiles minus 1000 kgm^{-3} (σ, left) and corresponding N^2 profiles (right) during period analyzed for source depth from the three experiments that have a non-constant initial stratification (see Table 3.1). Profiles for each simulation are taken on the days indicated in Fig. 3-10 at the location x=48 km and y=20 km.

3.5 Discussion

After proposing a general scaling relation for the source depth of upwelled water and verifying it with numerical experiments, we can revisit the original motivating case of the Arabian Sea and Bay of Bengal as an example of how Eq. (3.5) may be useful in understanding what drives the different upwelling responses. The climatological southwesterly wind stress for July in Fig. 3-1b-c is $\tau = 0.20$ Nm^{-2} in the AS and

$\tau = 0.07$ Nm^{-2} in the BoB. The depth-averaged climatological N^2 in the upper 250 m is 1.1×10^{-4} s^{-2} and 2.1×10^{-4} s^{-2} in the western AS and BoB, respectively. Taking f for the latitude 15°N and $\rho_0 = 1027$ kg m^{-3}, Eq. 3.5 yields $D_s = 181$ m in the AS and $D_s = 91$ m in the BoB. Converting source depth to the density offset yields $\Delta\rho =$ 2.1 kgm^{-3} in the AS and $\Delta\rho = 2.0$ kgm^{-3} for the BoB. Unsurprisingly, the source depth in the BoB is considerably shallower than the AS, which is consistent with the colder SST in the AS compared to BoB (Fig. 3-1). However, SST is not reflective of the similar density offset in both basins because the density in the BoB is primarily salinity driven due to large freshwater inputs from rivers and precipitation (**?**). But beyond that, Eq. (3.5) allows us to quantify the relative importance of the different wind forcing and stratification on the difference in D_s between the AS and BoB. For instance, using Eq. (3.5) we can estimate that if the AS wind stress were reduced to a third of its value, to be equal to the BoB wind stress, it would translate into a 41% reduction in source depth. If instead the AS stratification was doubled to match the BoB (but the AS maintained its original wind stress), it would result in a 15% reduction in source depth. The difference in wind stress plays a larger role in explaining the difference in upwelling D_s between the AS and BoB, but the stratification also plays a significant role.

Furthermore, a potential implication of a shallower source depth in the BoB is a positive feedback cycle involving the Southwest Monsoon. Shallow D_s means higher SST, which leads to more convection and precipitation over the Bay of Bengal (Izumo et al. 2008). The increased precipitation further enhances stratification (or at least counteracts the decrease in N^2 due to upwelling) in the BoB by providing a layer of buoyant freshwater at the surface. Lastly, the persistent strong stratification contributes to a shallow upwelling source depth. McGowan et al. (2003) suggested a similar positive feedback in the California Current System where ocean warming leads to increased stratification and suppressed upwelling or shallower source depth, which further maintains high stratification. This is currently speculative, but it is interesting to note that in Fig. 3-1c, N^2 decreases by 0.3×10^{-4} s^{-2} from May to August in the AS as a result of strong coastal upwelling, but in the BoB N^2 only decreases by

0.1×10^{-4} s^{-2} in the same time period. The maintenance of the strong stratification in the BoB might be an example of this stratification-source depth feedback at play.

While this work is originally motivated by observations of the Arabian Sea and Bay of Bengal, the theory developed here is general and can be applied to study other coastal upwelling regions such as the EBUS, and assess how they might change with global warming. There is abundant literature on how alongshore winds and upwelling intensity will change under future warming scenarios (e.g. Bakun 1990; Sydeman et al. 2014; Rykaczewski et al. 2015; Wang et al. 2015; deCastro et al. 2016), and there is a seasonal and latitudinal dependence on upwelling trends, with more intensification of summertime upwelling-favorable winds at higher latitudes (Rykaczewski et al. 2015). We might expect regions of increased upwelling intensity to experience greater primary production, but the effect is partially countered and mitigated by strong increases in stratification as a result of a warming oceans (deCastro et al. 2016; Lorenzo et al. 2005; Auad et al. 2006). For instance, Jacox et al. (2015a) found a strong positive correlation between upwelling winds and nitrate concentration (indicative of source depth) and a weaker negative correlation between increased heat flux and nitrate concentration, which is qualitatively consistent with our findings on how wind and stratification impacts source depth. Our work here provides an alternative theoretical method to quantitatively compare the relative effects of changing winds and changing stratification on upwelling source depth.

Additionally, this study has implications for the biological productivity of coastal upwelling regions. Observational and modeling studies have shown that intensifying upwelling-favorable winds do not necessarily correlate with increased primary productivity (e.g. Roemmich and McGowan 1995; Renault et al. 2016), which highlights the necessity of considering other factors that affect nutrient supply and productivity. For example, in the well-studied California Current System, long term warming and increased stratification trends have been observed and linked to a shallower source depth (McGowan et al. 2003; Bograd and Lynn 2003), diminished vertical fluxes of nutrients to the upper ocean (Lorenzo et al. 2005; Palacios et al. 2004), and significant ecosystem changes (McGowan et al. 2003). Our theory is consistent with these

findings, and our contribution is to quantify and demonstrate a mechanism by which stratification alters the source depth. In particular, since nitrate is known to be correlated with temperature or density (e.g. Omand and Mahadevan 2013; Palacios et al. 2013), the density offset given by Eq. (3.6) could be a useful metric for studying nutrient upwelling, provided that a density-nitrate relationship is known. However to fully assess biological impacts, it is important to also consider other factors. For example, reduced upwelling may be compensated by enhanced nutrients at depth (Rykaczewski and Dunne 2010; Xiu et al. 2018), nutrients and phytoplankton can be advected offshore and subducted (Gruber et al. 2011), and plankton biomass may not necessarily respond to nutrient changes if there are other controls such as ecosystem food web dynamics (Xiu et al. 2018).

One note is that when ψ_w and ψ_e fully balance, there is no more uplift of isopycnals. This does not necessarily mean that there is zero upwelling nutrient flux since there can still be upwelling of nutrients along sloping isopycnals (Freilich and Mahadevan 2019). Freilich and Mahadevan (2019) developed the following scaling for the ratio of along-isopycnal vertical velocity w_{iso} to total vertical velocity: $\frac{w_{iso}}{w} \sim \frac{M^2 L}{N^2 H}$, where H/L is the aspect ratio and M^2/N^2 is the isopycnal slope. We apply this scaling to our experiments using the following parameters: $H \sim 100$ m is the source depth, $L \sim 10^5$ m, $N^2 \sim 10^{-4}$ s^{-2}, and $M^2 = b_y = \frac{g}{L}\frac{\Delta\rho}{\rho_0} \sim 10^{-7}$ s^{-2} (with $\Delta\rho = 1$ kg m^{-3}). This yields $w_{iso}/w = 1$, in other words, all the upwelling is indeed occurring along isocpycnals and there is no more upwelling due to isopycnal uplift as expected. In this case, the source density will still be a useful consideration.

It is important to remember that our scaling relations, Eqs. (3.5) and (3.6), are tested using idealized numerical experiments which neglect several factors. To begin, we force the model with a constant wind that blows for months, as a result of which the surface along-shore current in the model is stronger than in observations. In reality, the wind is intermittent and varies on a time scale of days with strong bursts and weak periods. Our scaling does not account for variable τ in time or space, but is meant to represent the effects of the average alongshore wind stress over the course of an upwelling season. However, in the case of highly intermittent winds, it may

not be appropriate to use the time-averaged wind stress in the scaling relationship, because there is a time for spin up and equilibration. If the wind changes before the system equilibrates, the wind event's impact on upwelling source depth may not be fully realized. Additional work is needed to explore the effect of highly intermittent winds.

Furthermore, this work does not describe the increase in source depth over the course of days, such as when upwelling-favorable winds commence at the beginning of the upwelling season. Equations. (3.5) and (3.6) instead are meant to estimate D_s and $\Delta\rho$ over multiple weeks during the upwelling season, where we can assume an approximate balance of the mean ψ_w and ψ_e in that time span. Additionally, this work is focused on the near-shore region where Ekman transport dominates, and we do not consider the effects of wind-stress curl driven upwelling, though Jacox and Edwards (2012) found that the shape of the cross-shore wind profile did have an effect on the upwelling source depth. Capet et al. (2004) also showed that different cross-shore wind profiles impacted the patterns of upwelling circulation, surface temperature, and biogeochemistry off the Californian coast. Another limitation is that we do not have any geostrophic onshore transport or poleward undercurrent because there is no alongshore pressure gradient in our model, all of which would impact the upwelling circulation (Marchesiello and Estrade 2010). Furthermore, we present a source depth scaling based on local forcing, but remote forcing also plays an important role in setting surface variations in upwelling regions (Frischknecht et al. 2015). Thus we expect that source depth can also be affected by large scale climate variability modes such as the El Niño-Southern Oscillation (Jacox et al. 2015b), Pacific Decadal Oscillation (Chhak and Lorenzo 2007) and the North Pacific Gyre Oscillation (Di Lorenzo et al. 2008).

Lastly, the sloping topography, which is not addressed here, would result in some onshore transport along the bottom boundary layer (Lentz and Chapman 2004; Jacox and Edwards 2011, 2012) and also alter the eddy dynamics (Brink 2016). In addition, topographic variations such as canyons, capes, islands, banks, and headlands would also strongly affect the regional dynamics (Pitcher et al. 2010). The inclusion of

topography would require re-working the scaling relation to include bottom stress as another mechanism for balancing the wind, and this is beyond the scope of this study but is an important avenue for future research.

3.6 Conclusion

We investigate the role of stratification and alongshore wind stress on the source depth in a coastal upwelling region. To our knowledge, there has been no study to date on the source depth in coastal upwelling regions that considers the role of submesoscale eddies. We present a scaling relation for the source depth at dynamic equilibrium that depends on a balance between the wind-driven Ekman circulation and the eddy restratifying overturning circulation which shows that the source depth $D_s = C_s(\frac{\tau}{\rho_0 N f})^{1/2}$. This can be converted to a density offset scaling by considering the change in density from the surface to the source depth: $\Delta\rho = \frac{C_s}{g}(\frac{\rho_0 \tau}{f})^{1/2} N^{3/2}$. The result of increasing source depth with weaker stratification is qualitatively consistent with previous studies (Jacox and Edwards 2011, 2012; Oerder et al. 2015), but now we are able to quantify the effects of wind stress and stratification on the source depth. A main takeaway from our study is that both the source depth and the density offset depends nonlinearly on the stratification N and wind stress, and they contribute equally to the source depth. Thus, as stratification increases more drastically in a warming planet, the stratification will play a more important role in decreasing the source depth. That may have implications for increasing SST, which has a positive feedback, and in changing nutrient supply for primary production, which are areas of future study.

Acknowledgments We thank Kenneth H. Brink for discussions and for providing feedback on an early version of this manuscript, and two anonymous reviewers for their thoughtful questions and suggestions. This work was funded by the ONR grant N000014-17-1-2390, and JH was supported by the NASA FINESST grant 80NSSC19K1350).

Datasets for Fig. 3-1 are described in Dee et al. (2011) and Schmidtko et al. (2013), and they are accessible here https://www.ecmwf.int/en/forecasts/datasets/reanalysis-datasets/era-interim, https://www.pmel.noaa.gov/mimoc/. Source code to reproduce the model runs can be found at https://doi.org/10.5281/zenodo.4757609. Colormaps are from Thyng et al. (2016).

3.A Appendix

Supporting Information for "How the source depth of coastal upwelling relates to stratification and wind"

3.A.1 EKE

Here we provide additional information to illustrate how we choose the analysis period for the different simulations. The depth-averaged eddy kinetic energy EKE and source depth D_s is plotted with time for all the model runs analyzed, and the 20-day analysis period chosen for each simulation is shown (Figs. 3-12, 3-13). Details on how EKE and D_s is calculated and how the analysis period is identified can be found in Sec. 3.2 of the main text. The analysis period is the 20-day period over which the change in EKE is minimized.

3.A.2 Frontal width

Fig. 3-14 compares the frontal width calculated from the Rossby radius as $4ND_s/f$ and the surface width L of the coastal upwelling front diagnosed independently from the model simulations. To obtain L from the model output, we take the alongshore average of the surface density field during the identified 20-day period of minimal EKE change. This leaves us with a mean cross-shore surface density profile. The width L is identified as the offshore distance where the density gradient becomes nearly zero. More specifically, we identify where the density changes by less than a threshold of 0.001 kg/m^3/km for at least the next 20 consecutive km. This method for estimating L is adapted from similar, but more complex, gradient-threshold methods for identifying fronts and front widths (Oerder et al. 2018). We choose this criteria to yield front widths that qualitatively agree with what we would identify by eye from looking at the surface fields. The values of L range from 56 to 134 km, which are consistent with the range of values obtained from $L = 4ND_s/f$.

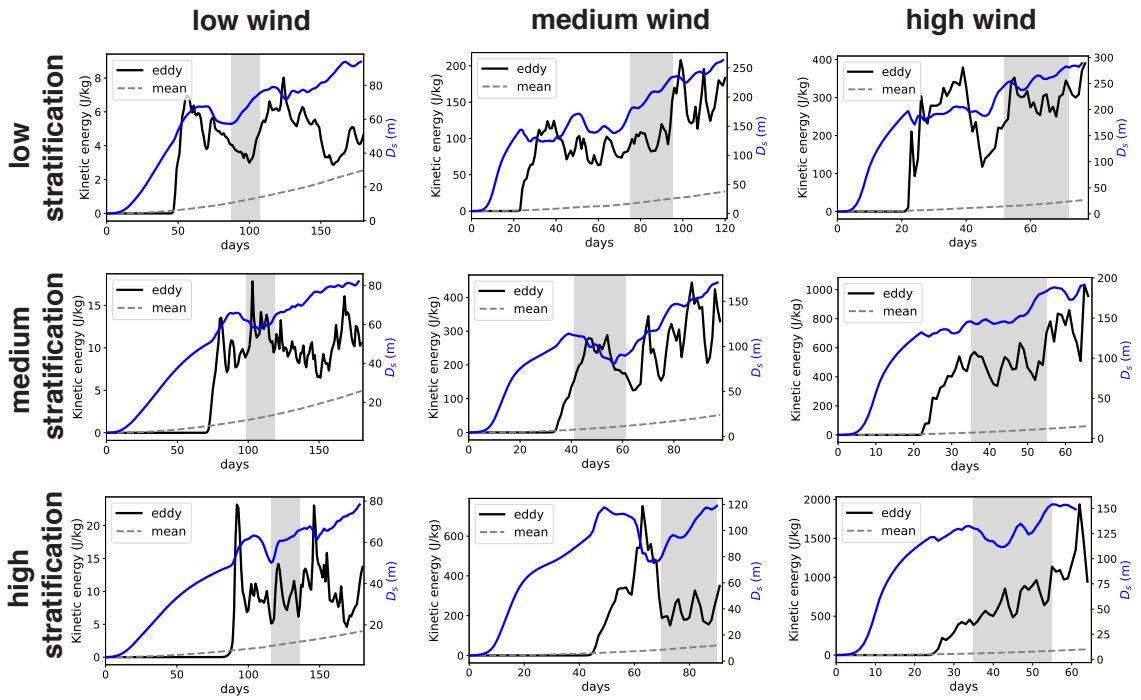

Figure 3-12: Eddy kinetic energy (EKE, black line), alongshore-mean kinetic energy (dashed gray), and source depth (D_s, blue line) with time in each of the nine simulations with constant N^2. The kinetic energy is calculated as a sum over all grid cells within a distance 150 km from the coast. The 20 day period with the minimum change in EKE that was used for calculating the source depth is highlighted in gray. Note the horizontal and vertical axes of each simulation are different.

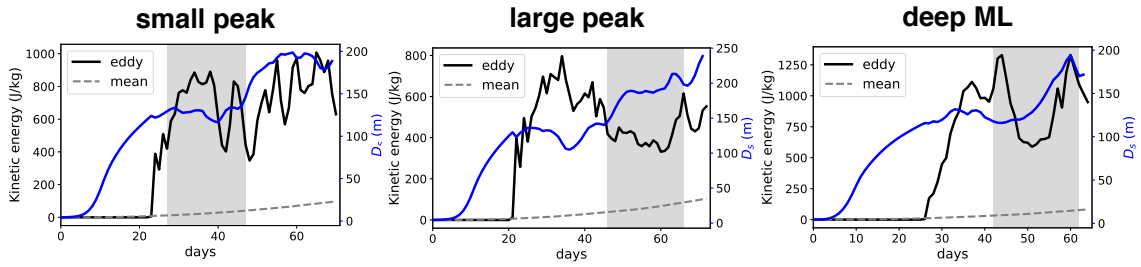

Figure 3-13: Same as Fig. 3-12, but for the three simulations initialized with non-constant N^2 profiles.

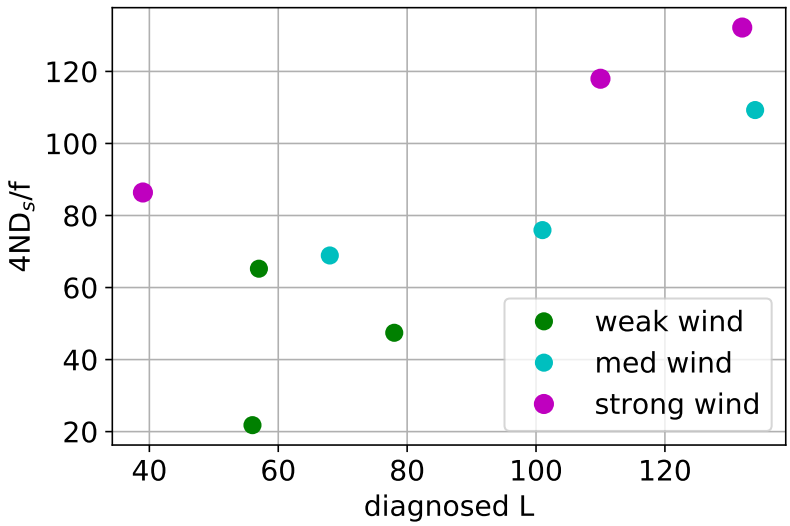

Figure 3-14: Comparison of the diagnosed surface width of the coastal upwelling front with the Rossby radius given by $4ND_s/f$ for the nine main simulations with constant initial N^2. Points are colored by the wind forcing.

Chapter 4

Vertical velocity diagnosed from surface data with machine learning

Abstract

Submesoscale vertical velocities w are important for the oceanic transport of heat and biogeochemical properties, but observing w in-situ is challenging. New remote sensing technologies of horizontal surface velocity $\vec{u_h}$ at $O(1)$ km resolution can resolve surface submesoscale dynamics and offer promise for diagnosing w subsurface. Using machine learning (ML) models, we examine relationships between the three-dimensional w field and remotely observable surface variables such as $\vec{u_h}$, density, and their horizontal gradients. We evaluate the ML models' sensitivities to different inputs, spatial resolution of surface fields, the addition of noise, and information about the subsurface density. We find that surface data is sufficient for reconstructing the 3D w field, and having high resolution $\vec{u_h}$ with minimal errors is crucial for accurate w predictions. This highlights the importance of finer scale $\vec{u_h}$ measurements and suggest that data-driven methods may be effective tools for linking surface observations with vertical velocity and transport subsurface.

Plain Language Summary

Vertical velocities w are associated with ocean currents that move towards or away from the ocean surface and are important for connecting the surface and deep ocean. It is extremely difficult to measure w directly, but there exists many measurements of other variables that are related to w, such as horizontal currents that move along the surface in the north-south or east-west directions. Thus, we investigate how feasible it is to infer w from other more easily measurable data. We compare 3 machine learning (ML) methods to see which is best at finding relationships between more easily measurable variables (the input data) and w at different depths. Furthermore, we test how using different input variables, adding noise to the input data, or changing the spatial resolution of the input data, impact the w predictions. Our results show that ML models are successful at reconstructing the 3D w field using high-resolution ($\sim$1 km) surface data, and in particular, surface horizontal velocities are the most important to include. This study shows that ML methods are promising for relating remotely-sensed surface measurements of the ocean to vertical velocities below the surface, which can help provide us with a better understanding of the 3D ocean.

4.1 Introduction

Resolving oceanic vertical velocities w at the submesoscale, defined here as $\mathcal{O}$(1-10) km spatial scales and $\mathcal{O}(1)$ Rossby number, is important for the vertical transport of heat, carbon, and nutrients between the surface and deep ocean (e.g. Su et al. 2018; Ruiz et al. 2019; Uchida et al. 2019). Directly measuring w is difficult as w is several orders of magnitude smaller than the horizontal velocity $\vec{u_h}$, and w is noisy since it includes the wave field and turbulent fluctuations. However, recent studies suggest it may be possible to infer w at the submesoscale from surface signatures since strong up- and down-welling are known to be associated with surface fronts, convergence, and cyclonic vorticity (D'Asaro et al. 2018; Ruiz et al. 2019; Tarry et al. 2021; Freilich and Mahadevan 2021). We also expect that surface $\vec{u_h}$ data will continue to improve in resolution and accuracy, leading to better estimates of divergence and vorticity at smaller scales. For instance, starting in 2023, the Surface Water and Ocean Topography (SWOT) mission plans to provide global surface horizontal geostrophic velocities down to $\sim$15 km, the highest resolution to date (Fu and Ubelmann 2014; Wang et al. 2018). And the NASA EVS-3 Submesoscale Ocean Dynamics Experiment (S-MODE) is utilizing Doppler Scatterometry on aircraft to measure surface $\vec{u_h}$ at $<$1 km resolution (Farrar et al. 2020). The latter methodology is also the basis for a proposed future mission that would remotely sense waves and current velocities that are not just geostrophic, at even higher resolution than SWOT (Rodríguez et al. 2019).

To leverage these advances in finer-scale surface observations, we explore the feasibility of using data-driven methods to link surface fields with subsurface w. Existing techniques, such as surface quasigeostrophic (SQG) methods, diagnose the 3D mesoscale horizontal and vertical velocities from sea surface data using sea surface temperature (density) and/or sea surface height (e.g. LaCasce and Mahadevan 2006; Lapeyre and Klein 2006; Isern-Fontanet et al. 2006, 2008; Wang et al. 2013; Qiu et al. 2020). However, these methods assume a quasi-geostrophic framework with Rossby number $\ll 1$, an assumption that does not hold at the submesoscale. More-

over, SQG methods mainly capture the balanced part of w and perform poorly in the surface mixed layer where unbalanced submesoscale dynamics dominate (Qiu et al. 2020; Uchida et al. 2019). This highlights a need to explore alternative methods for diagnosing the unbalanced, submesoscale w.

One simple approach, based on the incompressibility of seawater, is to depth-integrate the surface divergence of $\vec{u_h}$. But this approach leads to errors that increase with depth because the divergence of $\vec{u_h}$ is not constant with depth, especially below the mixed layer. Hence the relationship between w and the surface divergence of $\vec{u_h}$ is more complex, nonlinear, and dependent on other variables.

Here, we utilize machine learning methods which are good at finding complex nonlinear relationships from large data sets. They have been used in oceanography to estimate horizontal currents at the surface (Sinha and Abernathey 2021) and at depth (Chapman and Charantonis 2017; Bolton and Zanna 2019), among many other applications (Sonnewald et al. 2021). Our goal is to test how well ML methods perform for estimating the 3D submesoscale w field, which to our knowledge, has not been done before. We train and compare the performance of three ML models: multiple linear regression (MLR), random forest (RF), and convolutional neural networks (CNN). In addition, we evaluate the sensitivity of w predictions to data noise, spatial resolution, and to different input data variables, to provide insight into the type and quality of measurements needed for accurate estimations of w.

4.2 Methods

4.2.1 Training data

Since we lack measurements of the vertical velocity, the ML models are trained using the output from an ensemble of numerical simulations generated with the Process Study Ocean Model (PSOM), which solves the nonhydrostatic Bousinesq equations (Mahadevan et al. 1996a,b). The model simulations, described in He and Mahadevan (2021), represent a coastal upwelling front in a 500 m deep re-entrant channel that

extends 96 km in the alongshore (x) direction and 384 km in the cross-shore (y) direction. The horizontal grid resolution is 1 km, and there are 32 stretched vertical levels ranging in thickness from 1 m at the surface to 36 m at the bottom. Nine simulations with different combinations of alongshore wind stress and initial stratification generate a wide range of dynamics that form a rich training set. More details about the model can be found in the Supplementary Information and in He and Mahadevan (2021). Each simulation starts from rest and is forced with an alongshore wind stress that sets up an upwelling front at the eastern boundary. The upwelling front undergoes baroclinic instability, to form meanders, eddies, and filaments that support a range of vertical velocities (Fig. 4-1). The statistics of the modeled flow is representative of submesoscale dynamics (Shcherbina et al. 2013); the vertical component of the near surface relative vorticity is positively skewed and the distribution of w is negatively skewed. Snapshots from three of the simulations performed with the same stratification but different strengths of the wind stress show the range and distribution of w, as well as the vertical distribution of w (Figure 4-1). We focus on the upper 200 m, which is deeper than the mixed layer depth, as w at the base of the mixed layer is of interest for vertical transport. We limit our analysis to a region extending 150 km from the coast ($y < 150$ km) which includes the upwelling front and avoids the influence of the offshore boundary.

From each simulation in our ensemble, we select 5 snapshots—each separated by 5 days—of the model output to use for training and testing. We reserve 1 snapshot (20% of the data) for the test set, and the remaining time slices (80% of the data) are used for training. All the errors and results presented here are from the test set. Different combinations of input variables are used to train the ML models, which is detailed in Table 4.1. The inputs to the ML models include the surface density ρ, and the horizontal surface velocities $\vec{u_h} = (u, v)$ in the x and y direction, respectively. We also calculate the surface divergence $\delta = u_x + v_y$, vorticity $\zeta = v_x - u_y$, and cross-shore density gradient ρ_y to use as inputs, because w is known to be related to those quantities (D'Asaro et al. 2018; Ruiz et al. 2019; Tarry et al. 2021). The dominant density gradient is in the cross-shore direction. In addition, we include the mixed

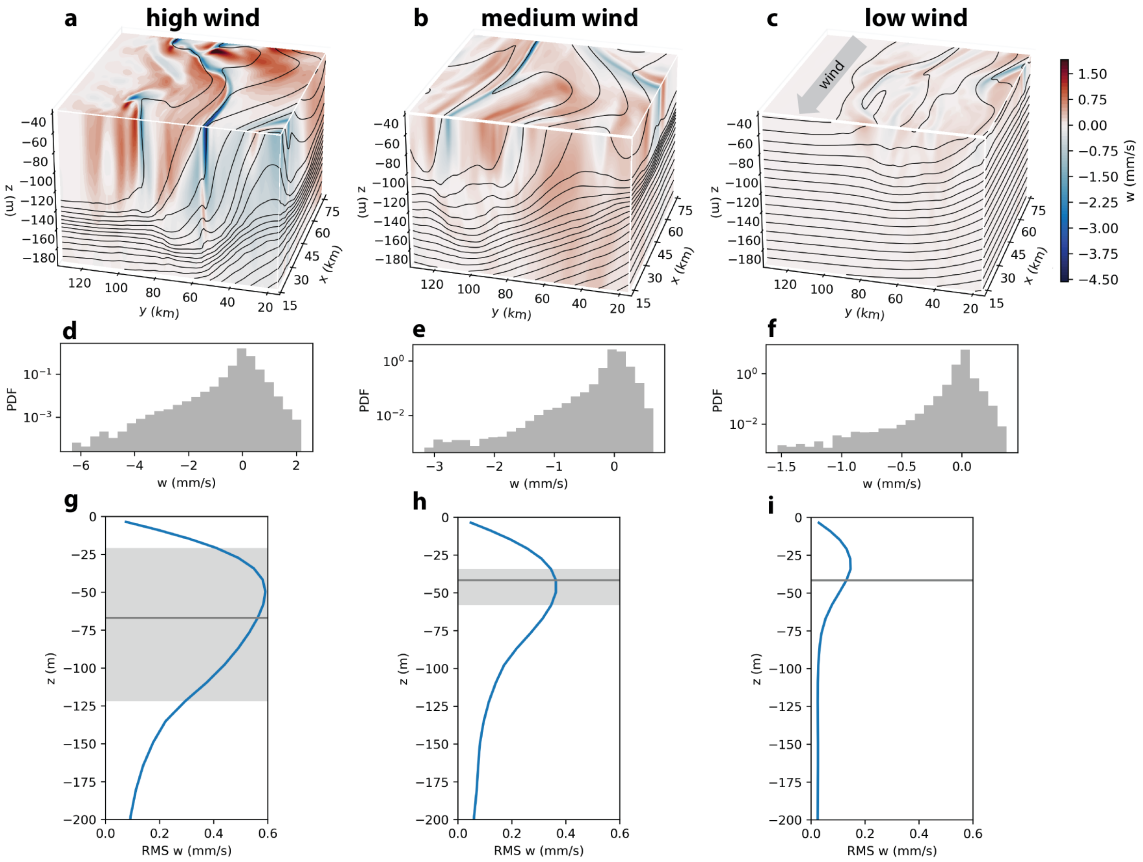

Figure 4-1: Top row: Snapshots of vertical velocity w from 3 simulations with high, medium, and low wind forcing and an initial stratification of $N^2 = 10^{-4}$ ms^{-2}. The colorbar is skewed as downward velocities are stronger. Only a portion of the numerical model domain that we focus on is shown, and black contours denote isopycnals with an interval of 0.1 kg m^{-3}. The direction of the wind stress is out of the page and shown in (c). Middle row: Normalized histograms of w in the upper 200 m from the snapshots shown in the top row. The vertical scale is a log axis and the horizontal scale differs. Bottom row: Root-mean-square (RMS) profiles of w (blue line) from the same snapshots in the top row. The horizontal lines denote the median mixed layer depth, with the interquartile ranges shaded in gray.

layer depth MLD, and the peak stratification below the mixed layer N^2, to test the importance of including information about the water column structure. To evaluate sensitivity to noisy data, we add random noise at different levels (1%, 5%, 10%) to $\vec{u_h}$ and re-calculate δ and ζ from the noisy velocities. The density is kept noise-free, as we expect errors in remotely sensed surface temperature to be smaller than in surface velocity. We also generate lower-resolution data by coarsening u and v from 1 km to 5 km, 10 km, and 15 km through spatial averaging, and then use the coarse $\vec{u_h}$ fields to calculate δ and ζ (see Supplementary Information for more details). The output we are trying to predict is the 3D vertical velocity at the same instant in time. For simplicity, we focus on predicting the full w, but there are many processes that contribute to the vertical velocity field and w can be decomposed into contributions from waves, balanced geostrophic motions, or unbalanced and turbulent motions that could be studied individually on depending on the application (Uchida et al. 2019; Qiu et al. 2020).

4.2.2 Machine Learning models

We compare three types of ML models: Multiple Linear Regression (MLRs), Random Forest (RFs), and Convolutional Neural Networks (CNNs). We summarize some key differences between these models below. More information about specific model implementation and parameters can be found in the Supporting Information. The ML models and the inputs they are trained with are listed in Table 4.1.

For MLR and RF, we use the surface $u, v, \rho, \delta, \zeta, \rho_y$, along with MLD, and peak N^2 values at each grid point to predict w in three dimensions. We fit separate MLR and RF models, using a mean square error loss function for each depth level, with the same inputs. This allows the ML models to learn different relationships for every depth and enables us to assess the importance of each input variable as a function of depth. The main difference between MLR and RF is that MLR assumes w is a linear function of the inputs, while RF allows w to be a nonlinear function of the input data since RF recursively splits the data into subsets and predicts the average over a subset of the training data. One consideration when choosing these 2 models

is that we need to explicitly provide the exact variables that we think are going to be important for their predictions, such as the gradient quantities δ, ζ, and ρ_y.

Additionally, since we expect spatial patterns to be important, we use CNNs because they can efficiently consider a wider field of view. We use a relatively simple CNN for the sake of demonstration in this paper that consists of 3 convolutional layers followed by 2 fully connected layers, and the loss function is mean square error. The CNN takes in a series of images as inputs, which are the 2D fields of u, v, ρ, MLD, and peak N^2. We choose the size of the input image to be 32 km $\times$ 32 km, and intentionally do not include δ, ζ, or ρ_y since CNNs are designed to learn filters that identify important patterns such as fronts and gradients to make its prediction. Since CNNs are more computationally expensive to train, we do not train a separate CNN for every depth. Instead, the final predicted output is the depth profile $w(z)$ at the center of the input image.

4.3 Results

The first set of w predictions are from the "MLR all," "RF all," and "CNN all" models, which are trained with the original noise-free 1 km resolution data. Inputs include both surface variables, and MLD and peak N^2 information (Table 4.1). For all 3 methods, 3D snapshots of the predicted w (Figure 4-2) closely resemble the true model w for the case of high winds in Fig. 4-1a. Qualitatively, all three ML models capture the locations and coherence of the downwelling and upwelling regions, such as the intense downwelling filaments at $y = 60$ km and $y = 90$ km. All three models accurately predict enhanced velocities in the mixed layer, and weaker w below the mixed layer. Scatterplots of the predicted w against the true w in upper 200 m of the entire test set that includes the ensemble of 9 simulations (middle row of Fig. 4-2) offer a more objective comparison. Random Forest and MLR have comparable r^2 with the true w of 0.64 and 0.62, respectively, while CNN has the highest correlation of 0.76. The CNN also does the best job of reconstructing the asymmetry in w, while MLR and RF are more likely to under-predict the negative velocities (Fig. 4-2, d–f).

Table 4.1: Overview of the different ML models evaluated: Multiple Linear Regression (MLR), Random Forest (RF), and Convolutional Neural Network (CNN). For the MLR and RF, the inputs are values at a single grid point, while the CNN input features are images with dimensions 32×32. For the experiments with noisy data, only noise was applied to the u, v velocities, and then divergence and vorticity were calculated from the noisy velocity fields. Likewise in the experiments with coarsened data, only the velocities are coarsened. The correlation coefficient r^2 of each ML model's predicted w with the true w in the upper 200 m of the test set is shown as an indication of its performance.

ML model	Inputs	r^2 in upper 200 m
MLR all	$u, v, \delta, \zeta, \rho, \rho_y, MLD, N^2$	0.62
MLR surface only	$u, v, \delta, \zeta, \rho, \rho_y$	0.62
MLR 1% noise	noisy: u, v, δ, ζ; original: ρ, ρ_y, MLD, N^2	0.38
MLR 5% noise	noisy: u, v, δ, ζ; original: ρ, ρ_y, MLD, N^2	0.22
MLR 10% noise	noisy: u, v, δ, ζ; original: ρ, ρ_y, MLD, N^2	0.18
MLR coarse 5 km	5 km: u, v, δ, ζ; 1 km:ρ, ρ_y, MLD, N^2	0.34
MLR no grad	u, v, ρ, MLD, N^2	0.11
RF all	$u, v, \delta, \zeta, \rho, \rho_y, MLD, N^2$	0.64
RF surface only	$u, v, \delta, \zeta, \rho, \rho_y$	0.62
RF 1% noise	noisy: u, v, δ, ζ; original: ρ, ρ_y, MLD, N^2	0.34
RF 5% noise	noisy: u, v, δ, ζ; original: ρ, ρ_y, MLD, N^2	0.23
RF 10% noise	noisy: u, v, δ, ζ; original: ρ, ρ_y, MLD, N^2	0.07
RF coarse 5 km	5 km: u, v, δ, ζ; 1 km:ρ, ρ_y, MLD, N^2	0.31
RF no grad	u, v, ρ, MLD, N^2	-0.19
CNN all	u, v, ρ, MLD, N^2	0.76
CNN surface only	u, v, ρ	0.73
CNN 1% noise	noisy: u, v; original: ρ, MLD, N^2	0.76
CNN 5% noise	noisy: u, v; original: ρ, MLD, N^2	0.74
CNN 10% noise	noisy: u, v; original: ρ, MLD, N^2	0.68
CNN coarse 5 km	5 km: u, v; original: ρ, MLD, N^2	0.60
CNN coarse 10 km	10 km: u, v; original: ρ, MLD, N^2	0.40
CNN coarse 15 km	15 km: u, v; original: ρ, MLD, N^2	0.36

Overall, at this stage, all 3 ML models do a decent job of reconstructing w in the upper 200 m.

4.3.1 Surface data only

To assess whether using surface data exclusively is sufficient for inferring w, we compare the ML "all" models against the "surface only" models that do not include MLD or peak N^2 as inputs (Table 4.1). Surprisingly, we find that training with only surface data results in a negligible decline in performance for RF (r^2 drops from 0.64 to 0.62) and CNN (r^2 drops from 0.76 to 0.73), while the MLR performance does not change (Table 4.1). We also do not see a large difference in the depth-dependence of errors between the "surface only" and "all" models in Fig. 4-2h and i, which show the root-mean-square error (RMSE) normalized by RMS w, and r^2 profiles across the entire test set for the different ML models. We normalize the RMSE profile by the RMS w profile rather than compute the percent error at each individual grid point and then average, because the latter results in dividing by zero in some locations. Generally, RMSEs are relatively small above the mixed layer depth and there r^2 is high. Below the mixed layer depth, RMSEs become the same order of magnitude as RMS w and r^2 becomes close to zero (Fig. 4-2 h,i). The solid profiles in Fig. 4-2h and i can be grouped into two categories based on model type—the "CNN surface" and "CNN all" models (pink and black lines) are very close together, while RF and MLR (blue, cyan, and green lines) models have very similar depth-dependencies.

To explain why surface data is by itself sufficient, we can look at Fig. 4-2g, which shows the "feature importance" as a function of depth. Feature importance is a metric from RF that measures the usefulness of each input feature by the total decrease in mean square error that results when the RF partitions the data based on that input. This metric ranges from 0 to 1, where 1 means the variable is most important and 0 means the variable is not used at all. We see that above the mixed layer depth, whose interquartile range is shaded in gray, divergence is by far the most important input (Fig. 4-2g). Thus, removing unimportant variables like MLD and peak N^2 does not significantly impact model performance. Moreover, w can be well approximated as a

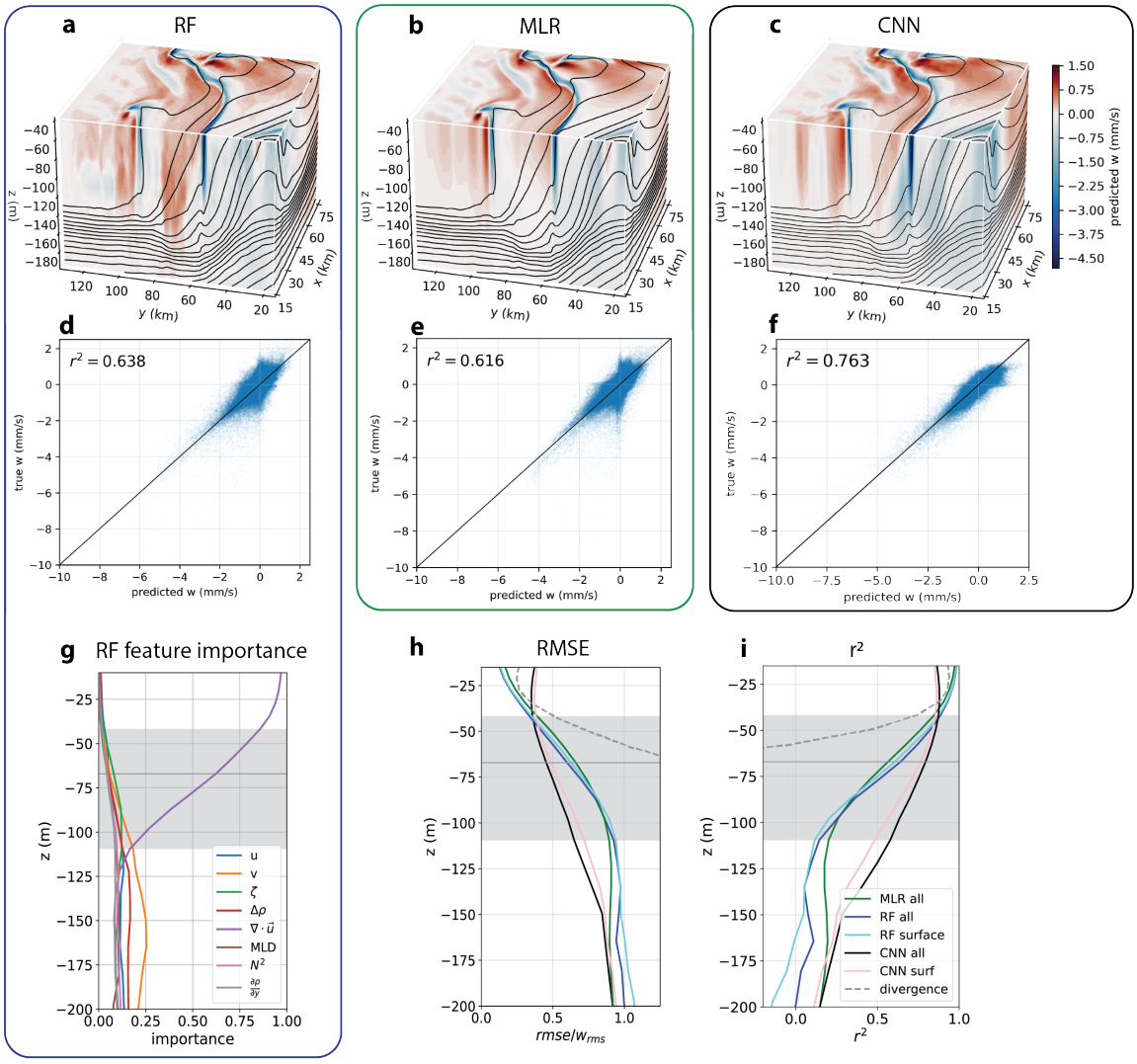

Figure 4-2: a) Snapshot of predicted w from the RF all model (see Table 4.1) to be compared with Fig. 4-1a, and scatterplot of predicted w with true w in the upper 200 m across the entire test set. The 1:1 line is shown. b and c) Same as a) but for MLR all and CNN all models (Table 4.1). d) Feature importance for the RF all model. e) Root-mean-square-error (RMSE) profiles across the entire test set, normalized by the RMS w at each depth. f) Correlation coefficient r^2 of the entire test set with depth. The median mixed layer depth is indicated by a horizontal gray line and interquartile range is shaded in gray.

linear function of surface divergence (and other variables), which explains why MLR performs so well and the non-linearity gained from the RF is not very beneficial. For comparison, we also show the results of depth-integrating the surface divergence in the dashed gray line, which performs well only in the surface layer above 40 m, but rapidly deteriorates below 50 m (Fig. 4-2e and f). Within 40 m of the surface, RF and MLR outperform CNN because divergence is a good predictor of w close to the surface (Fig. 4-2d–f). However at, or below, the mixed layer depth, CNN surpasses RF and MLR.

4.3.2 Noisy data

All results thus far make the unrealistic assumption of perfect data, so next we test the sensitivity of the ML models when trained with noisy velocity data. Adding just 1% random noise to $\vec{u_h}$ drastically decreases the performance of MLR (r^2 drops from 0.62 to 0.38) and RF (r^2 drops from 0.64 to 0.34). But the CNN is not impacted (r^2 remains 0.76) (Table 4.1). Even with a 10% noise level, the CNN still has a r^2 of 0.68. Visually, the RF w predictions are noticeably noisier and patchier than the CNN predictions (Fig. 4-3a–d), and the RF predicted vertical velocities are also weaker than the true w, while the CNN is closer to the correct magnitudes.

Figure 4-3e shows the normalized RMSE profiles for RF and CNN trained on data with varying levels of noise. The errors for the MLR and RF models are nearly the same, so only RF is shown for simplicity. Each color represents a noise level: the solid lines represent CNNs and dashed lines represent RFs. When we add 1% noise to the RF data, the normalized RMSE drastically increases from 0.09 to 0.69 near the surface at $z = 10$ m. Figure 4-3f shows the feature importance for the RF trained with 1% noisy data. Comparing Fig. 4-3f with Fig. 4-2g, we see that the importance of divergence drastically decreases when a small amount of noise is introduced in the velocities, and the RF prioritizes using the higher-quality surface density and cross-shore density gradient to compensate. But the loss of accurate divergence information ultimately renders the RF (and MLR) model useless. The dashed purple line in Fig. 4-3e shows the performance of a RF trained without any gradient-quantities used as

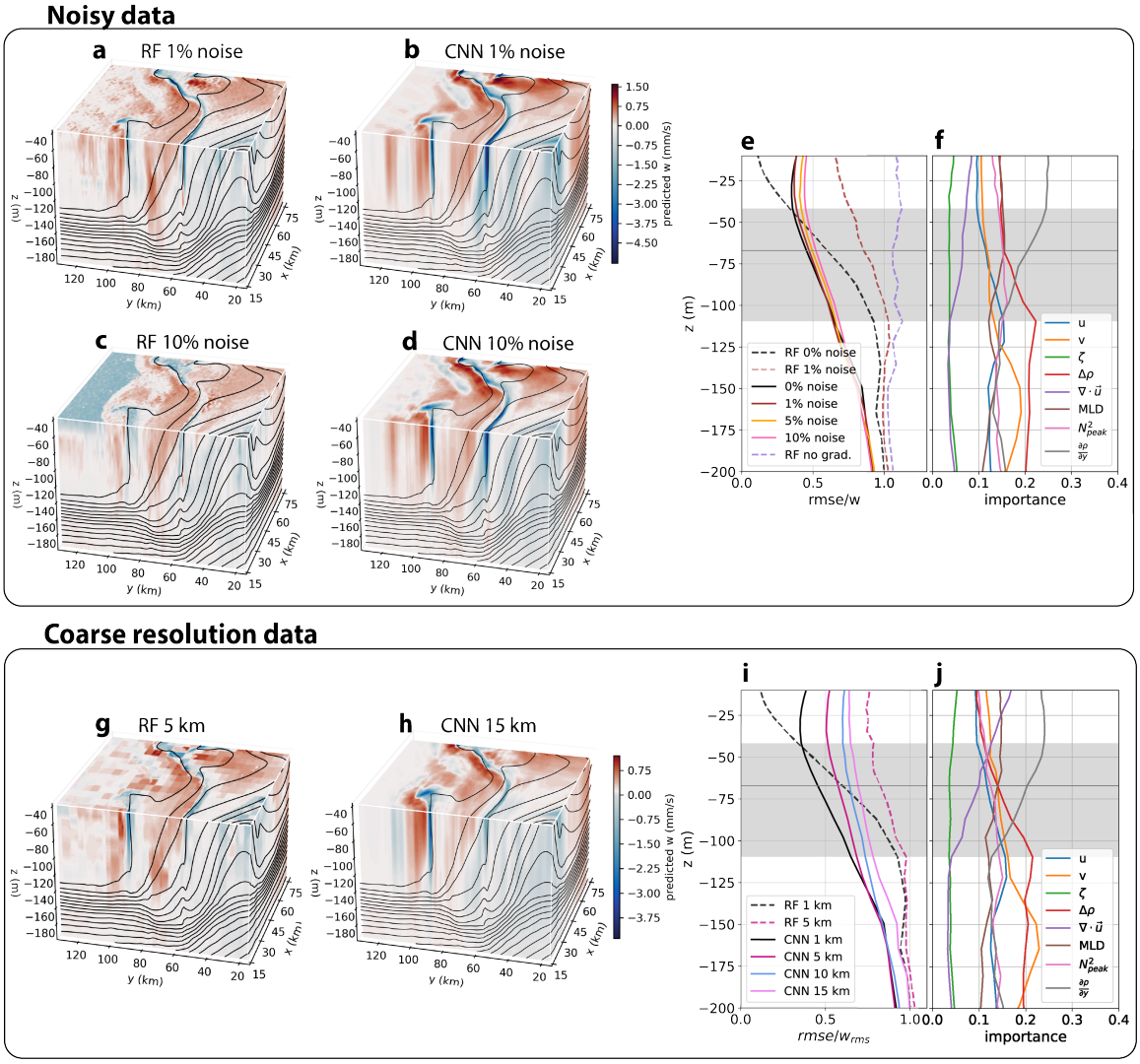

Figure 4-3: a–d) Snapshots of w from RF and CNN trained on velocity data with 1% or 10% noise, to be compared with Fig. 4-1a. e) Profiles of the normalized RMSE of w predictions from the CNN (solid line) and Random Forest (dashed line) for different levels of data noise. f) Feature importance for the RF 1% noise. g, h) Snapshots of w from RF and CNN using coarsened u, v velocities at 5 or 15 km resolution. i) Normalized RMSE for RF and CNN predictions trained on different resolution data. j) Feature importance for the RF 5 km model. See Table 4.1 for more information on each model.

inputs, and there is no skill at all. When the divergence, δ, is degraded in quality by noise, it is almost as if δ is not provided at all. In contrast, the CNN is much more robust to noisy data (solid lines in Fig. 4-3e). The CNN RMSE increases a little with higher noise levels, but not nearly as much as the RF errors. This main advantage of CNN comes from its inherent feature of convolving filters with the input images, and since the filters are learned during the training process, we hypothesize that the CNN is learning to filter out the noise.

4.3.3 Coarse resolution

Another challenge of surface ocean data is that there is often a mismatch in spatial resolution between different variables, such as surface horizontal velocities and sea surface temperature (SST). Here, we test the effect of coarsening $\vec{u_h}$ from 1 km to 5 km, 10 km, and 15 km resolution on the prediction of w at the scale of 1 km. The u, v fields at 1 km resolution are representative of Dopplerscatt (Rodríguez et al. 2018), the 5 km resolution of u, v is close to that of HF Radar (Paduan and Washburn 2013), while 15 km will be closest to SWOT's resolution (Fu and Ubelmann 2014). The surface density is kept at 1 km resolution, representative of L2 SST satellite data (Kilpatrick et al. 2015; Govekar et al. 2022).

Unsurprisingly, decreasing the spatial resolution of $\vec{u_h}$ yields worse predictions of w (Fig. 4-3i, Table 4.1). For MLR and RF, coarsening $\vec{u_h}$ to 5 km causes r^2 to drop significantly from $\sim$0.6 to $\sim$0.3 (Table 4.1). The feature importance of the 5 km RF model in Fig. 4-3j reveals that coarsening u and v strongly reduces the importance of divergence, which is expected because calculating δ on a larger grid size results in smaller values of δ. We can also see the effect of a coarse resolution δ reflected in the snapshot of 5 km RF predictions (Fig. 4-3g), which are visually pixelated and have weaker w magnitudes compared to Fig. 4-1a. The CNN is once again relatively less sensitive, with r^2 decreasing from 0.76 for 1 km resolution to 0.60, 0.40, and 0.36 for resolutions of 5 km, 10 km, and 15 km, respectively (Table 4.1). Impressively, the 15 km CNN predictions manage to capture fine-scale patterns in w (Fig. 4-3h), but the magnitudes are under-predicted because the fine scale velocity gradients that are

important for w are missing when the data is coarsened.

4.4 Discussion and Conclusion

Data-driven methods can be used to diagnose submesoscale vertical velocities in the upper ocean, within and just below the surface mixed layer. We find that exclusively using surface data yields skillful predictions with $r^2 > 0.6$ for all ML models tested, and including subsurface information in the form of MLD and peak N^2 results in only marginal improvements. Though this may seem surprising, it is consistent with known patterns of submesoscale dynamics where w is related to the surface divergence, vorticity, and density fronts (D'Asaro et al. 2018; Ruiz et al. 2019; Tarry et al. 2021; Freilich and Mahadevan 2021). It is thus reassuring that MLR ad RF accurately predict w when provided with δ, ζ, and ρ_y, but have no skill without those inputs. Specifically, δ turns out to be by far the most important input. One advantage of the CNN—the best performing model—over RF and MLR is that we do not need to explicitly calculate δ, ζ, or ρ_y and can just provide surface u, v, ρ. This is because by design, CNN learns to detect the important spatial patterns, including gradients, for making its predictions. Overall, we find that ML methods—when provided with accurate 1 km data—are successful at linking vertical velocities and surface patterns associated with submesoscale dynamics.

However, it is unrealistic to have perfect observations, and $\vec{u_h}$ at 1 km resolution is not yet commonplace. Adding a small 1–10% noise to the surface velocities results in an extremely noisy divergence field, which is detrimental for RF and MLR. Methods for predicting w that rely directly on δ should thus carefully consider the errors in the surface horizontal velocities. In contrast, the CNN is relatively insensitive to noisy velocity data, which may be because it learns to filter out the noise during the training process. A caveat is that we use white noise in our experiments, but realistically the form of measurement errors is more complex. For example, the Dopplerscatt noise structure has a radial dependence for each swath (Rodríguez et al. 2018), and further work is needed with more realistic noise forms for different types of measurements.

Additionally, we find that using coarser resolution $\vec{u_h}$ data degrades the performance of all ML models, with CNN being the most robust. This is expected since it is difficult to resolve these finer-scale velocity gradients with coarser resolution $\vec{u_h}$. Theses results emphasize the importance of obtaining accurate, high-resolution surface u and v measurements for estimating submesoscale vertical transport in the future.

This study is meant to be a first assessment of the applicability of ML models for learning physical relationships and vertical velocities in an idealized system without surface waves and boundary layer turbulence. We find the results promising even with relatively simple ML models, and expect that further advances can be made through additional experimentation with other types of ML models and architectures. All of the ML methods that are tested perform best near the surface, and errors increase with depth. This is contrary to QG methods, which are more successful at depths further below the mixed layer (Uchida et al. 2019; Qiu et al. 2020). Therefore, data-driven methods could be a good complement to SQG methods, and using both together could yield the best estimate of full water column vertical velocities. We think there is potential for much exciting future work to be done to move towards applying these methods to the real ocean.

Acknowledgments We thank Eric D'Asaro, Eli Tziperman, and Stephanie Dutkiewicz for discussions and feedback on this work, and thank you to Weiguant (Roger) Wu for providing code for the iSQG inversion. JH was supported by the NASA FINESST Grant 80NSSC19K1350 and AM by NASA Grant 80NSSC19K1256. The authors have no financial conflicts of interest.

4.A Appendix

Supporting Information for "Vertical velocity diagnosed from surface data with machine learning"

Text S1. Numerical ocean model

The ensemble of simulations used in this study is described in He and Mahadevan (2021), and we summarize more details about the simulations here. The model is initialized with a linearly increasing density profile (so N^2 is uniform throughout the domain), and it starts from a state of rest with no initial horizontal gradients. A constant wind stress τ is applied in the negative x direction, which drives upwelling at the coast located at $y = 0$. To get a broader range of conditions for training, we run a series of 9 experiments using different combinations of the initial stratification and wind forcing. The initial stratification is set to either 10^{-5} s^{-2}, 5.5×10^{-5} s^{-2}, and 10^{-4} s^{-2}, and τ takes on values of 10^{-2} Nm^{-2}, 5.5×10^{-2} Nm^{-2}, and 10^{-1} Nm^{-2}. Each simulation is integrated forward in time with a time step of 108 s (for $\tau_{max} = 0.1$ Nm^{-2}) or 216 s (all other experiments) for at least 30 days after the upwelling front becomes unstable and a submesoscale field develops. The total time period of the simulations ranged from 60 days to 120 days, depending on how long it takes for instabilities to emerge, and outputs are saved at 1-day intervals. A 20-day period is selected from each simulation after the spin-up period, determined by looking at the eddy kinetic energy and identifying the period where it is steady (see He and Mahadevan (2021)). Figure 4-4 shows snapshots of the Rossby number given by surface vorticity ζ normalized by f across the different simulations used. The Rossby number is $\mathcal{O}(1)$ at the submesoscale and the vorticity is positively skewed, consistent with observations (Shcherbina et al. 2013). Using these different simulations allows us to train the ML model with a range of conditions to help prevent overfitting.

Text S2. Data pre-processing

The "surface" data taken from the simulations used for training are taken from the top-most grid cell in the numerical model, whose thickness is 1 m and center is located at a depth of $z = -0.5$ m. Examples of the various input fields are shown in

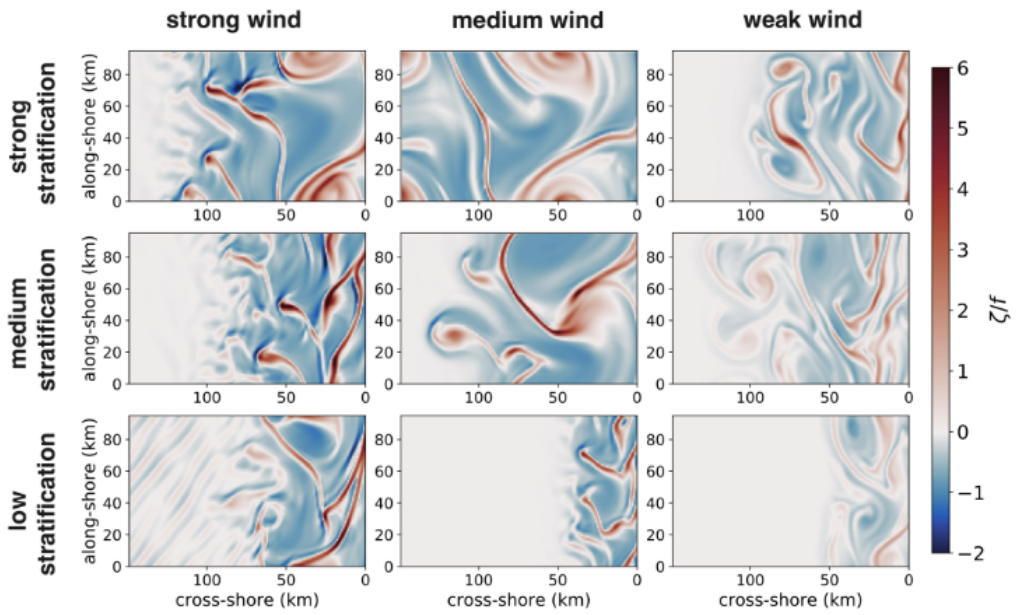

Figure 4-4: Snapshot of surface vorticity ζ normalized by f for the 9 simulations.

Fig. 4-5.

We first smooth all the model outputs to eliminate unphysical grid-scale numerical noise. This is done using a fourth-order biharmonic operator which selectively smooths out small scale noise while preserving the large scale features (Griffies and Hallberg 2000). For any variable c, the result of the filtering computes $c_{new} = c_{old} - \kappa\nabla^4 c_{old}$, where $\kappa = 0.062$ m^4.

Mixed layer depth, N^2, and ρ

The mixed layer depth (MLD) is identified following Montégut et al. (2004), which uses a threshold of 0.03 kgm^{-3} from the reference density at 10 dbar below the surface. We then linearly interpolate between depth levels to determine the exact depth at which the 0.03 kgm^{-3} threshold is reached. The N^2 value used in this paper is taken to be the maximum stratification value obtained below the MLD.

The surface density ρ that we use is an anomaly from an offshore value taken at y =150 km offshore. Furthermore, we tested using the full density gradient $\nabla\rho$ and its magnitude to train MLR and RFs. But we found that the cross-shore component of $\nabla\rho$, ρ_y, is the most useful because the upwelling front gradient is primary in the

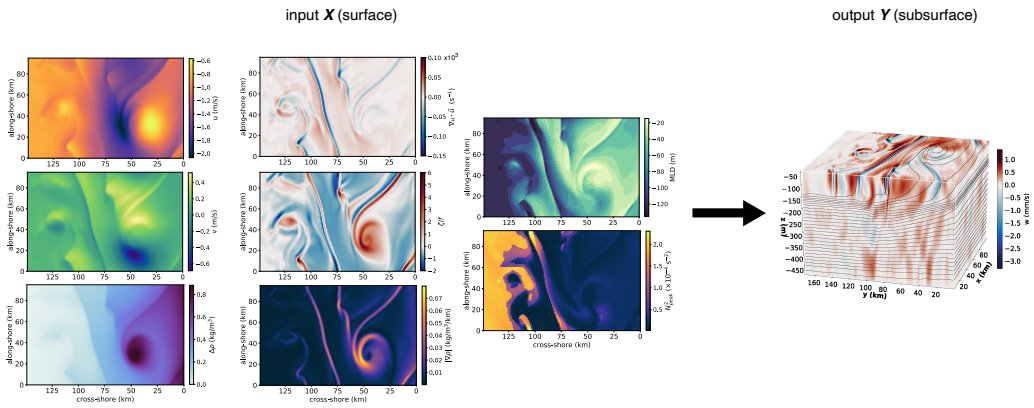

Figure 4-5: Example of input fields and the corresponding output that the RF is trained to predict. The far-left column, from top to the bottom, the inputs are u, v, ρ. The next column over, from top to bottom, the inputs are: $\delta, \zeta, |\nabla\rho|$. Then in the 3rd column from the left, the final 2 inputs are MLD (top) and N^2 (bottom). The output we are trying to predict is the 3D w field.

cross-shore direction, so that is the only component we retain.

Noise and coarsening

Different instruments have different forms of noise, which is important to consider carefully, but we start by taking a simple approach to the noise. We also focus on adding noise to just the velocities since (a) that is the more uncertain quantity compared to the surface density or SST, (b) we find that the surface velocities are the most important features. We start by re-writing u, v in terms of their speed A and angle from the coast θ, so that $u = Acos(\theta)$ and $v = Asin(\theta)$. This mimics how Dopplerscat and HF radar measure velocities—they do not measure u and v directly, but instead first obtain A and θ (Rodríguez et al. 2018; Paduan and Washburn 2013). Then, we add some level of random noise to A and θ by sampling from a uniform distribution between 0 and 1, scaling by the noise level, and then convert back to u and v. Furthermore, adding a small relative error to u and v results in a large relative error in the divergence, since the divergence is orders of magnitude smaller than u, v (Fig. 4-6). Given the dominance of the divergence importance in Fig. 2d, this stresses the importance of having u, v measurements with as little errors as possible.

To coarsen fields from the original 1 km resolution to a new resolution of k km,

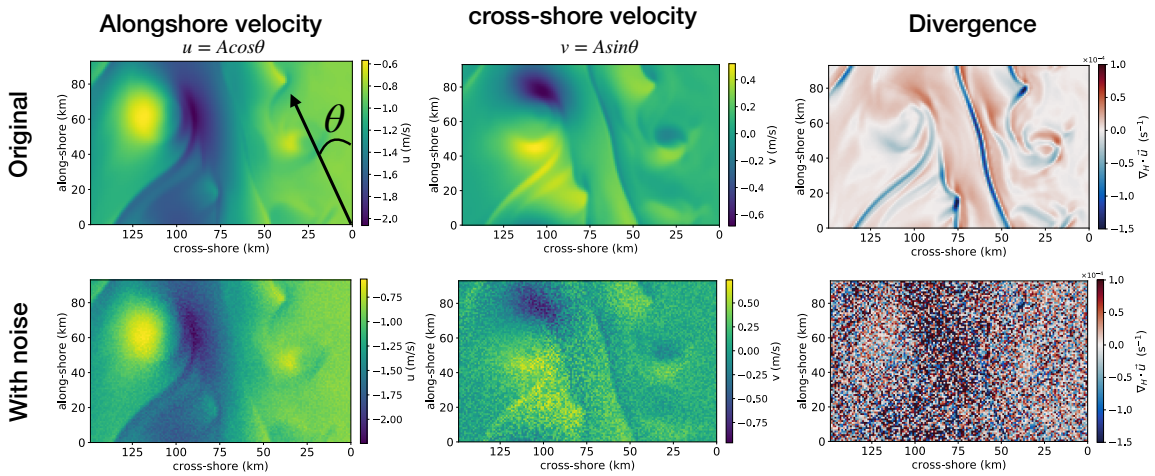

Figure 4-6: Top row: Example of original error-free surface velocities and the divergence field calculated from it. Bottom row: Same as top row, but now a 5% random white noise has been added to A and θ, resulting in a noisy u, v field. The divergence field calculated from the noisy u, v now has a very large relative error.

we divided the 2D field into $k \times k$ km squares and replaced all the grids in that $k \times k$ array with the median value in that array. We coarsen the u, v fields in this manner (see Fig. 4-7 for an example), and re-calculated divergence and vorticity from the coarsened fields. As a result, the velocity gradients calculated from coarse u, v fields are weaker since we lose the extreme values, and the gradients are computed over a larger distance.

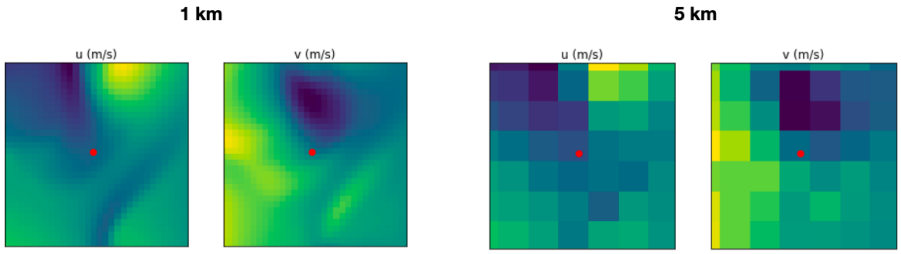

Figure 4-7: Example of an input image to the CNN of u, v at 1 km resolution (left) and 5 km resolution (right).

Text S3. Machine Learning Models

Random Forest

Random Forest is an ensemble of decision trees, where each tree recursively parti-

tions the data to minimize the mean square error (MSE) of its predictions (Breiman 2001; Hastie et al. 2001). Each tree is trained with a random bootstrapped subset of the training data. The prediction for a tree is a mean over a subset of the training data, and the prediction for the RF is a mean over all trees. Random Forest is a common popular model because it is very quick to train, it is able to fit the data well without overfitting, and it offers a level of interpretability as to how it makes its decisions (Breiman 2001; Hastie et al. 2001). However, because RF can only partition data, we need to explicitly provide it with the inputs that are important for making its decision, such as the divergence and density gradient. Thus, RF requires some prior knowledge about the system and/or experimentation with different inputs.

We train RF models using the RandomForestRegressor from the scikit-learn library (Pedregosa et al. 2011). The hyperparameters we varied are the number of trees in the forest ($n\_estimators$, default = 10), the maximum depth of each tree (max_depth, default = none), the minimum number of samples in a node in order to have a split ($min\_samples\_split$, default = 2), and the minimum number of samples in a leaf ($min\_samples\_leaf$, default = 1). In general, changing the hyperparameters to make the decision trees more complex (e.g. increasing max_depth, and decreasing $min\_samples\_split$ and $min\_samples\_leaf$) will result in a better fit to the training data, but may risk overfitting to the training data which yields poor test performance. Increasing $n\_estimators$ helps mitigates overfitting and improves test set errors, but it increases training time since more trees need to be fit. In the end, we found that the default settings of the hyperparameters yield the best performance on our test set. Using all grid points within 150 km from the coast gives a total of 127,395 input-output pairs per snapshot in time, and we find that training with just one snapshot of data is sufficient, and increasing the size of the training data set does not improve performance on a test set. The RFs are trained using data from day 10 of the 20-day period selected from the ensemble, and the test set is taken from day 5.

Convolutional Neural Network

CNNs applies filters across the input images to identify features to help make its prediction, and the weights of each pixel in the filters are learned during the training

process. A benefit of CNN over RF is that we are able to have a much larger field of view and can more efficiently consider neighboring grid points and look at spatial information. However, CNNs are more difficult to train and interpret than RF.

The CNN we use has 3 convolutional layers followed by 2 fully connected layers. The inputs to the CNN have dimensions $n \times 32 \times 32$, where n is the number of input variables or features used. All inputs to the CNN are standardized by subtracting the mean and dividing by the standard deviation for each variable. The first convolutional filter is of size 5×5, which was chosen to allow the calculation of gradients (using 2nd order centered-difference methods, or second derivatives can be calculated with 1st order finite-difference methods). The remaining two convolutional layers have filters of size 3×3. Each convolutional layer is followed by ReLU activations, and then a max pool layer with kernel size 2 and stride of 2. The result of the third and final max pool layer is then flattened and passed through 2 fully-connected layers, with rectified linear (ReLU) (Xu et al. 2015) activation in the hidden layer and linear activation in the final output layer. The final output is size 32×1, so a prediction is made for every vertical level. Because CNNs are more computationally expensive to train and require more data, we use 250,560 training samples across 4 snapshots for training. We train the CNN with Stochastic Gradient Descent using training data from days 0, 10, 15, and 20 of the 20 day period selected from the ensemble, while reserving day 5 for testing (the same day as RF for easier comparison). We use PyTorch to train the CNNs, and experimented with different architectures by varying the number of convolutional layers and fully connected layers, and the widths of each layer. We tested different batch sizes, learning rates, and optimization schemes including Adam and mini-batch stochastic gradient descent. The final hyperparameters used are a batch size of 8, learning rate of 1e-2, and we trained for 20 epochs.

Text S4. Alternative methods for estimating w

We test two alternative methods for diagnosing w, namely depth-integrating the surface divergence, and the interior + Surface Quasi Geostrophy (iSQG) method of Wang et al. (2013). We find that these two methods did not perform as well in our dataset, so the main focus of the paper is on the ML methods instead.

Surface divergence

From the continuity equation, we can relate the vertical gradient of vertical velocity to the horizontal divergence:

$$\frac{\partial w}{\partial z} = -\left(\frac{\partial u}{\partial x} + \frac{\partial v}{\partial y}\right), \tag{4.1}$$

where u, v are the horizontal velocities in the x and y directions, respectively. If the surface horizontal velocities u_0, v_0 are known, then we can calculate the surface horizontal divergence and obtain w at some depth z by depth-integrating the surface divergence:

$$w(z) = -\int_0^z \left(\frac{\partial u_0}{\partial x} + \frac{\partial v_0}{\partial y}\right) dz. \tag{4.2}$$

This method assumes that the divergence is constant with depth and is equal to the surface value, which is only a valid assumption above the mixed layer depth and very close to the surface. The farther below the surface you move, the more likely this assumption will break down and the worse the w estimates will become. Furthermore, Eq. (4.2) predicts that w increases in magnitude linearly with depth, which after a certain point breaks down since vertical velocities tend to be very small and near zero in the interior ocean. See Fig. 4-8 for an example of w diagnosed from this method.

Surface Quasi Geostrophy

The Surface Quasi Geostrophy (SQG) method is another way to reconstruct interior vertical velocities from sea surface temperature (SST) or sea surface height (SSH). There are a number of variations of the SQG method, and here we test out iSQG since it makes use of both SSH and SST and includes information on interior modes (Wang et al. 2013). These SQG methods typically assume small Rossby Number $Ro << O(1)$, which is not the case in our simulations since we have $Ro \geq 1$ (Fig. 4-4). Nevertheless, this has been a widely studied method in the past, so we test it out on our data set.

Following Wang et al. (2013), we use the surface 2D buoyancy anomaly field (anomaly is from the alongshore mean) to compute the 3D SQG streamfunction ψ_{sqg},

and we use an average buoyancy profile for the entire domain to obtain the interior modes ψ_{im}. The total streamfunction is thus $\psi_{tot} = \psi_{im} + \psi_{sqg}$. Then from ψ_{tot}, we can compute the reconstructed 3D buoyancy anomaly and horizontal velocity anomaly fields, and then use those reconstructed 3D fields to invert the omega equation to get the vertical velocity anomaly. Figure 4-8 shows the predicted w using this method (where we added back the mean fields to compare to the full w in Fig. 1a), and it does not capture the true w field very well at all.

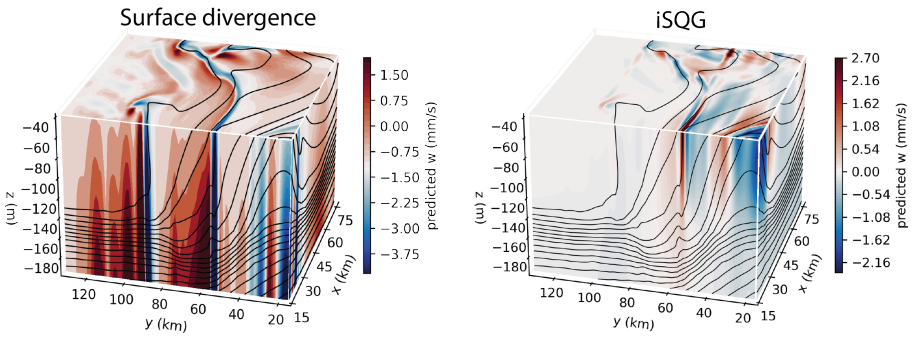

Figure 4-8: Predictions of w to be compared with Fig. 1a using the surface divergence method and the iSQG method.

Chapter 5

Vertical transport of nutrients and phytoplankton in an upwelling system

Abstract

Eastern boundary upwelling systems (EBUS) are among the most productive marine ecosystems due to the large influx of nutrients upwelled to the surface. Predicting and quantifying this nutrient flux is important for understanding bottom-up controls on primary production and how they might change in the future. In addition, upwelling fronts experience instabilities, and eddies are ubiquitous, which leads to additional eddy-driven vertical transport of nutrients and carbon. Using an idealized coupled bio-physical model of an upwelling front forced with realistic time-varying winds, we evaluate the importance of resolving the smaller scale eddy-driven fluxes for the average vertical nutrient and carbon transport over the upwelling region. For nutrient upwelling, Ekman transport theory is sufficient for diagnosing the spatially-averaged flux provided that the source depth is correctly parameterized and allowed to vary with time, and it is not necessary to resolve finer scale variability in w. However, diagnosing phytoplankton carbon biomass export is more difficult as that is not well explained by Ekman upwelling or parameterzations of eddy-driven subduction in this region. We show preliminary examples of how using the 3D w field predicted from a machine learning model, combined with surface observations of phytoplankton biomass, may enable us to predict vertical carbon transport across the base of the mixed layer from observations. This could lead to improved estimations of the contribution of eddy-driven subduction to the biological carbon pump.

5.1 Introduction

Eastern boundary upwelling systems (EBUS) experience sustained seasonal equatorward winds that drive coastal upwelling and supply nutrient-rich water to the euphotic zone. This stimulates phytoplankton growth, which helps to fuel the rest of the marine food web. As a result, EBUS are among the most productive marine ecosystems, supporting a disproportionate fraction of global fisheries despite their relatively small global area (Chavez and Toggweiler 1995; Pauly and Christensen 1995). In addition, upwelling of deep waters with higher DIC, and lower temperature and pH than surrounding surface waters, can further impact organisms (Feely et al. 2008; Rühmkorff et al. 2023) and air-sea CO_2 exchange in EBUS (Friederich et al. 2008; Torres et al. 2002). Quantifying the upwelling-induced vertical transport of biogeochemical tracers is thus important for monitoring and predicting ecosystem health.

The upwelling rate given by Ekman theory is solely based on the strength of the alongshore wind stress, latitude, and density. Upwelling indices based on Ekman theory have been in use for decades to estimate coastal upwelling intensity from wind data, starting with the Bakun Index in 1973 (Bakun 1973). Since the Bakun Index, there have been different indices created for upwelling intensity that accounts for additional dynamics such as wind-stress curl driven upwelling and the influence of onshore geostrophic flow (Estrade et al. 2008; Marchesiello and Estrade 2010; Rossi et al. 2013; Jacox et al. 2018). However, most indices only quantify the physical upwelling rate and do not account for the properties of the upwelled water itself, which is crucial when considering vertical transport of nutrients or any other tracer. For example, for the same wind stress, nutrient flux can differ significantly depending on nitrate concentration of the source waters for upwelling. The Biologically Effective Upwelling Transport Index (BEUTI) is one such index that does account for nutrient content (Jacox et al. 2018). Jacox et al. (2018) estimate the upward nitrate flux by multiplying the upwelling transport by the nitrate concentration at the base of the mixed layer. They find that while BEUTI is positively correlated to the coastal upwelling transport, the relationship is nonlinear, and that subsurface nitrate concentrations

can exhibit significant variability which is important to take into account.

In addition to the large scale coastal upwelling dynamics, satellite observations and models have revealed that mesoscale and submesoscale eddies and fronts are ubiquitous in EBUS (Kahru et al. 2012; Capet et al. 2008). In recent years, resolving the submesoscales in particular has gained more attention because the enhanced vertical velocities w at these smaller scales have been found to impact the vertical transport of heat, carbon, and nutrients (e.g. Su et al. 2018; Omand et al. 2015; Ruiz et al. 2019; Uchida et al. 2019). But, it is also suggested that while submesoscale fronts lead to local hotspots of intense carbon subduction, they contribute very little to the annual carbon flux on a regional scale due to compensation between upward and downward fluxes (Resplandy et al. 2019). In coastal upwelling systems specifically, eddies and fronts are also found to have myriad impacts on the distribution of nutrients and carbon, such as locally injecting nutrients to stimulate primary production at a front (Li et al. 2012), or enhancing eddy-driven carbon export (Stukel and Ducklow 2017). On the other hand, higher levels of eddy activity have been associated with a decrease in overall primary production and carbon export in the California Current System (CCS) because eddies transport and subduct upwelled nitrate offshore (Gruber et al. 2011). This raises the question of what is the overall contribution of eddy-induced vertical transport of nutrients and carbon in coastal upwelling systems, and how might we begin to capture them with observations?

A major challenge to observing vertical transport at these smaller scales is the difficulty of direct measurements of w, especially in capturing their temporal and spatial variability. In Chapter 4, we demonstrated that it is possible to infer the 3D submesoscale vertical velocity field from other more easily measurable quantities such as surface horizontal velocities, density, and a density profile. Here, we are interested in asking if having the fine scale vertical velocity field can help improve vertical transport estimates of nutrients and carbon in an upwelling system. We currently mostly rely on parameterizations for the spatially averaged vertical fluxes in a region. Nutrient upwelling or new production is typically estimated as an upwelling transport (consisting of Ekman transport and may include other contributions) multiplied by

a nutrient concentration, as described above. Typically, the nutrient concentration is determined by picking a source depth D_s, and using the nitrate concentration at that given depth. There are various ways of determining the source depth, such as using the mixed layer depth (Jacox et al. 2018), comparing offshore and inshore profiles (Carr and Kearns 2003), or using a parameterization that is a function of the wind and stratification (He and Mahadevan 2021). As for carbon export, a common parameterization of eddy-driven carbon subduction flux $\langle w'C' \rangle$ is given by Omand et al. (2015) as:

$$\langle w'C' \rangle = \psi_e \frac{M^2}{N^2} \frac{[POC]}{H}. \tag{5.1}$$

The overturning streamfunction $\psi_e = C_e M^2 h^2 f^{-1}$ comes from a parameterization for mixed layer eddies from Fox-Kemper et al. (2008), where $C_e = 0.8$ is a constant, M^2 is a characteristic lateral buoyancy gradient in the mixed layer, h is the mixed layer depth, and f is the Coriolis parameter. In addition, M^2/N^2 is the mean isopycnal slope, $[POC]$ is the spatial average of surface particulate organic carbon, and H is the euphotic depth.

Lastly, while the parameterizations above are useful for quantifying the average vertical flux in a region, they cannot give a detailed picture on where exactly the upwelling or export is happening. The spatial distribution can be important in some cases since it can tell us where new production is happening, and it could be useful to identify regions along a front where upwelling or downwelling of carbon export is occurring. Thus, our motivating questions in this chapter are:

1) How useful is it to know the 3D w field for diagnosing vertical transport? Does resolving the fine-scale variability in w and vertical transport change the average flux estimates over a region, or are existing parameterizations sufficient?

2) Can we get a better estimate of the spatial variability of vertical fluxes by using the 3D vertical velocity field?

We investigate these questions using an idealized bio-physical model where all the fluxes are known. The models and methods are described in Sec. 5.2. We evaluate the model, and present and discuss preliminary results in Sec. 5.3. Conclusions and

future steps are outlined in Sec. 5.4.

5.2 Methods

5.2.1 Physical model

Our idealized model setup is similar to that of He and Mahadevan (2021), except here it is based off of the California Upwelling System instead of the Arabian Sea and Bay of Bengal. We simulate coastal upwelling on an f-plane at a latitude of 35°N using the Process Study Ocean Model (PSOM), which solves the nonhydrostatic Bousinesq equations (Mahadevan et al. 1996a,b). The model domain is a 500 m deep re-entrant channel that extends 96 km in the alongshore (x) direction and 384 km in the cross-shore (y) direction. The coast is located at $y = 0$, and the horizontal grid resolution is 1 km. In the vertical, there are 32 stretched levels ranging in thickness from 1 m at the surface to 36 m at the bottom, and there is no bottom topography. Each simulation starts from rest with a constant initial stratification of $N^2 = 10^{-4}$ s^{-2}, and is forced with a spatially uniform alongshore wind stress, so there is no upwelling or downwelling driven by a wind-stress curl. A notable difference from the simulations in He and Mahadevan (2021) is that instead of using a constant wind stress in time, we force the model with a time-varying wind stress based on real wind data. This is motivated by previous modeling studies which found that high-frequency winds may be a crucial factor that influences the depth reached by nutrient fluxes at submesoscale fronts, and variable winds lead to enhanced vertical transport at the submesoscales (Franks and Walstad 1997; Lévy et al. 2009; Whitt et al. 2017). Wind data are obtained from the Cross-Calibrated Multi-Platform (CCMP) Ocean Surface Wind Vector Analyses data set (Atlas et al. 2011). Using 1 year of wind data from 2017, we compute a timeseries of the northwest component of the wind stress off the coast of California, which approximately represents the upwelling-favorable direction parallel to the coast, to force our simulations. More details can be found in Appendix 5.A.

Vertical mixing in the model is parameterized following Mahadevan et al. (2010)

to be a function of the wind stress, so that stronger wind leads to increased vertical mixing and deeper mixed layer depths. The vertical eddy diffusivity and viscosity K_z is given by

$$K_z = \max\left\{\frac{1}{2}K_{max}\left[1+\tanh\left(\frac{z+\delta_E}{\Delta}\pi\right)\right], K_{min}\right\}, \tag{5.2}$$

where $K_{max} = 10^{-2}$ m^{2}s^{-1}, $K_{min} = 10^{-5}$ m^{2}s^{-1}, and $\Delta = 0.5\delta_E$ are the same values used in Mahadevan et al. (2010). However, we decreased the coefficient in δ_E to reflect the shallower mixed layer depths observed off the coast of California, so that now $\delta_E = \frac{0.2}{f}\left(\frac{\tau}{\rho}\right)^{1/2}$. The horizontal eddy diffusivity and viscosity is constant at 1 m^{-2}s^{-1}.

To obtain an ensemble of simulations for computing statistics and uncertainty intervals, we run 9 numerical experiments by varying the start date of the wind forcing. For example, the wind forcing for experiment 1 starts on February 1, the wind forcing for experiment 2 starts on March 1, and so on. The full wind timeseries used to force the model is shown in Fig. 5-13. Each simulation is integrated forward in time with a timestep of 108 s and run for 65 days. The upwelling-favorable wind stress sets up an upwelling front at the eastern boundary that eventually undergoes baroclinic instability after about 20-30 days, forming meanders, eddies, and filaments. The model output is saved daily, and days 40-65 are used for analysis.

5.2.2 Biological model

To simulate the cycling of nutrients and carbon, we use a simplified phytoplankton-nutrient model adapted from Hodges and Rudnick (2004) and Freilich and Mahadevan (2019). This is a minimal model that captures the balance of light and nutrient limitation, which are the factors that determine the vertical structure of primary production in the California Current System (Deutsch et al. 2021). The nutrient pool is separated into "new" nutrients N representing nitrate, and recycled or "old" nutrients O (consisting mostly of ammonium) to distinguish between new and regenerated production, following Hodges and Rudnick (2004). Figure 5-1 shows schematic of the

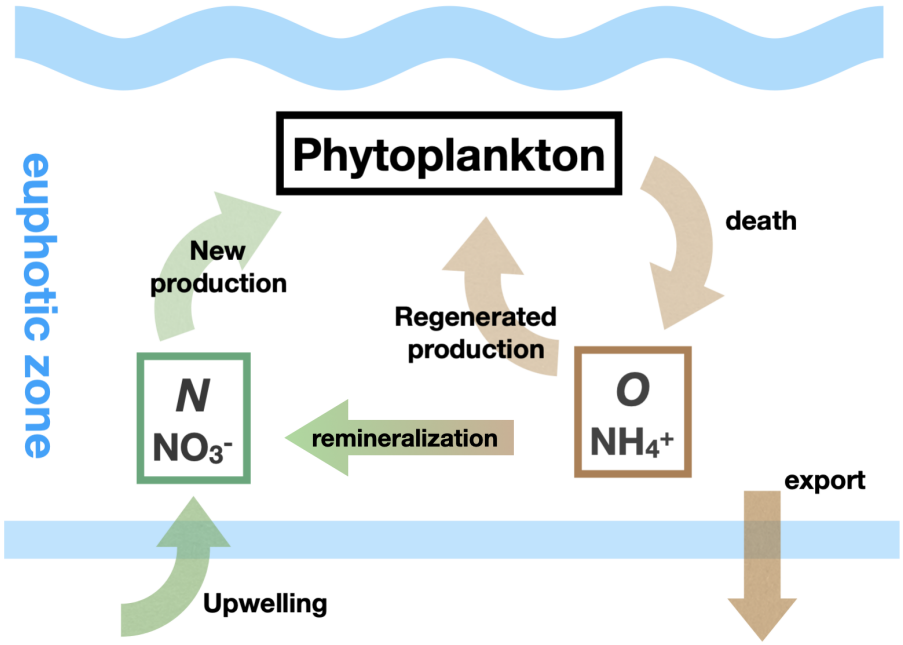

Figure 5-1: Schematic of nutrient cycling in the upper ocean represented by the biological model. Here, new nutrients given by nitrate N is supplied to the euphotic zone through upwelling, and it supports new production. Phytoplankton die naturally or are consumed through predation and are recycled into "old" nutrients O that is primarily ammonium, which supports regenerated production. Old nutrients are further remineralized to nitrate. In addition, there is an export of organic matter through the sinking of phytoplankton or zooplankton fecal pellets.

biological model. The evolution of phytoplankton P, nitrate N, and ammonium O are modeled by the following equations:

$$\frac{DP}{Dt} = GI(z)P\left[\left(\frac{N}{N+k_{sN}}\right)+\left(\frac{O}{O+k_{sO}}\right)\right] - mP + \nabla(\kappa\nabla P), \tag{5.3}$$

$$\frac{DN}{Dt} = -GI(z)P\frac{N}{N+k_{sN}} + RO + \nabla(\kappa\nabla N), \tag{5.4}$$

$$\frac{DO}{Dt} = -GI(z)P\frac{O}{O+k_{sO}} + mP - RO + \nabla(\kappa\nabla N), \tag{5.5}$$

The biological model parameters are summarized in Table 5.1, and values are adapted from Deutsch et al. (2021). Specifically we use the rates for diatoms, which

tend to dominate the phytoplankton community in coastal upwelling regions (Wilkerson et al. 2000). Parameters are tuned so that the model captures the correct depth of the chlorophyll maximum, indicating the right balance of light and nutrient limitation is represented. We also tuned the parameters so that the modeled f-ratio, defined as the ratio of new to total production, is similar to values reported for the nearshore CCS region of ∼0.4 (Frischknecht et al. 2018; Munro et al. 2013).

The growth of phytoplankton, represented by the first term on the right-hand-side of Eq. 5.3, is dependent on a maximum growth rate G, light availability $I(z)$, and nutrients whose uptake is represented with the Michaelis-Menten functional form. Phytoplankton can use either N or O as their nitrogen source, but there is a preference for O (Dortch 1990) which is reflected in the lower half-saturation constant (Table 5.1). The light available for photosynthesis decays exponentially with depth and is modeled as

$$I(z) = \exp\Big(- k_w z - k_p \int_z^0 P(z) dz \Big), \tag{5.6}$$

where k_w is attenuation of light in seawater, and k_p is the attenuation due to biomass. We choose $k_w = 0.08$ m^{-1} so that the euphotic depth—the depth at which the light is 1% of surface value—in the absence of phytoplankton is 57 m, to agree with photosynthetically available radiation (PAR) measurements made off the coast of California during the S-MODE campaign in October 2022. The loss of phytoplankton is returned to the O pool, which then fuels regenerated production. Old nutrients are broken down by bacteria and transformed back to nitrate at a rate given by the remineralization rate R.

Units of μM nitrogen are used for all tracers in the model, and P is converted to grams of chlorophyll-a or grams of carbon for comparison to observations and other studies. A note about semantics: for brevity, we may sometimes use the term "carbon" throughout the paper, but we are specifically referring to phytoplankton carbon, as there are no other sources of organic or inorganic carbon in our model. For the unit conversion, we assume a constant Redfield ratio C:N of 106:16. Deutsch et al. (2021) found that large diatoms make up 90% of modeled net primary production,

Table 5.1: Parameters and values for the biological model. Rates are adapted from Deutsch et al. (2021) for the California Current system, and k_p is from Olivieri and Chavez (2000).

Variable	Name	Units	Value
G	Maximum growth rate	day^{-1}	3
k_{zN}	half-saturation constant for N uptake	μM N	0.25
k_{zA}	half-saturation constant for O uptake	μM N	0.1
m	mortality rate	day^{-1}	0.15
R	remineralization rate	day^{-1}	0.01
k_w	attenuation coefficient of water	m^{-1}	0.08
k_p	attenuation coefficient per unit P	$\text{m}^{-1}(\mu\text{M N})^{-1}$	0.01

so we assume a high constant chlorophyll:carbon ratio of 0.065 used for diatoms from Li et al. (2010). The nitrate is initialized with a nitrate-density relationship of $N{=}\rho{\times}8\ \mu\text{M}/(\text{kg m}^{-3})$. Phytoplankton is initialized from a profile of chlorophyll-a off the coast of San Francisco, and O is initialized based on values Eppley et al. (1979) and Frischknecht et al. (2018). The initial conditions are shown in Fig. 5-14. The biological model spins up in about 20 days, after which there are no drastic sharp changes or adjustments in the primary production and mortality rates.

5.2.3 Nutrient upwelling flux

We evaluate the nutrient flux in the nearshore 72 km of the model, which is approximately double the Rossby deformation radius and encompasses the extent of the upwelling front in our simulations. Beyond that distance offshore, there is very little coastal upwelling or total vertical transport in our model. This is also the same cross-shore length scale used in Jacox et al. (2018). The horizontally averaged nutrient flux at a given depth is given by $\langle w'N'\rangle$, where $w' = w - \langle w\rangle$ and $N' = N - \langle N\rangle$, and the brackets denote a horizontal average. The nutrient flux $\langle w'N'\rangle$ is primarily positive, representing upwelling of positive N anomalies since N concentration is larger at depth and smaller at the surface. Since we do not have any wind stress curl nor an alongshore pressure gradient that drives cross-shore geostrophic flow, the Ekman transport alone is used as a proxy for the large scale upwelling transport. The Ekman

transport upwelling rate w_{Ek} is given by:

$$w_{\mathrm{Ek}} = \frac{\tau^{||}}{\rho_0 f} \cdot \frac{1}{L_y}, \tag{5.7}$$

where $\tau^{||}$ is the component of wind stress parallel to the coast, ρ_0 is a reference density, f is the Coriolis parameter, and L_y is the width of the upwelling band that we calculate $\langle w'N' \rangle$ over (72 km here). We then test five different ways to obtain a source nitrate concentration N_s to multiply with w_{Ek} for obtaining an upwelling nutrient flux, plus an additional fifth method where the direct w field is used.

a) D_s = MLD: First, we try using the mixed layer depth (MLD) as the source depth, which is the approach of Jacox et al. (2018). We calculate the the mixed layer depth at every point within the nearshore 30 km, which is approximately the Rossby deformation radius, by using a density threshold of 0.03 kg m^{-3} from the surface. The average MLD is usually around 30 m. The upwelled nitrate concentration is taken from the average nitrate profile in the nearshore 30 km, at the average mixed layer depth, since this is the immediate water that is being upwelled.

b) D_s from comparing inshore and offshore density profiles: Another common method to estimate the source depth is to match water mass properties in inshore and offshore temperature, salinity, or density profiles (Carr and Kearns 2003; Carmack and Aagaard 1977; Messié et al. 2009). To mimic this approach, we take the offshore density profile averaged from y =100–150 km, and compare it to the inshore (averaged between y =0–10 km) surface density in the mixed layer, ρ_{surf}. The depth in the offshore profile where the density equals ρ_{surf} is taken to be the source depth. The upwelled nitrate concentration is taken from the average nitrate profile from $y = 100$ to $y = 150$ km offshore, at the source depth. The choice of what offshore distance to average over does not make a significant difference in the results—taking the profile at $y = 100$ km vs. averaging over a wider region makes no difference because the far offshore region is fairly quiescent and homogeneous.

c) D_s from comparing inshore and offshore density profiles and correcting for mixing: The previous method assumes that there is no mixing as a water parcel is

upwelled, and thus will be an overestimate of the actual concentration of upwelled nitrate. To correct for the effects of mixing, we take the inshore profile and "unmix" the surface mixed layer by fitting a linear density profile from the base of the mixed layer to the surface with a stratification of $N = 10^{-2}$ s^{-1}. This is the stratification value that the model is initialized with, and it is the stratification in the interior of the model below the mixed layer depth. Using the un-mixed inshore density profile, we can again compare the surface density value to the offshore density profile to identify the depth where the densities match. This results in a shallower D_s and lower N_s.

d) Variable D_s from scaling: The three previous methods treat D_s and N_s to be fixed, so that only w_{Ek} varies in time with the wind. This is because we assume that it is unlikely to have profiles at the same locations every day to re-calculate the source depth each time (a case where this would be possible is if there is a mooring array). Alternatively, He and Mahadevan (2021) proposed a scaling relationship for the source depth as a function of the wind stress and stratification:

$$D_s = C_s \left(\frac{\tau}{\rho_0 N f} \right)^{1/2}, \tag{5.8}$$

where $C_s = 8.16$. This scaling assumes a steady state with a constant wind stress, while the real wind stress is highly variable in time. It does not make sense to use an instantaneous wind stress in the scaling since the source depth would likely not be able to respond immediately to sudden changes in the wind. To address this, we use the 7-day moving average of the wind stress to calculate the source depth in Eqn. 5.8. For each day, w_{Ek} is still calculated from the instantaneous wind stress that day, but the 7-day averaged τ is used to calculate D_s. The upwelled nitrate concentration is taken from the same offshore nitrate profile averaged from $y = 100$ to $y = 150$ km offshore, now at the source depth which changes each time step.

e) $w \cdot N(z = D_s)$, with variable D_s from Eqn. 5.8: We also examine if using the vertical velocity field directly provides any improvements of the nutrient flux over using the Ekman transport. The 3D w field can be predicted from surface observations, but as a first test, we use a horizontal slice of the true w field from the

model at the mixed layer depth. Ideally, we would have a way to measure the spatial field of N as well to multiply with the w field, but since we do not, we use the nitrate concentration from the source depth calculated from Eqn. 5.8. This way, comparing this method and the previous method e allows us to evaluate the importance of resolving finer scale vertical motions.

5.2.4 Vertical phytoplankton carbon biomass flux

Similar to the nutrient flux, the horizontally averaged phytoplankton carbon biomass flux at a particular depth is $\langle w'C' \rangle$, with $C' = C - \langle C \rangle$, and the brackets once again represent a horizontal mean over the region of interest (nearshore 72 km). In contrast to nutrient fluxes, $\langle w'C' \rangle$ is expected to be negative resulting in a net downward phytoplankton carbon export since phytoplankton are abundant in the upper ocean and nearly zero below the euphotic depth. We apply the parameteriazation of (Omand et al. 2015) in Eqn. 5.1 to estimate $\langle w'C' \rangle$ at the base of the mixed layer. From the model fields at each time step, we estimate $M^2 = |\nabla_h b|$ by taking the cross-shore (which is also the cross-front direction) lateral buoyancy gradient, where buoyancy is defined as $b = -g\rho_0^{-1}(\rho - \rho_0)$. The stratification N^2 is averaged over the upper 50 m, which encompasses the deepest mixed layer depths. We take the spatial average of the surface phytoplankton concentration in the upper 15 m for $[POC]$, and H is the average mixed layer depth. All variables are laterally averaged over the nearshore 72 km.

We find that it is more difficult to accurately capture $\langle w'C' \rangle$ in our simulations with a parameterization, which motivates finding ways to estimate $\langle w'C' \rangle$ directly from observations. From Chapter 4, we found that it was possible to diagnose the three-dimensional vertical velocity field in the upper ocean with fairly good accuracy using convolutional neural networks (CNNs) and surface observations. Here, we combine the w-field predicted by the CNN with surface phytoplankton concentration to evaluate the feasibility of directly estimating $\langle w'C' \rangle$. First, we re-train the CNN from Chapter 4 using the new set of simulations, since directly applying the CNN trained previously on the simulations in Chapter 4 did not produce as accurate w predictions.

This is not too surprising since we expect some differences in the models with the change in latitude, mixing scheme, and the inclusion of time-variable winds. After re-training, using the same input variables of surface u, v, ρ, as well as the mixed layer depth and N^2, the CNN is able to recreate the vertical velocity in the upper 100 m with a correlation of $r^2 = 0.77$ on a test set. This is comparable in performance to Chapter 4.

To estimate the 2D phytoplankton carbon biomass distribution at a given depth z, we use phytoplankton concentration averaged in the upper 15 m, denoted P_0. Because the phytoplankton concentration varies with depth and tends to reach a maximum subsurface, using the surface P concentration alone will tend to underestimate P deeper down. To better represent P at a particular depth z, we scale the surface P_0 by the average phytoplankton profile shape for each simulation over the model domain given by $P(z)/P_0$. The P anomaly is computed from subtracting the horizontal average, and converted to units of carbon to get C'. This estimate of C' is multiplied by w from the CNN to obtain an estimate of the phytoplankton carbon export at some depth, which we choose to be the average mixed layer depth.

5.3 Preliminary results and discussion

5.3.1 Model results

The model is intended to capture certain aspects of biological and physical processes, including upwelling of new nutrients to the euphotic zone for fueling phytoplankton blooms. The upwelling is evident from the isopycnals sloping upwards at the coast (Fig. 5-2), driven by the upwelling-favorable winds. During the peak upwelling season with the strongest upwelling-favorable winds, which is April–May in our simulations, there is an abundance of nitrate at the surface that is not entirely consumed (Fig. 5-2a). Surface nitrate concentrations are highest at the coast and decrease offshore, a similar pattern to what was measured from a flow-through SUNA optical nitrate sensor during S-MODE. This large influx of nitrate at the coast leads to enhanced

primary production nearshore, and phytoplankton concentration is further concentrated in the surface above 50 m since that is where there is enough light (Fig. 5-2b). The depth of the subsurface phytoplankton maximum, between -50 and -20 m, is similar to what was observed in Eco-CTD transects off the coast of California (Fig. 5-15). This indicates that our model is able to capture the right balance between light and nutrient limitation to accurately reflect the depth of the deep chlorophyll maximmum (DCM). The DCM offshore beyond 50 km in Fig. 5-2b is deeper than the onshore DCM because of the deeper nitracline offshore, a common feature in EBUS (Frischknecht et al. 2018; Deutsch et al. 2021). The old nutrient distribution is largest right below the phytoplankton maximum, since it is consumed within the euphotic zone. The f-ratio in the simulations, defined as the ratio of new to total production, varies spatially and temporally with the wind, but is around 0.4 in the nearshore 50 km, and decreases offshore, similar to what is reported in other studies (Frischknecht et al. 2018).

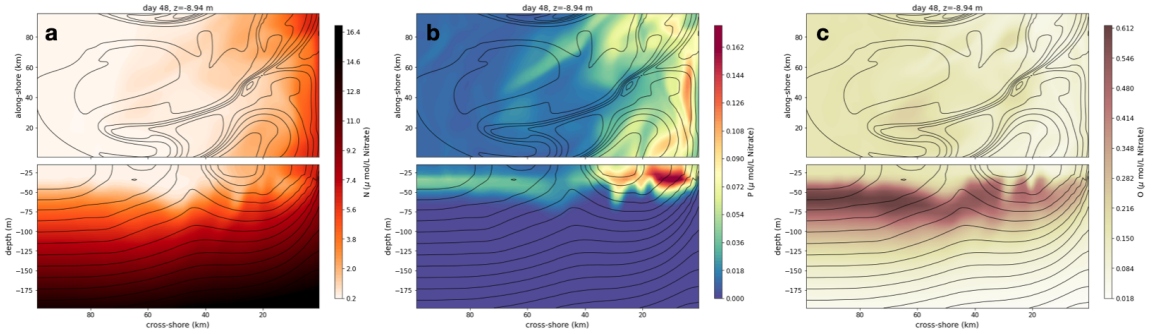

Figure 5-2: Example model output fields of (a) new nutrient, (b) phytoplankton, and (c) old nutrient in the nearshore 100 km of the model domain. All tracers are in nitrate units, which is the unit used in the model. Black contours denote isopycnals with an interval of 0.12 kg m^{-3}. This simulation is forced with wind fields starting in April, the start of the peak upwelling period. The top panel shows a plan view at a depth of $z = 8.9$ m, and the bottom panel is a cross-section transect.

The highest concentrations of N and P are within a narrow 30 km band nearshore, but there are filaments of elevated surface N and P that are advected up to 60 km offshore (Fig. 5-2). While the simulations generate a cross-shore gradient in nitrate and phytoplankton as expected, and we qualitatively see similar features such as

eddies and filaments, the model does not adequately represent how far offshore upwelled nitrate and phytoplankton are actually advected in the CCS. In satellite data of chlorophyll-a for instance, we see phytoplankton patches extending over 200 km offshore, but in our model, the upwelling front and P is usually confined to the inshore of 50–60 km (Fig. 5-2, 5-3b). A possible explanation for this discrepancy is that mesoscale eddies and filaments play a dominant role in the offshore transport of carbon and nutrients over 100s of km in the CCS (Nagai et al. 2015), and our model domain is too small to adequately capture this since there is only space in the alongshore direction for 1-2 mesoscale eddies to fit. Furthermore, the offshore extent of upwelled waters also covaries with large scale climate forcings such as the El Niño-Southern Oscillation and the North Pacific Gyre Oscillation (Chabert et al. 2021), which are not present in our model. Our model also lacks bottom topography and a continental shelf, which is about 50 km wide off the coast of San Francisco (Song and Chao 2004) and would alter the location of the upwelling front. The depth-averaged chlorophyll-a concentration in the mixed layer of the model is approximately the right order of magnitude and has a similar distribution to surface chlorophyll-a measured by MODIS (Fig. 5-3c), with the satellite chlorophyll-a being higher than what is seen in our model. However, we do not expect a perfect correlation since the model is not meant to recreate this specific time of satellite measurements. Furthermore, MODIS chlorophyll measurements have a 36% error at concentrations higher than 1 mg m^{-3}, which is surpassed in the coastal regions (Kahru et al. 2014).

The model generates an eddying field with vertical velocities on the order of 10s to 100 m d^{-1} depending on the simulation (Fig. 5-4c, Fig. 5-9b). The eddy vertical velocities are smaller in magnitude than the upwelling signature, but these vertical velocities can upwell or subduct nutrients and phytoplankton carbon outside of the upwelling band. For example, we see evidence of offshore nutrient injection into the euphotic zone fueling new production (Fig. 5-4). In the model, we can identify which regions of offshore elevated chlorophyll concentrations are a result of local new production (Fig. 5-4a), as opposed to being a result of regenerated production or offshore advection. These regions of new production coincide with hotspots of positive

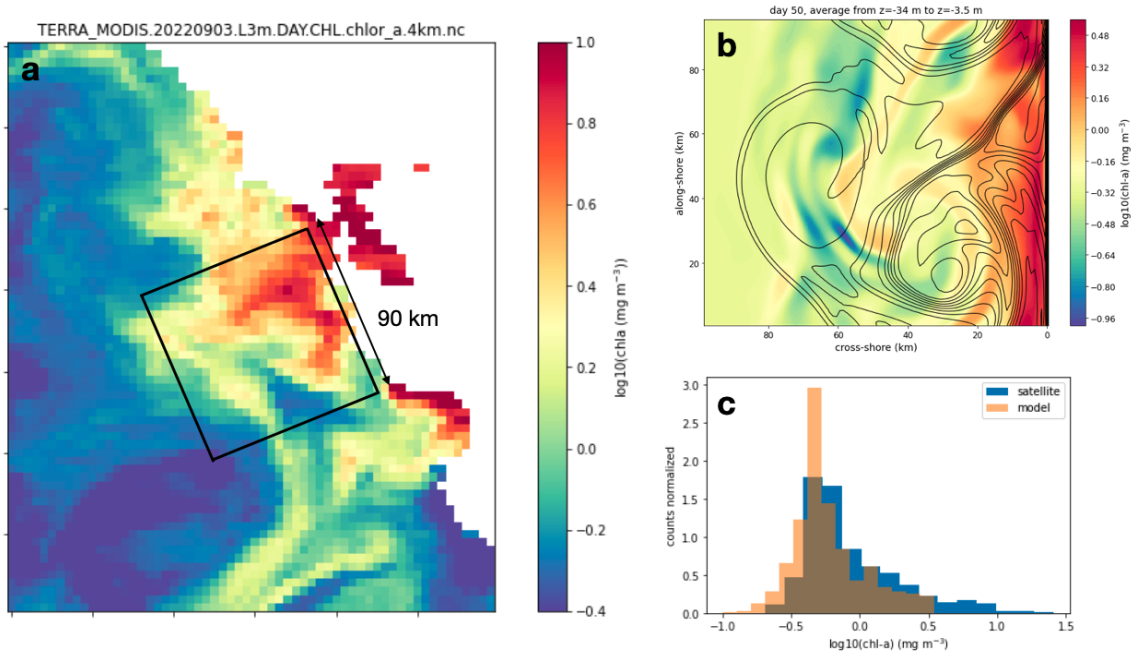

Figure 5-3: a) Chl-a concentration from MODIS TERRA on Sep. 3, 2022 off San Francisco Bay. b) Chl-a concentration averaged in the upper 34 m from the model simulation starting in September. The approximate size of the model output shown in (b) is outlined in the black box in (a) for reference. c) Histogram of satellite chl-a concentration shown in (a) and model chl-a concentration shown in (b).

upwelling nitrate flux (Fig. 5-4b), resulting from regions of positive vertical velocity and elevated nitrate (Fig. 5-4c,d). These hotspots of offshore nitrate injection and subsequent new production contribute around 10–20% to the total nutrient upwelling in the model, which is dominated by the wind-driven coastal upwelling.

5.3.2 Nutrient flux estimates

We focus on vertical nutrient fluxes at the average mixed layer depth, which is either $z = -34$ m or $z = -41$ m depending on the simulation. This is also the depth where the temporally-averaged $\langle w'N' \rangle$ profile (averaged over the analysis period from day 40–65) is maximized. The timeseries of $\langle w'N' \rangle$ at the base of the mixed layer is strongly correlated with the wind stress with a correlation of $r = 0.77$–0.94 across the ensemble, as expected from the dominance of the wind-driven coastal upwelling (Fig. 5-5). Because of the high correlation between the wind stress and $\langle w'N' \rangle$, all

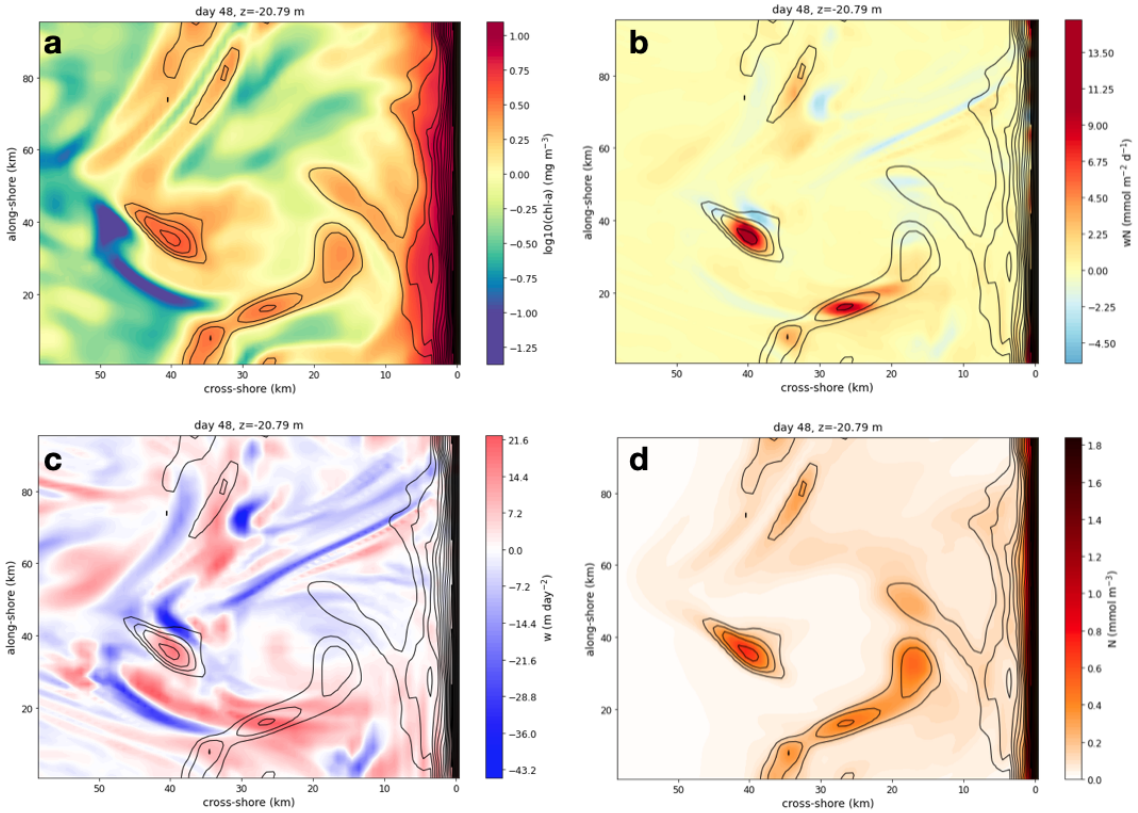

Figure 5-4: Example of new production as a result of offshore nutrient injection in to the euphotic zone. The black contours are new production rates and all snapshots are shown at -20 m depth, from day 48 of a simulation with winds starting in July 1. (a) Chlorophyll concentration. (b) Vertical nitrate flux wN at the same depth, where red positive values indicate upwelling of nitrate. (c) Vertical velocity, where red (positive) indicates upward and negative indicates downwelling. (d) Nitrate concentration.

the methods for estimating nutrient flux that rely on Ekman transport have equally high correlations with $\langle w'N' \rangle$ as well (Fig. 5-6). Figure 5-6a–e shows timeseries of the different nutrient flux estimates for one simulation (with winds starting in July), as well as the time-averaged fluxes in panel f. The time-averaged fluxes from each simulation is then used to compute the percent errors from different methods across the ensemble (Fig. 5-7).

To start, we find that using the nutrient concentration at the base of the mixed layer depth tends to under-estimate $\langle w'N' \rangle$, which is evident in a single simulation (orange line and bar in Fig. 5-6a, f) as well as across the ensemble as a whole (orange box in Fig. 5-7). This is because the mixed layer is within the euphotic depth in

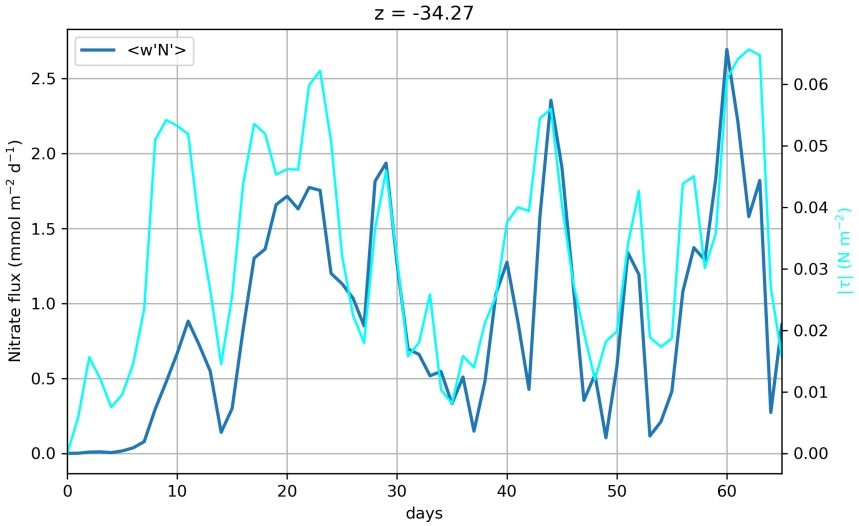

Figure 5-5: Timeseries of the average nutrient flux at $z = -34$ m computed directly from the model as $\langle w'N' \rangle$ and the magnitude of the upwelling-favorable wind stress for the simulation starting in July 1.

our simulations, so the nitrate concentration at the mixed layer depth is very low since it is consumed. The next approach of matching densities between an inshore and offshore profile tends to over-estimate the source depth and nutrient flux (green in Fig. 5-6, Fig. 5-7), since it does not account for any mixing diluting the nutrient concentration as it is upwelled. By correcting for the effects of mixing, the prediction bias is improved (red in Fig. 5-6, Fig. 5-7), but there is quite a large spread in the errors from $\sim -60\%$ to $\sim 30\%$. The large spread could be because the nutrient concentration is being held constant, when in reality it is variable in time. When we allow the source depth, and consequently N, to vary in time by using the scaling of He and Mahadevan (2021), we come very close to the true $\langle w'N' \rangle$ with a near-zero bias and smaller range of errors (purple in Fig. 5-6, Fig. 5-7). This agrees with Jacox et al. (2018)'s findings that upwelling indices based on Ekman transport alone do not necessarily fully capture the upwelling nitrate flux, because the nitrate concentration itself is also variable in space and time. Thus, it is important to take into account the temporal variability of N itself.

Lastly, we find that using the actual w field multiplied by time-varying nutrient

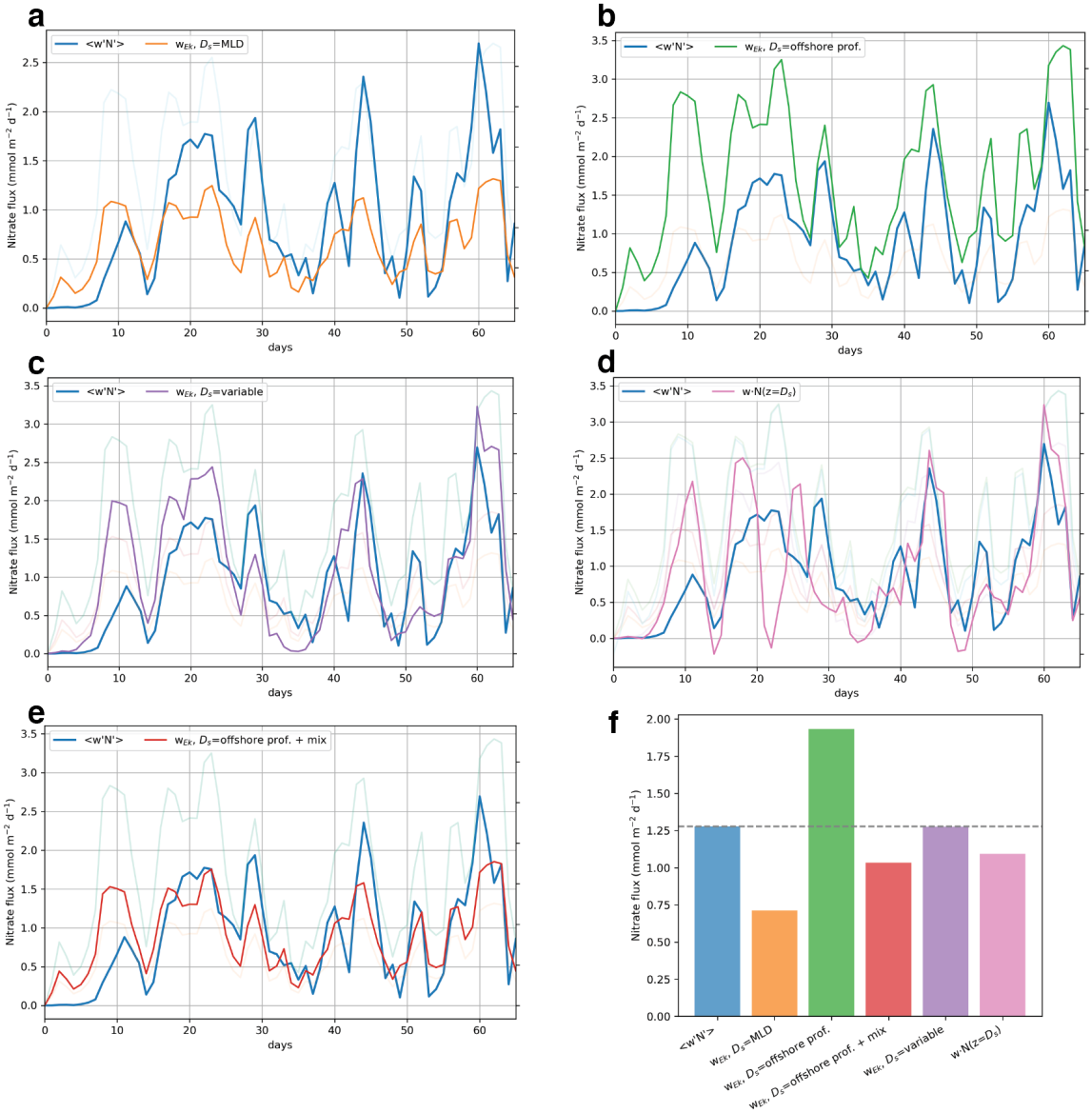

Figure 5-6: a–e) Timeseries of nutrient fluxes at $z = -34$ m estimated from different methods from a simulation starting July 1. f) Average nutrient flux from days 40–65 for this simulation.

concentration at the source depth (pink in Fig. 5-6, Fig. 5-7) is not a significant improvement over using Ekman transport with a varying source depth (purple). This initially was somewhat surprising since we expected that the direct w would be better than approximation of w_{Ek}, especially since Ekman transport explains approximately 70% of the variability in vertical transport across the ensemble (very similar to the 72% of variance explained in Jacox et al. (2018)'s model), which leaves a non-negligible

30% of the vertical transport variability that is not captured by Ekman transport. However, it appears that resolving the granularity of w is not that useful if we are unable to also resolve the 2D nitrate field at high resolution. Applying a single N concentration to the entire w field does not accurately capture the spatial distribution of $w'N'$ since not all regions with a positive w lead to a positive nutrient flux. The spatial variability in N is important for identifying offshore hotspots of nutrient injection and new production seen in Fig. 5-4. Interestingly, using the direct w multiplied with N at the source depth tends to under-predict the nutrient flux by about 10% (pink bar in Fig. 5-7), which makes one wonder if the errors are primarily due to not capturing the offshore injection hotspots.

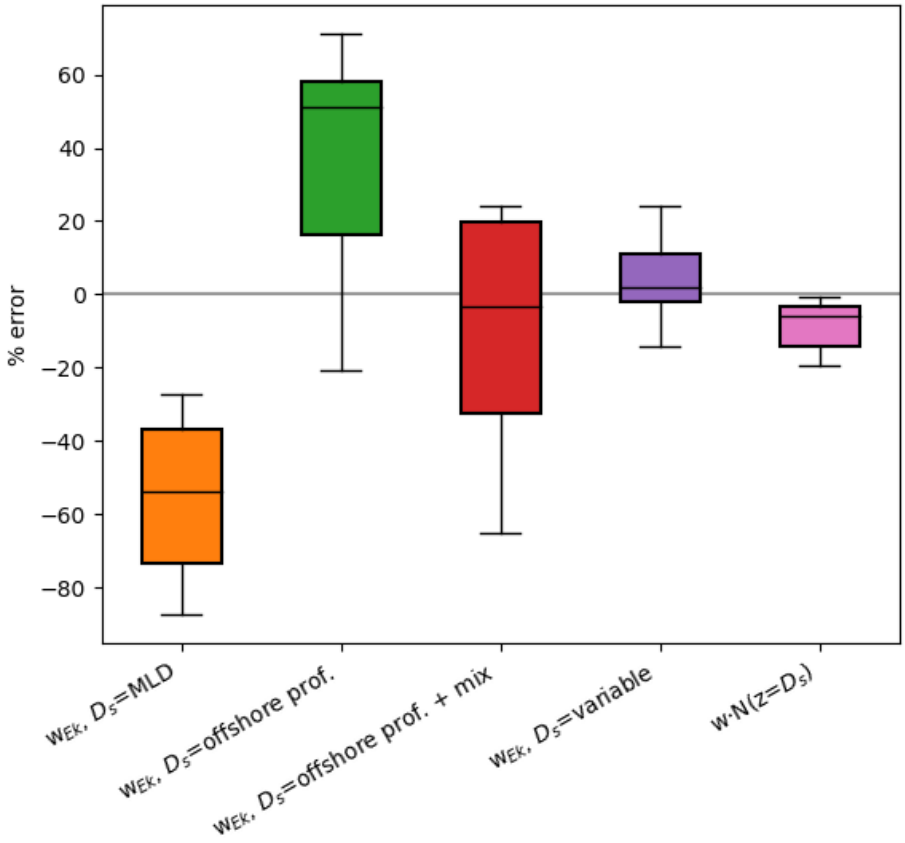

Figure 5-7: Percent error of each nutrient flux estimate method. Errors are averaged over a 25 day period in each simulation, so there are 9 error estimates for each method (one for each simulation).

5.3.3 Phytoplankton carbon biomass flux

The phytoplankton carbon flux $\langle w'C' \rangle$ proved to be more complicated to predict than nutrient fluxes. While nitrate concentration increases with depth, phytoplankton biomass is maximized subsurface around 30–40 m, right above the euphotic depth, in our simulations. We expect a net export of phytoplankton carbon below the euphotic depth since carbon rich waters are brought downwards, while carbon poor waters are upwelled (Omand et al. 2015). Ekman transport does not capture export since w_{Ek} is positive and in the nearshore upwelling region, C' is positive due to enhanced primary production, which would result in a positive flux. The eddy-subduction parameterization of Omand et al. (2015) in Eqn. 5.1 also does not fully capture $\langle w'C' \rangle$ in our model (Fig. 5-8). For example, during times of strong wind such as on day 63, $\langle w'C' \rangle$ is temporarily positive due to upwelling, but Eqn. 5.1 predicts a stronger negative flux. This is because stronger winds increase the mixed layer depth, which strengthens the mixed layer eddy parameterization ψ_e, since $\psi_e \propto H^2$. This is a case where trying to directly estimate $\langle w'C' \rangle$ from a reconstructed vertical velocity field and an estimate of C' at depth may be needed.

We showed in the previous chapter (Chapter 4) that it is possible to diagnose the 3D vertical velocity in the upper ocean and adequately capture its fine scale spatial structures and magnitude, which is still true for our new set of simulations with varying winds (Fig. 5-9a,b). The main challenge is with estimating C' since surface concentrations are not necessarily reflective of concentrations at depth. For example, in the snapshot in Fig. 5-9d, we see a typical cross-shore difference in the DCM depth (**?**Deutsch et al. 2021): the DCM beyond ~ 50 km offshore is at around 30 m depth, while in the nearshore 30 km, the phytoplankton maxima is at a shallower depth and reaches all the way to the surface. As a result, surface phytoplankton is only representative of subsurface concentrations above the depth of the offshore DCM. This is more clearly evident from the phytoplankton carbon anomaly in (Fig. 5-9c). The anomaly is from a horizontal average at each depth, and in the nearshore region, C' changes sign from positive to negative at the depth of the offshore DCM. This is a

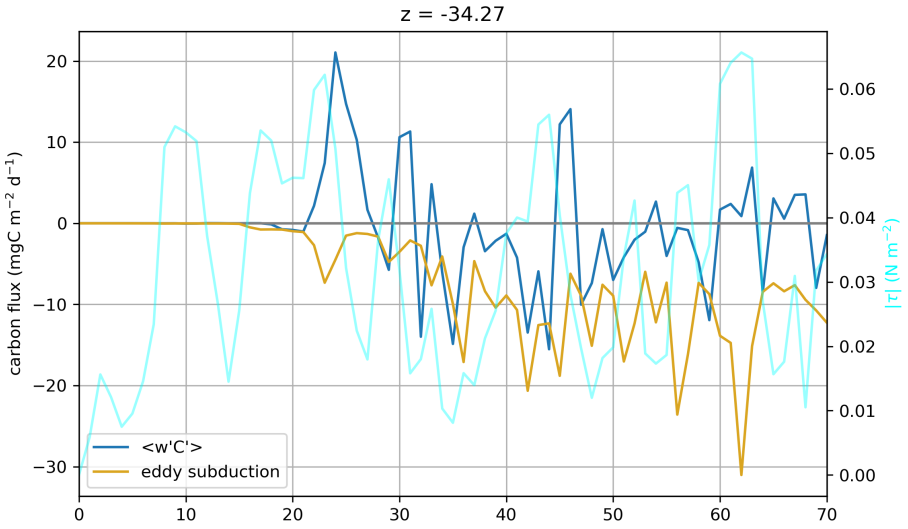

Figure 5-8: Timeseries of phytoplankton carbon flux at -34 m, the average mixed layer depth. The simulation shown is the same as in Fig. 5-6. The flux $\langle w'C' \rangle$ calculated directly from the model is shown in blue, and estimated flux from the parameterization in Eqn. 5.1 is shown in yellow. The upwelling-favorable wind stress magnitude is shown on the right-axis in cyan. The variability in $\langle w'C' \rangle$ is not well captured by the wind nor Eqn. 5.1.

consequence of the region over which we chose to average; if we limited the domain to be only the nearshore $\sim$ 30 km, then C' would not change sign with depth and would always be increasingly positive closer to the coast. Predicting the right magnitude of C' at depth is another challenge. The simple approach we take of scaling the surface value by an average phytoplankton profile for the whole domain is a rather crude method that generally gets the right order of magnitude for C', but can sometimes be off by a factor of two (Figs. 5-10, 5-11).

Figures 5-10 and 5-11 are examples from two different simulations showing snapshots of the true w, C', and $w'C'$ fields from the model in the top row, and in the bottom row is the corresponding predicted w, C', and $w'C'$ fields. In general, the spatial patterns in w and its negative skew are captured well. The w magnitudes are in good agreement in Fig. 5-11, while the strongest negative velocities are underpredicted by about 20% in Fig. 5-10. The C' predictions generally show similar signs and structures as the true C' at depth, but in Fig. 5-10, the positive C' located around 60 km offshore as part of the deeper offshore DCM is not captured by the

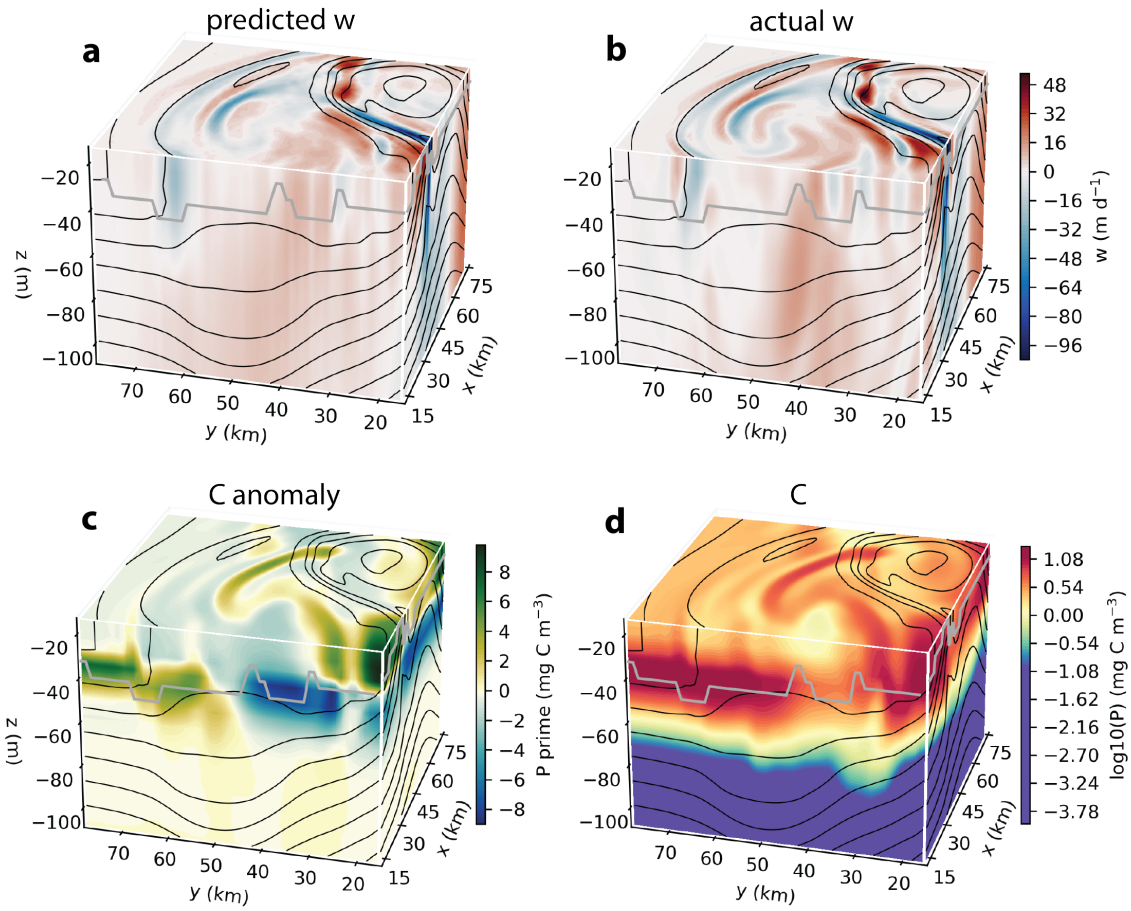

Figure 5-9: Example 3D fields of a) predicted w, b) actual w, c) carbon anomaly from horizontal mean at each depth, d) and carbon from day 45 of simulation that started in September. The surface shown is located at $z = -15\ m$. Black contours are isopycnals with contour intervals of 0.12 kg m^{-3}, and gray line indicates the mixed layer depth determined as change in density of 0.03 kg m^{-3} from the surface.

surface phytoplankton. Fortunately, vertical velocities are weak offshore, so this error in C' is does not appear too strongly in the flux. The general locations of positive and negative flux match pretty well, but the magnitude of $w'C'$ is significantly under-predicted. These preliminary results show that qualitatively, combining predictions of the 3D w field from the CNN with surface carbon concentrations, such as what is obtainable through remote-sensing, may be able to illuminate regions of positive and negative phytoplankton carbon biomass transport. But more work needs to be done to refine these methods to improve the magnitudes.

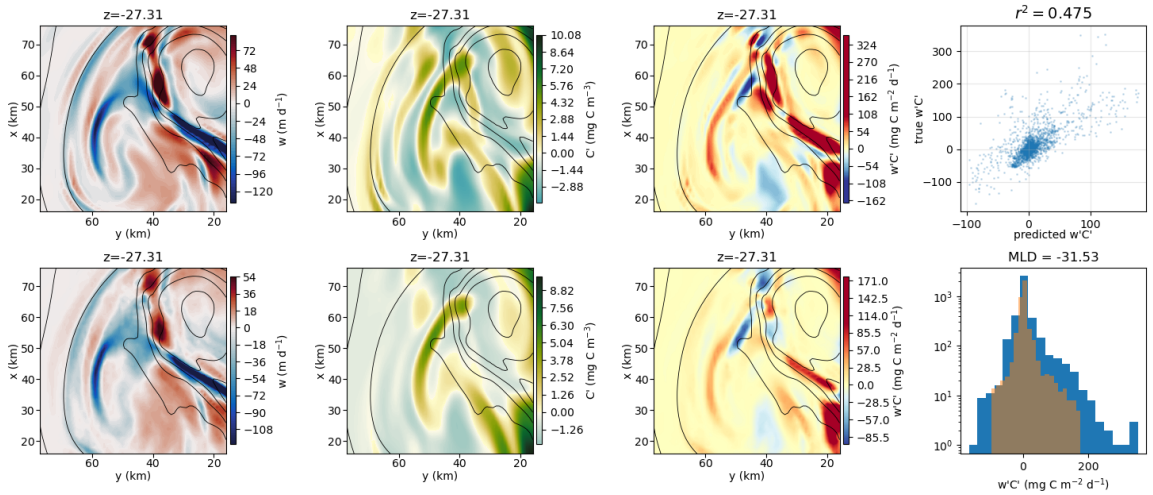

Figure 5-10: Vertical velocity, C', and wC' at the mixed layer depth, at the same snapshot in the simulation shown in Fig. 5-9. The top row shows the direct fields from the model, while the bottom row shows the predicted fields. A scatterplot of the true $w'C'$ and the predicted $w'C'$ is shown on the upper left with the correlation printed above, and a histogram of the true flux distribution (blue) and the predicted flux distribution (orange) is shown on the bottom right.

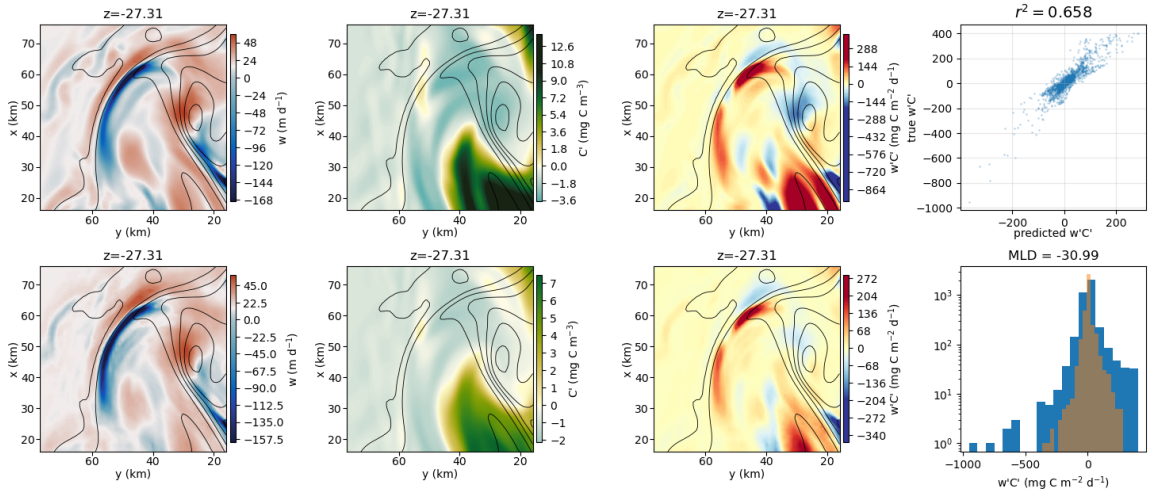

Figure 5-11: Same as Fig. 5-10, but for a different simulation starting in February.

5.4 Summary and future work

In this chapter, we make progress on evaluating the importance of resolving fine scale vertical eddy fluxes for vertical nutrient and phytoplankton transport in coastal up-

welling regions. In an idealized bio-physical model with realistic time-varying winds, the vertical nutrient transport within 72 km of the coast is sufficiently described with classic Ekman theory if we use a time-varying source depth given by scaling in Eqn. 5.8. Even though Eqn. 5.8 was developed for a steady state assuming constant winds, we find that it also works well when applied to time-varying winds if the winds are averaged over a 7-day period. Compared to using a fixed nutrient concentration determined by a single source depth value from offshore or onshore profiles, we find that using the source depth given by Eqn. 5.8 and a single offshore N profile leads to the smallest bias and smallest uncertainty in $\langle w'N' \rangle$. This supports Jacox et al. (2018)'s conclusion that the variability of the nitrate content of upwelled waters is important to consider for estimates of $\langle w'N' \rangle$. The importance of subsurface nitrate variability has implications for previous estimates of new production in coastal upwelling systems that assumed a fixed source depth and fixed nitrate concentration from climatology (Messié et al. 2009).

Quantifying the carbon export $\langle w'C' \rangle$ proves to be more difficult, as $\langle w'C' \rangle$ is influenced by upwelling and cannot be fully described by an eddy-driven export parameterization. It is also important to note there is a significant contribution to $\langle w'C' \rangle$ from gravitational sinking, which is neglected in our model for the time-being. The sinking flux could be a larger fraction than eddy fluxes, and better quantifying both components in upwelling systems is necessary to determine their relative contributions. Here, we focus finding ways to enable more direct estimates of the eddy-driven component of $\langle w'C' \rangle$ from observations. We propose an approach for estimating the vertical phytoplankton carbon biomass flux by separately estimating w from surface and density profile observations using a CNN, and then estimating C' from surface measurements of phytoplankton, similar to what might be available from remote-sensing observations. Our simplistic method for estimating C' only works well above the depth of the offshore DCM and in the nearshore $\sim$30 km where phytoplankton blooms have a surface signature. However, there is a lot of potential for improving estimates of C'.

There are more sophisticated algorithms for predicting subsurface chlorophyll pro-

files from surface data with more accuracy. An example is the method of Uitz et al. (2006), which consists of multiple steps of first sorting vertical chlorophyll-a profiles into different trophic categories based on their near-surface chlorophyll-a, and empirically fitting a Gaussian that varies depending on the trophic categories. This method perhaps may be able to better distinguish between the different chlorophyll-a profiles onshore and offshore, which should be treated differently. In addition, there is a new dataset of global 3D vertical particulate organic carbon and chlorophyll-a that was created using neural network trained on a combination of satellite and Argo data (Sauzède et al. 2016; Sauzède et al. 2021). This dataset is available on a 0.25° grid and at weekly resolution, which is too coarse for evaluating $\langle w'C' \rangle$ at the submesoscales. But, it is conceivable to learn from how they trained their neural network and apply a similar method to finer scale data. For instance, as input data, they use the surface remote sensing reflectance at five wavelengths, sea level anomaly, PAR, vertical profiles of temperature, salinity, N^2, the mixed layer depth, as well as the day of year and longitude/latitude coordinates. This indicates that having a lot of vertical profile information (full vertical profiles of temperature, salinity, in addition the mixed layer depth and N^2) is important, and we cannot get away with relying on just surface measurements alone. With the advent of more biogeochemical profiling instruments such as BGC-Argo (Argo 2023), and high-resolution profiling instruments such as the EcoCTD (Dever et al. 2020), it is possible to obtain more vertical profile data of physical and biological fields at the smaller scales, which is promising for applying methods such as that of (Sauzède et al. 2016) to predicting phytoplankton and POC subsurface.

5.A Appendix

Supporting Information for "Vertical transport of nutrients and phytoplankton in an upwelling system"

5.B Cruise observations

The modeling, particularly the biological model, is inspired by and based off of observations made about 100 km off the coast of San Francisco during two field campaigns as part of the NASA EVS-3 Submesoscale Ocean Dynamics Experiment (S-MODE) (Farrar et al. 2020). S-MODE is focused on the role of submesoscale dynamics on the vertical transport in the upper ocean. The first field campaign took place from Oct. 19–Nov. 6, 2021, and the second campaign occurred Oct. 3–Nov. 4, 2022. Observations that informed our modeling include underway nitrate measurements from an Optical UV nitrate sensor (SUNA) that measured near-surface nitrate concentration from the ship's flow through, which was calibrated against nutrients water samples taken from the underway system. In addition, underway profiling from the ship with an Eco-CTD (Dever et al. 2020) allowed for transects with high resolution (< 1 km) profiles of temperature, salinity, dissolved oxygen, and bio-optical properties including chlorophyll-a fluorescence, photosynthetically active radiation (PAR), and backscatter.

5.C Additional model information

Wind forcing: Wind velocity data are from the Cross-Calibrated Multi-Platform (CCMP) Ocean Surface Wind Vector Analyses data set (Atlas et al. 2011). The CCMP wind product integrates wind observations from multiple radiometers and scatterometers with a reanalysis wind field, and the data are available on a 0.25 grid at a 6-hour resolution. Wind stress is from the wind velocities following Large and Pond (1981). The alongshore component of wind stress that drives coastal upwelling

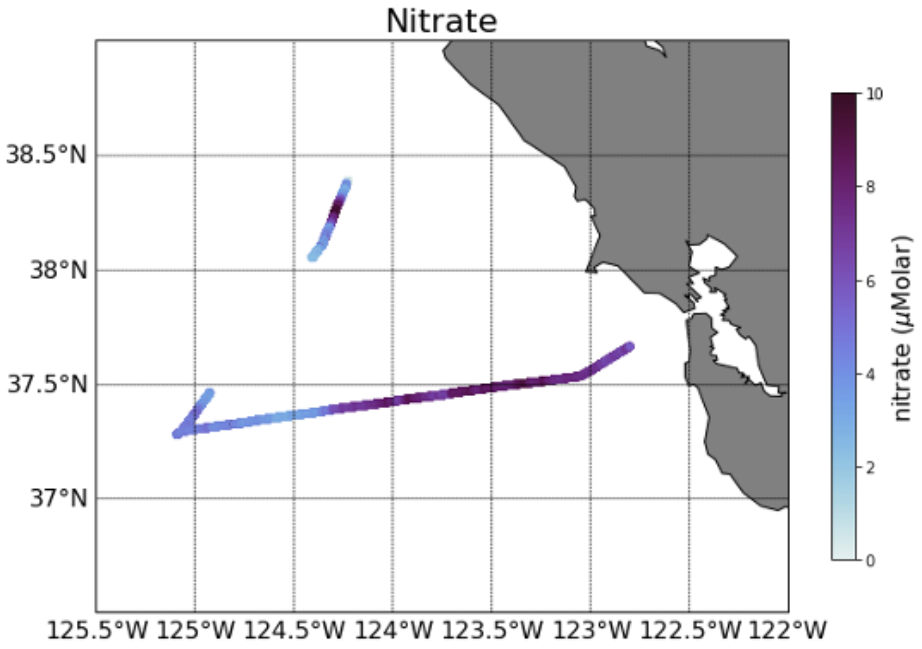

Figure 5-12: Surface nitrate off the coast of California measured on Oct. 22, 2021.

can be calculated as $\tau^{||} = \tau^x cos\theta + \tau^y sin\theta$, where (τ^x, τ^y) are the east-west and north-south components of the wind stress, respectively, and θ is the angle the coast makes with the equator. We take $\theta = -45°$ here to obtain the Northwest component of the wind stress, which is approximately the upwelling-favorable direction off the coast of California. We use a year's worth of wind data from 2017, and average the wind stress in a box from 125–115° W and 29–36° N (Fig. 5-13). During the upwelling season from March to October, the mean NW wind stress is about 0.05 N m^{-2} and is nearly always positive, which is the upwelling-favorable direction (Fig. 5-13). The 6-hourly wind stress is linearly interpolated to the numerical model time step of 108 s to force the model.

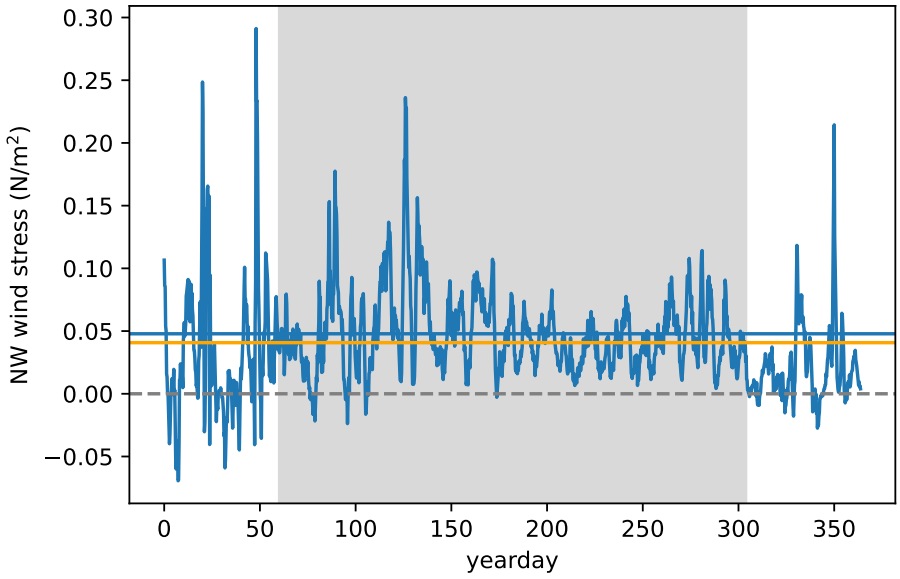

Figure 5-13: Average northwest wind stress timeseries off the coast of California in 2017. The upwelling season from March to October is shaded in gray, and the horizontal blue line indicates the average NW wind stress during the upwelling season. The orange line indicates the annual mean, and the dashed gray horizontal line is at zero.

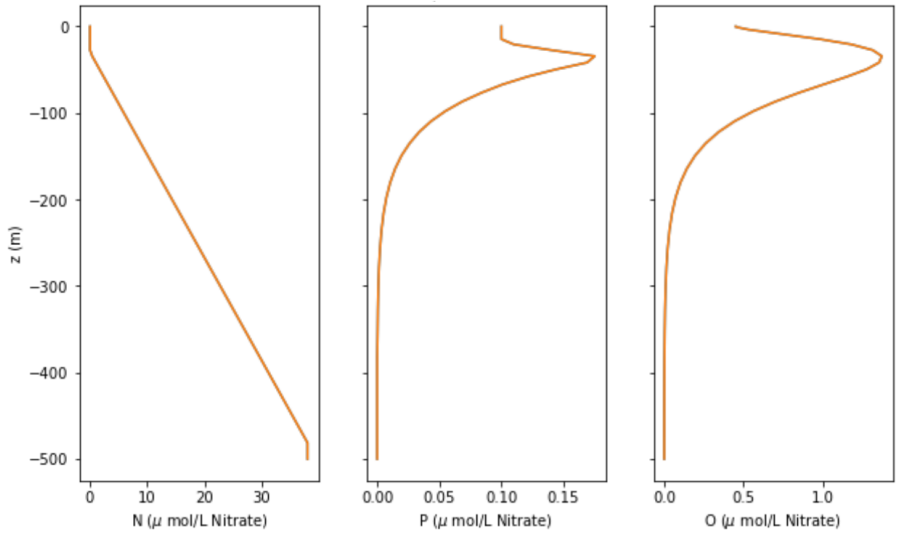

Figure 5-14: Initial conditions for nitrate, phytoplankton, and ammonium.

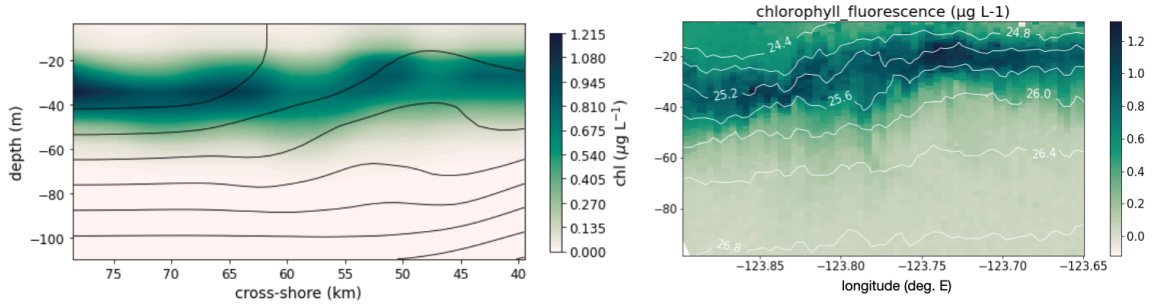

Figure 5-15: Comparison of model transect of chlorophyll-a (left) with observed transect from an Eco-CTD (right). The simulation shown is forced with winds starting September 1, and day 50 of the run is shown. The Eco-CTD observations are from November 2021. The transect is from 40–80 km offshore, while Eco-CTD transect is located about 100 km offshore of California. Black lines show the isopycals, and the contour interval shown is 0.4 kg m^{-3} to match the contour interval in the Eco-CTD transect.

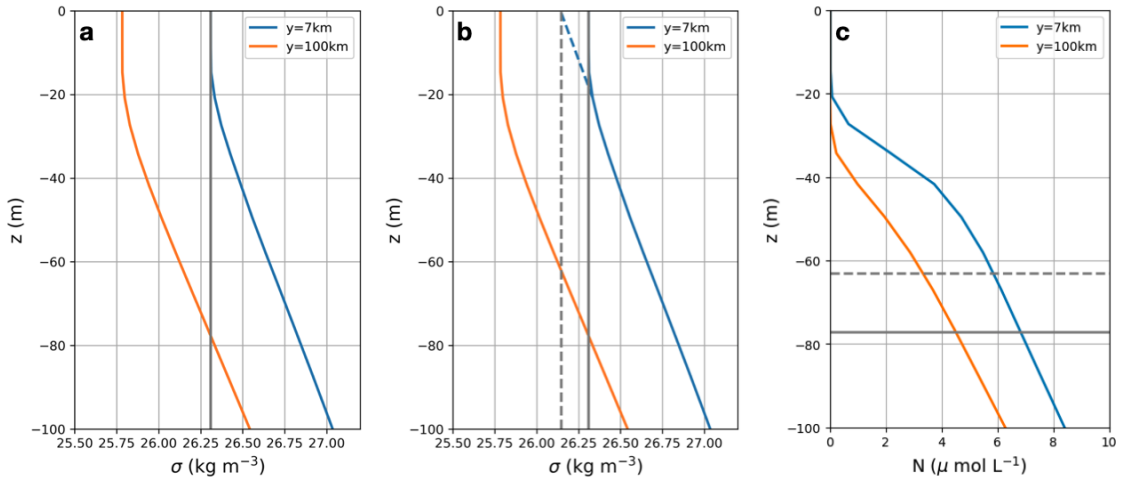

Figure 5-16: a) Example of inshore (y=7 km) and offshore (y = 100 km) density profiles from the center of the model domain at x = 48 km. The vertical gray line shows where ρ in the offshore profile matches the surface density in the inshore profile. b) Same as (a), but the dashed blue line shows what the inshore density profile would be if the surface was not mixed. The dashed gray line now indicates where the offshore ρ profile now matches the new inshore surface ρ value. c) Nitrate profiles from the same location as the 2 density profiles. Solid and gray dashed lines show the source depths estimated from (a) and (b). The offshore nitrate profile is used for the upwelled N concentration, since using the inshore values led to a large over-estimation of $\langle wN \rangle$.

Chapter 6

Conclusion

This thesis focuses on physical dynamics that play an important role in the ocean carbon cycle by controlling bottom-up limitation of phytoplankton growth, exporting carbon out of the surface ocean, and rapidly dispersing biogeochemical tracers. Particular emphasis is placed on coastal upwelling systems, which are some of the most biologically productive and ecologically diverse ecosystems in the ocean. This work contributes to improving fundamental estimates and understanding of vertical nutrient transport and carbon export in coastal upwelling systems (Chapters 3, 4, 5), which ultimately may lead to better quantification of the ocean's natural biological carbon pump. At the same time, climate change requires immediate action, and studies of negative emissions technologies needs to happen in parallel with basic science research. Thus, this thesis also explores the feasibility and practical constraints of coastal ocean alkalinity enhancement as a carbon dioxide removal (CDR) method (Chapter 2). Below, I summarize the main findings from each chapter and discuss remaining open questions and avenues of future research.

6.1 Summary

In Chapter 2, we use a mesoscale-permitting global ocean model to investigate the limits and potential of near-shore ocean alkalinity enhancement (OAE) strategies. We find that local ocean dynamics are crucial for determining the optimal alkalinity addition locations that maximize carbon removal, while avoiding potential adverse environmental impacts. Generally, we find that coastal upwelling regions can sustain

relatively high rates of alkalinity addition because the offshore Ekman transport is an effective way to quickly disperse alkalinity to the open ocean. Another aspect of maximizing carbon uptake is to identify regions with high CO_2 uptake efficiencies, defined as mols of carbon removed from the atmosphere per mol of alkalinity added. We find that upwelling systems also have relatively high uptake efficiencies, because Ekman transport mainly advects the alkalinity horizontally and it remains near the surface ocean. However, potential impacts to the rich ecosystems of upwelling systems need to be further studied before any at-scale deployment of OAE should be considered.

In Chapter 3, we turn our focus to coastal upwelling systems and sought to improve understanding of what sets the steady state upwelling source depth. By expanding beyond a traditional two-dimensional view of steady coastal upwelling and allowing for variability in the alongshore direction, we find that the baroclinic instability of the upwelling front is important for determining what depth water is upwelling from. We obtain a scaling relation for the source depth by balancing the wind-driven upwelling process with eddy restratification as a result of baroclinic instabilities. The source depth increases nonlinearly with the wind and decreases with higher stratification, and we test this theory rigorously in a numerical process-study ocean model. These findings have implications for the nutrient content of upwelled waters and consequently the nutrient flux and new production rates in coastal upwelling systems, and how they might be affected by climate change.

Next, in Chapter 4, we take a closer look the enhanced submesoscale vertical velocities found at an upwelling front in a high resolution (1 km) numerical ocean model. At the submesoscales, vertical velocities w are enhanced at fine-scale fronts, eddies, and filaments and can reach $\mathcal{O}(100\ \mathrm{m\ d^{-1}})$. These submesoscale vertical velocities can lead to enhanced vertical transport of nutrients or carbon, but they are very difficult to measure. We demonstrate that machine learning models may be effective tools for linking more readily observable surface ocean data with vertical velocities subsurface. In particular, convolutional neural networks are relatively robust to noisy input data compared to Random Forest or Multiple Linear Regression models. This work

shows promise for diagnosing the 3D submesoscale w field using remotely-observable surface ocean measurements, such as surface density, horizontal velocities, and their gradients. This motivates existing and future satellite missions for high-resolution remote-sensing of surface ocean horizontal velocities, and further development of machine learning methods to apply to real ocean observations is needed.

Chapters 3 and 4 aim to improve upon the physical aspects of vertical transport, and we apply these findings in Chapter 5 to evaluate nutrient and carbon fluxes in an upwelling system. We couple a nutrient-phytoplankton model, with two pools of nutrients representing "new" and "old" (or regenerated) nutrients, to our process model of an upwelling system. We find that the vertical nutrient flux is well captured by Ekman transport and a time-varying source depth given by the scaling from Chapter 3. This may help improve new production estimates in coastal upwelling regions, but more work is needed to first evaluate the applicability of this to observations. On the other hand, vertical eddy-driven phytoplankton carbon biomass flux is more difficult to predict, because it requires resolving not only the submesoscale vertical velocity field, but also the spatially-varying carbon field at depth. There is room for progress to be made by using vertical velocities obtained from machine learning with improved carbon estimates following methods of Uitz et al. (2006) or Sauzède et al. (2016), for example.

6.2 Outlook

This thesis uses a variety of models as experimental test beds in which we evaluate theories, and simulate realistic and idealized scenarios. Some of the models used are based on equations describing known physics or biology (Chapters 2, 3, 5), while other models are purely statistical and are based on large amounts of data (Chapters 4). To the best of our abilities, the models are tethered to real-world data, such as through using realistic initial conditions and forcing fields, or designed to recreate ocean observations. We primarily use models as a safe place to explore new ideas in, but key questions and avenues for future work revolve around how we can extend the

findings from this thesis to the real world, and move from theory towards practice.

For instance in Chapter 2, a global ocean model provides insight into the spatial variability of coastal OAE limitations and effectiveness, but there are still many remaining questions. The global model can tell us which regions might be promising places to focus on for OAE, but there are many important processes that are not resolved (in our case, the horizontal grid resolution of ~ 30 km is significantly larger than any realistic OAE project). Thus, regional models that can more realistically resolve smaller scale near-shore processes and topography are needed. Another big challenge in the space of OAE and other emerging marine carbon dioxide removal (CDR) technologies revolve around measurement, verification, and reporting (MRV). Models will no doubt be important MRV tools for OAE because the carbon uptake occurs over extremely large areas in the ocean, and tracking exactly where the alkalinity is dispersed to will be very difficult to do from measurements alone. Moreover, models are useful tools for demonstrating additionality of carbon removed, since we can easily quantify and compare CO_2 fluxes in a simulation with and without any OAE. Other big remaining questions of OAE include what are the uncertainties in the amount of carbon removed, and what are the potential negative consequences? I am hopeful that the Carbon Dioxide Removal Model Intercomparison Project (CDR-MIP) will be a useful tool to help answer some of these questions (Keller et al. 2018b). In addition, expanded ocean biogeochemical observations and monitoring will continue to be crucial, as well as more laboratory, microcosm, and mesocosm experiments to assess biological impacts.

Throughout this thesis, we also use a more simplified process-study model to test theories and ideas about the vertical transport of nutrients and carbon in coastal upwelling regions (Chapters 3, 4, 5). In science, we often like to simplify problems as much as possible in the hopes of finding elegant solutions and to gain explainability, but there is the risk that the simplified system is not necessarily an accurate reflection of reality. In Chapter 3, we use this idealized model to evaluate a theory for the upwelled source depth. For simplicity, we neglect other factors that may impact upwelling and source depth, such as bottom topography, uneven coastlines, β, coastal

waves, or intermittency of winds. As a result, while we find that the theory holds up in an idealized numerical model designed to capture the minimal processes necessary for setting up the source depth, more work is needed to assess how applicable the theory is in the real ocean, which is always more complex. We saw in Chapter 5 that the source depth scaling can be adapted to be used with realistic time-varying winds, and other modifications are likely needed for different scenarios. A next step can be to use a global ocean model or a more realistic regional model that has topography and realistic atmospheric forcing to evaluate the source depth and find where the scaling might break down. The eventual goal would be to evaluate upwelling source depth from observations, but in order to do so, we also need to distinguish between the effects of vertical mixing from upwelling.

Besides numerical models representing known physics, we also use machine learning models that require an abundance of data (Chapters 4 and 5). We are currently in the era of big ocean data, with more data arriving every day from satellites, Argo floats, and other autonomous ocean instruments. This presents opportunities for utilizing big data tools that previously may not have been applicable to oceanographic data sets. One such possibility that we envision is using surface observations to diagnose the full 3D submesoscale vertical velocity field, and to use that for estimating eddy-driven carbon export fluxes. We make progress towards this vision by demonstrating that machine learning models can indeed diagnose submesoscale vertical velocities much better than pre-existing methods in an idealized numerical model of an upwelling system. Questions remain regarding how to train machine learning models on real ocean data for predicting vertical velocities, as vertical velocity measurements are still very sparse. One potential avenue to explore is transfer learning, where the majority of the training is done using simulated data from ocean models, but then a smaller amount of real observations are used to fine-tune the machine learning model.

It is important to note that all of the modeling work presented are motivated and influenced by observations, which raise questions and present opportunities that we can further explore with models. Observations are also critical for informing model design and evaluating models, and models can further inform observational strategies.

The ocean is still severely under-sampled, and it is crucial to continue investing in more measurements and monitoring of ocean physics and biogeochemistry.

References

Albright, R., and Coauthors, 2016: Reversal of ocean acidification enhances net coral reef calcification. *Nature*, **531 (7594)**, 362–365, doi: 10.1038/nature17155.

Allen, J. S., P. A. Newberger, and J. Federiuk, 1995: Upwelling Circulation on the Oregon Continental Shelf. Part I: Response to Idealized Forcing. *Journal of Physical Oceanography*, **25 (8)**, 1843 – 1866, doi: 10.1175/1520-0485(1995)025<1843:UCOTOC>2.0.CO;2.

Andrews, D. G., and M. E. McIntyre, 1976: Planetary Waves in Horizontal and Vertical Shear: The Generalized Eliassen-Palm Relation and the Mean Zonal Acceleration. *Journal of the Atmospheric Sciences*, **33 (11)**, 2031–2048, doi: 10.1175/1520-0469(1976)033<2031:pwihav>2.0.co;2.

Archer, D., and Coauthors, 2009: Atmospheric lifetime of fossil fuel carbon dioxide. *Annual Review of Earth and Planetary Sciences*, **37 (1)**, 117–134, doi: 10.1146/annurev.earth.031208.100206.

Archibald, K. M., D. A. Siegel, and S. C. Doney, 2019: Modeling the impact of zooplankton diel vertical migration on the carbon export flux of the biological pump. *Global Biogeochemical Cycles*, **33 (2)**, 181–199, doi: 10.1029/2018GB005983.

Argo, 2023: Argo float data and metadata from Global Data Assembly Centre (Argo GDAC). *SEANOE*, doi: 10.17882/42182.

Atlas, R., R. N. Hoffman, J. Ardizzone, S. M. Leidner, J. C. Jusem, D. K. Smith, and D. Gombos, 2011: A Cross-calibrated, Multiplatform Ocean Surface Wind Velocity Product for Meteorological and Oceanographic Applications. *Bulletin of the American Meteorological Society*, **92 (2)**, 157–174, doi: 10.1175/2010BAMS2946.1.

Auad, G., A. Miller, and E. Di Lorenzo, 2006: Long-term forecast of oceanic conditions off California and their biological implications. *Journal of Geophysical Research: Oceans*, **111 (C9)**, doi: 10.1029/2005JC003219.

Bach, L. T., S. J. Gill, R. E. M. Rickaby, S. Gore, and P. Renforth, 2019: CO_2 Removal With Enhanced Weathering and Ocean Alkalinity Enhancement: Potential Risks and Co-benefits for Marine Pelagic Ecosystems. *Frontiers in Climate*, **1**, doi: 10.3389/fclim.2019.00007.

Bakun, A., 1973: Global climate change and intensification of coastal ocean upwelling. *U.S. Department of Commerce. National Oceanic and Atmospheric Administration, NOAA Technical Report NMFS SSRF-671*, 103.

Bakun, A., 1990: Global Climate Change and Intensification of Coastal Ocean Upwelling. *Science*, **247 (4939)**, 198–201, doi: 10.1126/science.247.4939.198.

Bograd, S. J., and R. J. Lynn, 2003: Long-term variability in the Southern California Current System. *Deep Sea Research Part II: Topical Studies in Oceanography*, **50 (14)**, 2355–2370, doi: 10.1016/S0967-0645(03)00131-0, CalCOFI: A Half Century of Physical, Chemical and Biological Research in the California Current System.

Bolton, T., and L. Zanna, 2019: Applications of Deep Learning to Ocean Data Inference and Subgrid Parameterization. *Journal of Advances in Modeling Earth Systems*, **11 (1)**, 376–399, doi: 10.1029/2018MS001472.

Boyd, P. W., H. Claustre, M. Levy, D. A. Siegel, and T. Weber, 2019: Multi-faceted particle pumps drive carbon sequestration in the ocean. *Nature*, **568 (7752)**, 327–335, doi: 10.1038/s41586-019-1098-2.

Boyd, P. W., and Coauthors, 2007: Mesoscale iron enrichment experiments 1993-2005: synthesis and future directions. *Science*, **315 (5812)**, 612–617, doi: 10.1126/science.1131669.

Breiman, L., 2001: Random Forests. *Machine Learning*, **45 (1)**, 5–32, doi: 10.1023/A:1010933404324.

Brink, K., 1983: The near-surface dynamics of coastal upwelling. *Progress in Oceanography*, **12 (3)**, 223–257, doi: 10.1016/0079-6611(83)90009-5.

Brink, K. H., 2016: Continental Shelf Baroclinic Instability. Part I: Relaxation from Upwelling or Downwelling. *Journal of Physical Oceanography*, **46 (2)**, 551 – 568, doi: 10.1175/JPO-D-15-0047.1.

Brink, K. H., and H. Seo, 2016: Continental Shelf Baroclinic Instability. Part II: Oscillating Wind Forcing. *Journal of Physical Oceanography*, **46 (2)**, 569 – 582, doi: 10.1175/JPO-D-15-0048.1.

Burt, D. J., F. Fröb, and T. Ilyina, 2021: The sensitivity of the marine carbonate system to regional ocean alkalinity enhancement. *Frontiers in Climate*, **3**, doi: 10.3389/fclim.2021.624075.

Byrne, C., R. Law, P. Hudson, J. Thain, and T. Fileman, 1988: Measurements of the dispersion of liquid industrial waste discharged into the wake of a dumping vessel. *Water Research*, **22 (12)**, 1577–1584, doi: 10.1016/0043-1354(88)90171-6.

Capet, X. J., P. Marchesiello, and J. C. McWilliams, 2004: Upwelling response to coastal wind profiles. *Geophysical Research Letters*, **31 (13)**, doi: 10.1029/2004GL020123.

Capet, X. J., J. C. McWilliams, M. J. Molemaker, and A. F. Shchepetkin, 2008: Mesoscale to submesoscale transition in the California Current System. Part II: Frontal processes. *Journal of Physical Oceanography*, **38 (1)**, 44 – 64, doi: 10.1175/2007JPO3672.1.

Carmack, E. C., and K. Aagaard, 1977: A note on volumetric considerations of upwelling in the Benguela Current. *Estuarine and Coastal Marine Science*, **5 (1)**, 135–142, doi: 10.1016/0302-3524(77)90078-0.

Carr, M.-E., 2001: Estimation of potential productivity in Eastern Boundary Currents using remote sensing. *Deep Sea Research Part II: Topical Studies in Oceanography*, **49 (1)**, 59–80, doi: 10.1016/S0967-0645(01)00094-7.

Carr, M.-E., and E. J. Kearns, 2003: Production regimes in four Eastern Boundary Current systems. *Deep Sea Research Part II: Topical Studies in Oceanography*, **50 (22)**, 3199–3221, doi: 10.1016/j.dsr2.2003.07.015.

Carroll, D., and Coauthors, 2020: The ECCO-Darwin Data-Assimilative Global Ocean Biogeochemistry Model: Estimates of Seasonal to Multidecadal Surface Ocean pCO_2 and Air-Sea CO_2 Flux. *Journal of Advances in Modeling Earth Systems*, **12 (10)**, doi: 10.1029/2019MS001888.

Carroll, D., and Coauthors, 2022: Attribution of Space-Time Variability in Global-Ocean Dissolved Inorganic Carbon. *Global Biogeochemical Cycles*, **36 (3)**, doi: 10.1029/2021GB007162.

Cerovečki, I., R. A. Plumb, and W. Heres, 2009: Eddy Transport and Mixing in a Wind- and Buoyancy-Driven Jet on the Sphere. *Journal of Physical Oceanography*, **39 (5)**, 1133–1149, doi: 10.1175/2008JPO3596.1.

Cessi, P., 1996: Gridscale instability of convective-adjustment schemes. *Journal of Marne Research*, **54 (3)**, 407–420, doi: 10.1357/0022240963213529.

Chabert, P., F. d'Ovidio, V. Echevin, M. Stukel, and M. D. Ohman, 2021: Cross-shore flow and implications for Carbon Export in the California Current Ecosystem: a Lagrangian analysis. *Journal of Geophysical Research: Oceans*, **126 (2)**, e2020JC016 611, doi: 10.1029/2020JC016611.

Chapman, C., and A. A. Charantonis, 2017: Reconstruction of subsurface velocities from satellite observations using iterative self-organizing maps. *IEEE Geoscience and Remote Sensing Letters*, **14 (5)**, 617–620, doi: 10.1109/LGRS.2017.2665603.

Chavez, F. P., and M. Messié, 2009: A comparison of Eastern Boundary Upwelling Ecosystems. *Progress in Oceanography*, **83 (1-4)**, 80–96, doi: 10.1016/j.pocean.2009.07.032.

Chavez, F. P., and J. R. Toggweiler, 1995: Physical estimates of global new production: The upwelling contribution. *Upwelling in the Ocean: Modeling Processes and Ancient Records*, C. P. S. et al, Ed., John Wiley, Hoboken, N. J., 313–320.

Chhak, K., and E. D. Lorenzo, 2007: Decadal variations in the California Current upwelling cells. *Geophysical Research Letters*, **34 (14)**, doi: 10.1029/2007GL030203.

Choboter, P. F., D. Duke, J. P. Horton, and P. Sinz, 2011: Exact solutions of wind-driven coastal upwelling and downwelling over sloping topography. *Journal of Physical Oceanography*, **41 (7)**, 1277 – 1296, doi: 10.1175/2011JPO4527.1.

Chou, H.-T., 1996: On the dilution of liquid waste in ships' wakes. *Journal of Marine Science Technology*, **1**, 149–154, doi: 10.1007/BF02391175.

Dall'Olmo, G., J. Dingle, L. Polimene, R. J. Brewin, and H. Claustre, 2016: Substantial energy input to the mesopelagic ecosystem from the seasonal mixed-layer pump. *Nature Geoscience*, **9 (11)**, 820–823, doi: 10.1038/ngeo2818.

Davies, P. A., Q. Yuan, and R. De Richter, 2018: Desalination as a negative emissions technology. *Environmental Science: Water Research & Technology*, **4 (6)**, 839–850, doi: 10.1039/C7EW00502D.

De Baar, H. J., and Coauthors, 2005: Synthesis of iron fertilization experiments: from the iron age in the age of enlightenment. *Journal of Geophysical Research: Oceans*, **110 (C9)**, doi: 10.1029/2004JC002601.

de Lannoy, C.-F., M. D. Eisaman, A. Jose, S. D. Karnitz, R. W. DeVaul, K. Hannun, and J. L. Rivest, 2018: Indirect ocean capture of atmospheric CO_2: Part I. Prototype of a negative emissions technology. *International Journal of Greenhouse Gas Control*, **70**, 243–253, doi: 10.1016/j.ijggc.2017.10.007.

deCastro, M., M. C. Sousa, F. Santos, J. M. Dias, and M. Gómez-Gesteira, 2016: How will Somali coastal upwelling evolve under future warming scenarios? *Scientific Reports*, **6 (1)**, doi: 10.1038/srep30137.

Dee, D. P., and Coauthors, 2011: The ERA-Interim reanalysis: configuration and performance of the data assimilation system. *Quarterly Journal of the Royal Meteorological Society*, **137 (656)**, 553–597, doi: 10.1002/qj.828.

Deutsch, C., and Coauthors, 2021: Biogeochemical variability in the California Current system. *Progress in Oceanography*, **196**, 102 565, doi: 10.1016/j.pocean.2021.102565.

Dever, E., C. Dorman, and J. Largier, 2006: Surface boundary-layer variability off northern california, usa, during upwelling. *Deep Sea Research Part II: Topical Studies in Oceanography*, **53 (25)**, 2887–2905, doi: 10.1016/j.dsr2.2006.09.001, the Role of Wind-Driven Flow in Shelf Productivity.

Dever, M., M. Freilich, J. T. Farrar, B. Hodges, T. Lanagan, A. J. Baron, and A. Mahadevan, 2020: Ecoctd for profiling oceanic physical–biological properties from an underway ship. *Journal of Atmospheric and Oceanic Technology*, **37 (5)**, 825–840.

Di Lorenzo, E., and Coauthors, 2008: North Pacific Gyre Oscillation links ocean climate and ecosystem change. *Geophysical Research Letters*, **35 (8)**, doi: 10.1029/2007GL032838.

Digdaya, I. A., I. Sullivan, M. Lin, L. Han, W.-H. Cheng, H. A. Atwater, and C. Xiang, 2020: A direct coupled electrochemical system for capture and conversion of CO_2 from oceanwater. *Nature communications*, **11 (1)**, 1–10, doi: 10.1038/s41467-020-18232-y.

Doney, S. C., V. J. Fabry, R. A. Feely, and J. A. Kleypas, 2009: Ocean Acidification: The Other CO_2 Problem. *Annual Review of Marine Science*, **1 (1)**, 169–192, doi: 10.1146/annurev.marine.010908.163834, pMID: 21141034.

Dortch, Q., 1990: The interaction between ammonium and nitrate uptake in phytoplankton. *Marine ecology progress series. Oldendorf*, **61 (1)**, 183–201.

Dugdale, R. C., and J. J. Goering, 1967: Uptake of New and Regenerated Forms of Nitrogen in Primary Productivity1. *Limnology and Oceanography*, **12 (2)**, 196–206, doi: 10.4319/lo.1967.12.2.0196.

Durski, S. M., and J. Allen, 2005: Finite-amplitude evolution of instabilities associated with the coastal upwelling front. *Journal of physical oceanography*, **35 (9)**, 1606–1628, doi: 10.1175/JPO2762.1.

Dutkiewicz, S., A. P. Sokolov, J. Scott, and P. H. Stone, 2005: A three-dimensional ocean-seaice-carbon cycle model and its coupling to a two-dimensional atmospheric model: uses in climate change studies.

D'Asaro, E. A., and Coauthors, 2018: Ocean convergence and the dispersion of flotsam. *Proceedings of the National Academy of Sciences*, **115 (6)**, 1162–1167, doi: 10.1073/pnas.1718453115.

Ebbesmeyer, C. C., and W. J. Ingraham Jr, 1994: Pacific toy spill fuels ocean current pathways research. *Eos, Transactions American Geophysical Union*, **75 (37)**, 425–430, doi: 10.1029/94EO01056.

Eisaman, M. D., J. L. Rivest, S. D. Karnitz, C.-F. de Lannoy, A. Jose, R. W. DeVaul, and K. Hannun, 2018: Indirect ocean capture of atmospheric co$_2$: Part ii. understanding the cost of negative emissions. *International Journal of Greenhouse Gas Control*, **70**, 254–261, doi: 10.1016/j.ijggc.2018.02.020.

Ekman, V. W., 1905: On the influence of the earth's rotation on ocean-currents.

Enriquez, A. G., and C. A. Friehe, 1995: Effects of wind stress and wind stress curl variability on coastal upwelling. *Journal of Physical Oceanography*, **25 (7)**, 1651–1671, doi: 10.1175/1520-0485(1995)025<1651:EOWSAW>2.0.CO;2.

Eppley, R. W., and B. J. Peterson, 1979: Particulate organic matter flux and planktonic new production in the deep ocean. *Nature*, **282 (5740)**, 677–680, doi: 10.1038/282677a0.

Eppley, R. W., E. Render, W. Harrison, and J. Cullen, 1979: Ammonium distribution in southern California coastal waters and its role in the growth of phytoplankton 1. *Limnology and Oceanography*, **24 (3)**, 495–509, doi: 10.4319/lo.1979.24.3.0495.

Estrade, P., P. Marchesiello, A. C. De Verdière, and C. Roy, 2008: Cross-shelf structure of coastal upwelling: A two dimensional extension of Ekman's theory and a mechanism for inner shelf upwelling shut down. *Journal of Marine Research*, **66 (5)**, 589–616, doi: 10.1357/002224008787536790.

Fakhraee, M., Z. Li, N. Planavsky, and C. Reinhard, 2022: Environmental impacts and carbon capture potential of ocean alkalinity enhancement. *Research Square*, doi: 10.1016/j.ijggc.2018.02.020, Preprint.

Farrar, J. T., and Coauthors, 2020: S-MODE: The Sub-Mesoscale Ocean Dynamics Experiment. *IGARSS 2020 - 2020 IEEE International Geoscience and Remote Sensing Symposium*, 3533–3536, doi: 10.1109/IGARSS39084.2020.9323112.

Fassbender, A. J., J. C. Orr, and A. G. Dickson, 2021: Technical note: Interpreting pH changes. *Biogeosciences*, **18 (4)**, 1407–1415, doi: 10.5194/bg-18-1407-2021.

Feely, R. A., C. L. Sabine, J. M. Hernandez-Ayon, D. Ianson, and B. Hales, 2008: Evidence for upwelling of corrosive "acidified" water onto the continental shelf. *Science*, **320 (5882)**, 1490–1492, doi: 10.1126/science.1155676.

Feng, E. Y., D. P. Keller, W. Koeve, and A. Oschlies, 2016: Could artificial ocean alkalinization protect tropical coral ecosystems from ocean acidification? *Environmental Research Letters*, **11 (7)**, 074 008, doi: 10.1088/1748-9326/11/7/074008.

Feng, E. Y., W. Koeve, D. P. Keller, and A. Oschlies, 2017: Model-based assessment of the co_2 sequestration potential of coastal ocean alkalinization. *Earth's Future*, **5 (12)**, 1252–1266, doi: 10.1002/2017EF000659.

Ferderer, A., Z. Chase, F. Kennedy, K. G. Schulz, and L. T. Bach, 2022: Assessing the influence of ocean alkalinity enhancement on a coastal phytoplankton community. *Biogeosciences*, **19 (23)**, 5375–5399, doi: 10.5194/bg-19-5375-2022.

Fountain, H., 2012: A rogue climate experiment outrages scientists. *The New York Times*.

Fox-Kemper, B., and R. Ferrari, 2008: Parameterization of Mixed Layer Eddies. Part II: Prognosis and Impact. *Journal of Physical Oceanography*, **38 (6)**, 1166–1179, doi: 10.1175/2007JPO3788.1.

Fox-Kemper, B., R. Ferrari, and R. Hallberg, 2008: Parameterization of Mixed Layer Eddies. Part I: Theory and Diagnosis. *Journal of Physical Oceanography*, **38 (6)**, 1145–1165, doi: 10.1175/2007JPO3792.1.

Franks, P. J., and L. J. Walstad, 1997: Phytoplankton patches at fronts: A model of formation and response to wind events. *Journal of Marine Research*, **55 (1)**, 1–29, doi: 10.1357/0022240973224472.

Freilich, M., and A. Mahadevan, 2021: Coherent pathways for subduction from the surface mixed layer at ocean fronts. *Journal of Geophysical Research: Oceans*, **126 (5)**, e2020JC017 042, doi: 10.1029/2020JC017042.

Freilich, M. A., G. Flierl, and A. Mahadevan, 2022: Diversity of Growth Rates Maximizes Phytoplankton Productivity in an Eddying Ocean. *Geophysical Research Letters*, **49 (3)**, e2021GL096 180, doi: 10.1029/2021GL096180.

Freilich, M. A., and A. Mahadevan, 2019: Decomposition of vertical velocity for nutrient transport in the upper ocean. *Journal of Physical Oceanography*, **49 (6)**, 1561 – 1575, doi: 10.1175/JPO-D-19-0002.1.

Friederich, G. E., J. Ledesma, O. Ulloa, and F. P. Chavez, 2008: Air–sea carbon dioxide fluxes in the coastal southeastern tropical Pacific. *Progress in Oceanography*, **79 (2)**, 156–166, doi: 10.1016/j.pocean.2008.10.001.

Friedlingstein, P., and Coauthors, 2022: Global carbon budget 2021. *Earth System Science Data*, **14 (4)**, 1917–2005, doi: 10.5194/essd-14-1917-2022.

Frischknecht, M., M. Münnich, and N. Gruber, 2018: Origin, transformation, and fate: The three-dimensional biological pump in the California Current System. *Journal of Geophysical Research: Oceans*, **123 (11)**, 7939–7962, doi: 10.1029/2018JC013934.

Frischknecht, M., M. Münnich, and N. Gruber, 2015: Remote versus local influence of ENSO on the California Current System. *Journal of Geophysical Research: Oceans*, **120 (2)**, 1353–1374, doi: 10.1002/2014JC010531.

Fu, L.-L., and C. Ubelmann, 2014: On the transition from profile altimeter to swath altimeter for observing global ocean surface topography. *Journal of Atmospheric and Oceanic Technology*, **31 (2)**, 560 – 568, doi: 10.1175/JTECH-D-13-00109.1.

Fuhr, M., S. Geilert, M. Schmidt, V. Liebetrau, C. Vogt, B. Ledwig, and K. Wallmann, 2022: Kinetics of olivine weathering in seawater: An experimental study. *Frontiers in Climate*, **4**, doi: 10.3389/fclim.2022.831587.

Gernon, T. M., T. K. Hincks, A. S. Merdith, E. J. Rohling, M. R. Palmer, G. L. Foster, C. P. Bataille, and R. D. Müller, 2021: Global chemical weathering dominated by continental arcs since the mid-palaeozoic. *Nature Geoscience*, **14 (9)**, 690–696, doi: 10.1038/s41561-021-00806-0.

Goldberg, D. S., T. Takahashi, and A. L. Slagle, 2008: Carbon dioxide sequestration in deep-sea basalt. *Proceedings of the National Academy of Sciences*, **105 (29)**, 9920–9925, doi: 10.1073/pnas.0804397105.

González, M. F., and T. Ilyina, 2016: Impacts of artificial ocean alkalinization on the carbon cycle and climate in earth system simulations. *Geophysical Research Letters*, **43 (12)**, 6493–6502, doi: 10.1002/2016GL068576.

Govekar, P. D., C. Griffin, and H. Beggs, 2022: Multi-Sensor Sea Surface Temperature Products from the Australian Bureau of Meteorology. *Remote Sensing*, **14 (15)**, doi: 10.3390/rs14153785.

Griffies, S. M., and R. W. Hallberg, 2000: Biharmonic friction with a smagorinsky-like viscosity for use in large-scale eddy-permitting ocean models. *Monthly Weather Review*, **128 (8)**, 2935 – 2946, doi: 10.1175/1520-0493(2000)128<2935:BFWASL>2.0.CO;2.

Gruber, N., Z. Lachkar, H. Frenzel, P. Marchesiello, M. Münnich, J. C. McWilliams, T. Nagai, and G.-K. Plattner, 2011: Eddy-induced reduction of biological production in eastern boundary upwelling systems. *Nature Geoscience*, **4 (11)**, 787–792, doi: 10.1038/ngeo1273.

Gruber, N., and Coauthors, 2019: The oceanic sink for anthropogenic CO_2 from 1994 to 2007. *Science*, **363 (6432)**, 1193–1199, doi: 10.1126/science.aau5153.

Guo, J. A., R. Strzepek, A. Willis, A. Ferderer, and L. T. Bach, 2022: Investigating the effect of nickel concentration on phytoplankton growth to assess potential side-effects of ocean alkalinity enhancement. *Biogeosciences*, **19 (15)**, 3683–3697, doi: 10.5194/bg-19-3683-2022.

Hales, B., T. Takahashi, and L. Bandstra, 2005: Atmospheric CO_2 uptake by a coastal upwelling system. *Global Biogeochemical Cycles*, **19 (1)**, doi: 10.1029/2004GB002295.

Hangx, S. J., and C. J. Spiers, 2009: Coastal spreading of olivine to control atmospheric co_2 concentrations: A critical analysis of viability. *International Journal of Greenhouse Gas Control*, **3 (6)**, 757–767, doi: 10.1016/j.ijggc.2009.07.001.

Hartmann, J., and Coauthors, 2022: Stability of alkalinity in Ocean Alkalinity Enhancement (OAE) approaches–consequences for durability of CO_2 storage. *Biogeosciences Discussions*, 1–29, doi: 10.5194/bg-2022-126, in review, 2022.

Hastie, T., R. Tibshirani, and J. Friedman, 2001: *The elements of statistical learning*. 2nd ed., Springer, New York, NY, USA.

He, J., and A. Mahadevan, 2021: How the source depth of coastal upwelling relates to stratification and wind. *Journal of Geophysical Research: Oceans*, **126 (12)**, e2021JC017 621, doi: 10.1029/2021JC017621.

He, J., and M. D. Tyka, 2023a: Limits and CO_2 equilibration of near-coast alkalinity enhancement. *Biogeosciences*, **20**, 27–43, doi: 10.5194/bg-20-27-2023.

He, J., and M. D. Tyka, 2023b: Limits and equilibration dynamics of near-coast alkalinity enhancement (version 0). *Zenodo*, doi: 10.5281/zenodo.7460358.

Held, I. M., and T. Schneider, 1999: The Surface Branch of the Zonally Averaged Mass Transport Circulation in the Troposphere. *Journal of the Atmospheric Sciences*, **56 (11)**, 1688–1697, doi: 10.1175/1520-0469(1999)056<1688:TSBOTZ>2.0.CO;2.

Hernández-Carrasco, I., V. Rossi, E. Hernández-García, V. Garçon, and C. López, 2014: The reduction of plankton biomass induced by mesoscale stirring: A modeling study in the Benguela upwelling. *Deep Sea Research Part I: Oceanographic Research Papers*, **83**, 65–80, doi: 10.1016/j.dsr.2013.09.003.

Hodges, B. A., and D. L. Rudnick, 2004: Simple models of steady deep maxima in chlorophyll and biomass. *Deep Sea Research Part I: Oceanographic Research Papers*, **51 (8)**, 999–1015, doi: 10.1016/j.dsr.2004.02.009.

House, K. Z., C. H. House, D. P. Schrag, and M. J. Aziz, 2007: Electrochemical acceleration of chemical weathering as an energetically feasible approach to mitigating anthropogenic climate change. *Environmental Science & Technology*, **41 (24)**, 8464–8470, doi: 10.1021/es0701816, pMID: 18200880.

Humphreys, M. P., A. J. Schiller, D. Sandborn, L. Gregor, D. Pierrot, S. M. A. C. van Heuven, E. R. Lewis, and D. W. R. Wallace, 2020: Pyco$_2$sys: marine carbonate system calculations in python (v1.8.1). *Zenodo*, doi: 10.5281/zenodo.6560756.

Huyer, A., 1983: Coastal upwelling in the California current system. *Progress in Oceanography*, **12 (3)**, 259–284.

Ilyina, T., D. Wolf-Gladrow, G. Munhoven, and C. Heinze, 2013: Assessing the potential of calcium-based artificial ocean alkalinization to mitigate rising atmospheric CO_2 and ocean acidification. *Geophysical Research Letters*, **40 (22)**, 5909–5914, doi: 10.1002/2013GL057981.

IMCO, 1975: Procedures and arrangements for the discharge of noxious liquid substances. method for calculation of dilution capacity in the ship's wake. *IMCO document MEPC III-7*.

IPCC, 2021: Climate Change 2021: The Physical Science Basis. Contribution of Working Group14 I to the Sixth Assessment Report of the Intergovernmental Panel on Climate Change; Technical Summary.

Isern-Fontanet, J., B. Chapron, G. Lapeyre, and P. Klein, 2006: Potential use of microwave sea surface temperatures for the estimation of ocean currents. *Geophysical Research Letters*, **33 (24)**, doi: 10.1029/2006GL027801.

Isern-Fontanet, J., G. Lapeyre, P. Klein, B. Chapron, and M. W. Hecht, 2008: Three-dimensional reconstruction of oceanic mesoscale currents from surface information. *Journal of Geophysical Research: Oceans*, **113 (C9)**, doi: 10.1029/2007JC004692.

Izumo, T., C. B. Montégut, J.-J. Luo, S. K. Behera, S. Masson, and T. Yamagata, 2008: The Role of the Western Arabian Sea Upwelling in Indian Monsoon Rainfall Variability. *Journal of Climate*, **21 (21)**, 5603–5623, doi: 10.1175/2008JCLI2158.1.

Jacox, M. G., S. J. Bograd, E. L. Hazen, and J. Fiechter, 2015a: Sensitivity of the California Current nutrient supply to wind, heat, and remote ocean forcing. *Geophysical Research Letters*, **42 (14)**, 5950–5957, doi: 10.1002/2015GL065147.

Jacox, M. G., and C. A. Edwards, 2011: Effects of stratification and shelf slope on nutrient supply in coastal upwelling regions. *Journal of Geophysical Research*, **116 (C3)**, doi: 10.1029/2010JC006547.

Jacox, M. G., and C. A. Edwards, 2012: Upwelling source depth in the presence of nearshore wind stress curl. *Journal of Geophysical Research: Oceans*, **117 (C5)**, doi: 10.1029/2011JC007856.

Jacox, M. G., C. A. Edwards, E. L. Hazen, and S. J. Bograd, 2018: Coastal Upwelling Revisited: Ekman, Bakun, and Improved Upwelling Indices for the U.S. West Coast. *Journal of Geophysical Research: Oceans*, **123 (10)**, 7332–7350, doi: 10.1029/2018JC014187.

Jacox, M. G., J. Fiechter, A. M. Moore, and C. A. Edwards, 2015b: ENSO and the California Current coastal upwelling response. *Journal of Geophysical Research: Oceans*, **120 (3)**, 1691–1702, doi: 10.1002/2014JC010650.

Jones, D. C., T. Ito, Y. Takano, and W.-C. Hsu, 2014: Spatial and seasonal variability of the air-sea equilibration timescale of carbon dioxide. *Global Biogeochemical Cycles*, **28 (11)**, 1163–1178, doi: 10.1002/2014GB004813.

Jones, S. D., C. Le Quéré, and C. Rödenbeck, 2012: Autocorrelation characteristics of surface ocean pCO_2 and air-sea CO_2 fluxes. *Global Biogeochemical Cycles*, **26 (2)**, doi: 10.1029/2010GB004017.

Kahru, M., E. Di Lorenzo, M. Manzano-Sarabia, and B. G. Mitchell, 2012: Spatial and temporal statistics of sea surface temperature and chlorophyll fronts in the California Current. *Journal of plankton research*, **34 (9)**, 749–760, doi: 10.1093/plankt/fbs010.

Kahru, M., R. M. Kudela, C. R. Anderson, M. Manzano-Sarabia, and B. G. Mitchell, 2014: Evaluation of Satellite Retrievals of Ocean Chlorophyll-a in the California Current. *Remote Sensing*, **6 (9)**, 8524–8540, doi: 10.3390/rs6098524.

Keller, D. P., E. Y. Feng, and A. Oschlies, 2014: Potential climate engineering effectiveness and side effects during a high carbon dioxide-emission scenario. *Nature communications*, **5 (1)**, 1–11, doi: 10.1038/ncomms4304.

Keller, D. P., A. Lenton, E. W. Littleton, A. Oschlies, V. Scott, and N. E. Vaughan, 2018a: The effects of carbon dioxide removal on the carbon cycle. *Current climate change reports*, **4 (3)**, 250–265, doi: 10.1007/s40641-018-0104-3.

Keller, D. P., and Coauthors, 2018b: The carbon dioxide removal model intercomparison project (CDRMIP): rationale and experimental protocol for CMIP6. *Geoscientific Model Development*, **11 (3)**, 1133–1160, doi: 10.5194/gmd-11-1133-2018.

Kheshgi, H. S., 1995: Sequestering atmospheric carbon dioxide by increasing ocean alkalinity. *Energy*, **20 (9)**, 915–922, doi: 10.1016/0360-5442(95)00035-F.

Kilpatrick, K., and Coauthors, 2015: A decade of sea surface temperature from modis. *Remote Sensing of Environment*, **165**, 27–41, doi: 10.1016/j.rse.2015.04.023.

Koračin, D., C. E. Dorman, and E. P. Dever, 2004: Coastal Perturbations of Marine-Layer Winds, Wind Stress, and Wind Stress Curl along California and Baja California in June 1999. *Journal of Physical Oceanography*, **34 (5)**, 1152–1173, doi: 10.1175/1520-0485(2004)034<1152:CPOMWW>2.0.CO;2.

Köhler, P., J. F. Abrams, C. Völker, J. Hauck, and D. A. Wolf-Gladrow, 2013: Geoengineering impact of open ocean dissolution of olivine on atmospheric CO_2, surface ocean pH and marine biology. *Environmental Research Letters*, **8 (1)**, 014 009, doi: 10.1088/1748-9326/8/1/014009.

LaCasce, J. H., and A. Mahadevan, 2006: Estimating subsurface horizontal and vertical velocities from sea-surface temperature. *Journal of Marine Research*, **64 (5)**, 695–721, doi: 10.1357/002224006779367267.

Lapeyre, G., and P. Klein, 2006: Dynamics of the upper oceanic layers in terms of surface quasigeostrophy theory. *Journal of Physical Oceanography*, **36 (2)**, 165 – 176, doi: 10.1175/JPO2840.1.

Large, W. G., and S. Pond, 1981: Open Ocean Momentum Flux Measurements in Moderate to Strong Winds. *Journal of Physical Oceanography*, **11 (3)**, 324–336, doi: 10.1175/1520-0485(1981)011<0324:OOMFMI>2.0.CO;2.

Lauvset, S. K., and Coauthors, 2016: A new global interior ocean mapped climatology: The 1× 1 GLODAP version 2. *Earth System Science Data*, **8 (2)**, 325–340, doi: 10.5194/essd-8-325-2016.

Lee, M.-M., D. P. Marshall, and R. G. Williams, 1997: On the eddy transfer of tracers: Advective or diffusive? *Journal of Marine Research*, **55 (3)**, 483–505, doi: 10.1357/0022240973224346.

Lentz, S. J., 1992: The surface boundary layer in coastal upwelling regions. *Journal of Physical Oceanography*, **22 (12)**, 1517 – 1539, doi: 10.1175/1520-0485(1992)022<1517:TSBLIC>2.0.CO;2.

Lentz, S. J., and D. C. Chapman, 2004: The Importance of Nonlinear Cross-Shelf Momentum Flux during Wind-Driven Coastal Upwelling. *Journal of Physical Oceanography*, **34 (11)**, 2444–2457, doi: 10.1175/JPO2644.1.

Lévy, M., L. Bopp, P. Karleskind, L. Resplandy, C. Éthé, and F. Pinsard, 2013: Physical pathways for carbon transfers between the surface mixed layer and the ocean interior. *Global Biogeochemical Cycles*, **27 (4)**, 1001–1012, doi: 10.1002/gbc.20092.

Lévy, M., P. Klein, and M. Ben Jelloul, 2009: New production stimulated by high-frequency winds in a turbulent mesoscale eddy field. *Geophysical Research Letters*, **36 (16)**, doi: 10.1029/2009GL039490.

Lewis, R., 1985: The dilution of waste in the wake of a ship. *Water Research*, **19 (8)**, 941–945, doi: 10.1016/0043-1354(85)90360-4.

Lewis, R. E., and A. M. Riddle, 1989: Sea disposal: Modelling studies of waste field dilution. *Marine Pollution Bulletin*, **20 (3)**, 124–129, doi: 10.1016/0025-326X(88)90817-X.

Li, J.-j., and M. Hitch, 2015: Ultra-fine grinding and mechanical activation of mine waste rock using a high-speed stirred mill for mineral carbonation. *International Journal of Minerals, Metallurgy, and Materials*, **22 (10)**, 1005–1016, doi: 10.1007/s12613-015-1162-3.

Li, Q. P., P. J. Franks, M. D. Ohman, and M. R. Landry, 2012: Enhanced nitrate fluxes and biological processes at a frontal zone in the southern California current system. *Journal of plankton research*, **34 (9)**, 790–801, doi: 10.1093/plankt/fbs006.

Li, Q. P., P. J. S. Franks, M. R. Landry, R. Goericke, and A. G. Taylor, 2010: Modeling phytoplankton growth rates and chlorophyll to carbon ratios in California coastal and pelagic ecosystems. *Journal of Geophysical Research: Biogeosciences*, **115 (G4)**, doi: 10.1029/2009JG001111.

Lorenzo, E. D., A. J. Miller, N. Schneider, and J. C. McWilliams, 2005: The Warming of the California Current System: Dynamics and Ecosystem Implications. *Journal of Physical Oceanography*, **35 (3)**, 336 – 362, doi: 10.1175/JPO-2690.1.

Mahadevan, A., 2016: The impact of submesoscale physics on primary productivity of plankton. *Annual Review of Marine Science*, **8 (1)**, 161–184, doi: 10.1146/annurev-marine-010814-015912, pMID: 26394203.

Mahadevan, A., J. Oliger, and R. Street, 1996a: A Nonhydrostatic Mesoscale Ocean Model. Part I: Well-Posedness and Scaling. *Journal of Physical Oceanography*, **26 (9)**, 1868–1880, doi: 10.1175/1520-0485(1996)026<1868:ANMOMP>2.0.CO;2.

Mahadevan, A., J. Oliger, and R. Street, 1996b: A Nonhydrostatic Mesoscale Ocean Model. Part II: Numerical Implementation. *Journal of Physical Oceanography*, **26 (9)**, 1881–1900, doi: 10.1175/1520-0485(1996)026<1881:ANMOMP>2.0.CO;2.

Mahadevan, A., A. Tandon, and R. Ferrari, 2010: Rapid changes in mixed layer stratification driven by submesoscale instabilities and winds. *Journal of Geophysical Research: Oceans*, **115 (C3)**, doi: 10.1029/2008JC005203.

Marchesiello, P., and P. Estrade, 2010: Upwelling limitation by onshore geostrophic flow. *Journal of Marine Research*, **68 (1)**, 37–62, doi: 10.1357/002224010793079004.

Marshall, J., A. Adcroft, C. Hill, L. Perelman, and C. Heisey, 1997: A finite-volume, incompressible navier stokes model for studies of the ocean on parallel computers. *Journal of Geophysical Research: Oceans*, **102 (C3)**, 5753–5766, doi: 10.1029/96JC02775.

Marshall, J., and T. Radko, 2003: Residual-Mean Solutions for the Antarctic Circumpolar Current and Its Associated Overturning Circulation. *Journal of Physical Oceanography*, **33 (11)**, 2341–2354, doi: 10.1175/1520-0485(2003)033<2341:RSFTAC>2.0.CO;2.

Martin, J. H., 1990: Glacial-interglacial CO_2 change: The iron hypothesis. *Paleoceanography*, **5 (1)**, 1–13, doi: 10.1029/PA005i001p00001.

Matter, J. M., and Coauthors, 2009: Permanent Carbon Dioxide Storage into Basalt: The CarbFix Pilot Project, Iceland. *Energy Procedia*, **1 (1)**, 3641–3646, doi: 10.1016/j.egypro.2009.02.160.

McDougall, T., and P. Barker, 2011: Getting started with the TEOS-10 and the Gibbs Seawater (GSW) Oceanographic Toolbox. SCOR/IAPSO WG127.

McGowan, J. A., S. J. Bograd, R. J. Lynn, and A. J. Miller, 2003: The biological response to the 1977 regime shift in the California Current. *Deep Sea Research Part II: Topical Studies in Oceanography*, **50 (14)**, 2567–2582, doi: 10.1016/S0967-0645(03)00135-8.

McGrail, B. P., H. T. Schaef, A. M. Ho, Y.-J. Chien, J. J. Dooley, and C. L. Davidson, 2006: Potential for carbon dioxide sequestration in flood basalts. *Journal of Geophysical Research: Solid Earth*, **111 (B12)**, doi: 10.1029/2005JB004169.

Messié, M., J. Ledesma, D. D. Kolber, R. P. Michisaki, D. G. Foley, and F. P. Chavez, 2009: Potential new production estimates in four eastern boundary upwelling ecosystems. *Progress in Oceanography*, **83 (1)**, 151–158, doi: 10.1016/j.pocean.2009.07.018.

Metz, B., O. Davidson, H. De Coninck, M. Loos, and L. Meyer (Eds.), 2005: *IPCC special report on carbon dioxide capture and storage*. Cambridge: Cambridge University Press, URL `https://www.ipcc.ch/report/carbon-dioxide-capture-and-storage/`.

Meysman, F. J. R., and F. Montserrat, 2017: Negative CO_2 emissions via enhanced silicate weathering in coastal environments. *Biology Letters*, **13 (4)**, 20160 905, doi: 10.1098/rsbl.2016.0905.

Middelburg, J. J., K. Soetaert, and M. Hagens, 2020: Ocean alkalinity, buffering and biogeochemical processes. *Reviews of Geophysics*, **58 (3)**, e2019RG000 681, doi: 10.1029/2019RG000681.

Montserrat, F., P. Renforth, J. Hartmann, M. Leermakers, P. Knops, and F. J. R. Meysman, 2017: Olivine dissolution in seawater: Implications for co_2 sequestration through enhanced weathering in coastal environments. *Environmental Science & Technology*, **51 (7)**, 3960–3972, doi: 10.1021/acs.est.6b05942, pMID: 28281750.

Montégut, C. d. B., G. Madec, A. S. Fischer, A. Lazar, and D. Iudicone, 2004: Mixed layer depth over the global ocean: An examination of profile data and a profile-based climatology. *Journal of Geophysical Research: Oceans*, **109 (C12)**, doi: 10.1029/2004JC002378.

Moras, C. A., L. T. Bach, T. Cyronak, R. Joannes-Boyau, and K. G. Schulz, 2022: Ocean alkalinity enhancement–avoiding runaway $CaCO_3$ precipitation during quick and hydrated lime dissolution. *Biogeosciences*, **19 (15)**, 3537–3557, doi: 10.5194/bg-19-3537-2022.

Morse, J. W., and S. He, 1993: Influences of T, S and PCO_2 on the pseudo-homogeneous precipitation of $CaCO_3$ from seawater: implications for whiting formation. *Marine Chemistry*, **41 (4)**, 291–297, doi: 10.1016/0304-4203(93)90261-L.

Mukherjee, S., S. Ramachandran, A. Tandon, and A. Mahadevan, 2016: Production and destruction of eddy kinetic energy in forced submesoscale eddy-resolving simulations. *Ocean Modelling*, **105**, 44–59, doi: 10.1016/j.ocemod.2016.07.002.

Munro, D. R., P. D. Quay, L. W. Juranek, and R. Goericke, 2013: Biological production rates off the Southern California coast estimated from triple O2 isotopes and O2: Ar gas ratios. *Limnology and Oceanography*, **58 (4)**, 1312–1328, doi: doi.org/10.4319/lo.2013.58.4.1312.

Nagai, T., N. Gruber, H. Frenzel, Z. Lachkar, J. C. McWilliams, and G.-K. Plattner, 2015: Dominant role of eddies and filaments in the offshore transport of carbon and nutrients in the California Current System. *Journal of Geophysical Research: Oceans*, **120 (8)**, 5318–5341, doi: 10.1002/2015JC010889.

National Academies of Sciences, E., and Medicine, 2021: *A research strategy for ocean-based carbon dioxide removal and sequestration*.

Nowicki, M., T. DeVries, and D. A. Siegel, 2022: Quantifying the carbon export and sequestration pathways of the ocean's biological carbon pump. *Global Biogeochemical Cycles*, **36 (3)**, e2021GB007 083, doi: 10.1029/2021GB007083.

Oerder, V., J. P. Bento, C. E. Morales, S. Hormazabal, and O. Pizarro, 2018: Coastal Upwelling Front Detection off Central Chile (36.5-37°S) and Spatio-Temporal Variability of Frontal Characteristics. *Remote Sensing*, **10 (5)**, 690, doi: 10.3390/rs10050690.

Oerder, V., F. Colas, V. Echevin, F. Codron, J. Tam, and A. Belmadani, 2015: Peru-Chile upwelling dynamics under climate change. *Journal of Geophysical Research: Oceans*, **120 (2)**, 1152–1172, doi: 10.1002/2014JC010299.

Olivieri, R. A., and F. P. Chavez, 2000: A model of plankton dynamics for the coastal upwelling system of Monterey Bay, California. *Deep Sea Research Part II: Topical Studies in Oceanography*, **47 (5-6)**, 1077–1106, doi: 10.1016/S0967-0645(99)00137-X.

Olsen, A., and Coauthors, 2017: Global Ocean Data Analysis Project, Version 2 (GLODAPv2) (NCEI Accession 0162565). Version 2. *NOAA National Centers for Environmental Information. Dataset.*, doi: 10.7289/v5kw5d97.

Omand, M. M., E. A. D'Asaro, C. M. Lee, M. J. Perry, N. Briggs, I. Cetinić, and A. Mahadevan, 2015: Eddy-driven subduction exports particulate organic carbon from the spring bloom. *Science*, **348 (6231)**, 222–225, doi: 10.1126/science.1260062.

Omand, M. M., and A. Mahadevan, 2013: Large-scale alignment of oceanic nitrate and density: Nitrate-Density Alignment. *Journal of Geophysical Research: Oceans*, **118 (10)**, 5322–5332, doi: 10.1002/jgrc.20379.

Omand, M. M., and A. Mahadevan, 2015: The shape of the oceanic nitracline. *Biogeosciences*, **12 (11)**, 3273–3287, doi: 10.5194/bg-12-3273-2015.

Paduan, J. D., and L. Washburn, 2013: High-frequency Radar Observations of Ocean Surface Currents. *Annual Review of Marine Science*, **5**, 115–136, doi: https://10.1146/annurev-marine-121211-172315.

Palacios, D. M., S. J. Bograd, R. Mendelssohn, and F. B. Schwing, 2004: Long-term and seasonal trends in stratification in the california current, 1950–1993. *Journal of Geophysical Research: Oceans*, **109 (C10)**, doi: 10.1029/2004JC002380.

Palacios, D. M., E. L. Hazen, I. D. Schroeder, and S. J. Bograd, 2013: Modeling the temperature-nitrate relationship in the coastal upwelling domain of the California Current. *Journal of Geophysical Research: Oceans*, **118 (7)**, 3223–3239, doi: 10.1002/jgrc.20216.

Pan, Y., and Coauthors, 2021: The role of Mg2+ in inhibiting $CaCO_3$ precipitation from seawater. *Marine Chemistry*, **237**, 104 036, doi: 10.1016/j.marchem.2021.104036.

Pauly, D., and V. Christensen, 1995: Primary production required to sustain global fisheries. *Nature; London*, **374 (6519)**, 255, doi: 10.1038/374255a0.

Pedregosa, F., and Coauthors, 2011: Scikit-learn: Machine Learning in Python. *Journal of Machine Learning Research*, **12 (85)**, 2825–2830, URL `http://jmlr.org/papers/v12/pedregosa11a.html`.

Penman, D. E., J. K. Caves Rugenstein, D. E. Ibarra, and M. J. Winnick, 2020: Silicate weathering as a feedback and forcing in earth's climate and carbon cycle. *Earth-Science Reviews*, **209**, 103 298, doi: 10.1016/j.earscirev.2020.103298.

Pickett, M. H., and J. D. Paduan, 2003: Ekman transport and pumping in the California Current based on the U.S. Navy's high-resolution atmospheric model (COAMPS). *Journal of Geophysical Research: Oceans*, **108 (C10)**, doi: 10.1029/2003JC001902.

Pineda, J., J. A. Hare, and S. Sponaugle, 2007: Larval transport and dispersal in the coastal ocean and consequences for population connectivity. *Oceanography*, **20 (3)**, 22–39, doi: 10.5670/oceanog.2007.27.

Pitcher, G., F. Figueiras, B. Hickey, and M. Moita, 2010: The physical oceanography of upwelling systems and the development of harmful algal blooms. *Progress in Oceanography*, **85 (1)**, 5–32, doi: 10.1016/j.pocean.2010.02.002, Special Issue on Harmful Algal Blooms in Upwelling Systems.

Pokrovsky, O., 1994: Kinetics of $CaCO_3$ homogeneous precipitation in seawater. *Mineralogical Magazine*, **58**, 738–739, doi: 10.1180/minmag.1994.58A.2.121.

Pokrovsky, O., 1998: Precipitation of calcium and magnesium carbonates from homogeneous supersaturated solutions. *Journal of Crystal Growth*, **186 (1)**, 233–239, doi: 10.1016/S0022-0248(97)00462-4.

Pokrovsky, O., and V. Savenko, 1995: The role of magnesium at homogeneous precipitation of calcium carbonate from seawater. *Oceanology of the Russian Academy of Sciences*, **34 (4)**, 493–497.

Pollard, R. T., P. B. Rhines, and R. O. R. Y. Thompson, 1973: The deepening of the wind-Mixed layer. *Geophysical Fluid Dynamics*, **4 (4)**, 381–404, doi: 10.1080/03091927208236105.

Prasanna Kumar, S., P. M. Muraleedharan, T. G. Prasad, M. Gauns, N. Ramaiah, S. N. d. Souza, S. Sardesai, and M. Madhupratap, 2002: Why is the Bay of Bengal less productive during summer monsoon compared to the Arabian Sea? *Geophysical Research Letters*, **29 (24)**, 88–1–88–4, doi: 10.1029/2002GL016013.

Qiu, B., S. Chen, P. Klein, H. Torres, J. Wang, L.-L. Fu, and D. Menemenlis, 2020: Reconstructing upper-ocean vertical velocity field from sea surface height in the presence of unbalanced motion. *Journal of Physical Oceanography*, **50 (1)**, 55 – 79, doi: 10.1175/JPO-D-19-0172.1.

Rau, G. H., 2009: Electrochemical CO_2 capture and storage with hydrogen generation. *Energy Procedia*, **1 (1)**, 823–828, doi: 10.1016/j.egypro.2009.01.109, Greenhouse Gas Control Technologies 9.

Renault, L., C. Deutsch, J. C. McWilliams, H. Frenzel, J.-H. Liang, and F. Colas, 2016: Partial decoupling of primary productivity from upwelling in the California Current system. *Nature Geoscience*, **9 (7)**, 505–508, doi: 10.1038/ngeo2722.

Renforth, P., 2012: The potential of enhanced weathering in the UK. *International Journal of Greenhouse Gas Control*, **10**, 229–243, doi: 10.1016/j.ijggc.2012.06.011.

Renforth, P., and G. Henderson, 2017: Assessing ocean alkalinity for carbon sequestration. *Reviews of Geophysics*, **55 (3)**, 636–674, doi: 10.1002/2016RG000533.

Resplandy, L., M. Lévy, and D. J. McGillicuddy Jr, 2019: Effects of eddy-driven subduction on ocean biological carbon pump. *Global Biogeochemical Cycles*, **33 (8)**, 1071–1084, doi: 10.1029/2018GB006125.

Richardson, L. F., and H. Stommel, 1948: Note on eddy diffusion in the sea. *Journal of the Atmospheric Sciences*, **5**, 238–240, doi: 10.1175/1520-0469(1948)005<0238:NOEDIT>2.0.CO;2.

Riebesell, U., and P. D. Tortell, 2011: Effects of Ocean Acidification on Pelagic Organisms and Ecosystems. *Ocean Acidification*, Oxford University Press, doi: 10.1093/oso/9780199591091.003.0011.

Rigopoulos, I., A. L. Harrison, A. Delimitis, I. Ioannou, A. M. Efstathiou, T. Kyratsi, and E. H. Oelkers, 2018: Carbon sequestration via enhanced weathering of peridotites and basalts in seawater. *Applied Geochemistry*, **91**, 197–207, doi: 10.1016/j.apgeochem.2017.11.001.

Rodríguez, E., M. Bourassa, D. Chelton, J. T. Farrar, D. Long, D. Perkovic-Martin, and R. Samelson, 2019: The Winds and Currents Mission Concept. *Frontiers in Marine Science*, **6**, doi: 10.3389/fmars.2019.00438.

Rodríguez, E., A. Wineteer, D. Perkovic-Martin, T. Gál, B. W. Stiles, N. Niamsuwan, and R. Rodriguez Monje, 2018: Estimating Ocean Vector Winds and Currents Using a Ka-Band Pencil-Beam Doppler Scatterometer. *Remote Sensing*, **10 (4)**, doi: 10.3390/rs10040576.

Roemmich, D., and J. McGowan, 1995: Climatic Warming and the Decline of Zooplankton in the California Current. *Science*, **267 (5202)**, 1324–1326, doi: 10.1126/science.267.5202.1324.

Rogelj, J., and Coauthors, 2018: Scenarios towards limiting global mean temperature increase below 1.5 C. *Nature Climate Change*, **8 (4)**, 325–332, doi: 10.1038/s41558-018-0091-3.

Rossi, V., M. Feng, C. Pattiaratchi, M. Roughan, and A. M. Waite, 2013: On the factors influencing the development of sporadic upwelling in the Leeuwin Current system. *Journal of Geophysical Research: Oceans*, **118 (7)**, 3608–3621, doi: 10.1002/jgrc.20242.

Rühmkorff, S., F. Wolf, J. Vajedsamiei, F. R. Barboza, C. Hiebenthal, and C. Pansch, 2023: Marine heatwaves and upwelling shape stress responses in a keystone predator. *Proceedings of the Royal Society B*, **290 (1991)**, 20222 262, doi: 10.1098/rspb.2022.2262.

Ruiz, S., and Coauthors, 2019: Effects of Oceanic Mesoscale and Submesoscale Frontal Processes on the Vertical Transport of Phytoplankton. *Journal of Geophysical Research: Oceans*, **124 (8)**, 5999–6014, doi: 10.1029/2019JC015034.

Rykaczewski, R. R., and J. P. Dunne, 2010: Enhanced nutrient supply to the California Current Ecosystem with global warming and increased stratification in an earth system model. *Geophysical Research Letters*, **37 (21)**, doi: 10.1029/2010GL045019.

Rykaczewski, R. R., J. P. Dunne, W. J. Sydeman, M. García-Reyes, B. A. Black, and S. J. Bograd, 2015: Poleward displacement of coastal upwelling-favorable winds in the ocean's eastern boundary currents through the 21st century. *Geophysical Research Letters*, **42 (15)**, 6424–6431, doi: 10.1002/2015GL064694.

Rypina, I. I., S. R. Jayne, S. Yoshida, A. M. Macdonald, E. Douglass, and K. Buesseler, 2013: Short-term dispersal of fukushima-derived radionuclides off japan: modeling efforts and model-data intercomparison. *Biogeosciences*, **10 (7)**, 4973–4990, doi: 10.5194/bg-10-4973-2013.

Sabine, C. L., and Coauthors, 2004: The Oceanic Sink for Anthropogenic CO_2. *Science*, **305 (5682)**, 367–371, doi: 10.1126/science.1097403.

Sano, Y., Y. Hao, and F. Kuwahara, 2018: Development of an electrolysis based system to continuously recover magnesium from seawater. *Heliyon*, **4 (11)**, e00 923, doi: 10.1016/j.heliyon.2018.e00923.

Sarmiento, J. L., and N. Gruber, 2006: Ocean Biogeochemical Dynamics. Princeton University Press.

Sauzède, R., and Coauthors, 2016: A neural network-based method for merging ocean color and argo data to extend surface bio-optical properties to depth: Retrieval of the particulate backscattering coefficient. *Journal of Geophysical Research: Oceans*, **121 (4)**, 2552–2571.

Sauzède, R., H. Claustre, R. P. Remanan, J. Uitz, and S. Guinehut, 2021: New global vertical distribution of gridded particulate organic carbon and chlorophyll-a concentration using machine learning for CMEMS. *9th EuroGOOS International conference*, 313–320, URL `https://hal.science/hal-03335370v2f`.

Schmidtko, S., G. C. Johnson, and J. M. Lyman, 2013: MIMOC: A global monthly isopycnal upper-ocean climatology with mixed layers. *Journal of Geophysical Research: Oceans*, **118 (4)**, 1658–1672, doi: 10.1002/jgrc.20122.

Schuiling, R., and P. De Boer, 2011: Rolling stones; fast weathering of olivine in shallow seas for cost-effective CO_2 capture and mitigation of global warming and ocean acidification. *Earth System Dynamics Discussions*, **2**, 551–568, doi: 10.5194/esdd-2-551-2011.

Sein, D. V., and Coauthors, 2015: Regionally coupled atmosphere-ocean-sea ice-marine biogeochemistry model rom: 1. description and validation. *Journal of Advances in Modeling Earth Systems*, **7 (1)**, 268–304, doi: 10.1002/2014MS000357.

Shcherbina, A. Y., E. A. D'Asaro, C. M. Lee, J. M. Klymak, M. J. Molemaker, and J. C. McWilliams, 2013: Statistics of vertical vorticity, divergence, and strain in a developed submesoscale turbulence field. *Geophysical Research Letters*, **40 (17)**, 4706–4711, doi: 10.1002/grl.50919.

Siegel, D. A., T. DeVries, S. Doney, and T. Bell, 2021: Assessing the sequestration time scales of some ocean-based carbon dioxide reduction strategies. *Environmental Research Letters*, **16 (10)**, 104 003, doi: 10.1088/1748-9326/ac0be0.

Sinha, A., and R. Abernathey, 2021: Estimating Ocean Surface Currents With Machine Learning. *Frontiers in Marine Science*, **8**, 612, doi: 10.3389/fmars.2021.672477.

Song, Y. T., and Y. Chao, 2004: A theoretical study of topographic effects on coastal upwelling and cross-shore exchange. *Ocean Modelling*, **6 (2)**, 151–176, doi: 10.1016/S1463-5003(02)00064-1.

Sonnewald, M., R. Lguensat, D. C. Jones, P. Dueben, J. Brajard, and V. Balaji, 2021: Bridging observations, theory and numerical simulation of the ocean using machine learning. *Environmental Research Letters*, **16 (7)**, doi: 10.1088/1748-9326/ac0eb0.

Steinberg, D. K., and M. R. Landry, 2017: Zooplankton and the ocean carbon cycle. *Annual review of marine science*, **9**, 413–444, doi: 10.1146/annurev-marine-010814-015924.

Stukel, M. R., and H. W. Ducklow, 2017: Stirring up the biological pump: Vertical mixing and carbon export in the southern ocean. *Global Biogeochemical Cycles*, **31 (9)**, 1420–1434, doi: 10.1002/2017GB005652.

Su, Z., J. Wang, P. Klein, A. F. Thompson, and D. Menemenlis, 2018: Ocean submesoscales as a key component of the global heat budget. *Nature communications*, **9 (1)**, 1–8, doi: 10.1038/s41467-018-02983-w.

Subhas, A. V., L. Marx, S. Reynolds, A. Flohr, E. W. Mawji, P. J. Brown, and B. Cael, 2022: Microbial ecosystem responses to alkalinity enhancement in the north atlantic subtropical gyre. *Frontiers in Climate*, **4**, doi: 10.3389/fclim.2022.78499.

Sun, W., S. Jayaraman, W. Chen, K. A. Persson, and G. Ceder, 2015: Nucleation of metastable aragonite caco$_3$ in seawater. *Proceedings of the National Academy of Sciences*, **112 (11)**, 3199–3204, doi: 10.1073/pnas.1423898112.

Sydeman, W. J., M. García-Reyes, D. S. Schoeman, R. R. Rykaczewski, S. A. Thompson, B. A. Black, and S. J. Bograd, 2014: Climate change and wind intensification in coastal upwelling ecosystems. *Science*, **345 (6192)**, 77–80, doi: 10.1126/science.1251635.

Szoeke, R. A. D., and J. G. Richman, 1984: On wind-driven mixed layers with strong horizontal gradients—a theory with application to coastal upwelling. *Journal of Physical Oceanography*, **14 (2)**, 364 –377, doi: https:/doi.org/10.1175/1520-0485(1984)014<0364:OWDMLW>2.0.CO;2.

Tarry, D. R., and Coauthors, 2021: Frontal Convergence and Vertical Velocity Measured by Drifters in the Alboran Sea. *Journal of Geophysical Research: Oceans*, **126 (4)**, e2020JC016 614, doi: 10.1029/2020JC016614.

Thomas, L. N., A. Tandon, and A. Mahadevan, 2008: Submesoscale processes and dynamics. *Geophysical Monograph Series*, **177**, doi: 10.1029/177GM04.

Thomsen, S., X. Capet, and V. Echevin, 2021: Competition between baroclinic instability and ekman transport under varying buoyancy forcings in upwelling systems: An idealized analog to the southern ocean. *Journal of Physical Oceanography*, doi: 10.1175/JPO-D-20-0294.1.

Thorsen, T. G., R. I. Hagen, O. Wærnes, and B. Langseth, 2000: Method for production of magnesium hydroxide from sea water. URL `https://patentscope.wipo.int/search/en/detail.jsf?docId=WO2000029326`, last access: 1 June 2022.

Thyng, K. M., C. A. Greene, R. D. Hetland, H. M. Zimmerle, and S. F. DiMarco, 2016: True Colors of Oceanography: Guidelines for Effective and Accurate Colormap Selection. *Oceanography*, **29 (3)**, 9 – 13, doi: 10.5670/oceanog.2016.66.

Torres, R., D. Turner, J. Rutllant, M. Sobarzo, T. Antezana, and H. E. Gonzalez, 2002: CO_2 outgassing off central Chile (31–30°S) and northern Chile (24–23°S) during austral summer 1997: the effect of wind intensity on the upwelling and ventilation of CO_2-rich waters. *Deep Sea Research Part I: Oceanographic Research Papers*, **49 (8)**, 1413–1429, doi: 10.1016/S0967-0637(02)00034-1.

Tyka, M. D., C. Van Arsdale, and J. C. Platt, 2022: Co_2 capture by pumping surface acidity to the deep ocean. *Energy & Environmental Science*, **15 (2)**, 786–798, doi: 10.1039/D1EE01532J.

Uchida, T., D. Balwada, R. Abernathey, G. McKinley, S. Smith, and M. Lévy, 2019: The Contribution of Submesoscale over Mesoscale Eddy Iron Transport in the Open Southern Ocean. *Journal of Advances in Modeling Earth Systems*, **11 (12)**, 3934–3958, doi: 10.1029/2019MS001805.

Uitz, J., H. Claustre, A. Morel, and S. B. Hooker, 2006: Vertical distribution of phytoplankton communities in open ocean: An assessment based on surface chlorophyll. *Journal of Geophysical Research: Oceans*, **111 (C8)**, doi: 10.1029/2005JC003207.

van Geen, A., R. Takesue, J. Goddard, T. Takahashi, J. Barth, and R. Smith, 2000: Carbon and nutrient dynamics during coastal upwelling off cape blanco, oregon. *Deep Sea Research Part II: Topical Studies in Oceanography*, **47 (5)**, 975–1002, doi: 10.1016/S0967-0645(99)00133-2.

van Sebille, E., and Coauthors, 2018: Lagrangian ocean analysis: Fundamentals and practices. *Ocean Modelling*, **121**, 49–75, doi: 10.1016/j.ocemod.2017.11.008.

Volk, T., and M. I. Hoffert, 1985: Ocean carbon pumps: Analysis of relative strengths and efficiencies in ocean-driven atmospheric CO_2 changes. *The carbon cycle and atmospheric CO2: natural variations Archean to present*, **32**, 99–110.

Wang, D., T. C. Gouhier, B. A. Menge, and A. R. Ganguly, 2015: Intensification and spatial homogenization of coastal upwelling under climate change. *Nature*, **518 (7539)**, 390–394, doi: 10.1038/nature14235.

Wang, H., D. J. Pilcher, K. A. Kearney, J. N. Cross, O. M. Shugart, M. D. Eisaman, and B. R. Carter, 2023: Simulated impact of ocean alkalinity enhancement on atmospheric co_2 removal in the bering sea. *Earth's Future*, **11 (1)**, e2022EF002 816, doi: 10.1029/2022EF002816, e2022EF002816 2022EF002816.

Wang, J., G. R. Flierl, J. H. LaCasce, J. L. McClean, and A. Mahadevan, 2013: Reconstructing the Ocean's Interior from Surface Data. *Journal of Physical Oceanography*, **43 (8)**, 1611 – 1626, doi: 10.1175/JPO-D-12-0204.1.

Wang, J., L.-L. Fu, B. Qiu, D. Menemenlis, J. T. Farrar, Y. Chao, A. F. Thompson, and M. M. Flexas, 2018: An Observing System Simulation Experiment for the Calibration and Validation of the Surface Water Ocean Topography Sea Surface Height Measurement Using In Situ Platforms. *Journal of Atmospheric and Oceanic Technology*, **35 (2)**, 281 – 297, doi: 10.1175/JTECH-D-17-0076.1.

Wanninkhof, R., 1992: Relationship between wind speed and gas exchange over the ocean. *Journal of Geophysical Research: Oceans*, **97 (C5)**, 7373–7382, doi: 10.1029/92JC00188.

Whitt, D., M. Lévy, and J. R. Taylor, 2017: Low-frequency and high-frequency oscillatory winds synergistically enhance nutrient entrainment and phytoplankton at fronts. *Journal of Geophysical Research: Oceans*, **122 (2)**, 1016–1041, doi: 10.1002/2016JC012400.

Wijesekera, H. W., J. S. Allen, and P. A. Newberger, 2003: Modeling study of turbulent mixing over the continental shelf: Comparison of turbulent closure schemes. *Journal of Geophysical Research: Oceans*, **108 (C3)**, doi: 10.1029/2001JC001234.

Wilkerson, F., R. Dugdale, R. Kudela, and F. Chavez, 2000: Biomass and productivity in Monterey Bay, California: contribution of the large phytoplankton. *Deep Sea Research Part II: Topical Studies in Oceanography*, **47 (5-6)**, 1003–1022, doi: 10.1016/S0967-0645(99)00134-4.

Wunsch, C., and P. Heimbach, 2013: Chapter 21 - dynamically and kinematically consistent global ocean circulation and ice state estimates. *Ocean Circulation and Climate*, G. Siedler, S. M. Griffies, J. Gould, and J. A. Church, Eds., International Geophysics, Vol. 103, Academic Press, 553–579, doi: 10.1016/B978-0-12-391851-2.00021-0.

Wunsch, C., P. Heimbach, R. M. Ponte, I. Fukumori, and E.-G. C. MEMBERS, 2009: The global general circulation of the ocean estimated by the ecco-consortium. *Oceanography*, **22 (2)**, 88–103, doi: 10.5670/oceanog.2009.41.

Xiu, P., F. Chai, E. Curchitser, and F. Castruccio, 2018: Future changes in coastal upwelling ecosystems with global warming: The case of the California Current System. *Scientific Reports*, **8 (2866)**, doi: 10.1038/s41598-018-21247-7.

Xu, B., N. Wang, T. Chen, and M. Li, 2015: Empirical evaluation of rectified activations in convolutional network. *arXiv preprint arXiv:1505.00853*, doi: 10.48550/arXiv.1505.00853.

Yoon, J.-E., and Coauthors, 2018: Reviews and syntheses: Ocean iron fertilization experiments–past, present, and future looking to a future Korean Iron Fertilization Experiment in the Southern Ocean (KIFES) project. *Biogeosciences*, **15 (19)**, 5847–5889, doi: 10.5194/bg-15-5847-2018.

Zeebe, R. E., and D. Wolf-Gladrow, 2001: *CO_2 in seawater: equilibrium, kinetics, isotopes*. 65, Elsevier Oceanography Series, Elsevier Science, London, UK.

Zhang, H., D. Menemenlis, and I. Fenty, 2018: ECCO LLC270 Ocean-Ice State Estimate. URL `https://dspace.mit.edu/handle/1721.1/119821`.